Anal. Methods Environ. Chem. J. 7 (4) (2024) 5-16

AMECJ

Research Article, Issue 4
Analytical Methods in Environmental Chemistry Journal
Journal home page: www.amecj.com/ir

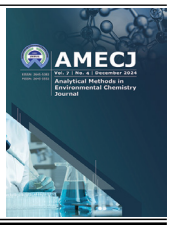

Removal of p-nitrophenol from industrial wastewater using electrochemical oxidation with Mn-PbO_2 electrode: Analysis by high-performance liquid chromatography technique

Mahla Mazloomian [a], Ali Asghar Ebrahimi [a,*], Maryam Dolatabadi [b], and Saeid Ahmadzadeh [c, d,*]

[a] *Environmental Science and Technology Research Center, Department of Environmental Health Engineering, School of Public Health, Shahid Sadoughi University of Medical Sciences, Yazd, Iran.*

[b] *Environmental Health Engineering Research Center, Kerman University of Medical Sciences, Kerman, Iran*

[c] *Pharmaceutics Research Center, Institute of Neuropharmacology, Kerman University of Medical Sciences, Kerman, Iran*

[d] *Pharmaceutical Sciences and Cosmetic Products Research Center, Kerman University of Medical Sciences, Kerman, Iran*

ARTICLE INFO:

Received 12 Aug 2024

Revised form 14 Oct 2024

Accepted 15 Nov 2024

Available online 29 Dec 2024

Keywords:
Anodic Oxidation,
Modified Electrode,
P-nitrophenol,
Degradation,
High-performance liquid chromatography

ABSTRACT

The compound known as *p*-nitrophenol (PNP) possesses toxic properties and exhibits considerable resistance to natural degradation upon its introduction into the environment. Consequently, devising efficient and secure approaches to remove PNP is imperative. The current study synthesized a Mn-PbO_2 electrode with a Sn-Sb intermediate layer via an electrochemical deposition approach. The fabricated electrode was then utilized for the electrocatalytic oxidation of PNP. The high-performance liquid chromatography (HPLC) measured the residual of PNP in the treated samples. The results obtained from the regression analysis determined that the experimental data exhibited the highest level of conformity with the second-order polynomial model. The coefficient of determination (R^2) was determined to be 0.9960. Furthermore, the adjusted R^2 (Adj. R^2) value was found to be 0.9941, Lastly, the predicted R^2 (pred. R^2) value was calculated as 0.9866. The maximum removal efficiency of PNP, reaching 98.4%, was achieved by employing the optimal conditions, which included an initial PNP concentration of 2.0 mg L^{-1}, intensity of 25 mA, and oxidation time of 40 min. The kinetics of the process follow the pseudo-first-order model with R^2=0.9892. This study confirms that utilizing the Mn-PbO_2 electrode in an anodic oxidation process is an efficient and highly effective method for removing PNP.

1. Introduction

The rapid advancement of industries has resulted in the generation of a significant quantity of perilous waste materials and contaminants, including pharmaceuticals, pesticides, dyes, heavy metals, and phenolic compounds [1, 2]. These substances are being released into the environment, posing a substantial threat to human health and the well-being of organisms. The exponential expansion of the chemical and petrochemical industries in recent years has generated significant concern regarding the disposal practices employed for nitroaromatic compounds [3, 4]. Frequently, these compounds are discarded inappropriately by industrial sectors [5, 6]. Among these compounds, *p*-nitrophenol (PNP) stands out as a notable example, extensively utilized

*Corresponding Author: Ali Asghar Ebrahimi and Saeid Ahmadzadeh
Email: saeid.ahmadzadeh@kmu.ac.ir and ebrahimi20007@gmail.com
https://doi.org/10.24200/amecj.v7.i04.331

as an intermediate in the synthesis of plastics, dyes, pesticides, explosives, and other related substances [7, 8]. PNP is extensively employed as a raw material or intermediate compound in the production of specific pharmaceuticals, pesticides, explosives, dyes, etc. Industries involved, release substantial volumes of wastewater containing PNP into the environment [9, 10]. The detection of various concentrations of PNP has been commonly identified in various environmental samples (surface and groundwater, soil). PNP has been found to possess carcinogenic, mutagenic, and teratogenic properties. Specifically, exposure to PNP can result in the development of blood disorders. It may potentially cause harm to the kidneys, pancreas, central nervous system, and liver, as well as induce methemoglobin formation and systemic poisoning in cases of acute exposure [11]. Due to the presence of PNP residue in different environmental settings and its detrimental effects on living organisms and the environment, the United States Environmental Protection Agency (USEPA) has classified PNP as a contaminant of high priority in wastewater [12]. Over the past few decades, extensive endeavors have been dedicated to the degradation of PNP through various strategies, including physical adsorption, chemical transformation, biological degradation, coagulation, and membrane processes. These conventional approaches have demonstrated the ability to decompose PNP [13-15]. Nonetheless, their widespread adoption has been impeded by the high operational expenses and limited efficiency of these technologies. It is worth noting the biological treatment processes to break down PNP; these methods encounter challenges arising from the elevated concentration of PNP and the extended hydraulic retention time required, primarily due to PNP's toxic or resistant nature. Consequently, there is a need to establish an efficient, durable, and viable treatment methodology that can effectively remove PNP and enhance the biodegradation of wastewater containing high concentrations of PNP [16]. The generation of reactive radical species and their significant potential for the degradation and complete mineralization of persistent organic pollutants have led to the notable interest of numerous researchers in advanced oxidation processes (AOPs). Within AOPs, the anodic oxidation (AO) process is an efficient, promising, and environmentally friendly approach [17, 18]. The effectiveness and elimination of contaminants in the AO process heavily rely on the capabilities of the anodic materials. A range of anodic materials, including SnO_2, PbO_2 , etc., have been utilized in the AO process [19, 20]. Among these materials, PbO_2 is an ideal choice for anode material due to its ease of preparation, suitable electrical conductivity, high efficiency, and substantial potential for oxygen evolution [21]. Consequently, the present investigation employs the anodic oxidation process to remove PNP. This study involved the fabrication and optimization of SnO_2-Sb_2O_3, PbO_2, and Mn-PbO_2 electrodes, followed by an investigation into their characteristics and performance. The impact of operational parameters, including initial concentration, pH, current density, and electrolysis time, on the removal of PNP was examined and optimized using a response surface methodology (RSM). The service lifetime, linear polarization, safety evaluation, and stability of the prepared electrodes were assessed. Additionally, the intermediate products and degradation pathway were proposed.

2. Material and methods

2.1. Chemicals

$C_6H_5NO_3$ (*p*-nitrophenol, CAS #: 100-02-7), NaOH (sodium hydroxide, CAS #: 1310-73-2), HCl (hydrochloric acid, CAS #: 100317), $SnCl_4.5H_2O$ (tin(IV) chloride, CAS #: 1310-73-2), HNO_3 (nitric acid, CAS #:7697-37-2), $Pb(NO_3)_2$ (lead (II) nitrate, CAS #: 10099-74-8), MnO_2 (manganese(IV) oxide, CAS #: 1313-13-9), NaF (sodium fluoride, CAS #: 7681-49-4), $SbCl_3$ (antimony(III) chloride, CAS #: 9-91-10025), and H_2PO_4 (ortho-phosphoric acid, CAS #:7664-38-2), were purchased from Merck® Millipore Co (Germany). Methanol UHPLC grade ≥99.99 % was prepared from Scharlau® Co. (Sapin). All chemicals used without further purification as received.

2.2. Preparation of electrode

This study employed a high-purity titanium electrode (Ti, 99.5%) as the primary substrate for the modified

electrodes. To eliminate undesirable impurities, such as oxide films, from the surface of the titanium plate (with dimensions of 10 cm × 2.0 cm × 0.1 cm), the plate was polished using sandpaper and then subjected to ultrasonic pretreatment in an ethanol solution. To remove any oil stains present on the electrode's surface, the plate was exposed to a 40% sodium hydroxide solution and heated at 80 °C for a duration of 180 minutes. Subsequently, the electrode was immersed in a boiling 20% hydrochloric acid solution for 60 minutes to etch its surface. Finally, the electrode was thoroughly rinsed with a sample amount of deionized distilled water (DDW). To enhance the catalytic properties of the electrode under investigation, the SnO_2-Sb_2O_3 sub-layer (Sn/Sb) was thermally deposited onto its surface using the dip-coating method, as previously described by Yao *et al.* [22]. Following that, an intermediate α/PbO_2 layer was electrochemically deposited onto the Sn/Sb sub-layer to reduce the interfacial resistance of the fabricated electrode, as outlined by Duan et al. [23]. In the final stage, the fabrication procedure of the Mn-PbO_2 electrode was refined using the electrochemical deposition technique as previously described by Yu *et al*. [24].

2.3. Analysis methods

The residual of PNP in the treated samples was evaluated quantitatively by the HPLC system. The HPLC system utilized in this study was from Smartline Knauer, Germany. It comprised an online vacuum degasser, a quaternary pump, an autosampler, a column oven, and a photodiode-array detector. The mobile phase MeOH: H_2O (water with 0.1% phosphorous acid) 40/60 (%v/v), C_{18} (250 mm × 4.6 mm, 5 µm), temperature of the column oven 25˚C, flow rate 0.8 mL min^{-1}, and detector was set to a wavelength of 280 nm [25]. The morphology and X-ray diffraction patterns of surface electrodes were examined during the manufacturing process using field-emission scanning electron microscopy (FESEM- MIRA3 FE-SEM, Tescan®, Czech) and X-ray diffraction (XRD-Rigaku D/Max 2500, Rigaku).

2.4. Electrochemical treatment setup

The electrochemical treatment procedure was performed in a Pyrex reactor with a batch capacity of 500 mL, utilizing an MP-3005D Megatek power supply and a Heidolph magnetic stirrer. Two electrodes were used: a stainless-steel plate serving as the cathode and the proposed electrode functioning as the anode. Both electrodes had identical dimensions, with an immersed area of 15 cm^2 (5.0 cm × 2.0 cm × 0.1 cm), and were positioned at a distance of 4.0 cm from each other. A supporting electrolyte consisting of 50 mM Na_2SO_4 was employed in all experimental trials.

2.5. Design of Experiments

Response surface methodology (RSM) was adopted to optimize the process variables, with the PNP removal efficiency as the response. RSM offers the advantages of process modeling and enables a faster and more systematic investigation with fewer experimental runs compared to the laborious approach of varying one factor at a time. The treatment experiments were designed, and the response was analyzed using Design-Expert software (Version 11.0.4.0). The central composite design (CCD) approach under the RSM model was employed to describe the relationship between variables and the response and the interactions between variables. The independent variables consisting of PNP concentration, current, solution pH, and oxidation time were coded at five levels (+α, +1, 0, -1, -α), and these levels are presented in Table 1.

Table 1. Levels of main variables for the PNP removal using an anodic oxidation process.

Variables (X_i)	Levels				
	-α	**-1**	**0**	**+1**	**+α**
X_1 = Initial PNP concentration (mg L^{-1})	1	2	3	4	5
X_2 = Intensity (mA)	10	15	20	25	30
X_3 = Oxidation time (min)	10	20	30	40	50

A proposed model based on a second-order polynomial was employed to estimate the PNP removal efficiency of the AO process. This model aimed to describe the relationship between the main operating parameters, which were treated as independent variables [26, 27].

$$Y = \beta_0 + \sum_{i=1}^{n} \beta_i X_i + \sum_{i=1}^{n} \beta_{ii} X_i^2 + \sum_{i=1}^{n-1} \sum_{j=i+1}^{n} \beta_{ij} X_i X_j + \varepsilon \quad \text{(Eq.1)}$$

YIn the developed model, Y represents the response variable, which consists of PNP removal efficiency as a response (Eq.1). The constant coefficient is denoted as β_0, while β_i, β_{ii}, and β_{ij} represent the linear, quadratic, and interaction coefficients, respectively. The variable number is denoted as n, and ε represents the error in the model. Statistical analysis of the developed model was conducted using Analysis of Variance (ANOVA), with the *p*-value set at a significance level of ≤ 0.05 and a confidence level (CI) of 95%. A total of 30 runs were performed based on the CCD [28, 29].

3. Result and Discussion

3.1. Characterization of prepared electrode

Figure 1a displays the FE-SEM image of the Mn-PbO2 electrode at 50,000X magnification, which demonstrates a notable enhancement in the surface morphology of the fabricated electrode. The electrocatalytic performance of the electrode in producing hydroxyl radicals is enhanced by the presence of a uniform surface devoid of pores and cracks, as depicted in Figure 1a. This surface is supported by smaller-sized crystals, leading to improved performance. Figure 1b demonstrates the X-ray diffraction pattern of the prepared electrode. Also, Figure 1b demonstrates the XRD pattern of the Mn-PbO_2 electrode.

3.2. Analysis of variance (ANOVA)

RSM as a statistical approach employed to optimize the treatment process variables and reduce the number of experimental runs and the obtained removal efficiencies as the response values of the developed process summarized in Table 2.

The results of the variance analysis (ANOVA) are presented in Table 3. The coefficients of determination were calculated to assess the proposed model's fit. It can be observed that the coefficients of determination (R^2), adjusted R^2 (Adj.R^2), and predicted R^2 (Pred.R^2) for the removal efficiency of PNP were determined to be 0.9960, 0.9941, and 0.9866, respectively. The results indicated that the Adj.R^2 closely approximated the Pred.R^2. The findings suggested that if the

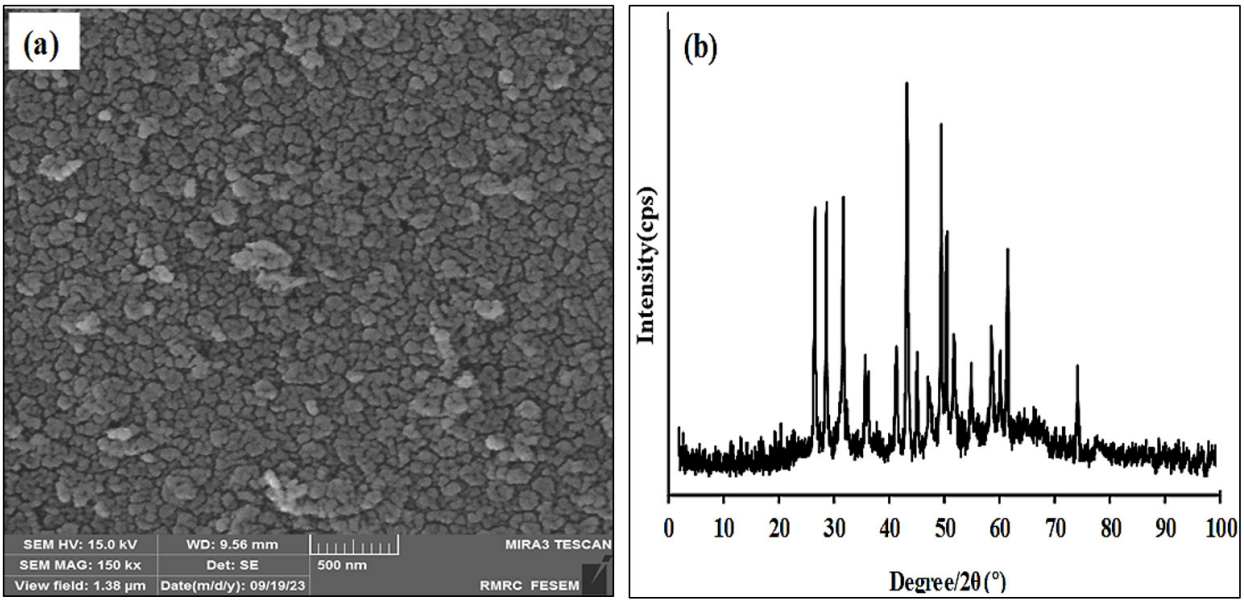

Fig. 1. (a) FE-SEM micrograph **(b)** XRD pattern of the Mn-PbO_2 electrode

Table 2. Experimental factors and the obtained PNP removal efficiency

Run	Actual values			Coded values			PNP removal (%)
	A (mg L^{-1})	B (mA)	C (min)	X_1	X_2	X_3	
1	4	15	40	1	-1	1	80.2
2	3	20	30	0	0	0	89.4
3	4	25	20	1	1	-1	85.4
4	3	20	10	0	0	-2	80.2
5	3	20	30	0	0	0	89.8
6	2	25	40	-1	1	1	98.4
7	2	15	20	-1	-1	-1	83.1
8	3	30	30	0	+2	0	91.7
9	3	10	30	0	-2	0	73.8
10	3	20	30	0	0	0	89.1
11	3	20	50	0	0	2	91.5
12	2	15	40	-1	-1	1	88.0
13	4	15	20	1	-1	-1	76.4
14	3	20	30	0	0	0	89.6
15	4	25	40	1	1	1	92.1
16	1	20	30	-2	0	0	95.8
17	5	20	30	2	0	0	82.1
18	3	20	30	0	0	0	89.6
19	3	20	30	0	0	0	90.1
20	2	25	20	-1	1	-1	91.5

Table 3. ANOVA results for the developed model

Source	Sum of squares	df	Mean square	F-value	p-value
Model	752.91	6	125.48	534.68	<0.0001
X_1	184.28	1	184.28	785.21	<0.0001
X_2	356.27	1	356.27	1518.02	<0.0001
X_3	126.00	1	126.00	536.88	<0.0001
$X_2 X_3$	3.00	1	3.00	12.79	0.0034
X_2^2	73.54	1	73.54	313.36	<0.0001
X_3^2	21.13	1	21.13	90.05	<0.0001
Residual	3.05	13	0.2347	---	---
Lack of Fit	2.47	8	0.3089	2.66	0.1478
Pure Error	0.5800	5	0.1160	---	---
Cor Total	755.96	19	---	---	---

discrepancy between the values of R^2 for the Adj. R^2 and Pred.R^2 responses is less than 0.20, it would indicate a reasonable level of agreement between them. The precision of the developed degradation model, as indicated by the adequate precision (AP) representing the signal-to-noise ratio, was found to be 87.5, exceeding the threshold of 4 [30, 31]. Additionally, to assess the adequacy of the model, the *p*-value for lack of fit, which reflects the variation in the data within the developed models, was utilized. The results obtained indicated that there was no significant lack of fit error for any of the responses. This suggests that the developed model was statistically significant and capable of explaining the relationship between the primary operating parameters and the removal efficiencies of PNP, with a confidence level (CI) of 95%.

Based on the evaluation of the model's degree of fitness, considering the model's low p-value (<0.0001) and high R^2, it can be inferred that the second-order regression model provides the best fit for predicting the removal efficiencies of PNP. Equation 2 (PNP removal efficiency=R %) presents the quadratic regression model in this study.

$$R\,(\%) = 89.4 - 3.29\,X_1 + 4.72\,X_2 + 2.81\,X_3 + 0.61\,X_2\,X_3 - 1.67\,X_2^2 - 0.90\,X_3^2 \quad \text{(Eq.2)}$$

In this context, Y represents PNP removal efficiency. The coded variables X_1, X_2, and X_3 correspond to the three main factors: PNP concentration, intensity, and oxidation time. It is worth noting that within the constructed regression model, a positive sign indicates synergistic effects, while a negative sign signifies antagonistic effects.

Figure 2a compares the observed and predicted values of PNP removal efficiency. It can be observed that these values closely align along a straight line, the obtained data have a normal distribution, and indicating a satisfactory agreement between the experimental results and the predicted response. Figure 2b displays the residuals plotted against the externally studentized residuals, revealing the data composition pattern. The residuals scatter randomly around the baseline without any discernible trend for the developed models. Both plots provide evidence for the reliability and adequacy of the proposed models.

3.3. Effect of parameters on the removal efficiency

PNP concentrations and intensity were investigated, as well as the removal efficiency of PNP. The outcomes of this investigation are graphically represented and demonstrated through a 3D plot, depicted in Figure 3.

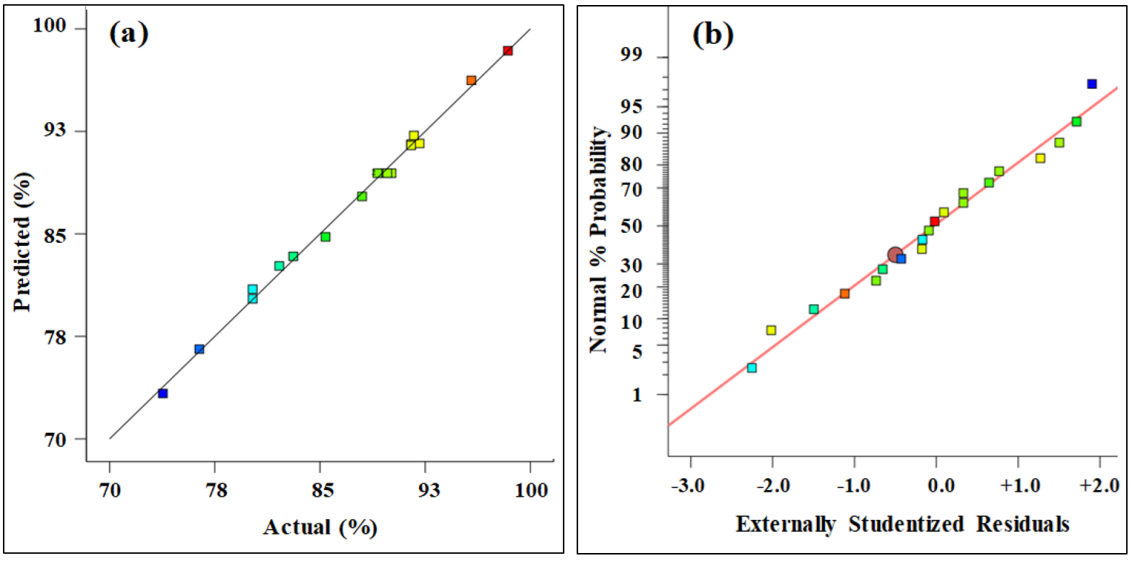

Fig. 2. (a) plot of the actual and predicted value of PNP removal efficiency, (b) normal plot of the externally studentized residuals.

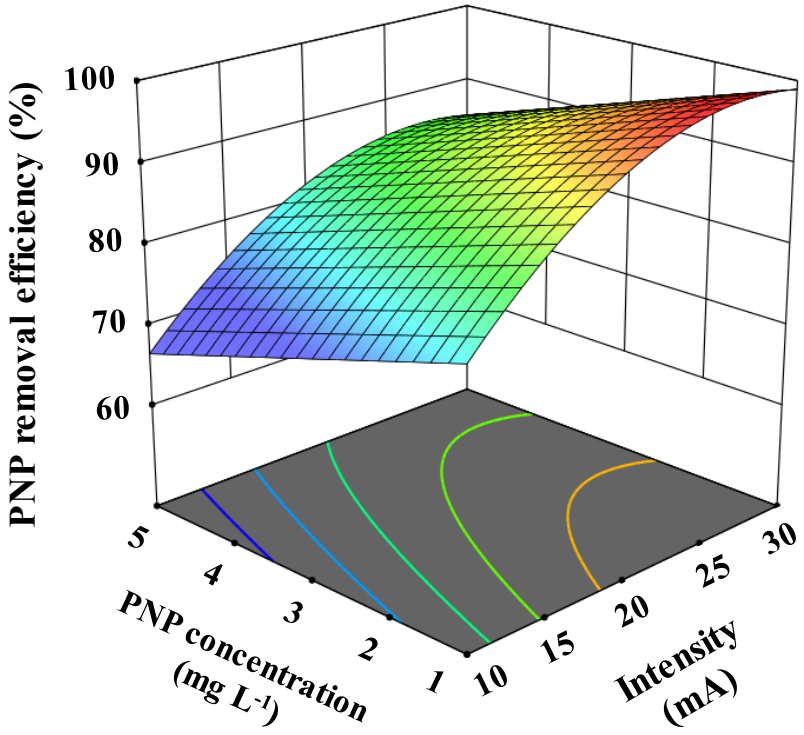

Fig. 3. 3D plot of PNP concentration and intensity for PNP removal efficiency

The increase in PNP concentration from 1.0 mg L^{-1} to 5.0 mg L^{-1} led to a substantial reduction in the removal efficiencies of PNP (96.2% to 82.7%). These changes occurred while maintaining the intensity and oxidation time at their central values. The reduction in removal efficiencies of the treatment processes was observed when the initial concentration of PNP was increased. This phenomenon can be elucidated by considering the following factors. Firstly, the surplus presence of PNP molecules and their intermediates on the electrode surface led to contamination, thereby diminishing the production of OH radicals through electrochemical generation [32]. Secondly, in the consistent state of the treatment procedure, the quantity of OH radicals produced remained constant, irrespective of the increasing concentration of contaminant molecules. Consequently, the efficacy of the processes in eliminating contaminants decreased [33].

The intensity in electro-catalytic reactions is of significant importance as it manages the electron transfer rate by generating OH radicals. The findings in Figure 3 illustrate a noteworthy improvement in the effectiveness of PNP removal, ranging from 73.3% to 92.1%, when the intensity is raised from 10 to 30 mA. It is worth noting that the initial concentration and oxidation time were kept constant throughout the experiment at their average values. The increase in current density resulted in an increased production of OH radicals, thereby enhancing removal efficiency. However, it should be noted that this improvement only sometimes positively impacts the process. Excessive current density values can lead to the decomposition of the electrode and result in energy loss. Moreover, it can promote the oxygen evolution reaction and water electrolysis, which have detrimental effects on the treatment process [34, 35]. Additionally, the combined influence of oxidation time and intensity on the efficiencies of PNP removal was investigated. The results of this investigation are presented in the contour plot depicted in Figure 4.

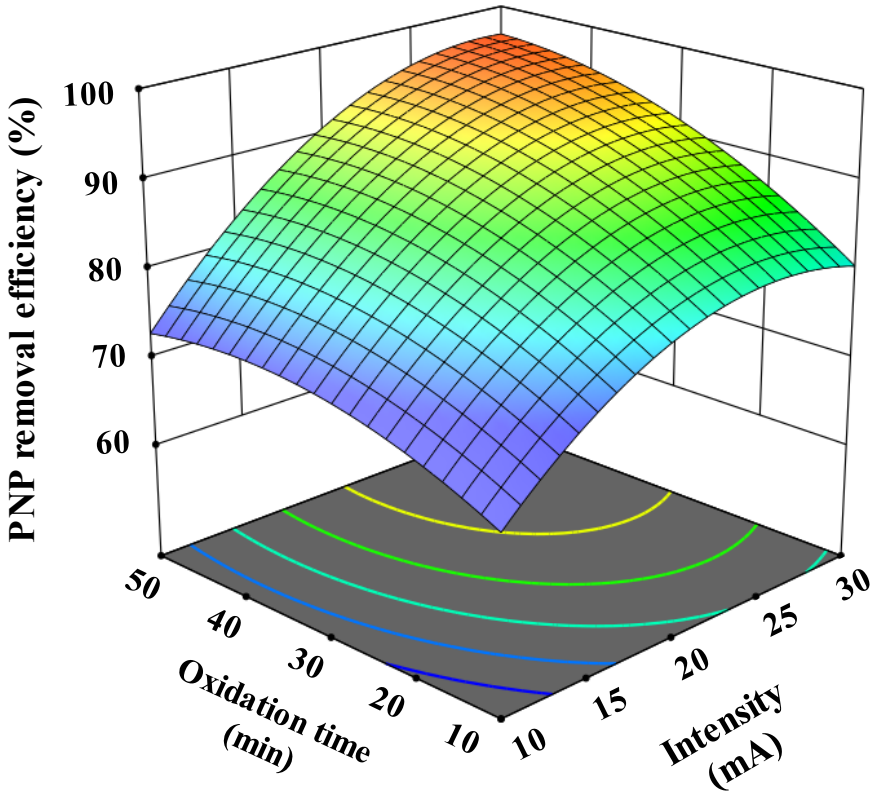

Fig. 4. 3D plot of oxidation time and intensity for PNP removal efficiency

As seen, the removal efficiencies of PNP significantly increased from 80.4% to 91.5% by increasing the oxidation time from 10 min to 50 min. Increasing the oxidation duration led to a greater production of OH radicals, thereby enhancing the advancement of the treatment process. However, an excessively extended oxidation time resulted in higher energy consumption without a significant corresponding increase in the rate of PNP removal [36, 37].

3.4. Optimization of PNP removal using anodic oxidation

The numerical section of the developed model incorporated the desirability parameter to optimize the efficiency of PNP removal. The operating parameters were configured to fall within the "in range" option, and the model determined the optimal treatment condition based on the highest desirability factor value, which ranged from 0 to 1. Based on the strategies proposed by the developed model, the optimized treatment condition, which exhibits the highest removal efficiency, was chosen as the most effective approach, particularly for treating high concentrations of PNP. The maximum removal efficiency of PNP, reaching 98.4%, was achieved by employing the optimal conditions, which included an initial PNP concentration of 2.0 mg L^{-1}, intensity of 25 mA, and oxidation time of 40 min.

3.5. Kinetics study

Kinetic investigations were conducted using first and second-order models to explain the precise mechanism for removing PNP. The outcomes of these investigations revealed that the first-order model exhibited the most favorable fit to the experimental data by a satisfactory correlation coefficient of 0.9892.

4. Conclusion

This study employed a central composite design (CCD) to maximize the efficacy of removing PNP by implementing the anodic oxidation process. An analysis of variance (ANOVA) was conducted at a 95% confidence level to assess the significance of the independent variables and their interactions. The primary factors considered during the optimization process were the initial concentration of PNP (ranging from 1 to 5 mg L^{-1}), intensity (ranging from 10 to 30 mA), and oxidation time (ranging from 10 to 50 min). Under the optimum operating conditions, a maximum PNP removal efficiency of 98.4% was achieved. The modification of the catalytic electrode with Mn can be used as a promising anode for the degradation of PNP in the electrochemical oxidation process. The precise mechanism of the anodic oxidation process demonstrated that the removal process was primarily managed by the OH radicals, which served as the principal oxidative species.

5. Acknowledgements

The authors thank Shahid Sadoughi University of Medical Sciences, Yazd, Iran [Grant number 17609], and Kerman University of Medical Sciences, Kerman, Iran [Grant number 402001063], for supporting the current work. The authors declare that they have no conflict of interest regarding the publication of the current paper.

6. References

[1] R.K. Mishra, S.S. Mentha, Y. Misra, N. Dwivedi, Emerging pollutants of severe environmental concern in water and wastewater: A comprehensive review on current developments and future research, Water-Energy Nexus, 6 (2023) 74-95. https://doi.org/10.1016/j.wen.2023.08.002.

[2] S. Teimoori, H. Shirkhanloo, A.H. Hassani, M. Panahi, N. Mansouri, Rapid extraction of BTEX in water and milk samples based on functionalized multi-walled carbon nanotubes by dispersive homogenized-micro-solid phase extraction, Food Chem., 421 (2023) 136229. https://doi.org/10.1016/j.foodchem.2023.136229.

[3] Y. Wang, H. Li, W. Xia, et al., Synthesis of carbon microsphere-supported nano-zero-valent iron sulfide for enhanced removal of Cr(VI) and p-nitrophenol complex contamination in peroxymonosulfate system, J. Mol. Liq., 390 (2023) 123089. https://doi.org/10.1016/j.molliq.2023.123089.

[4] S. Teimoori, H. Shirkhanloo, A.H. Hassani, M. Panahi, N. Mansouri, An immobilization of aminopropyl trimethoxysilane-phenanthrene carbaldehyde on graphene oxide for toluene extraction and separation in water samples, Chemosphere, 316 (2023) 137800. https://doi.org/10.1016/j.chemosphere.2023.137800.

[5] S. Teimoori, H. Shirkhanloo, A. Hassani, M. Panahi, N. Mansouri, New extraction of toluene from water samples based on nano-carbon structure before determination by gas chromatography, Int. J. Environ. Sci. Technol., 20 (2023) 6589-608. https://doi.org/10.1007/s13762-023-04906-9.

[6] R. Ashouri, H. Shirkhanloo, A. Rashidi, S. Mirzahosseini, N. Mansouri, Dynamic and static removal of benzene from air based on task-specific ionic liquid coated on MWCNTs by sorbent tube-headspace solid-phase extraction procedure, Int. J. Environ. Sci. Technol., 18 (2021) 2377-90. https://doi.org/10.1007/s13762-020-02995-4.

[7] R. Huang, J. Yang, Y. Cao, D.D. Dionysiou, C. Wang, Peroxymonosulfate catalytic degradation of persistent organic pollutants by engineered catalyst of self-doped iron/carbon nanocomposite derived from waste toner powder, Sep. Purif. Technol., 291 (2022) 120963. https://doi.org/10.1016/j.seppur.2022.120963.

[8] Z. Fei, M. Yoosefian, Design and development of polymeric micelles as nanocarriers for anti-cancer Ribociclib drug, J. Mol. Liq., 329 (2021) 115574. https://doi.org/10.1016/j.molliq.2021.115574.

[9] S. Cai, J. Wu, Y. Mo, Supramolecular Fe3O4-

gluconic acid@β-cyclodextrin magnetic composite: green synthesis using sucrose and application in removal of p-nitrophenol, J. Environ. Chem. Eng., 12 (2023) 111503. https://doi.org/10.1016/j.jece.2023.111503.

[10] Z. Hao, Q. Zhao, Y. Wang, et al., Porous N-doped carbon converted from protein-rich shrub enables record-high removal of p-nitrophenol: superior performance and mechanism, Mater. Today Sustain, 23 (2023) 100440. https://doi.org/10.1016/j.mtsust.2023.100440.

[11] Z. Kang, X. Jia, Y. Zhang, et al., A review on application of biochar in the removal of pharmaceutical pollutants through adsorption and persulfate-based AOPs, Sustainability, 14 (2022) 10128. https://doi.org/10.3390/su141610128.

[12] C. Borras, C. Berzoy, J. Mostany, J.C. Herrera, B.R. Scharifker, A comparison of the electrooxidation kinetics of p-methoxyphenol and p-nitrophenol on Sb-doped SnO2 surfaces: Concentration and temperature effects, Appl. Catal. B: Environ., 72 (2007) 98-104. https://doi.org/10.1016/j.apcatb.2006.09.017.

[13] M. Teimouri, F. Khosravi-Nejad, F. Attar, et al., Gold nanoparticles fabrication by plant extracts: synthesis, characterization, degradation of 4-nitrophenol from industrial wastewater, and insecticidal activity – A review, J. Clean. Prod., 184 (2018) 740-53. https://doi.org/10.1016/j.jclepro.2018.02.268.

[14] A. Balakrishnan, G.J. Gaware, M. Chinthala, Heterojunction photocatalysts for the removal of nitrophenol: A systematic review, Chemosphere, 310 (2023) 136853. https://doi.org/10.1016/j.chemosphere.2022.136853.

[15] J. Rakhtshah, H. Shirkhanloo, N. Esmaeili, A rapid extraction of toxic styrene from water and wastewater samples based on hydroxyethyl methylimidazolium tetrafluoroborate immobilized on MWCNTs by ultra-assisted dispersive cyclic conjugation-micro-solid phase extraction, Microchem. J., 170 (2021) 106759. https://doi.org/10.1016/j.microc.2021.106759.

[16] T. Shahraki, M.R. Naroui Rad, H.R. Ganjali, H. Kamaladini, H.R. Mobaser, Metallic and metal oxide nanoparticles synthesized from melon juice. Synthesis, biological application, antioxidant, anticancer, and green catalyst in p-nitrophenol reduction, Inorg. Chem. Commun., 158 (2023) 111636. https://doi.org/10.1016/j.inoche.2023.111636.

[17] P. Mishra, P. Sudarsanam, D.M. Mahapatra, Progressions in cathodic catalysts for oxygen reduction and hydrogen evolution in bioelectrochemical systems: Molybdenum as the next-generation catalyst, Catal. Rev., 65 (2023) 986-1078. 10.1080/01614940.2021.2003085. https://doi.org/10.1080/01614940.2021.2003085.

[18] S. Singh, T.S.S.K. Naik, B. Uppara, Novel and sustainable green sulfur-doped carbon nanospheres via hydrothermal process for Cd (II) ion removal, Chemosphere, 328 (2023) 138533. https://doi.org/10.1016/j.chemosphere.2023.138533.

[19] T. Wang, M. Chen, J. Zhu, N. Li, X. Wang, Anodic ammonium oxidation in microbial electrolysis cell: Towards nitrogen removal in low C/N environment, Water Research, 242 (2023) 120276. https://doi.org/10.1016/j.watres.2023.120276.

[20] R. Qi, X. Zhang, A. Wu, K. Sheng, H. Lin, Controlling the thickness and composition of stainless steel surface oxide film for anodic sulfide removal, J. Clean. Prod., 389 (2023) 136076. https://doi.org/10.1016/j.jclepro.2023.136076.

[21] S. Rathinavelu, S.N. Gummadi, I.M. Nambi, Electro-oxidative removal of five antibiotics of different classes and their mixture using Ti/Sb-SnO2/PbO2 anode: Kinetics, degradation pathway, and toxicity evaluation, J. Water Process Eng., 53 (2023) 103859. https://doi.org/10.1016/j.jwpe.2023.103859.

[22] Y. Yao, M. Zhao, C. Zhao, H. Zhang, Preparation and properties of PbO2-ZrO2 nanocomposite electrodes by pulse electrodeposition, Electrochim. Acta, 117 (2014) 453-59. https://doi.org/10.1016/j.electacta.2013.11.150.

[23] X. Duan, F. Ma, Z. Yuan, L. Chang, X. Jin, Lauryl benzene sulfonic acid sodium-carbon nanotube-modified PbO2 electrode for the degradation of 4-chlorophenol, Electrochim. Acta, 76 (2012) 333-43. https://doi.org/10.1016/j.electacta.2012.05.036.

[24] B. Yu, R. Xu, X. Wang, S. He, B. Chen, Electrodeposition of MnO2-doped Pb-0.6% Sb/α-PbO2/β-PbO2 novel composite energy-saving anode for zinc electrowinning, J. Energy Storage., 61 (2023) 106264. https://doi.org/10.1016/j.est.2022.106264.

[25] Y. Tian, X. Wang, R. Bai, Y. Nie, X. Tian, Hydroxylamine-assisted retarding surface passive layer of zero-valent iron for highly efficient p-nitrophenol removal via direct electron transfer, Sep. Purif. Technol., 330 (2024) 125635. https://doi.org/10.1016/j.seppur.2023.125635.

[26] L. Zhang, Y. Wang, Y. Liu, Chloride removal from sewage using bismuth trioxide: Characterization and optimization by response surface methodology (RSM), J. Environ. Chem. Eng., 11 (2023) 110868. https://doi.org/10.1016/j.jece.2023.110868.

[27] K. Prerana, D. Leela Prasanna, J. Rahul Kumar, The significance of synthesized marine algae/ZnO nanoparticles for the degradation of sodium do-decyl sulphate: Response surface methodology, Mater. Today Proc., (2023). https://doi.org/10.1016/j.matpr.2023.11.115.

[28] S.M. Asaad, A. Inayat, C. Ghenai, A. Shanableh, Response Surface Methodology in Biodiesel Production and Engine Performance Assessment, Int. J. Thermofluids., (2023) 100551. https://doi.org/10.1016/j.ijft.2023.100551.

[29] G. Liu, D. Luo, L. Wang, Current status and future perspective in electro-Fenton techniques for wastewater treatment: a bibliometric review, Appl. Nanosci., 13 (2023) 5885-902. https://doi.org/10.1007/s13204-023-02855-w.

[30] M.S.M. Sarip, F.K.S. Lyna, M.R. Mansor, K.-I. Sotowa, Modelling of the Rice Bran Protein Extraction using Response Surface Methodology, in: Y. Yamashita, M. Kano (Eds.) Comput. Aided Chem. Eng., Elsevier, pp. 823-28, 2022. https://doi.org/10.1016/B978-0-323-85159-6.50137-8.

[31] S. Mujtaba, I. Bibi, F. Majid, Optical, dielectric and photocatalytic properties of Ag-doped Sr1−xAgxFe12O19 and CV dye degradation under visible light irradiation, J. Alloys Compd., 972 (2024) 172793. https://doi.org/10.1016/j.jallcom.2023.172793.

[32] R. Fu, P.-S. Zhang, Y.-X. Jiang, L. Sun, X.-H. Sun, Wastewater treatment by anodic oxidation in electrochemical advanced oxidation process: Advance in mechanism, direct and indirect oxidation detection methods, Chemosphere, 311 (2023) 136993. https://doi.org/10.1016/j.chemosphere.2022.136993.

[33] M. Khamidun, M. Ali Fulazzaky, A. Al-Gheethi, Adsorption of ammonium from wastewater treatment plant effluents onto the zeolite; A plug-flow column, optimisation, dynamic and isotherms studies, J. Environ. Anal. Chem., 102 (2022) 8445-8466.. https://doi.org/10.1080/03067319.2020.1849659.

[34] E. Muchuweni, E.T. Mombeshora, C.M. Muiva, T.S. Sathiaraj, Lithium-ion batteries: Recent progress in improving the cycling and rate performances of transition metal oxide anodes by incorporating graphene-based materials, J. Energy Storage., 73 (2023) 109013. https://doi.org/10.1016/j.est.2023.109013.

[35] M. Roestamy, A.Y. Martin, R.K. Rusli, M.A. Fulazzaky, A review of the reliability of land bank institution in Indonesia for effective land management of public interest, Land

Use Policy, 120 (2022) 106275. https://doi.org/10.1016/j.landusepol.2022.106275.

[36] M.C. Sheikh, M.M. Hasan, M.N. Hasan, Toxic cadmium(II) monitoring and removal from aqueous solution using ligand-based facial composite adsorbent, J. Mol. Liq., 389 (2023) 122854. https://doi.org/10.1016/j.molliq.2023.122854.

[37] M. Arjomandi, A review: analytical methods for heavy metals determination in environment and human samples, Anal. Methods Environ. Chem. J., 2 (2019) 97-126. https://doi.org/10.24200/amecj.v2.i03.73

[38] C. Jamshidzadeh, A new analytical method based on bismuth oxide-fullerene nanoparticles and photocatalytic oxidation technique for toluene removal from workplace air, Anal. Methods Environ. Chem. J., 2 (2019) 73-86. https://doi.org/10.24200/amecj.v2.i01.55

[39] M. Yoosefian, E. Ayoubi, L.I. Atanase, Palladium-doped single-walled carbon nanotubes as a new adsorbent for detecting and trapping volatile organic compounds: A first principle study, J. Nanomater., 12 (2022) 2572. https://doi.org/10.3390/nano12152572.

Anal. Methods Environ. Chem. J. 7 (4) (2024) 17-32

AMECJ

Research Article, Issue 4
Analytical Methods in Environmental Chemistry Journal
Journal home page: www.amecj.com/ir

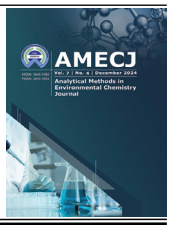

Evaluation and quantification of Fe_3O_4 concentrations in deposits formed inside Iraqi gas supply pipelines using a chemiluminescence method based on flow injection analysis

Nagham S. Al-Awadi[a], Zaineb Falah Hassan[b] and Hussein Fares Abd-Alrazack[c*]
[a] *Department of Chemistry College of Science, University of Baghdad, Baghdad, Iraq*
[b] *Petroleum research & development center, Iraq*
[c] *National Oil Company, Iraq Drilling Company, Baghdad, Iraq*

ARTICLE INFO:
Received 6 Aug 2024
Revised form 27 Oct 2024
Accepted 18 Nov 2024
Available online 30 Dec 2024

Keywords:
Chemiluminescence,
Flow injection analysis,
Gas pipelines contamination,
Iron oxide,
Black powder

ABSTRACT
The accumulation of black powder deposits inside gas pipelines can lead to various issues affecting pipeline operation and integrity. The presence of black powder has the potential to contaminate the gas product, promote increased wear on pipeline internals, and cause clogging that reduces flow rates. From a safety perspective, black powder buildup may pose health and environmental concerns. Previous studies have analyzed the composition of black powder deposits from pipelines using techniques like XRF, XRD, TG-DTA, and FTIR. Their findings show that Iron oxide (Fe_3O_4) is the primary component of black powder. This study developed a novel flow injection-chemiluminescence (FI-CL) method under basic conditions for determining Fe_3O_4 concentrations in black powder deposits because Fe_3O_4 can catalyze the chemiluminescence reaction. Compared to traditional analytical techniques, the proposed CL-based flow injection approach is characterized by good selectivity, simplicity, low cost, and without consuming additional materials. The CL mechanism was investigated through CL spectral, revealing the involvement of Fe_3O_4 in enhancing the luminol-NaOH-H_2O_2 reaction. Experimental conditions for the FI-CL system were optimized. Under optimal parameters, the relative CL intensity showed a linear relationship with Fe_3O_4 concentration over the range of 0.5-100 µg mL^{-1}, and the detection limit was 0.47 µg mL^{-1} with a relative standard deviation (%RSD) of 2.0% at 5.0 µg mL^{-1}. The method was successfully applied to black powder samples extracted from gas pipelines, showing 92.59-107.69% recoveries and a precision of 0.8-3.1%. Results agreed well with an alternative technique. The proposed FI-CL method offers a fast, convenient, and cost-effective means for iron oxide quantification in pipeline deposits and corrosion products.

1. Introduction

Natural gas has gained widespread use as a relatively clean energy source for industrial and domestic applications. Continuous supply and delivery of natural gas relies on extensive pipeline transmission networks that transport the fuel over long distances. As demand for natural gas grows, ongoing development and expansion of these pipeline infrastructures are necessary [1, 2]. However, pipelines present unique engineering challenges due to their large scales, diverse terrains

*Corresponding Author: Hussein Fares Abd-Alrazack
Email: hiban2127@gmail.com
https://doi.org/10.24200/amecj.v7.i04.332

traversed, and exposure to high operating pressures and temperatures during gas transmission. Pipeline materials and diameters must be carefully selected to ensure structural integrity under the demanding operating conditions experienced over decades of service. Reliable transportation of natural gas hinges on pipelines maintaining pressure containment across various geographies and weather patterns throughout their lifespan [3, 4]. The formation of black powder deposits on the internal pipeline surfaces can impact the underground transportation of natural gas through pipelines. Black powder accumulates due to corrosion processes occurring when trace amounts of water and oxygen interact with the gas and pipe material composition. Black powder poses several disadvantages to natural gas quality and efficient transport [5-9]. Black powder deposits can contaminate the gas stream and potentially compromise gas specifications. Its buildup also increases drag forces on the flowing gas, restricting flow rates and resulting in lost pipeline capacity. From a material integrity standpoint, black powder exacerbates pipeline corrosion and erosion problems [10, 11]. Its abrasive nature accelerates pipeline wear and weakens the pipe wall. Additionally, loose black powder particles risk plugging instrumentation lines and valves if mobilized [12]. Previous characterization studies have shown that black powder predominantly comprises iron oxide compounds such as magnetite (Fe_3O_4) and ferric sulfides [13]. As a product of corrosion reactions involving iron-based steel pipelines, iron oxides are the primary constituent species within black powder. Corrosion of steel pipelines under typical operating conditions leads to the formation of iron oxides. The main corrosion products of iron gas pipelines contain iron (II, III) oxide compounds. Recent reports suggest several possible origins for the iron oxides observed in deposit buildup. One potential source is milling scale, a persistent iron (II, III) oxide that adheres to pipe surfaces during high-temperature manufacturing. Another is flash rust containing Fe_2O_3 and FeO_2H from hydro-testing water exposure. Ongoing internal corrosion within operating pipelines can contribute to black powder iron oxide content [12, 14-16]. Accurate quantification of iron oxide levels in deposited black powder can provide insight into pipeline corrosion behavior and predict future challenges from deposit formation. However, traditional analytical techniques for iron oxide determination, such as microwave [17], thermal analysis [18], Ion mobility-mass spectrometry [19], X-ray Fluorescence [20], Infrared desorption [21], Solid-Liquid gas phase extraction [22, 23], colorimetry [24, 25], flow injection [26-28] and X-ray [29], are often complicated, time-consuming and costly. Chemiluminescence (CL) techniques have gained significant interest in analytical applications due to their inherent advantages over other methods. Compared to traditional approaches, CL assays often have lower detection limits, higher sensitivity, more comprehensive linear dynamic ranges, shorter analysis times, and more straightforward instrumentation requirements. These attributes have supported the extensive use of CL in diverse areas of analytical chemistry, such as environmental monitoring, biomedical analysis, and materials characterization [30-34]. Determination of analytes by CL avoids many of the limitations of other approaches. Iron oxide is a primary constituent of black powder deposits formed through corrosion processes in natural gas pipelines. Determining iron oxide concentrations within these deposits provides insight into the extent and causes of internal corrosion over time. Higher iron oxide levels may indicate increased wall thinning and weakening of the pipe material. This influences integrity assessment and replacement scheduling. Additionally, iron oxides can catalyze exothermic reactions when exposed to hydrogen under certain conditions. Quantifying iron oxide concentrations helps assess the propensity for self-heating and potentially dangerous temperature escalations within pockets of built-up deposits. While various analytical techniques exist, there remains a need for sensitive, selective, and convenient methods. Chemiluminescence-based assays address these needs but require a suitable catalyst system. Recent

studies have shown that iron oxide nanoparticles can strongly catalyze the chemiluminescence reaction between luminol and hydrogen peroxide [35, 36]. Iron oxides are highly effective catalysts that accelerate the reaction kinetics and enhance light output. The mechanism is believed to involve the Fenton-like redox cycling of Fe ions to generate reactive oxygen species, resulting in intensified oxidation of luminol. Significantly, the chemiluminescence intensity produced has been demonstrated to correlate directly with iron oxide concentration over a wide range. Therefore, a facile method for sensitive and selective iron oxide determination can be developed by leveraging the catalytic properties of iron oxides to boost chemiluminescence to quantifiable levels. However, to our knowledge, CL-based determination of iron oxide concentrations under basic conditions has not been reported.

This work aims to develop a novel chemiluminescence-based technique for determining iron oxide concentrations in black powder formed within natural gas pipelines. The study will optimize a flow injection chemiluminescence (CL-FI) method leveraging the enhancing effect of iron oxides on the luminol-NaOH-H_2O_2 system. Pairing such compositional data obtained through efficient analytical techniques (CL-FI) with a systematic compilation of historical operational parameters and pipeline design/material selection records would allow for developing kinetic models linking deposition rates to influencing factors. Such predictive models, incorporating cross-sectional concentration profiling and longitudinal operational data, can potentially optimize pipeline maintenance planning.

2. Experimental

2.1. Materials

All chemicals used were of at least analytical reagent grade. Ultrapure deionized water was used for all solution preparations and dilutions. A 100 µg mL^{-1} stock solution of luminol (3-aminophthal-hydrazide, CAS No:521-31-3, Sigma-Aldrich) was prepared by dissolving 1.0 mg in 100 mL of 0.05 mmol L^{-1} sodium carbonate (CAS No:497-19-8, Sigma-Aldrich) solution. A 100-µg mL^{-1} hydrogen peroxide (H_2O_2, 30% v/v, CAS No: 87003-224, BDH) working solution was obtained by diluting 5.15 mL of the commercial solution to 500 mL with ultrapure water. The standardized solution was verified against a potassium permanganate standard (CAS No:7722-64-7, Sigma-Aldrich). To prepare 100 mL of a 1000 mg L^{-1} of Fe_3O_4 standard solution (CAS No: 1317-61-9, Sigma-Aldrich), 0.01 g of iron (II, III) oxide powder (Fe_3O_4) is accurately weighed using an analytical balance. The Fe_3O_4 is transferred to a clean, dry 100 mL beaker. 10 mL of concentrated hydrochloric acid (HCl, CAS No: 7647-01-0, BDH) is then added to the beaker to dissolve the iron oxide. The beaker is placed on a magnetic stir plate, and the solution is stirred for 30 minutes to ensure complete dissolution of the Fe_3O_4. Once dissolution is confirmed, the beaker's contents are quantitatively transferred to a 100 mL volumetric flask using deionized water to rinse any residue off the walls. The volumetric flask is then filled to the 100 mL graduation line with deionized water. The solution is mixed thoroughly by inverting the flask several times. All stock and working solutions were stored in amber bottles at 4ºC when not in use. Fresh preparations were made as needed to maintain reagent integrity throughout experiments.

2.2. Apparatus

The FI-CL system configuration is shown in Figure 1. Reagent and sample delivery was facilitated by multi-channel peristaltic pumps (HL-2D, Shanghai BQ Instruments). Polytetrafluoroethylene (PTFE) tubing (0.8 mm internal diameter) was employed to interconnect all components. A six-port injection valve (Rheodyne, USA) equipped with a 100 µL sample loop was used to introduce samples into the flowing carrier stream. Chemiluminescence signals were measured using an ultraweak luminescence analyzer (Institute of Biophysics, Beijing, China). This detector utilizes a flat spiral flow cell interfaced with a photomultiplier tube (RCA 931A, UK). Data

acquisition and processing were performed using the accompanying software. The photomultiplier tube was powered by a stable high-voltage power supply (Jobin Yvon, France) operated over the 0-1.6 kV range. Signals from the photomultiplier were amplified using a low-noise preamplifier (United Detector Technology, USA) before interfacing with a data recording instrument. A Kompen Sograph Model C1032 recorder (Siemens, Germany) was used to measure the amplified chemiluminescence signals over 1-500 mV as a linear range. This provided analog tracing of the light emission dynamics throughout kinetic experiments.

2.3. General Procedure

The FI-CL method was straightforward to implement. As illustrated in Figure 1, the peristaltic pumps continuously propelled the luminol, H_2O_2, double distilled water (carrier stream), NaOH, and sample solutions (either a standard or unknown sample containing the analyte) through the system at 2.0 mL min^{-1} of flow rate. Initially, the general procedure involved three main steps. At the first confluence point Y_1, a 0.5 mmol L^{-1} sodium hydroxide solution was combined and mixed with the luminol solution 0.5 mmol L^{-1} to form the dianion luminol. Secondly, a hydrogen peroxide solution of 0.006 mmol L^{-1} was pumped via a peristaltic pump and merged with the dianion luminol stream at the secondary confluence point Y_2. Finally, when the injection valve was switched to injection mode, the carrier flow delivered the standard or sample solution downstream to the tertiary confluence point Y_3. At Y_3, the standard/sample merged with the mixed hydrogen peroxide and dianion luminol stream. This allowed for online chemiluminescence detection from the resultant reaction as the combined stream passed through the flow cell for measurement. With the injection valve in the load position initially, the H_2O_2 solution merged with the luminol-NaOH mixture at the second confluence point (Y_2). It flowed through the entire flow system to establish a stable baseline signal. Once baseline stabilization was achieved, the injection valve was switched to the inject position. This allowed the distilled water carrier to transport the contents of the 100 µL sample loop directly into the flowing reaction stream within the flow cell. The ensuing chemiluminescent emission was simultaneously measured and recorded. Mixing coils (M_1-M_3) were included at various points throughout the flow lines to facilitate the complete intermixing of the components in the moving fluid stream.

2.4. Sample preparation of black powder

Black powder deposit samples were collected from the inner surfaces of in-service natural gas transmission pipelines near Karbala, Mosul, and Diwaniya, Iraq. These three sites were selected to represent different

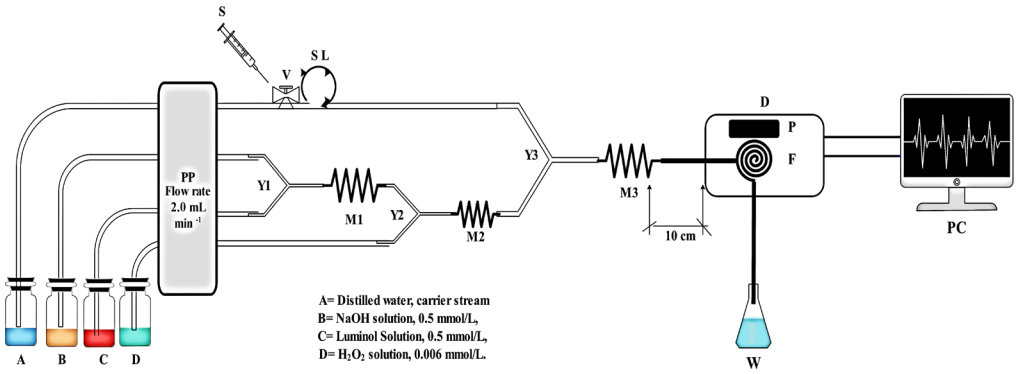

Fig. 1. Schematic diagram of the chemiluminescence-flow injection (CL-FI) system configuration for determining Fe_3O_4. A: carrier stream (MQ water); B: NaOH 0.5 mmol L^{-1}; C: luminol solution 0.5 mmol L^{-1}, H_2O_2 0.006 mmol L^{-1}, PP: peristaltic pump; S: syringe for injection of standard or sample; V: six ports injection valve; SL: sample loop; Y_1-Y_3: confluence points; M_1-M_3: 30 cm mixing coils; D: chemiluminescence detector; P: photomultiplier tube; F: flow cell; w: waste; PC: personal computer.

geographic regions across the country as the pipelines transport gas from fields to power plants in Karbala, Mosul, and Diwaniya provinces. Pipe spool pieces approximately 15 km upstream from the major gas delivery stations were extracted for sampling. Pipelines selected represented a range of diameters (6-24 inches) and compositions (carbon steel). Samples were scraped directly from the pipe wall using a cleaned stainless-steel spatula and placed into pre-cleaned polyethylene containers. The pretreatment step to selectively isolate Fe_3O_4 is important before further analysis of black powder samples collected from pipe walls. A 0.5 g subsample was weighed out and pretreated following the method of Chen and his colleagues [41]. First, the subsample was added to a beaker containing 6M HCl and refluxed for 1 hour with occasional stirring, which dissolved any carbonates and sulfides in the sample. Then, 30% H_2O_2 was slowly added, and heating continued for an additional hour to oxidize any Fe^{2+} to the Fe^{3+} state. The pretreated residue was vacuum filtrated through a Whatman #41 filter paper. The residue on the filter paper was washed with deionized water until the filtrate reached neutral pH. Subsequently, the pretreated residue was dried overnight at 80°C and weighed to calculate recovery. Next, the dried pretreated residue was resuspended in deionized water and separated magnetically using a neodymium magnet. The Fe_3O_4 fraction was attracted to the side of the vial nearest the magnet and decanted, while the supernatant containing non-magnetic fractions was discarded. Finally, the Fe_3O_4 fraction was washed 3 times with deionized water. This procedure selectively isolates Fe_3O_4 from the black powder sample before further digestion and analysis, removing potential interference from Fe^{2+} ions. To prepare the sample for the FL-CL reaction, the samples were air-dried for 24 hours in the laboratory, then gently ground with an agate mortar and pestle to homogenize and break up agglomerates. The powdered solids were then sieved through a 150 µm mesh to obtain a fine fraction suitable for acid digestion. The sieved black powder was accurately transferred into digestion vessels. A mixture of 25 mL concentrated HNO_3 and 10 mL concentrated HCl was added to each vessel, and the solutions were heated to 95ºC for 2 hours with reflux to digest the solid phase fully. After cooling, the extracts were filtered through Whatman No. 42 filter paper into 100 mL volumetric flasks and made up to the mark with 2% HNO_3 [42]. These prepared sample solutions were analyzed using the proposed method (CL-FI) to quantify levels of iron oxide content in the original black powder deposits.

3. Results and Discussion

The literature reports black powder forms due to dissolved oxygen corrosion caused by small amounts of oxygen and water in the gas stream reacting with pipe material. Quantifying the concentration of Fe_3O_4 present in black powder deposits at different time points during pipeline operation can provide valuable insight into the rate and dynamics of corrosion product accumulation over time. The method proposed in this study is more sensitive, speedy, and simple than numerous other reported analytical methods (Table 1).

Table 1. The proposed CL-FI for the determination of iron oxide exhibits excellent linearity compared to other analytical techniques.

Used Methods	LR (µg mL^{-1})	Remarks	References
FAAS	0.2-90	More sensitive but narrow response range	[37]
HPLC/MS	0.05–20	More sensitive but low response range	[38]
Colorimetric	12.0-120.9	Less sensitive	[39]
Electrochemical	2.0-60	Less sensitive	[40]
CL-FI	0.5-100	Using a simple instrument and more sensitive	This work

LR: Linearity Range
Note: The sensitivity of the analytical method is represented by the lowest concentration in the calibration curve that can be accurately and precisely quantified

3.1. Kinetic study

Before developing the FI-CL method, the kinetic characteristics of the proposed chemiluminescent reaction between luminol, H_2O_2, NaOH, and Fe_3O_4 were investigated using a batch approach. In the batch setup, experimental conditions were held constant while the intensity-time profile of the luminol-NaOH-H_2O_2- Fe_3O_4 system was recorded to study the reaction kinetics. As shown in Figure 2, the CL system exhibited a rapid response. The CL intensity peak appeared within 0.5 seconds of luminol-NaOH-H_2O_2 solution injection and quickly decreased to the baseline level within 10 seconds. These results demonstrated that Fe_3O_4 effectively enhances the weak luminescence of the luminol-NaOH-H_2O_2 system. Therefore, the CL method provides a fast and sensitive means for Fe_3O_4 determination. The brief kinetic window is suitable for flowing injection analysis, where samples are rapidly introduced and swept through the flow cell.

3.2. The effect of luminol solution

The CL reaction between Fe_3O_4, luminol, NaOH, and H_2O_2 involves the oxidation of luminol by the reaction of H_2O_2 with the iron oxide (oxidizing agent). The concentration of luminol impacts both the assay sensitivity and linear dynamic range. The effect of luminol concentration on the resulting CL intensity was evaluated in the 0.05-1.0 mmol range. L^{-1}. As shown in Figure 3, the CL signal increased with rising luminol concentration up to 0.5 mmol. L^{-1}. Above this level, a decrease in CL intensity was observed, likely due to self-absorption of the higher concentration of brightly colored product. A luminol concentration of 0.5 mmol. L^{-1} provided the maximum signal response. Therefore, this optimal concentration was carried forward for subsequent optimization studies and analytical method development.

3.3. Effect of H_2O_2 concentration

H_2O_2 is the oxidizing agent in the CL reaction between luminol, NaOH, and the analyte. Its concentration, therefore, significantly impacts the resulting CL signal intensity. To determine the optimal H_2O_2 concentration, its effect was studied over the range of 0.002-0.07 mmol L^{-1}, keeping all other reaction conditions constant. As shown in Figure 4, the CL intensity increased with rising H_2O_2 concentration up to 0.006 mmol L^{-1}. Beyond this level, further increases in peroxide concentration resulted in decreased

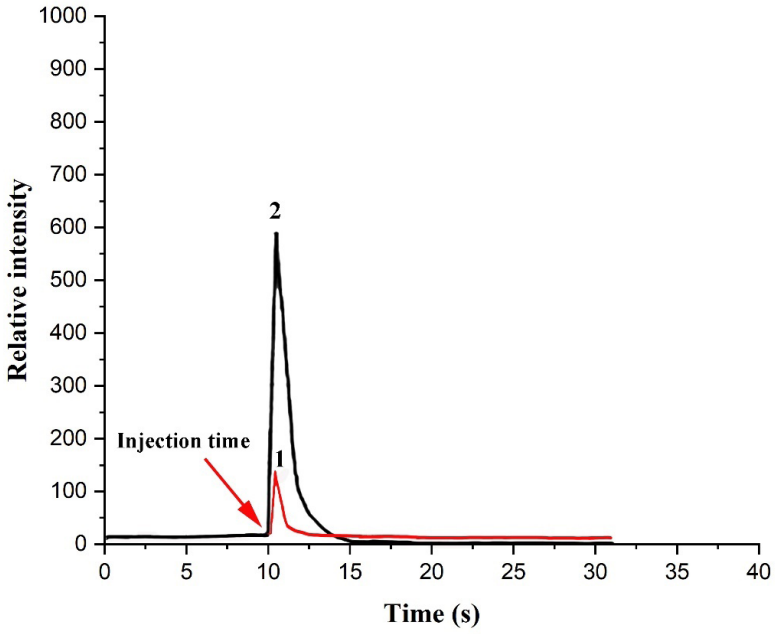

Fig. 2. Kinetic curves of luminol-H_2O_2-NaOH system. (1) Using of mixture of luminol-H_2O_2-NaOH and water system without Fe_3O_4; (2) 100 µL Fe_3O_4 injected into the mixture of luminol-H_2O_2-NaOH system. Luminol: 0.4 mmol/L; H_2O_2: $2x10^{-3}$ mmol L^{-1}; NaOH: 0.5 mmol L^{-1}; Fe_3O_4: 50 µg mL^{-1}

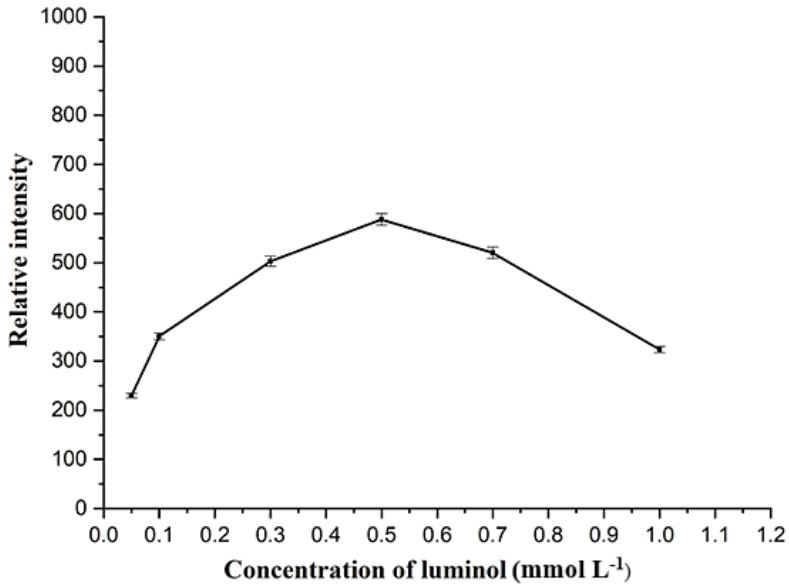

Fig. 3. Effect of luminol concentration on the CL intensity for the determination of Fe_3O_4using the proposed CL-FI method under the following experimental conditions: Flow rate 2.0 mL min^{-1}; sample loop 100 µL; NaOH concentration 0.3 mmol L^{-1}; H_2O_2 concentration 0.004 mmol L^{-1}; Fe_3O_4: 50 µg mL^{-1}

light output. The mechanism of the CL process can explain this observation. At lower H_2O_2 levels, the availability of oxidizing agents limits the reaction kinetics. However, increasing the concentration of H_2O_2 above 0.006 mmol L^{-1} did not lead to any additional enhancement of the CL intensity. The maximum CL intensity obtained at 0.006 mmol L^{-1} H_2O_2 indicates this concentration provides the ideal balance between sufficient oxidation power and avoidance of catalytic interference. Therefore, 0.006 mmol L^{-1} was selected as the optimum H_2O_2 concentration and used in subsequent method optimization and analytical applications to ensure maximum assay sensitivity and performance.

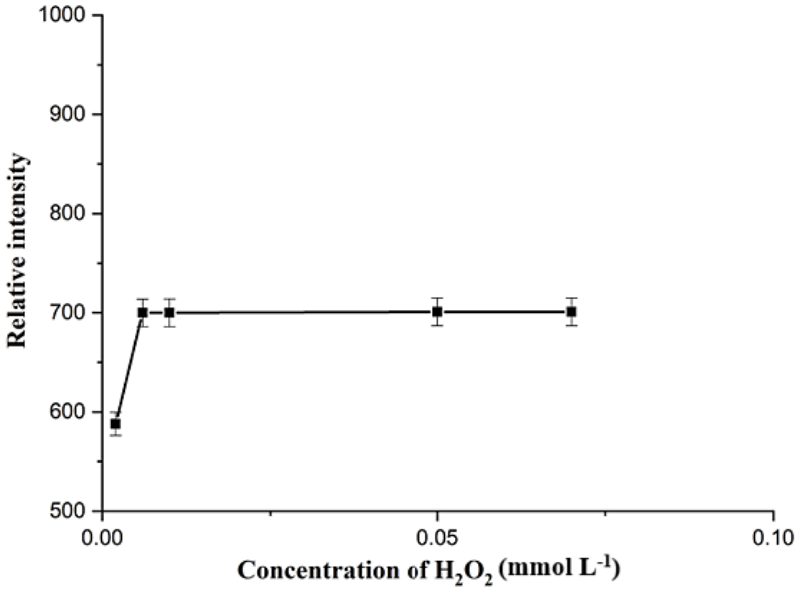

Fig. 4. Effect of H_2O_2 concentration on the CL intensity for the determination of Fe_3O_4 using the proposed CL-FI method under the following experimental conditions: Flow rate 2.0 mL min^{-1}; sample loop 100 µL; NaOH concentration 0.3 mmol L^{-1}; luminol concentration 0.5 mmol L^{-1}; Fe_3O_4: 50 µg mL^{-1}

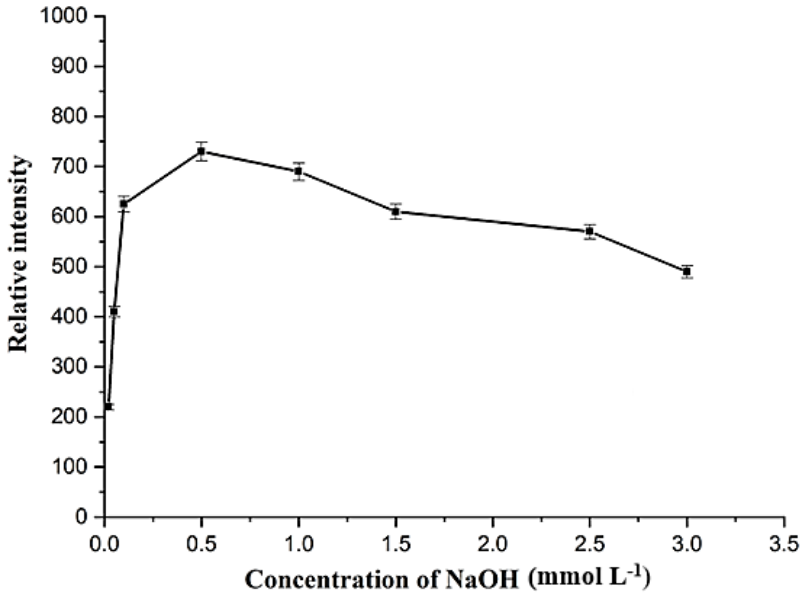

Fig. 5. Effect of NaOH concentration on the CL intensity for the determination of Fe_3O_4 using the proposed CL-FI method under the following experimental conditions: Flow rate 2.0 mL min^{-1}; sample loop 100 µL; H_2O_2 concentration 0.006 mmol L^{-1}; luminol concentration 0.5 mmol L^{-1}; Fe_3O_4: 50 µg mL^{-1}

3.4. The effect of basic medium

NaOH enhances the chemiluminescent reaction between luminol and the oxidizing agent. The effect of NaOH concentration, ranging from 0.02 mol L^{-1} to 2.0 mol L^{-1}, was examined. As shown in Figure 5, the CL intensity of the luminol-H_2O_2-Fe_3O_4 system increased with rising NaOH concentration up to 0.5 mol L^{-1}. Beyond this level, further increases in base concentration led to decreased light output. The reaction mechanism can explain this observation. At lower concentrations, the basic environment is insufficient to deprotonate reagents and initiate the chemiluminescent oxidative cleavage of luminol. However, above 0.5 mol L^{-1} NaOH, the excess hydroxyl ions may interfere with the reaction kinetics rather than catalyze it. Therefore, 0.5 mol L^{-1} NaOH optimized the balance between developing an alkaline environment conducive to redox signaling without introducing interfering effects. This concentration of sodium hydroxide solution was carried forward for subsequent experimentation.

3.5. Optimization of FI-CL conditions

Several flow parameters were optimized to achieve maximum CL output while maintaining efficient analyte processing. Using 30 cm reaction coils, flow rates from 0.4 to 4.0 mL min^{-1} were evaluated for their effects on signal intensity and peak characteristics. Lower flow rates enhanced chemiluminescence as they allowed longer contact time between reagents. However, extremely slow flows produced overly broad peaks and lengthy analysis times; meanwhile, higher flow rates reduced signal by shortening the reaction window. The optimal balance was 2.0 mL min^{-1}, as this flow rate provided sufficient time for the chemiluminescent reaction while avoiding peak widening or throughput limitations. Injection loop volumes from 25-200 µL were also examined. Larger loops generated broader peaks undesirable for sensitivity, while smaller volumes diminished the signal. A 100 µL injection volume demonstrated the best signal-to-noise ratio. These flow optimization studies enabled the maximization of analytical parameters for accurate and precise analyte quantitation using this flow injection chemiluminescence system, as shown in Figures 6 and 7. Also, Table 2 summarizes the optimized experimental conditions for the flow injection chemiluminescence methodology.

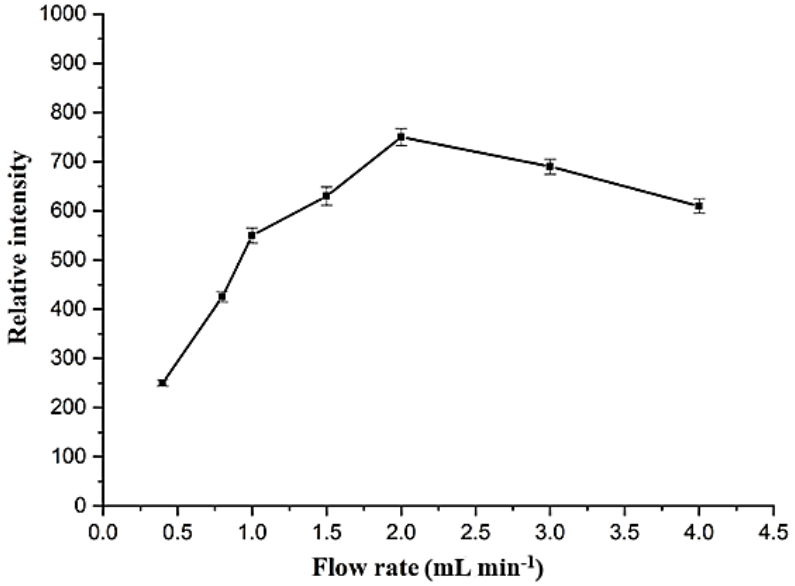

Fig. 6. Effect of using variable flow rates on the CL intensity for the determination of Fe_3O_4 using the proposed CL-FI method under the following experimental conditions: sample loop 100 µL; H_2O_2 concentration 0.006 mmol L^{-1}; luminol concentration 0.5 mmol L^{-1}; Fe_3O_4: 50 µg mL^{-1}

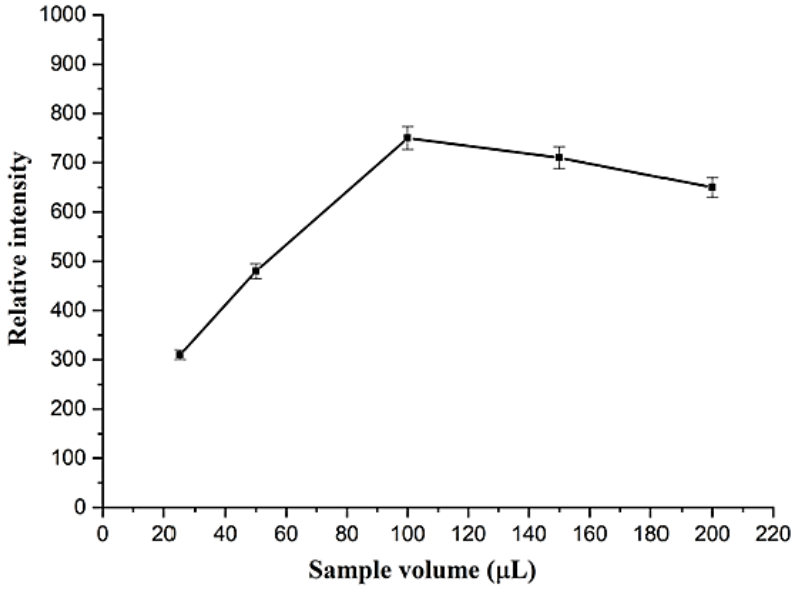

Fig. 7. Effect of using variable sample loops on the CL intensity for the determination of Fe_3O_4 using the proposed CL-FI method under the following experimental conditions: flow rate 2.0 mL min^{-1}; H_2O_2 concentration 0.006 mmol L^{-1}; luminol concentration 0.5 mmol L^{-1}; Fe_3O_4: 50 µg mL^{-1}

Table 2. Summary of ideal operating protocol defined for the CL-FI system

CL-FI parameter	Examined ranges	Selected
[Luminol](mmol L^{-1})	0.05-1.0	0.5
[H_2O_2](mmol L^{-1})	0.002-0.07	0.006
[NaOH] (mmol L^{-1})	0.02-2.0	0.5
Flow rate (mL min^{-1})	0.4- 4.0	2.0
Sample volume (Injected, µL)	25-200	100

3.6. Evaluation of the FI-CL method

A FI-CL method was developed to determine iron oxide using the luminol-NaOH-H_2O_2-Fe_3O_4 system. Method validation studies were performed under optimized operating conditions to evaluate the technique. The linear dynamic range was determined to be 0.5-100 µg mL^{-1} with a limit of detection of 0.47 µg mL^{-1} (calculated as 3σ of the standard error of intercept). The regression equation derived from the linear calibration curve was ΔCL_I = 80.051±3.283+20.787±2.321c, where c is the iron oxide concentration in µg mL^{-1}, and exhibited excellent correlation (R^2 = 0.9970). Intra-assay precision was investigated by analyzing an iron standard of 5.0 µg mL^{-1} eleven times, yielding a relative standard deviation of 2.0%. These quantitative parameters demonstrated the method's suitability for accurate and sensitive measurement of iron oxide levels. Its analytical performance validated the technique and compared favorably to literature methods.

3.7. The effects of potential interferents

The selectivity of the optimized FI-CL method was examined by investigating potential interferences from common excipients. Metal ions present in samples were evaluated for their effects on chemiluminescence intensity. Comparative measurements were made of the CL signal obtained with and without adding individual excipients to a 10 µg mL^{-1} iron oxide standard. The results in Table 3 show that some substances like Cu^{+2}, $Mn^{+2,}$ and Fe^{+2} can interfere by more than 5% relative error under the selected conditions. This demonstrates that pretreatment would be necessary before directly analyzing real black powder samples using this method. X-ray diffraction (XRD) analysis was conducted on the black powder sample to verify the potential presence of interfering metal ions. The XRD results revealed that any amounts of the specified metals were highly minor and below the detection limit of the technique. Therefore, it can be concluded that the examined sample does not contain appreciable quantities

Table 3. Effect of Common Foreign Species on the analysis of 10 µg mL^{-1} Fe_3O_4 by CL method

Interferences species	Tolerance limits
CH_4	100
C_2H_6	100
C_3H_8	100
H_2S	100
Cu^{+2}	5.0
Fe^{+2}	4.0
NO^{3-}	100
Co^{+2}	50
Mg^{+2}	100
CO^{3-}	100
$SO4^{-2}$	100
NH^{4+}	40
Cl^-	50
Cr^{+3}	25
Al^{+3}	20
Zn^{+2}	50
Ni^{+2}	50
Mn^{+2}	8.0
NO^{2-2}	100
Ca^{+2}	75
Na^+	100

of these interfering ions that could impact the analysis. To achieve accurate quantification, interferent matrix components requiring removal or compensation were identified.

3.8. FI-CL analytical method for determination of iron oxide in real black powder sample

Quantitative recovery experiments were performed on real black powder samples according to the established procedure to validate the optimized FI-CL method's applicability. Iron oxide contents determined with the proposed technique were compared to measurements made using an independent X-ray diffraction (XRD) validation method [43]. XRD analysis is the most suitable technique for positively identifying the constituent compounds in the collected black powder samples. XRD employs non-destructive testing utilizing X-rays, crystalline diffraction and Bragg's law. Only a small amount of sample, typically 1 g or less of the black powder, is needed for XRD analysis. The technique generates diffractograms that can be matched to reference patterns to conclusively determine all of the crystalline phase's present in the sample. Through full compositional analysis, XRD allows unambiguous identification of each compound comprising the multi-component black powder. As a well-established method for material characterization, XRD is highly effective for obtaining a complete breakdown of a sample's constituent mineralogical makeup from just a minor quantity of input material. Results presented in Table 4 demonstrate recovery percentages ranging from 92.59% to 107.69% with low precision values (RSD 0.8% - 3.1%). Close agreement was observed between the iron oxide levels in samples derived from FI-CL analysis and those obtained via XRD. This suggests the proposed method offers accuracy comparable to the reference standard when quantifying real-world matrices. The successful recovery study outcomes using authentic test materials establish the validity and reliability of this analytical approach for iron oxide determination in black powder formulations. Quantifying real samples has proven the capabilities of FI-CL to meet validation criteria. Therefore, this flow injection platform can be appropriately applied in laboratory testing.

3.9. Elucidating the underlying chemiluminescence reaction mechanism

This study aims to elucidate the underlying mechanism of the CL reaction involving luminol. Luminol exhibits blue-colored light emission when it undergoes oxidation in a basic environment Figure 8 [44]. However, the detailed steps of the light-generating process have yet to be fully understood. By investigating the roles of key reaction components such as sodium hydroxide, hydrogen peroxide, and iron, we seek insights

Table 4. The analytical results from the analysis of real black powder samples to determine the Fe_3O_4 using the proposed method

Location	Sample weight (g)	Detected (g)	Added (g)	Found (g)	Recovery (%)	RSD[a] (%)	XRD reference [43]
Mosul	0.5	0.11	0.1	0.22	104.76	2.1	0.12
			0.07	0.19	105.50	2.2	
			0.05	0.17	106.25	0.8	
Karbala	0.5	0.17	0.1	0.25	92.59	1.9	0.16
			0.07	0.24	100.00	1.1	
			0.05	0.23	104.54	2.8	
Diwaniya	0.5	0.16	0.1	0.28	107.69	3.1	0.14
			0.07	0.22	95.65	0.9	
			0.05	0.20	95.23	1.4	

[a] Each sample was analyzed in triplicate ($n=3$)

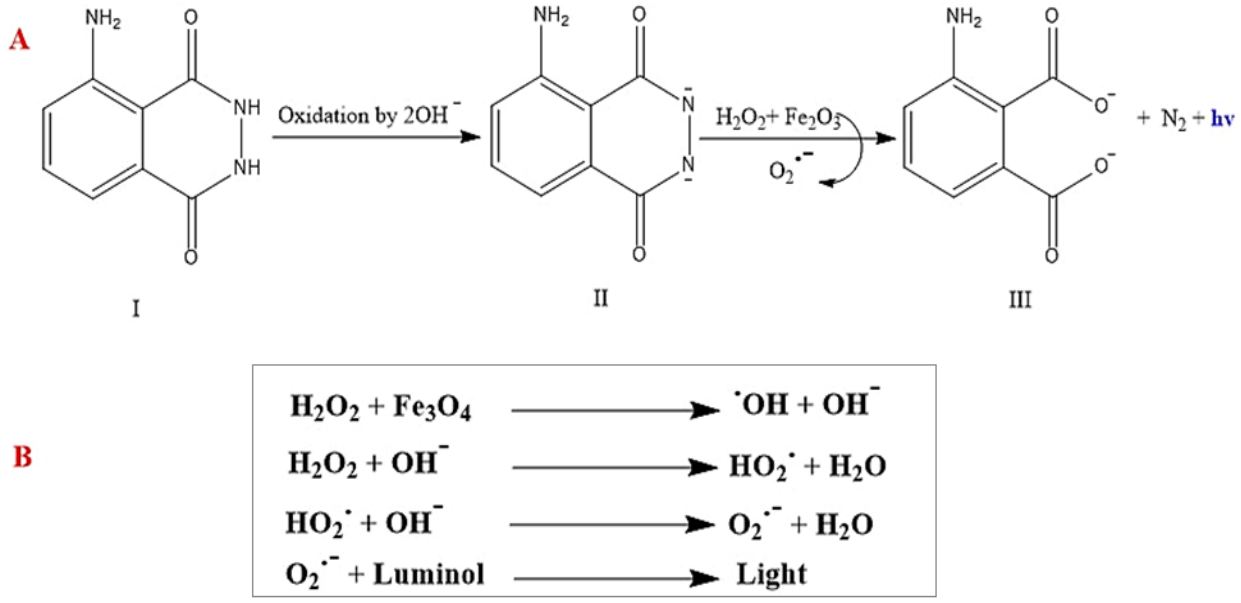

Fig. 8. Mechanism illustration for detection of iron oxide using luminol-H_2O_2-NaOH system. (A): The chemiluminescence process involves the oxidation of luminol ($C_8H_7N_3O_2$, structure I) under moderately basic conditions, which leads to the formation of 3-aminophthalate ion (structure III) as an electronically excited product. Importantly, this 3-aminophthalate intermediate is the light-emitting species responsible for the visible blue emission observed during chemiluminescence. (B): The role of iron oxide in decomposing the H_2O_2.

into how luminol progresses from its initial state to the formation of electronically excited species responsible for photon release. Sodium hydroxide increases the pH of the reaction environment. This promotes the deprotonation of luminol. At high pH, luminol exists predominantly as a dianion due to hydroxide ions' deprotonation of its amino groups [44]. Sodium hydroxide activates luminol by making it more nucleophilic. Fe_3O_4 molecules can catalyze the chemiluminescent reaction due to significantly excess Fe (II) ions on their surfaces [35]. SRXPS analysis revealed that the ratio of Fe (II)/Fe (III) on the Fe_3O_4 surface is around 0.93 [45]. Consequently, in the presence of H_2O_2, these surface Fe (II) ions mediate a heterogeneous Fenton-like reaction, wherein Fe_3O_4 catalyzes the decomposition of H_2O_2 [46]. This decomposition generates reactive superoxide anion radicals (O_2*-), as evidenced by in situ STXM showing the formation of a Fe_2O_3 phase on the surfaces during the reaction. Notably, the superoxide anions rapidly capture luminol, producing an unstable endoperoxide intermediate whose decay results in light emission or chemiluminescence, which can be quantitatively measured for Fe_3O_4 detection. Therefore, Fe_3O_4 effectively catalyzes the chemiluminescent reaction through surface Fe (II)-mediated decomposition of H_2O_2. The unstable organic peroxide then loses a nitrogen molecule (N_2) and undergoes decomposition. During the decomposition process, the electrons of the reaction products change from the triplet excited state to the lower energy ground state. This transition releases energy in the form of a blue-colored photon. The emitted light is the observable chemiluminescence resulting from the overall reaction of luminol dianion with oxygen radicals. Therefore, the combined reaction produces the characteristic blue glow through chemiluminescence. In this mechanism, sodium hydroxide enhances the reaction by increasing pH and activating luminol, allowing the formation of reactive intermediates and excited state emission, leading to light production.

4. Conclusion

In this work, we report the development and validation of a novel FI-CL method for determination of Fe_3O_4 in black powder. The

method exploits the enhancing effect of Fe_3O_4 on the luminol-NaOH-H_2O_2 system. Under optimized conditions, the method demonstrated suitable quantitative performance for Fe_3O_4 detection, with a linear range of 0.5-100 µg mL^{-1}, limit of detection of 0.47 µg mL^{-1}, and intra-assay precision of RSD (2.0%) at 5.0 µg mL^{-1}. Validation studies via real sample analysis of black powder confirmed applicability to complex matrices. A preliminary examination of the underlying chemiluminescence reaction mechanism provided insights into how Fe_3O_4 initiates and amplifies light emission. The automated flow injection format offers rapid analyses, simple operation, and reagent consumption advantages. This new chemiluminescence-based flow injection technique shows promise as a screening tool for Fe_3O_4 quantification, given its demonstrated sensitivity, low cost, and reagent-free nature. Precise Fe_3O_4 analysis thus aids in evaluating pipeline integrity and developing mitigation strategies to prevent fires, explosions, and unplanned outages. It provides critical data for maintaining the safety and reliability of gas transmission operations over the lifetime of pipeline assets.

5. Acknowledgment

The authors thank Prof Dr Issam M. A. Shakir for his support. The authors confirm that there are no relevant financial or non-financial competing interests to report.

6. Reference

[1] P. Q. Gas, Natural gas processing: the crucial link between natural gas production and its transportation to market, Los Alamos, 20 (2006) 1-11.https://www.eia.gov/naturalgas/articles/ngprocessindex.php

[2] M. A. Adewumi, Natural gas transportation issues, J. Pet. Technol., 49 (1997) 139-143. https://doi.org/10.2118/37369-JPT

[3] T. S. Khan, M. S. Al-Shehhi, Review of black powder in gas pipelines–An industrial perspective, J. Nat. Gas Sci. Eng., 25 (2015) 66-76. https://doi.org/10.1016/j.jngse.2015.04.025

[4] G. Guandalini, P. Colbertaldo, S. Campanari, Dynamic modeling of natural gas quality within transport pipelines in presence of hydrogen injections, Appl. Energy, 185 (2017) 1712-1723. https://doi.org/10.1016/j.apenergy.2016.03.006

[5] T. S. Khan, Review of black powder in gas pipelines – An industrial perspective, J. Nat. Gas Sci. Eng., 25 (2015) 423-436. https://doi.org/10.1016/j.jngse.2015.04.025

[6] F. Golbabai, A. Ebrahimi, H. Shirkhanloo, M. R. Baneshi, A. Faghihi, M. J. Kian, Performance comparison survey of multi-walled and single-walled carbon nanotubes for adsorption and desorption and of mercury vapors in air, Iran Occup. Health, 10 (2013) 21-31. https://espace.library.uq.edu.au/view/UQ:9d03f02

[7] F. Golbabaei, A. Ebrahimi, H. Shirkhanloo, A. Koohpaei, A. Faghihi-Zarandi, Single-walled carbon nanotubes (SWCNTs), as a novel sorbent for determination of mercury in air, Global J. Health Sci., 8 (2016) 273-280. https://doi.org/10.5539/gjhs.v8n7p273

[8] H. Shirkhanloo, F. Golbabaei, A. Vahid, A. Faghihi Zarandi, A novel nano-palladium embedded on the mesoporous silica nanoparticles for mercury vapor removal from air by the gas field separation consolidation process, Appl. Nanosci., 12 (2022) 1667-1682. https://doi.org/10.1007/s13204-022-02366-0

[9] H. Shirkhanloo, F. Golbabaei, H. Hassani, F. Eftekhar, M. J. Kian, Occupational exposure to mercury: air exposure assessment and biological monitoring based on dispersive ionic liquid-liquid microextraction, Iran. J. Public Health, 43 (2014) 793-799. http://ijph.tums.ac.ir

[10] A. Sherik, Study examines sources, makeup in dry gas systems, Oil Gas J., 106 (2008) 54-54. https://ogj.com/general-interest/hse/article/17218468/

[11] R. M. Baldwin, Here are procedures

for handling persistent black-powder contamination, Oil Gas J., 96 (1998) 66-75. https://ogj.com/general-interest/hse/article/17218477/

[12] J. He, D. Wang, D. Guo, F. Xie, Y. Qin, Generation causes of black powder in the east line of the gas supply pipeline from the Liaohe oilfield: Analysis and discussion, Eng. Fail. Anal., 139 (2022) 106506. https://doi.org/10.1016/j.engfailanal.2022.106506

[13] J. E. Onwunalu, L. J. Durlofsky, Application of a particle swarm optimization algorithm for determining optimum well location and type, Comput. Geosci., 14 (2010) 183-198. https://doi.org/10.1007/s10596-009-9142-1

[14] A. Bhardwaj, B. Kumar, S. R. Prasad, S. K. Srivastava, Characterization of black powder in gas pipelines, Mater. Perform., 55 (2016) 54-59. https://doi.org/10.1016/B978-0-323-99304-3.00017-0

[15] T. S. Khan, M. Alshehhi, S. Stephen, L. Khezzar, Characterization and preliminary root cause identification of black powder content in a gas transmission network–a case study, J. Nat. Gas Sci. Eng., 27 (2015) 769-775. https://doi.org/10.1016/j.jngse.2015.09.022

[16] R. P. Downham, T. M. Ciuksza, H. J. Desai, V. G. Sears, Black iron (II/III) oxide powder suspension (2009 CAST Formulation) for fingermark visualization, Part 1: Formulation component and shelf-life studies, J. Forensic Identif., 67 (2017) 145-167. https://www.proquest.com/docview/1871397275

[17] W. Taha, M. Abou-Khousa, A. Haryono, M. AlShehhi, K. Al-Wahedi, A. Al-Durra, I. AlNabulsieh, M. Daoud, F. Geuzebroek, M. Faraj, Field demonstration of a microwave black powder detection device in gas transmission pipelines, J. Nat. Gas Sci. Eng., 73 (2020) 103058. https://doi.org/10.1016/j.jngse.2019.103058

[18] R. Turcotte, R. C. Fouchard, A. M. Turcotte, D. E. G. Jones, Thermal analysis of black powder, J. Therm. Anal. Calorim., 73 (2003) 105-118. https://doi.org/10.1023/A:1025181424038

[19] C. L. Crawford, H. Boudries, R. J. Reda, K. M. Roscioli, K. A. Kaplan, W. F. Siems, H. H. Hill Jr, Analysis of black powder by ion mobility−time-of-flight mass spectrometry, Anal. Chem., 82 (2010) 387-393. https://doi.org/10.1021/ac902168a

[20] J. Yamada, H. Kaneta, K. Nakayama, Black powder formation in natural gas pipeline networks: associated issues and root cause analysis, Challenges and Recent Advances in Sustainable Oil and Gas Recovery and Transportation, Chapter 15 (2023) 329-346. https://doi.org/10.1016/B978-0-323-99304-3.00017-0.

[21] T. P. Forbes, J. R. Verkouteren, Forensic analysis and differentiation of black powder and black powder substitute chemical signatures by infrared thermal desorption–DART-MS, Anal. Chem., 91 (2018) 1089-1097. https://doi.org/10.1021/acs.analchem.8b04624

[22] M. Arjomandi, H. Shirkhanloo, A review: analytical methods for heavy metals determination in environment and human samples, Anal. Methods Environ. Chem. J., 2 (2019) 97-126. https://doi.org/10.24200/amecj.v2.i03.73

[23] A. F. Zarandi, H. Shirkhanloo, P. Paydar, A novel method based on functionalized bimodal mesoporous silica nanoparticles for efficient removal of lead aerosols pollution from air by solid-liquid gas-phase extraction, J. Environ. Health Sci. Eng., 18 (2020) 177–188. https://doi.org/10.1007/s40201-020-00450-7

[24] M. K. Hammood, J. N. Jeber, M. A. Khalaf, Rapid colorimetric sensing of chlorpromazine HCl antipsychotic through in situ growth of gold nanoparticles, RSC Adv., 14 (2024) 2327-2339. https://doi.org/10.1039/D3RA05516G

[25] A. Al-Ani, J.N. Jeber, A. Elewi, Development of a nanostructured double-layer coated tablet based on polyethylene glycol/gelatin as a

platform for hydrophobic molecules delivery, Egypt. J. Chem., 64 (2021) 1759-1767. https://doi.org/10.21608/ejchem.2021.52019.3066

[26] N. S. Turkey, J. N. Jeber, Turbidimetric determination of mebeverine hydrochloride in pharmaceutical formulations using two consecutive detection zones under continuous flow conditions, Chem. Chem. Technol., 16 (2022) 600-613. https://doi.org/10.23939/chcht16.04.600

[27] N. S. Turkey, J. N. Jeber, Light scattering detector based on light-emitting diodes-solar cells for a flow analysis of Warfarin in pure form and pharmaceutical formulations, J. Phys.: Conf. Ser.,2063 (2021) 012006. https://doi.org/10.1088/1742-6596/2063/1/012006

[28] N. Jeber Jalal, F. Hassan Raed, K. Hammood Mohammad, Solid phase extraction of theophylline in aqueous solutions by modified magnetic iron oxide nanoparticles as an extractor material and spectrophotometry technique for the determination, Res. J. Chem. Environ., 23 (2019) 94-100. https://www.worldresearchersassociations.com/ChemSpecialMay2019/12.pdf

[29] B. M. Trzcińska, Classification of black powder toners on the basis of integrated analytical information provided by Fourier transform infrared spectrometry and X-ray fluorescence spectrometry, J. Forensic Sci., 51 (2006) 919-924. https://doi.org/10.1111/j.1556-4029.2006.00167.x

[30] M. Iranifam, Revisiting flow-chemiluminescence techniques: pharmaceutical analysis, Lumin., 28 (2013) 798-820. https://doi.org/10.1002/bio.2441

[31] N. S. Turkey, J. N. Jeber, A flow analysis system integrating an optoelectronic detector for the quantitative determination of active ingredients in pharmaceutical formulations, Microchem. J., 160 (2021) 105710. https://doi.org/10.1016/j.microc.2020.105710

[32] J. N. Jeber, N. S. Turkey, An optoelectronic flow-through detectors for active ingredients determination in the pharmaceutical formulations, J. Pharm. Biomed. Anal., 201 (2021) 114128. https://doi.org/10.1016/j.jpba.2021.114128

[33] N. S. Turkey, J. N. Jeber, Flow Injection analysis with turbidity detection for the quantitative determination of mebeverine hydrochloride in pharmaceutical formulations, Baghdad Sci. J., 19 (2022) 141-154. https://doi.org/10.21123/bsj.2022.19.1.0141

[34] J. A. Ocaña-González, M. Ramos-Payán, R. Fernández-Torres, M. V. Navarro, M. Á. Bello-López, Application of chemiluminescence in the analysis of wastewaters–a review, Talanta, 122 (2014) 214-222. https://doi.org/10.1016/j.talanta.2014.01.028

[35] H. Wang, M. Li,B. Wang, M. Wang, I. Kurash, X. Zhang, W. Feng, Magnetic Fe_3O_4 nanoparticle catalyzed chemiluminescence for detection of nitric oxide in living cells, Anal. Bioanal. Chem., 408 (2016) 5479-5488. https://doi.org/10.1007/s00216-016-9646-1

[36] M. J. Chaichi, M. Ehsani, A novel glucose sensor based on immobilization of glucose oxidase on the chitosan-coated Fe_3O_4 nanoparticles and the luminol–H_2O_2–gold nanoparticle chemiluminescence detection system, Sens. Actuators. B Chem., 223 (2016) 713-722. https://doi.org/10.1016/j.snb.2015.09.125

[37] N. Kaewkhomdee, C. Kalambaheti, S. Predapitakkun, A. Siripinyanond, J. Shiowatana, Iron fractionation for corrosion products from natural gas pipelines by continuous-flow sequential extraction, Anal. Bioanal. Chem., 386 (2006) 363-369. https://doi.org/10.1007/s00216-006-0633-9

[38] T. R. Lenhart, K. E. Duncan, I. B. Beech, J. A. Sunner, W. Smith, V. Bonifay, B. Biri, J. M. Suflita, Identification and characterization of microbial biofilm communities associated with corroded oil pipeline surfaces, Biofouling, 30 (2014) 823-835. https://doi.org/10.1080/08927014.2014.931379

[39] R. N. Montagnolli, P. R. Lopes, E. D. Bidoia,

Screening the toxicity and biodegradability of petroleum hydrocarbons by a rapid colorimetric method, Arch. Environ. Contam. Toxicol., 68 (2015) 342-353. https://doi.org/10.1007/s00244-014-0112-9

[40] A. U. Ammar, M. Shahid, M. K. Ahmed, M. Khan, A. Khalid, Z. A. Khan, Electrochemical study of polymer and ceramic-based nanocomposite coatings for corrosion protection of cast iron pipeline, Materials, 11 (2018) 332. https://doi.org/10.3390/ma11030332

[41] L. Chen, D. Xiong, Magnetic techniques for mineral processing, Progress in Filtration and Separation, (2015) 287-324. https://doi.org/10.1016/B978-0-12-384746-1.00007-0

[42] J. R. Dean, Extraction techniques in analytical sciences, John Wiley & Sons, pp. 1-336, 2010. https://www.wiley.com

[43] T. S. Khan, Review of black powder in gas pipelines – An industrial perspective, J. Nat. Gas Sci. Eng., 25 (2015) 66-76. https://doi.org/10.1016/j.jngse.2015.04.025

[44] A. Karabchevsky, A. Mosayyebi, A. V. Kavokin, Tuning the chemiluminescence of a luminol flow using plasmonic nanoparticles, Light sci. Appl., 5 (2016) e16164. https://doi.org/10.1038/lsa.2016.164

[45] S. Yan, S. Ge, W. Qiao, Y. Zuo, Synthesis of ferromagnetic semiconductor 0.67 $FeTiO_3$–0.33 Fe_2O_3 powder by chemical co-precipitation, J. Magn. Magn. Mater., 322 (2010) 824-826. https://doi.org/10.1016/j.jmmm.2009.11.011

[46] X. Xue, K. Hanna, N. Deng, Fenton-like oxidation of Rhodamine B in the presence of two types of iron (II, III) oxide, J. Hazard. Mater., 166 (2009) 407-414. https://doi.org/10.1016/j.jhazmat.2008.11.089

Anal. Methods Environ. Chem. J. 7 (4) (2024) 33-50

AMECJ

Research Article, Issue 4
Analytical Methods in Environmental Chemistry Journal
Journal home page: www.amecj.com/ir

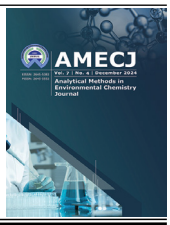

Removal and determination of basic fuchsin from wastewater using natural sugar cane bagasse by UV-Vis Spectrophotometry

Smail Imame[a], Hafssa Atlas[a], Jamal Houssaini[a], Mohamed Sadoq[a], Mohammed Legsaier[a], Khaoula Loukili[a], Karim Mohamed EL Bakkali[a], Ilham Kirm[a], Abdullah Palsan Sannasi[b] and Fatima Boukhlifi[a,*]

[a] *Laboratory of Chemistry and Biology Applied to the Environment, URL-CNRST-N◦13, Faculty of Sciences, Moulay Ismail University, Meknes 50050, Morocco.*

[b] *Faculty of Agro-Based Industry, University Malaysia, Kelantan Jeli Campus, Jeli Kelantan 17600, Malaysia*

ARTICLE INFO:

Received 29 Jul 2024

Revised form 10 Oct 2024

Accepted 7 Nov 2024

Available online 28 Dec 2024

Keywords:
Adsorption,
Basic fuchsin,
Sugarcane bagasse,
Kinetic study,
UV-Vis spectrophotometry

ABSTRACT

Recently, utilizing biomass for adsorption has become a widely adopted approach to diminish contaminants in wastewater before its discharge into the environment. Our objective is to scrutinize the adsorption process of Basic Fuchsin (BF) on sugarcane bagasse (SCB). The investigation involves optimizing the process by exploring parameters such as bio-adsorbent mass, contact time, temperature, and the pH of the BF solution; the solutions studied were analyzed using UV-Vis spectrophotometry to assess the concentration of the BF dye. The basic fuchsin dye has a limit of detection (LOD) of 0.06 mg L^{-1} by UV-Vis spectrophotometry, while the limit of quantification (LOQ) is 0.1 mg L^{-1}. The method's measurement range varies from 0.1 to 10 mg L^{-1}, guaranteeing precise, reproducible measurements. The findings indicate that BF adsorption on SCB is most effective in a basic environment, attributed to electrostatic interactions between the negatively charged SCB surface within this pH range and the organic cations of the dye. Under optimal conditions, BF removal by SCB reaches 97%. Kinetic modeling of adsorption reveals that the pseudo-second-order model best describes BF adsorption on SCB. In contrast, isotherm modeling indicates that Langmuir and Freundlich's models provide the most accurate descriptions. The Langmuir separation coefficient R_L and the Freundlich parameter 1/n both fall below one, signifying the favorability of BF adsorption on SCB. Thermodynamic assessments underscore the spontaneity of the BF adsorption process on SCB. Overall, the study results emphasize the capability of SCB as a bio-adsorbent for removing organic dyes from aqueous solutions.

1. Introduction

The dyeing industry's discharge of harmful substances into the environment significantly threatens aquatic wildlife and human health. These discharges, frequently containing toxic chemicals and synthetic dyes, exert a destructive influence on aquatic ecosystems [1-3]. Nevertheless, basic fuchsin, also known as Basic Violet 14, is a cationic dye that has been identified as a potential carcinogen in several countries due to its toxic and carcinogenic properties [4] It also stains collagen, muscles, mitochondria, and tuberculosis bacilli. It has anesthetic, bactericidal (against Gram-

*Corresponding Author: Fatima Boukhlifi
Email: f.boukhlifi@umi.ac.ma
https://doi.org/10.24200/amecj.v7.i04.337

positive bacteria), and fungicidal properties. Direct contact with the dye may result in significant irritation to the eyes and skin [5]. Because of its low biodegradability, toxicity, carcinogenicity, and unsightly appearance, the removal of BF from wastewater systems should be a significant concern, requiring imminent experimentation and implementation [6]. Until now, numerous efforts have been undertaken to remove this dye from solutions, employing various methods to mitigate its concentration in wastewater. Diverse methods for eliminating contaminants from wastewater include biological oxidation, membrane separation, photocatalytic degradation, ion exchange, chemical precipitation, and adsorption [7]. Nevertheless, these techniques have drawbacks such as cost, regeneration, or reusability concerns. Bio-sorption emerges as a cost-effective and environmentally friendly alternative for eliminating contaminants from water, especially those that are not readily biodegradable, such as dyes [8]. Biomasses are particularly suitable for this purpose due to their large-scale availability, ability to grow in inexpensive media, ease of handling, and cost-effectiveness. In addition, they contain various functional groups that can serve as adsorption sites [9].Several agricultural wastes have been used (biosorbent) to treat wastewater. These include waste-bottom ash and de-oiled soya [6], Micro Fungi Fusarium Oxysporum F. Sp. Pisi [9], mussel shell biomass waste [10], Aspergillus niger and Humicola grisea [11]. In this investigation, sugarcane bagasse, a fibrous residue derived from sugarcane grinding during juice extraction in sugar mills and refineries, was selected as a bio-adsorbent for treating wastewater containing basic fuchsin. This material has effectively eliminated contaminants, including dyes and heavy metals, from wastewater due to its advantageous attributes, such as biodegradability, availability, buoyancy, and cost-effectiveness. Additionally, it primarily comprises cellulose, hemicellulose, and lignin, featuring a polymer structure abundant in hydroxyl and carboxyl groups that interact with the chemical pollutants present in the treated solution [12]Some organic pollutants can also be adsorbed by nanomaterials [13-14]. We examined the influence of various experimental parameters on the adsorption process, including the amount of material used, contact time, solution pH, and temperature. To demonstrate the viability of this method, we also assessed thermodynamic factors, including enthalpy, entropy, and free energy.

2. Materials and Methods

2.1. Materials

In this study, the dye under investigation is basic fuchsin (CAS No: 632-99-5, Sigma-Aldrich, France). This is a triamino-triphenyl methane dye with the molecular formula of $C_{20}H_{20}ClN_3$. It is composed of three dyes: Pararosaniline, Rosaniline, and Magenta II, and is commonly referred to as Magenta II [6].

Basic fuchsin (MW= 337.85 g mol^{-1}, λmax = 543nm) generated effluents containing a similar dye. Scheme 1 illustrates the molecular structure of basic fuchsin. Analytical-grade chemicals were employed for all experiments, and distilled water was used in the procedures.

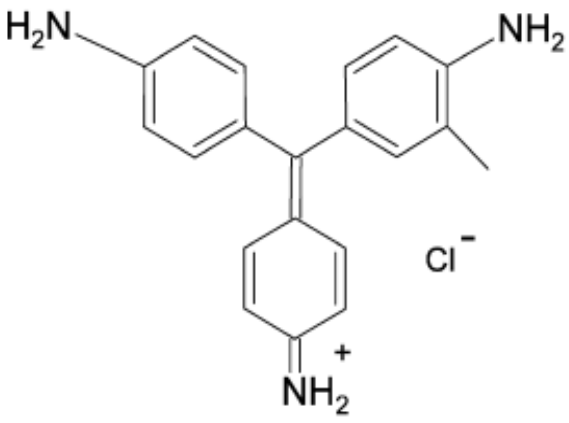

Scheme 1. Chemical structure of basic fuchsin.

2.2. Preparation of the solid

The preparation of sugarcane bagasse (SCB), derived from the fibrous residue obtained after crushing sugarcane for juice extraction in sugar mills, is carried out by several operations: the

bagasse is rinsed repeatedly with warm distilled water, followed by vacuum filtration, and then dried at 60°C for one night. Finally, the solid obtained is ground, the particle size used has been determined, and the size of the particles is less than or equal to 0.2mm.

2.3. Characterization Techniques

The powder X-ray diffraction pattern (XRD) of the sample was collected with a Bruker AXS model (D8-advance A25) diffractometer using Cu-K_α foundation (λ = 1.5418Å) at 40Kv, 20mA. XRD results were recorded in the 2θ range between 5° and 70° in 0.02° angle increments. Infrared spectra were performed using a Shimadzu IRAFFINIY-1S Fourier transform spectrometer (FTIR) equipped with a detector (TGS) and a ceramic source, separated by an optical system using a Michelson interferometer. The samples were prepared as 12mm diameter pellets with a mass of 3.0 mg of solid diluted in 97mg of KBr. Absorption spectra were analyzed with a resolution of 20 cm^{-1} in the wavelength range between 400 and 4000 cm^{-1}. UV-visible spectrophotometry is a method of qualitative and quantitative analysis to identify the presence and concentration of a chemical species. For this purpose, the spectrophotometer used is of the type (SHIMADZU-UV 1800) that allows the measurement of the absorbance of a solution at a precise wavelength in the range between (190 to 900 nm) from the concentrations deduced from the Beer-Lambert law (A = ε. ℓ.C). The point of zero charge refers to the pH at which the solid's surface charge becomes zero, and it was determined using the solid addition method.

2.4. Adsorption procedure

In this research, all experiments were conducted using the same experimental setup, except for the temperature study, where a water bath was employed to regulate the temperature to the desired level. To this end, a series of samples was prepared by suspending a precise quantity in milligrams of the biomass in a 20 mL volume of an aqueous solution of the basic fuchsin of known initial concentration C_0 (50 mg L^{-1}). The suspensions are then stirred until equilibrium is reached using a stirrer. This device creates movement in the mixture to ensure even distribution and improve contact between the adsorbent and the adsorbate. After this period, the centrifuge is a device that exerts a continuous centrifugal force generated by rotation and is used to extract the supernatant from the liquid phase. The solution was analyzed by UV-visible spectrophotometry at a wavelength of 543 nm. The quantities of BF adsorbed were determined from the calibration curve. The adsorption capacity (qe in mg g^{-1}) and the percentage of BF elimination were calculated by Equations 1 and 2.

$$q_{ads} = \frac{(C_0 - C_e).\ V}{m} \qquad \text{(Eq.1)}$$

$$\text{Yield (\%)} = \frac{(C_0 - C_e)}{C_0}.100 \qquad \text{(Eq.2)}$$

Where C_0 and Ce are, respectively, the initial and dye equilibrium concentration (mgL^{-1}); m is the mass of the solid in g; V is the volume of the dye solution BF in L, and q_{ads} is the adsorbed amount per gram of adsorbent (mg g^{-1}).

2.5. Modeling of adsorption kinetics

Throughout the literature, diverse kinetic models have been utilized to characterize and compute theoretical rates and to elucidate potential adsorption mechanisms in adsorption experiments. In this context, an exploration of the adsorption behavior of BF on SCB was conducted through the examination of three commonly employed kinetic models: pseudo-first-order (PFO), pseudo-second-order (PSO), and intra-particle diffusion. Linear regression analysis was employed for this investigation.

2.5.1.Pseudo first-order model

Equation 3a defines the pseudo-first-order model proposed by Lagergren [15]

$$\frac{dqt}{dt} = K_1(q_e - q_t) \qquad \text{(Eq.3a)}$$

Where k_1 is the first-order reaction rate constant for the adsorption of BF onto SCB in (min-1), qe, qt the quantity of BF adsorbed at equilibrium and at time t in (mg g^{-1}), t is the contact time in (min). After integration with initial conditions q_{t0} at t = 0, Equation 3a converts to Equation 3b. The representation of Log(qe-qt) = f(t), gives us a straight line which gives k_1 and qe.

$$q_t = q_e(1 - e^{K_1 t}) \quad \text{(Eq.3b)}$$

2.5.2. Pseudo-second-order model

The pseudo-second-order model is given by Equation 4. K_2 is the second-order reaction rate constant for the adsorption of BF onto SCB in (g mg^{-1} min^{-1}). After integration of Equation 4, we obtain Equation 5a. Linearization of the Equation 5 gives the Equation 5b. The representation of $\frac{t}{q_t}$ = f(t) in Equation 5a gives us a straight line from which we can determine k_2 and qe.

$$\frac{dqt}{dt} = K_2(q_e - q_t)^2 \quad \text{(Eq.4)}$$

$$q_t = \frac{K_2 q_e^2 t}{K_2 q_e t + 1} \quad \text{(Eq.5a)}$$

$$\frac{t}{q_t} = \frac{1}{K_2 q_e^2} + \frac{1}{q_e} t \quad \text{(Eq.5b)}$$

2.5.3. Intra-particle diffusion model

Intra-particle diffusion is described by Equation 6 described by Weber and Morris and used to calculate k_d and C[16].

$$q_t = K_d t^{1/2} + C \quad \text{(Eq.6)}$$

With K_d the intra-particle diffusion rate constant and C the boundary layer thickness.

2.6. Thermodynamic parameters

The thermodynamic parameters (ΔG°), (ΔH°), and (ΔS°) for the studied system (BF/SCB) were determined and calculated at different temperatures (25°C, 35°C and 45°C) [17]. The adsorption-free energy (ΔG°) is calculated according to the standard Gibbs formula defined by Equation 7a. The thermodynamic parameters of the BF's adsorption on the adsorbent can be estimated from the curve representing the variation ln (K_d) as a function of 1/T in Equation 7b.

$$\Delta G° = - RT. \ln(K_d) \quad \text{(Eq.7a)}$$

$$\ln K_c = \frac{\Delta S^\circ_{ads}}{R} - \frac{\Delta H^\circ_{ads}}{RT} \quad \text{(Eq.7b)}$$

In Equation 7a, K_d is the equilibrium distribution constant defined by $K_d = \frac{q_e}{Ce}$. q_e (mg g^{-1}) represents the amount of adsorbed dye at equilibrium, and Ce (mg L^{-1}) is the residual concentration of the adsorbate at equilibrium. In Equation 7b, the values of (ΔH°_{ads}) and (ΔS°_{ads}) are computed from the slope and intercept, respectively, of the line obtained by plotting ln (Kc) against 1/T.

2.7. Modeling of adsorption isotherms

2.7.1. Langmuir isotherm model

This is relevant to the adsorption occurring on specific uniform sites with a finite number of identical sites in a monolayer. Langmuir's model relies on fundamental assumptions, commonly known as the ideal localized monolayer model. These assumptions posit that molecules are adsorbed onto specific sites on the adsorbent surface and that each site can accommodate only one molecule, forming a monolayer. Initially employed for systems featuring monolayer adsorption on the adsorbent surface, the Langmuir model operates under the assumption that all adsorption sites are uniform, independent of surface coverage, and occur without lateral interaction with adsorbate molecules [18]. Equation 8a presents the model's expression. To ascertain its adsorption parameters, we utilize the linearized form of the Langmuir isotherm, expressed by Equation 8b. Moreover, a crucial feature of the Langmuir isotherm is the separation factor R_L, which is defined by Equation 8c. The separation factor, R_L, indicates the shape of the isotherm and the nature of the adsorption process, as reported in Table 1 [19].

$$qe = \frac{q_m.K_l.C_e}{1+K_l.C_e} \quad \text{(Eq.8a)}$$

$$\frac{1}{qe} = \frac{1}{K_l.q_m.C_e} + \frac{1}{q_m} \quad \text{(Eq.8b)}$$

$$R_l = \frac{1}{1+K_l.C_e} \quad \text{(Eq.8c)}$$

Where q_m is the maximum adsorbed quantity in mg g^{-1}, K_L is the Langmuir constant in Lmg^{-1}. C_i is the initial concentration of the dye (mg L^{-1}).

Table 1. The separation factor R_L

Nature of the process	R_L values
Unfavorable	$R_L > 1$
Linear	$R_L = 1$
Favorable	$0 < R_L < 1$
Irreversible	$R_L = 0$

2.7.2. Freundlich isotherme model

The Freundlich model for isotherms assumes that adsorption takes place on a heterogeneous surface, and the distribution of the heat of adsorption across the adsorbent surface is non-uniform. The linearized expression of the Freundlich model is given in Equation 9a [18].The parameters K_f and n are determined from the linear form of the isotherm by plotting in Equation 9b.The linearization of Equation 9b implies a passage of the terms in the logarithmic form of Equation 9c.

$$qe = \frac{q_m.K_l.C_e}{1+K_l.C_e} \quad \text{(Eq.9a)}$$

$$\frac{1}{qe} = \frac{1}{K_l.q_m.C_e} + \frac{1}{q_m} \quad \text{(Eq.9b)}$$

$$R_l = \frac{1}{1+K_l.C_e} \quad \text{(Eq.9c)}$$

Where qe is the amount adsorbed at equilibrium, Ce is the residual concentration of the dye at equilibrium, and n represents the adsorption intensity and indicates whether the adsorption is favorable. If n<1 linear adsorption, if n>1 physical adsorption is favorable [17].

2.7.3. Temkin isotherme model

The Temkin isotherm relies on the heat of adsorption of ions resulting from interactions between the adsorbate and adsorbent, expressed in linear form. Equation 10 typically gives the general representation of the Temkin isotherm [20].

$$q_e = \frac{R.T}{b_T} \mathrm{Ln}\ (A_T.C_e) \quad \text{(Eq.10)}$$

The b_T and A_T are Temkin isotherm constants, R is the perfect gas constant (8.314 Kj mol^{-1}), Ce is the equilibrium concentration of dye ions (mgL^{-1}), and T is the absolute temperature.

2.7.4. Dubinin–Radushkevich isothermal model

The Dubinin-Radushkevich (D-R) model is commonly employed to differentiate between physical and chemical adsorption, which was shown in Equation 11 [18]:

$$\ln(q_e) = \ln(q_D) - \beta\varepsilon^2 \quad \text{(Eq.11)}$$

where qe is the equilibrium adsorption capacity (mmol g^{-1}), q_D is the D–R adsorption capacity (mmol g^{-1}), β ($mol^2\ kj^{-2}$) is the activity coefficient related to the mean adsorption energy, and e the Polanyi potential given by Equation 12.

$$\varepsilon = RT\ln\left(1 + \frac{1}{C_e}\right) \quad \text{(Eq.12)}$$

Here, R represents the universal gas constant (8.314 $J.mol^{-1}K^{-1}$), and T stands for the absolute temperature in Kelvin (K). Consequently, when we plot $\ln(q_e)$ against ε^2, we obtain a linear relationship characterized by a slope of β and a y-intercept of $\ln(q_D)$. The constant β provides valuable insights into the mean free energy E (Kj mol^{-1}) of adsorption per adsorbate molecule when it transitions from an infinite distance in the solution to the solid surface. This value can be computed using Equation 13.

$$E = \frac{1}{\sqrt{2\beta}} \quad \text{(Eq.13)}$$

The E value is a frequently utilized parameter for discerning the nature of adsorption. In an ion

exchange process, the E value typically falls within the range of 8.0 to 16.0 kJ mol^{-1}, whereas in a physic-sorption process, the E value is generally below 8.0 kJ mol^{-1} [18].

3. Results and Discussion

3.1. Characterizations

3.1.1.XRD Analysis

The XRD diffractogram of sugarcane bagasse is shown in Figure 1. The SCB is mainly composed of lignin, cellulose, and hemicelluloses. The two peaks detected have values of 2 around 16° and 22° due to the semi-crystalline structure of the cellulose contained in the biomass [21]. Moreover, the XRD spectrum is similar to that of other lignocellulosic wastes [22].

3.1.2.FT-IR Analysis

Fourier transform infrared spectroscopy was utilized to analyze the SCB solid, and the resulting FT-IR spectrum is presented in Figure 2. The FTIR spectrum of SCB powder (Figure 2) reveals several peaks that can be identified as follows: The strong band appearing at 3337 cm^{-1} is attributed to OH groups (alcohols, phenols, and carboxylic acids) [23,24] and NH of amides [25], C-H bonds (alkanes) were confirmed by the band appearing at 2913 cm^{-1} [23]. The band at 1732 cm^{-1} is characteristic of the stretching vibration of the C=O of xylan carboxylic acids present in hemicelluloses [26]. The band at 1611 cm^{-1} is attributed to C=C deformation (lignin aromatic) [27], while the band at 1370 cm^{-1} confirms the presence of methoxy -C-O groups in lignin [28], the bands at 1250 and 1052 cm^{-1} are attributed to the elongation vibration of the C-O bonds of aromatic compounds and acid, alcohol, phenol, ether and ester functions [23]; and the band appears at 606 cm^{-1} attributed to the elongation of the C-X bond (alkyl halide) [23].

3.1.3.Point of zero charge

The point of zero charge (pH_{PZC}) represents the pH of the solution in which the surface is neutrally charged, and its position defines the affinity of the surface for ionic species [29]. The difference between the initial pH and the final pH (pH_f - pH_i) was plotted as a function of the initial pH (pH_i), and the point where pH_f - pH_i =0 was taken as the pHpzc . Figure 3 shows that the pH at which the solid surface has a zero charge corresponds to pH= 7.3. Thus, above pH > 7.3, the solid surface is negative, and below pH 7.3, it is positive.

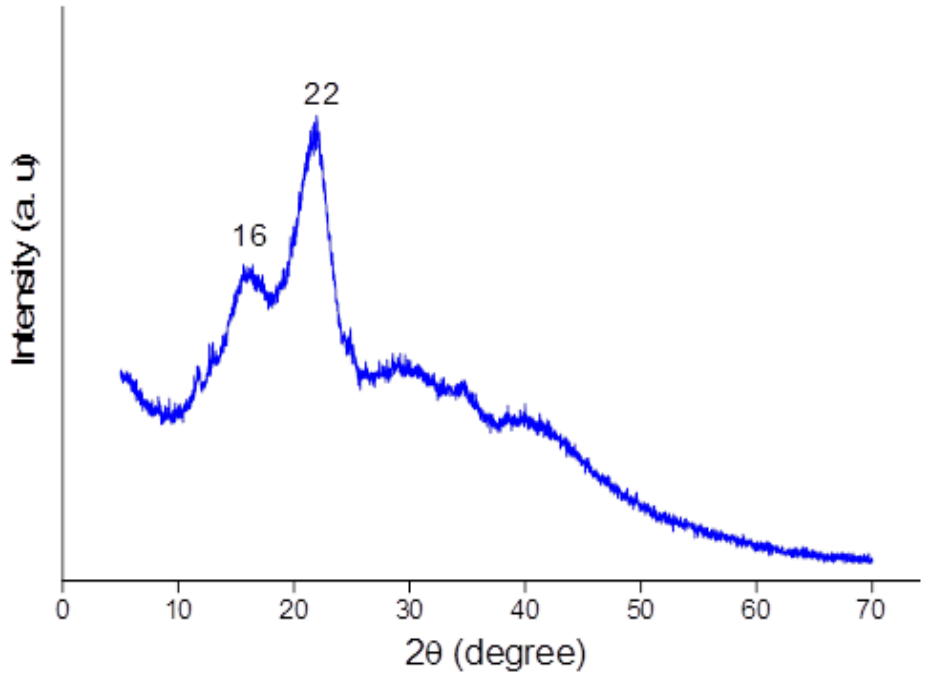

Fig. 1. Powder XRD patterns of SCB

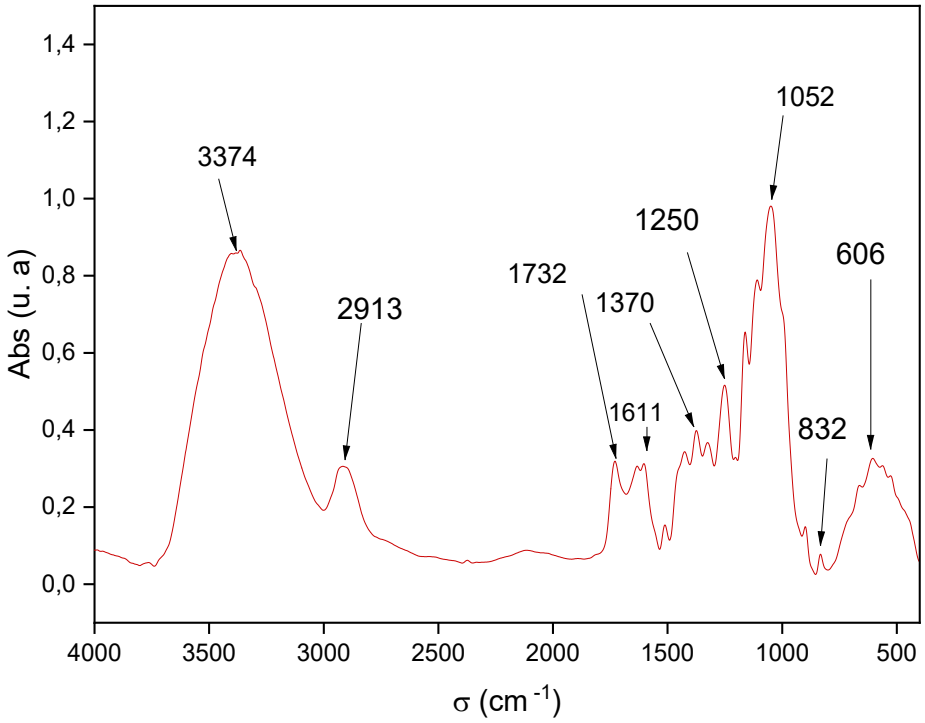

Fig. 2. FT-IR spectra of the SCB solid

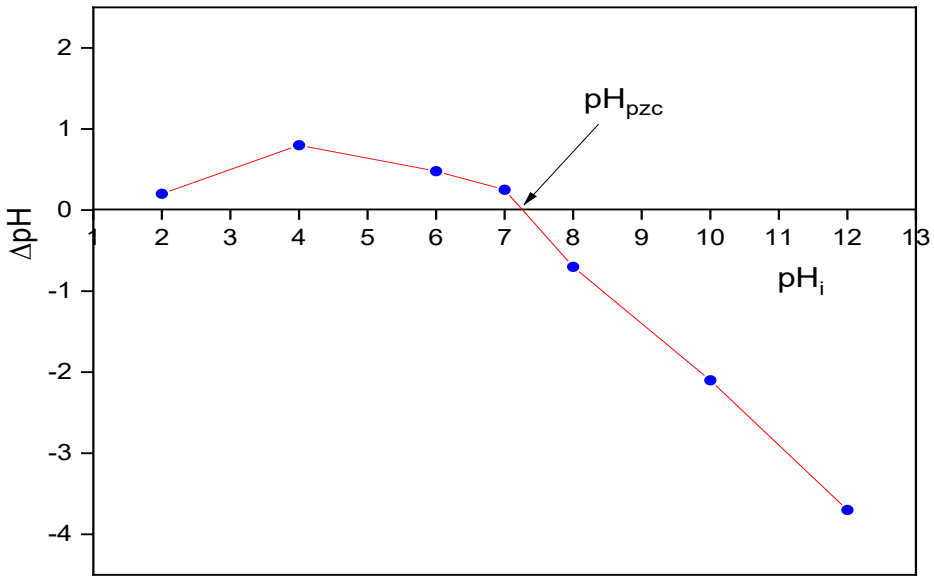

Fig. 3. Point of zero charge of SCB

3.2. Study of BF adsorption on SCB

Various parameters influencing the adsorption phenomenon are examined: the mass of the adsorbate, the solution's initial pH, the adsorbent-adsorbate contact time, and the solution temperature.

3.2.1.Effect of adsorbent mass.

To determine the quantity of adsorbent required to remove the maximum amount of dye, variable masses of adsorbent ranging from 0.01 to 0.14 g were introduced separately into 20 mL of an aqueous

solution of 50 mg L^{-1} of the dye, and the mixture was stirred magnetically until adsorption equilibrium was reached. The results are shown in Figure 4.

Figure 4 illustrates that the dye removal rate escalates as the adsorbent mass increases up to 70 mg, beyond which it stabilizes nearly constant. This increase in dye removal as a function of adsorbent mass can be ascribed to the increase in adsorbent surface area, increasing adsorption sites' availability. However, after adding 70 mg bio-sorbent, the process reached equilibrium, and adsorption capacity converged to a constant value of 6.94 mg g^{-1}, corresponding to 97% removal. Subsequent experiments confirmed that the optimum adsorbent mass is 70 mg.

3.2.2.Effect of contact time

The figure below demonstrates the influence of contact time on the adsorption of BF dye at various temperatures. Figure 5 illustrates the influence of time on BF adsorption by SCB at different temperatures (25°C, 35°C and 45°C). All curves show an increase in adsorption capacity over time. The rate initially is rapid, then evolves gradually until equilibrium is reached. The initial phase is attributed to many vacant adsorption sites and the high affinity of the solute concentration with the surface. Subsequently, the rate of adsorption slows down, marking the second stage. Finally, a dynamic equilibrium is reached with a maximum adsorption value (q_{max}) after 30 minutes of stirring the solution of BF dye and SCB bio-adsorbent at different temperatures. The curves show that the amount of BF adsorbed by the biomass exhibits a slight dependence on temperature; an increase in temperature has an adverse effect on the adsorption process, suggesting an exothermic character [30].

3.2.3.Effect of pH

The solution's pH influences the charging characteristics of bio-adsorption, consequently affecting dye adsorption. This study conducted a sequence of experiments, altering the pH within the range of 2 to 12 for suspensions of biomass in 20 mL of dye solution for a contact time sufficient to reach equilibrium. The pH of the suspensions was adjusted to the desired value by adding HCl (0.1M) or NaOH (0.1M). Figure 6 displays the outcomes of the fluctuation in adsorption percentage concerning solution pH. Figure 6 shows an increase in the adsorption of BF on SCB, rising from 73% to a maximum of 97% in the pH range 2-8. To elucidate the mechanism of the pH

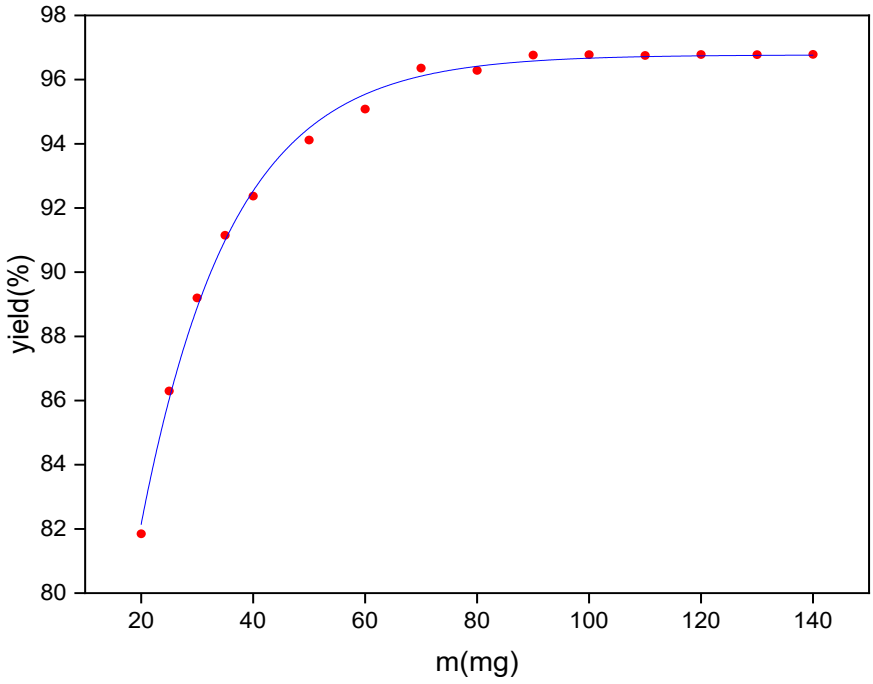

Fig. 4. Percentage of BF removal as a function of SCB mass

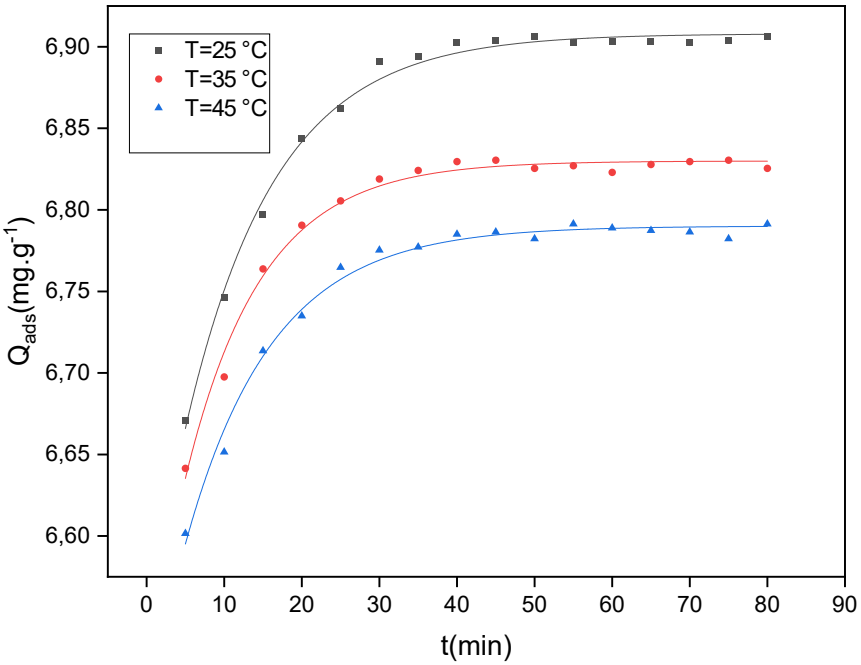

Fig. 5. Effect of contact time

impact on adsorption, it is crucial to comprehend the surface charge of both the adsorbent and adsorbate. When the solution pH is below 7.3 (pH_{pzc}=7.3), the adsorbent surface charge is positive as the pH rises, additional electronegative active sites emerge on the surface of the biomass. These active sites have the capability to bind with positively charged dye molecules, leading to a notable increase in the percentage removal of basic fuchsin. Conversely, when the solution pH exceeds pH_{pzc}, the surface of the adsorbent becomes negatively charged, and there is a robust interaction between the adsorbent and cationic dye molecules. Consequently, the best pH range for FB removal is between 8 and 12. This outcome can be clarified by the electrostatic interaction between the bio-sorbent surface and the particles of the cationic dye.

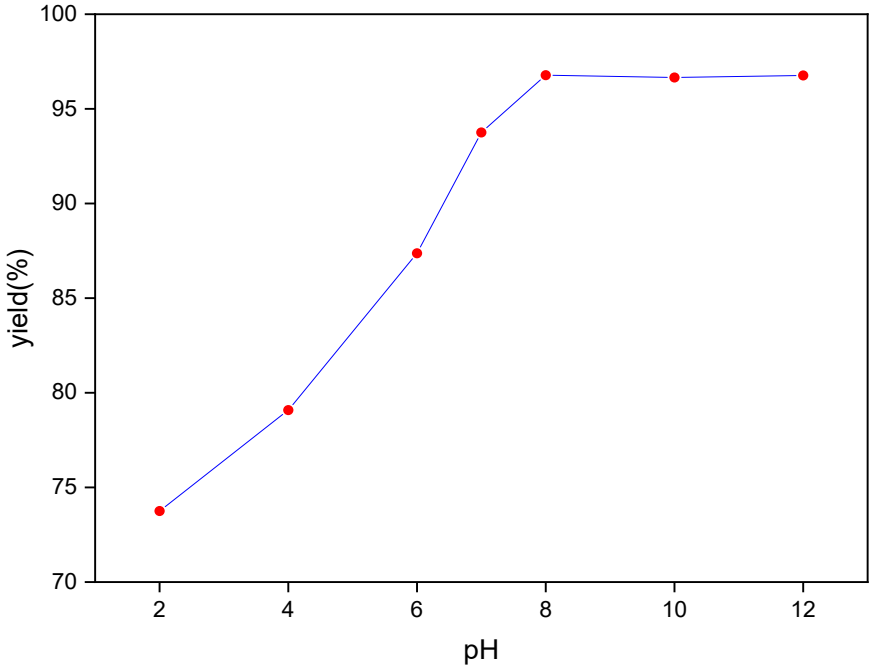

Fig. 6. Influence of pH on BF adsorption.

3.3. Thermodynamics parameters

To determine the thermodynamic quantities of BF adsorption by SCB, the representation of the variation of ln(Kc) as a function of $\frac{1}{T}$ is used (Fig.7). The activation energy of the adsorption process is determined by applying the Arrhenius equation ($k = A.e^{-Ea/RT}$) The thermodynamic parameters are grouped in Table 2. The negative value of ΔH° confirms the exothermic nature of the adsorption [31]. Positive ΔS° values suggest an increase in randomness at the solid solution interface in the internal structure of BF adsorption on the bio-adsorbent [17]. Negative ΔG° values were observed at all three temperatures, which indicates that the spontaneous process is favored at these temperatures [32]. Additionally, the activation energy value, calculated using the Arrhenius equation, is below 40 Kj mol^{-1}, indicating that the adsorption process follows a physisorption mechanism.

3.4. Modeling of adsorption kinetics

3.4.1.Pseudo-first-order kinetics

The rate of FB adsorption by SCB was determined using an FB solution with an initial FB concentration of 50 mg L^{-1} using a bio-adsorbent dose of 7.0 g L^{-1}. Experimental adsorption rate data were fitted to the three kinetic models: (PFO), (PSO) and (IPD). All kinetic information regarding the adsorption of FB by SCB, derived from the respective diagrams (Figures 8 to 10), is summarized in both Table 4 and Table 5. The R^2 correlation coefficient was also used to compare the goodness of fit of the models used.

3.4.2.Pseudo-first-order kinetics

Figure 5 shows a plot of ln(qe -qt) versus time using the linearized pseudo-first-order model. The rate constant (k) and equilibrium capacity (qe) were determined by utilizing the slope and y-intercept obtained from the plot.

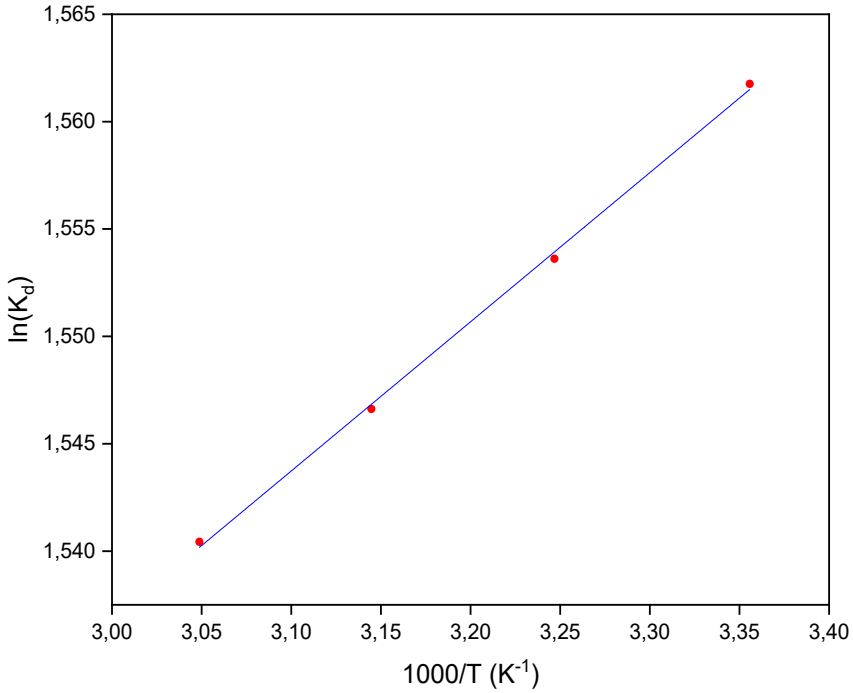

Fig. 7. Evolution of $\ln(K_c)$ as a function of T^{-1}

Table 2. Thermodynamic parameters

Temperature (K)	$\Delta H°_{ads}$ (Kjmol^{-1})	$\Delta S°_{ads}$ (j.K^{-1}mol^{-1})	$\Delta G°_{ads}$ (Kj.mol^{-1})	R^2	Ea (Kj.mol^{-1})
298	-5.82	11.05	-9.11	0.998	23.83
303			-9.17		
308			-9.22		
313			-9.27		

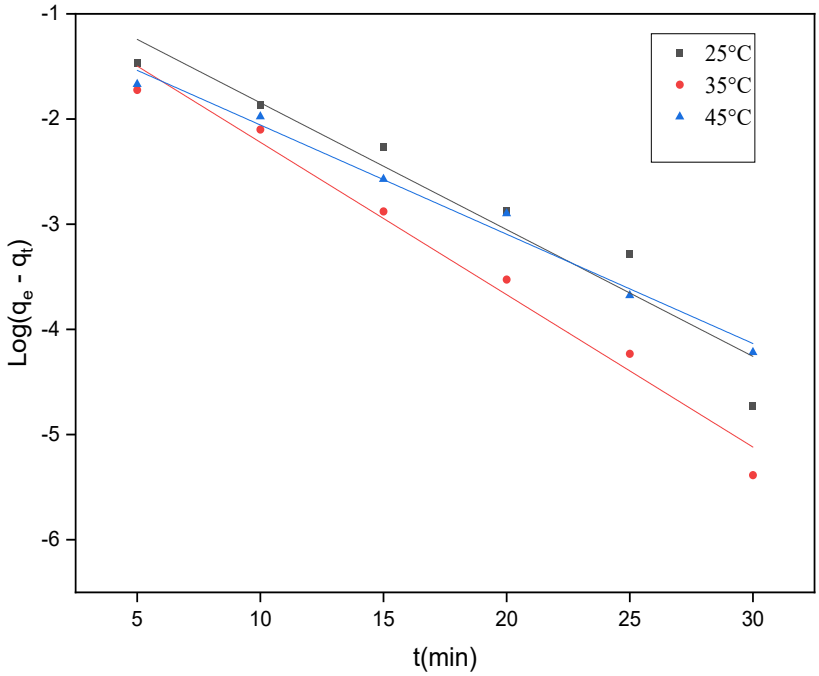

Fig. 8. Application of the pseudo-first-order model on BF-SCB adsorption.

On the basis of the results obtained (Figure 8 and Table 3), it is clear that the experimental data points of this model do not show a perfect linear relationship. Furthermore, the quantities of BF adsorbed obtained experimentally differ significantly from the calculated values (q_{cal}), and the R^2 coefficients deviate considerably from 1. Consequently, the results of BF adsorption on our adsorbent do not fit this model.

3.4.3. Pseudo-second order kinetics

Similarly, $\frac{t}{q_t}$ was plotted as a function of time according to the linearized pseudo-second-order model (Fig.9). The experimental results were also compared with the pseudo-second-order kinetic model described by Equation 5. The kinetic parameters determined from the straight lines obtained are listed in Table 3. As predicted by this model, the adsorption capacity is closely aligned with the experimental value, and the

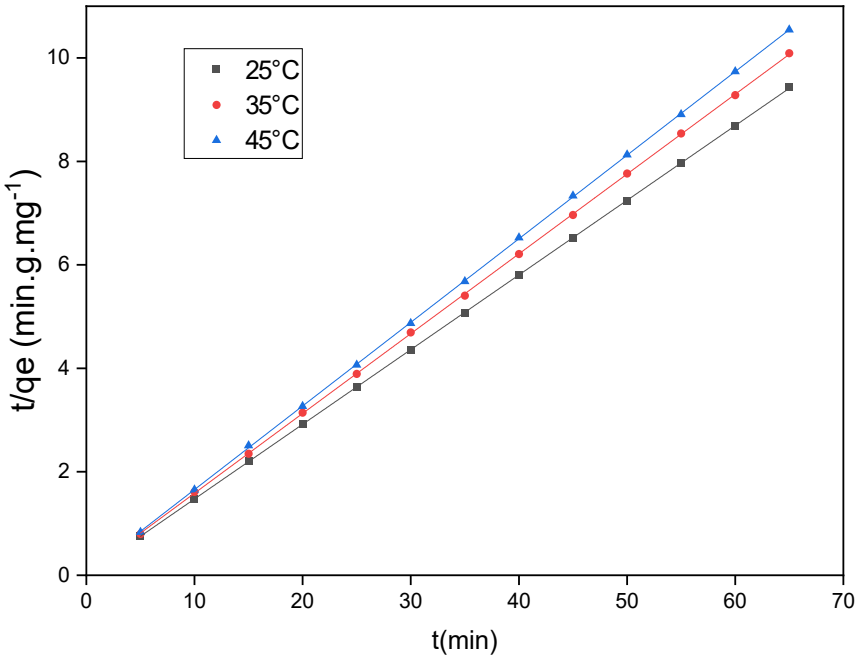

Fig. 9. Application of the pseudo-second-order model to adsorption BF-SCB

Table 3. Parameters for linear modeling of Basic Fuchsin dye adsorption kinetics.

Temperature (K)	Adsorption	Pseudo-first-order model			Pseudo-second-order model		
	q_{exp}(mg/g)	q_{cal}	K_1	R^2	q_{cal}	K_2	R^2
298	6.901	0.50	0.121	0.93	6.94	1.51	0.999
308	6.82	0.461	0.145	0.96	6.50	1.81	0.999
318	6.77	0.360	0.104	0.97	6.21	1.54	0.999

correlation coefficient was 0.999, Suggesting that the adsorption kinetics of Basic Fuchsin on SCB adhere to the second-order model.

3.4.4.Intra-particle diffusion model

Intra-particle diffusion is described by Equation 6. The fit of the variation in the amount of dye adsorbed at each time increment (q_t) to the square root of time ($t^{1/2}$), and its parameters have been determined and illustrated in Figure 10 and Table 4. Considering these findings, it is evident that the curves depicting [q_e = f ($t^{1/2}$)] deviate from the origin, suggesting that the mechanism determining adsorption kinetics is not solely reliant on dye diffusion into the pores of the biomass. The dual linearity observed in the curves points to a combination of two distinct stages, signifying a variation in the speed of adsorption kinetics from one stage to the next. Table 4 reveals that the diffusion rate constant (K_d) values are greater in the initial stage than in the subsequent stage, implying a significantly faster dye diffusion in the first stage. In the initial phase, dye diffusion occurs on the external surface of the adsorbent, whereas the subsequent stage entails the slower diffusion of dye molecules through the internal pores within the biomass particles [33,34]. The non-zero values of the constant C, which denote the thickness of the diffused layer, suggest that the adsorption rate of BF on the adsorbent is influenced by factors extending beyond intra-particle diffusion alone [35].

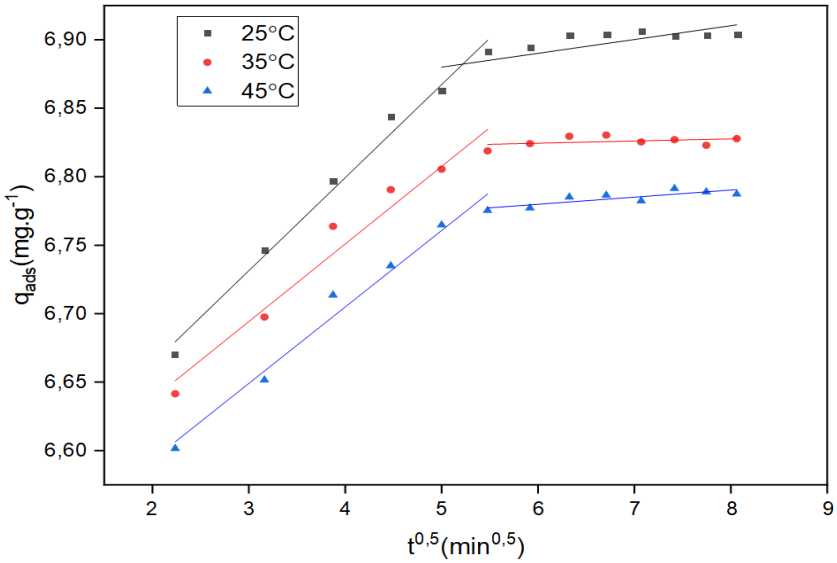

Fig. 10. Application of the external diffusion model to adsorption BF-SCB

Table 4. Parameters of the BF intra-particle diffusion model on SCB.

T (°K)	1st right			2nd right		
	C_1	K_1	R^2	C_2	K_2	R^2
298	6.53	0.058	0.98	6.83	0.010	0.59
308	6.52	0.056	0.97	6.81	0.002	0.37
318	6.48	0.067	0.99	6.74	0.005	0.69

3.5. Modeling of adsorption isotherm

The findings unequivocally demonstrate that all four models exhibit a good fit, characterized by high correlation coefficients ($R^2 > 0.99$). The obtained values for $\frac{1}{n}$ ($0 < \frac{1}{n} < 1$) affirm the favorable nature of adsorption across all the examined temperatures. Moreover, with increasing temperature, the $\frac{1}{n}$ values rise, indicating less favorable adsorption under elevated temperatures [36]. Furthermore, a decrease in the K_F value is noted with rising temperatures, indicating an exothermic process [37]. Modeling of adsorption isotherm is shown in Figure 11 and Table 5. Conversely, the computation of the R_L parameter indicated values below one at all three temperatures, signifying favorable adsorption within the studied temperature range [38]. Moreover, the Langmuir constant (K_L) decreases with rising temperature, indicating a reduction in the affinity between the adsorbent and adsorbate as the temperature increases [39]. In the investigated temperature range, the adsorption energy of the dye from the aqueous solution, as per Temkin's model (b_T), is positive, indicating an exothermic characteristic of the adsorption [40]. The Dubinin-Radushkevich (D-R) isotherm coefficients have been computed and documented in Table 5. The E value is commonly employed to evaluate the adsorption nature. An ion exchange process typically exhibits an E-value ranging from 8.0 to 16.0 kJ mol^{-1}, whereas a physic-sorption process is characterized by an E-value less than 8.0 kJ mol^{-1}[18]. In this investigation, the E values were below 2.0 kJ mol^{-1}, indicating that the BF adsorption process on biomass was a physisorption process. The adsorption of the contaminating BF cations in water occurs due to their solubility in water and their interactions with the surface of the adsorbent. These interactions can be chemical, electrostatic, or Van der Waals.

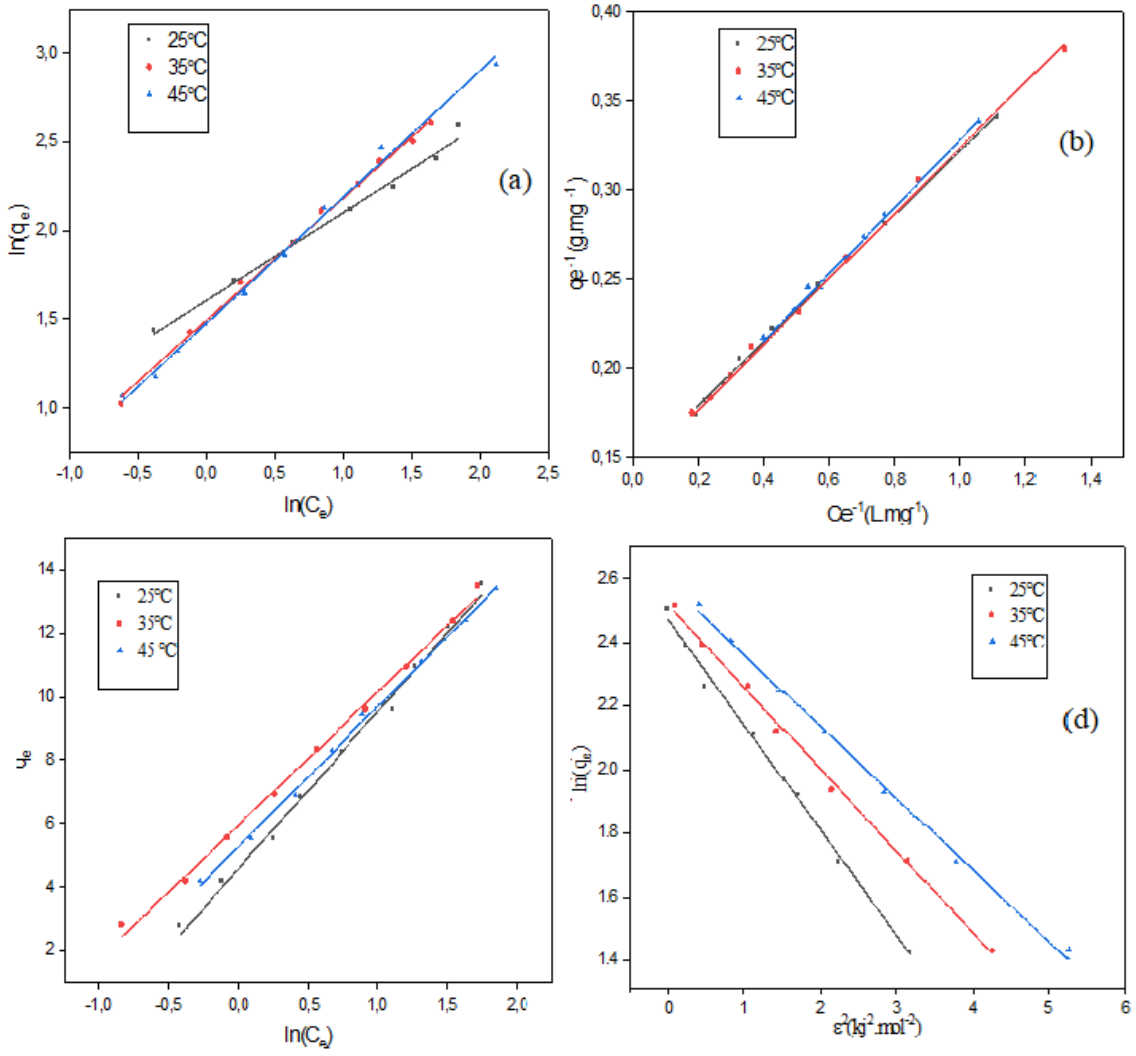

Fig. 11. (**a**) Freundlich isotherm, (**b**)Langmuir isotherm, (**c**)Temkin isotherm (**d**)D-R isotherm at different temperatures.

Table 5. Parameters of four adsorption isotherm models for BF by SCB

Isotherm Model	Parametrs	Temperature (°C)		
		25	35	45
Langmuir	K_L	0.80	0.765	0.739
	q_{max}	6.94	7.14	7.69
	R_L	0.024	0.025	0.027
	R^2	0.997	0.997	0.996
Freundlich	K_f	1.008	1.007	1.0013
	1/n	0.495	0.688	0.712
	R^2	0.996	0.998	0.997
Temkin	A_T	0.11	0.09	0.034
	b_T	501.52	611.58	600.87
	R^2	0.99	0.99	0.99
D–R	q_D (mg.g^{-1})	11.89	12.36	13.34
	b(mol^2.kj^{-2})	0.329	0.257	0.228
	E(kj.mol^{-1})	1.233	1.394	1.480
	R^2	0.99	0.99	0.99

3.6. Mechanism of BF adsorption on SCB

A crucial examination using Fourier transform infrared spectroscopy is necessary to suggest a mechanism for BF's adsorption on SCB.

This analysis, conducted before and after BF adsorption, is vital for investigating the interaction between dye molecules and the active sites on the surface of the solid material. No new bands appear after comparing the Fourier transform infrared (FTIR) spectra for the solid material before and after dye adsorption (Fig.12). The solid material primarily comprises cellulose, hemicellulose, and lignin. Alkylation of the hydroxide groups of these polymers occurs at elevated pH levels. Therefore, it can be inferred that the adsorption mechanism is associated with hydrogen bonding or electrostatic interactions. Schema 2 shows the adsorption mechanism for Basic Fuchsin by fresh SCB.

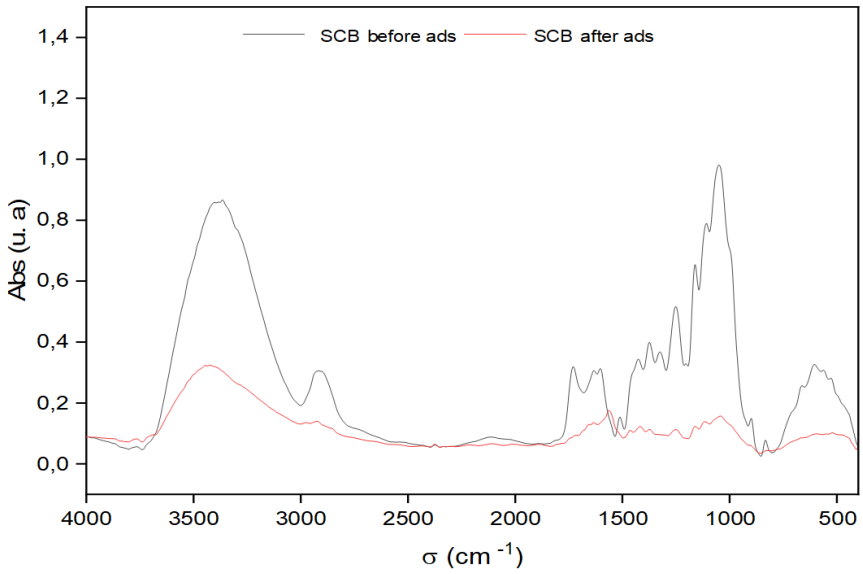

Fig. 12. FTIR spectrum of raw SCB and after adsorption of dye molecules

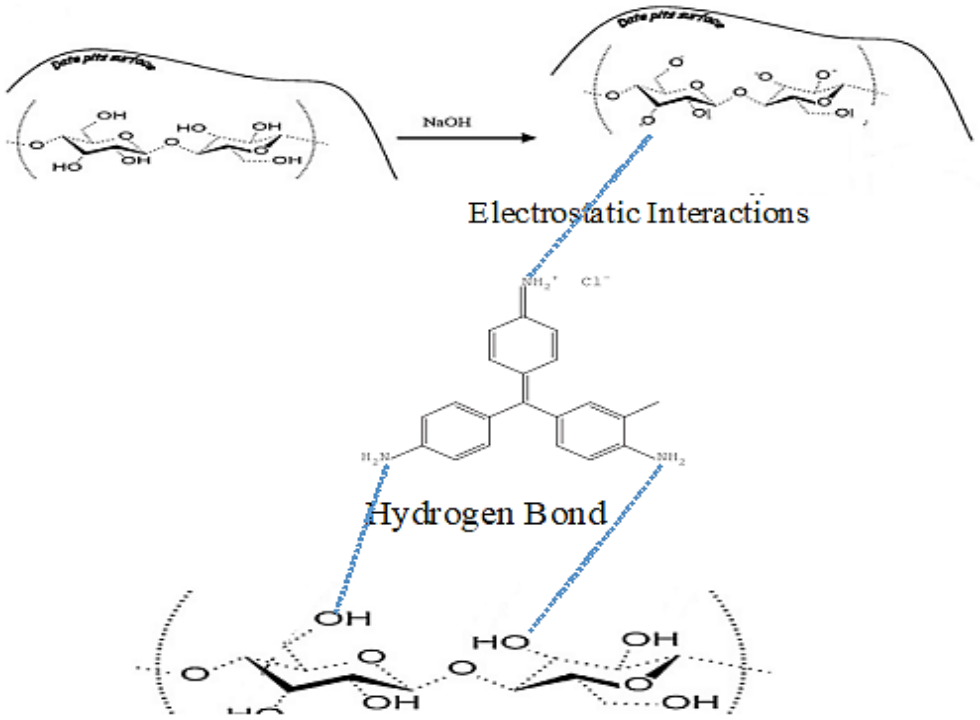

Scheme 2. Proposed mechanism for the adsorption of Basic Fuchsin by fresh SCB

4. Conclusion

This study highlights the effectiveness of using SCB in its natural form as a bio-sorbent material for removing cationic dyes from water, particularly in the BF adsorption process. SCB performed remarkably well, removing around 6.94 mg g^{-1} BF from wastewater, equivalent to a 97% removal rate at room temperature. UV-Vis spectrophotometry is used to assess the concentrations of BF dye solutions. However, this rate decreases with increasing temperature.

Langmuir, Freundlich, Dubin-Radushkevich and Temkin adsorption models are applied to describe the associated isotherms. In addition, we have employed pseudo-first-order, pseudo-second-order, and intra-particle diffusion models to describe the adsorption kinetics. Our results clearly indicate that the adsorption of BF onto the biosorbent follows the pseudo-second-order model. Finally, we calculated variations in adsorption enthalpy (ΔH°), entropy (ΔS°), and Gibbs free energy (ΔG°), demonstrating that BF adsorption proceeds spontaneously according to an exothermic process.

5. References

[1] S. Teimoori, H. Shirkhanloo, A. H. Hassani, M. Panahi, N. Mansouri, An immobilization of aminopropyl trimethoxysilane-phenanthrene carbaldehyde on graphene oxide for toluene extraction and separation in water samples, Chemosphere, 316 (2023) 137800. https://doi.org/10.1016/j.chemosphere.2023.137800

[2] J. Rakhtshah, H. Shirkhanloo, N. Esmaeili, A rapid extraction of toxic styrene from water and wastewater samples based on hydroxyethyl methylimidazolium tetrafluoroborate immobilized on MWCNTs by ultra-assisted dispersive cyclic conjugation-micro-solid phase extraction, Microchem. J., 170 (2021)106759. https://doi.org/10.1016/j.microc.2021.106759

[3] S. Teimoori, H. Shirkhanloo, A. H. Hassani, M. Panahi, N. Mansouri, Rapid extraction of BTEX in water and milk samples based on functionalized multi-walled carbon nanotubes by dispersive homogenized-micro-solid phase extraction, Food Chem., 421(2023) 136229. https://doi.org/10.1016/j.foodchem.2023.136229

[4] X. Yang, Highly effective removal of basic fuchsin from aqueous solutions by anionic polyacrylamide/graphene oxide aerogels, J. Colloid Interface Sci., 453 (2015)107–114. https://doi.org/10.1016/j.jcis.2015.04.042

[5] V. K. Gupta, A. Mittal, V. Gajbe, J. Mittal, Adsorption of basic fuchsin using waste materials-bottom ash and deoiled soya-as adsorbents, J. Colloid Interface Sci., 319 (2008) 30–39. https://doi.org/10.1016/j.jcis.2007.09.091

[6] L. H. Huang, J. J. Kong, W. L. Wang, C. L. Zhang, S. F. Niu, B. Y. Gao, Study on Fe(III) and Mn(II) modified activated carbons derived from Zizania latifolia to removal basic fuchsin, Desalination, 286 (2012) 268–276. https://doi.org/https://doi.org/10.1016/j.desal.2011.11.034

[7] M. Arjomandi, H. Shirkhanloo, A Review: Analytical methods for heavy metals determination in environment and human samples, Anal. Methods Environ. Chem. J., 2 (2019) 97–126. https://doi.org/10.24200/amecj.v2.i03.73

[8] M. Sadoq, Elimination of crystal violet from aqueous solution by adsorption on naturel polysaccharide: Kinetic, isotherm, thermodynamic studies and mechanism analysis, Arab. J. Chem., 17 (2024) 105453. https://doi.org/10.1016/j.arabjc.2023.105453

[9] F. Z. Batana, H. D. Bouras, H. Aouissi, Biosorption of congo red and basic fuchsin using micro fungi fusarium oxysporum F. Sp. Pisi as a biosorbent: Modeling optimization and kinetics study, Egypt. J. Chem., 65 (2022) 225–235. https://doi.org/10.21608/EJCHEM.2022.113994.5188

[10] M. El Haddad, Removal of Basic Fuchsin dye from water using mussel shell biomass waste as an adsorbent: Equilibrium, kinetics, and thermodynamics, J. Taibah Univ. Sci., 10 (2016) 664–674. https://doi.org/10.1016/j.jtusci.2015.08.007

[11] N. Kumari, B. L. Yadav, P. Kumar, Equilibrium studies on sorption of basic fuchsin dye using living biomass of aspergillus niger and humicola grisea,, Bio Sci. Res. Bull., 34 (2018) 19. https://doi.org/10.5958/2320-3161.2018.00006.8

[12] T. L. Bezerra, A. J. Ragauskas, A review of sugarcane bagasse for second-generation bioethanol and biopower production, Biofuels Bioprod. Biorefin., 10 (2016) 634–647. https://doi.org/10.1002/bbb.1662

[13] R. Ashouri, Dynamic and static removal of benzene from air based on task-specific ionic liquid coated on MWCNTs by sorbent tube-headspace solid-phase extraction procedure, Int. J. Environ. Sci. Technol., 18 (2021) 2377-2390. https://doi.org/10.1007/s13762-020-02995-4

[14] J. Rakhtshah, A rapid extraction of toxic styrene from water and wastewater samples based on hydroxyethyl methylimidazolium tetrafluoroborate immobilized on MWCNTs by ultra-assisted dispersive cyclic conjugation-micro-solid phase extraction, Microchem. J., 170 (2021) 106759. https://doi.org/10.1016/j.microc.2021.106759

[15] K. D. Belaid, S. Kacha, Study of the kinetics and thermodynamics of the adsorption of a basic dye on sawdust, J. Water Sci., 24 (2011) 131–144. https://doi.org/10.7202/1006107ar.

[16] A. Dehbi, Y. Dehmani, Comparative study of malachite green and phenol adsorption on synthetic hematite iron oxide nanoparticles (α-Fe_2O_3), Surf. Interfac., 21(2020)100637. https://doi.org/10.1016/j.surfin.2020.100637

[17] S. Dawood, T. K. Sen, Removal of anionic dye Congo red from aqueous solution by raw pine and acid-treated pine cone powder as adsorbent : Equilibrium, thermodynamic, kinetics, mechanism and process design, Water Res., 46 (2012) 1933–1946. https://doi.org/10.1016/j.watres.2012.01.009

[18] Q. Du, Highly enhanced adsorption of congo red onto graphene oxide/chitosan fibers by wet-chemical etching off silica nanoparticles, Chem. Eng. J., 245 (2014) 99–106. https://doi.org/10.1016/j.cej.2014.02.006

[19] M. Mohammadi Asl, N. Mansouri, S. A. R. Haji Seyed Mirzahosseini, F. Atabi, Simultaneity comparative evaluation of toluene removal from the air by adsorption and UV semi-degradation-based adsorption procedure, Int. J. Environ. Sci. Technol., 21 (2024) 6677-6694. https://doi.org/10.1007/s13762-024-05503-0

[20] D. Kavitha, C. Namasivayam, Experimental and kinetic studies on methylene blue adsorption by coir pith carbon, Bioresour. Technol., 98 (2007) 14–21. https://doi.org/10.1016/j.biortech.2005.12.008

[21] M. Ertaş, M. Hakki Alma, Pyrolysis of laurel (Laurus nobilis L.) extraction residues in a fixed-bed reactor: Characterization of bio-oil and bio-char, J. Anal. Appl. Pyrolysis, 88 (2010) 22–29. https://doi.org/10.1016/j.jaap.2010.02.006

[22] A. Kali, A. Amar, Efficient adsorption removal of an anionic azo dye by lignocellulosic waste material and sludge recycling into combustible briquettes, Colloids and Interfaces, 6 (2022) 22. https://doi.org/10.3390/colloids6020022

[23] A. F. Abbas, M. J. Ahmed, Mesoporous activated carbon from date stones (Phoenix dactylifera L.) by one-step microwave-assisted K_2CO_3 pyrolysis, J. Water Process Eng., 9 (2016) 201–207. https://doi.org/10.1016/j.jwpe.2016.01.004

[24] Z. Belala, M. Jeguirim, M. Belhachemi, F. Addoun, G. Trouvé, Biosorption of basic dye from aqueous solutions by Date Stones and Palm-Trees Waste : Kinetic, equilibrium and thermodynamic studies, Desalination, 271 (2011) 80–87. https://doi.org/10.1016/j.desal.2010.12.009

[25] W. Bessashia, Y. Berredjem, Z. Hattab, M. Bououdina, Removal of Basic Fuchsin from water by using mussel powdered eggshell membrane as novel bioadsorbent: Equilibrium, kinetics, and thermodynamic studies, Environ. Res., 186 (2020) 109484. https://doi.org/10.1016/j.envres.2020.109484

[26] A. Faghihi-Zarandi, H. Shirkhanloo, C. Jamshidzadeh, A new method for removal of hazardous toluene vapor from air based on ionic liquid-phase adsorbent, Int. J. Environ. Sci. Technol., 16 (2019) 2797-2808. https://doi.org/10.1007/s13762-018-1975-5

[27] N. El Messaoudi, M. El Khomri, S. Bentahar, A. Dbik, A. Lacherai, B. Bakiz, Evaluation of performance of chemically treated date stones: Application for the removal of cationic dyes from aqueous solutions, J. Taiwan Inst. Chem. Eng., 67 (2016) 244–253. https://doi.org/10.1016/j.jtice.2016.07.024

[28] M. A. Al-Ghouti, J. Li, Y. Salamh, N. Al-Laqtah, G. Walker, M. N. M. Ahmad, Adsorption mechanisms of removing heavy metals and dyes from aqueous solution using date pits solid adsorbent, J. Hazard. Mater., 176 (2010) 510–520. https://doi.org/10.1016/j.jhazmat.2009.11.059

[29] E. N. Bakatula, D. Richard, C. M. Neculita, G. J. Zagury, Determination of point of zero charge of natural organic materials, Environ. Sci. Pollut. Res., 25 (2018) 7823–7833. https://doi.org/10.1007/s11356-017-1115-7

[30] E. K. Guechi, O. Hamdaoui, Biosorption of methylene blue from aqueous solution by potato (Solanum tuberosum) peel: equilibrium modelling, kinetic, and thermodynamic studies, Desalin. Water Treat., 57 (2016) 10270–10285. https://doi.org/10.1080/19443994.2015.1035338

[31] A. El Jery, H. S. Kariem Alawamleh, Isotherms, kinetics and thermodynamic mechanism of methylene blue dye adsorption on synthesized activated carbon, Sci. Rep., 14 (2024) 970. https://doi.org/10.1038/s41598-023-50937-0

[32] H. Atlas, M.Sadoq, S. Imame, M. N. Bennani, Sustainable biosorption of methylthioninium chloride in wastewaters using new cystoseira barbata seaweed : Equilibrium isotherm, kinetic modeling and mechanism analysis, Arab. J. Chem., 17 (2023) 105532. https://doi.org/10.1016/j.arabjc.2023.105532

[33] Z. B. Bouabidi, M. H. El-naas, D. Cortes, G. Mckay, Steel-Making dust as a potential adsorbent for the removal of lead (II) from an aqueous solution, Chem. Eng. J., 334 (2018) 837–844. https://doi.org/10.1016/j.cej.2017.10.073

[34] Z. Khademi, B. Ramavandi, M. Taghi, The behaviors and characteristics of a mesoporous activated carbon prepared from Tamarix hispida for Zn (II) adsorption from wastewater, J. Environ. Chem. Eng., 3 (2015) 2057–2067. https://doi.org/10.1016/j.jece.2015.07.012

[35] F. Wu, R. Tseng, S. Huang, R. Juang, Characteristics of pseudo-second-order kinetic model for liquid-phase adsorption : A mini-review, Chem.Eng. J., 151 (2009) 1–9. https://doi.org/10.1016/j.cej.2009.02.024

[36] M. S. Manzar, Adsorption behaviour of green coffee residues for decolourization of hazardous congo red and eriochrome black T dyes from aqueous solutions, Int. J. Environ. Anal. Chem., 102 (2022) 6405–6421. https://doi.org/10.1080/03067319.2020.1811260

[37] Y. Zhang, F. Yu, W. Cheng, J. Wang, J. Ma, Adsorption, equilibrium and kinetics of the removal of ammoniacal nitrogen by zeolite X/activated carbon composite synthesized from elutrilithe, J. Chem., 2017 (2017) 936829. https://doi.org/10.1155/2017/1936829

[38] E. Kalkan, H. Nadaroglu, N. Celebi, H. Celik, E. Tasgin, Experimental study to remediate acid fuchsin dye using laccase-modified zeolite from aqueous solutions, Polish J. Environ. Stud., 24 (2015) 115–124. https://doi.org/10.15244/pjoes/23797

[39] H. Zeghache, S. Hafsi, N. Gherraf, Adsorption of organic dyes onto commercial activated carbon by using non-linear regression method, Environ. Asia, 12 (2019) 127–142. https://doi.org/10.14456/ea.2019.15

[40] P. Sampranpiboon, Equilibrium Isotherm models for adsorption of zinc (II) ion from aqueous solution on pulp waste, WSEAS Trans. Environ. Dev. Panida, 10 (2014) 35-47. https://wseas.com/reviewers/review.php?id=5394

Anal. Methods Environ. Chem. J. 7 (4) (2024) 51-62

AMECJ

Research Article, Issue 4
Analytical Methods in Environmental Chemistry Journal
Journal home page: www.amecj.com/ir

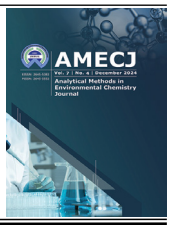

Chloride removal from reverse osmosis reject water based on Strychnos Potatorum seeds by analytical method and Artificial neural network

Avinash Rai Kola[a], V. D. N. Kumar Abbaraju[*,a], Rabhya Asthana[a], and Mandava Bhagya Tej[b]
[a] *Department of Environmental Sciences, GSS, GITAM Deemed to be University, Andhra Pradesh, Visakhapatnam, 530045, India*
[b] *Department of MBBS, NRI Academy of Medical Sciences, Chinakakani, Guntur, Andhra Pradesh, 522503, India*

ARTICLE INFO:
Received 14 Aug 2024
Revised form 22 Oct 2024
Accepted 24 Nov 2024
Available online 30 Dec 2024

Keywords:
Chloride,
Removal,
Natural coagulants,
Analytical methods,
Artificial neural network,
Nirmali seeds

ABSTRACT
In today's world, effective water treatment is necessary for safe and clean drinking water. The chloride can be decreased in water after coagulant treatment. The use of natural coagulants has the upper hand as chemical coagulant has a lot of negative impacts. In the present study aimed to use ANN to model the chloride removal using Strychnos Potatorum seeds. The supporting parameters for the model were pH, electrical conductivity (EC), and total dissolved solids (TDS). Using the Jar test and EC measurements, this study assesses using Nirmali seeds (Strychnos Potatorum) as a natural coagulant in water treatment. Ionic concentration changes and overall water quality are evaluated by EC measurements, whereas the Jar test establishes the ideal dosage and settling time for efficient turbidity reduction. The outcomes show that Nirmali seeds have the potential to be a more affordable and environmentally responsible coagulant than traditional chemicals. Apart from this, the Non-linear autoregressive neural network with external input (NARX) model that was trained using all three algorithms, i.e., the Levenberg-Marquardt (LM), the Bayesian Regularization (BR), and the Scaled Conjugate Gradient (SCG), was compared, in which the model trained with SCG algorithm showed the most promising test results. Hence, the Non-linear autoregressive neural network with external input (NARX) model trained with the SCG algorithm is the best-suited model for our study. The LOD of 1.28 mg L^{-1} and LOQ of 3.87 mg L^{-1} were obtained. The removal percentage of chloride content after adding different dosages of SPS, i.e., 0.2 mg, 0.4 mg, and 0.8 mg per liter, was achieved at 21.05%, 29.82%, and 38.59%, respectively.

1. Introduction

Growing concern about water treatment methods for consumption has severely impacted numerous communities worldwide. Water contamination as a result of multiple pollutants like mercury [1.2] lead [3], Nickel [4,5], manganese [1,6], and many other contaminations, including chloride and its ions, is becoming a nightmare and requires urgent action. Numerous cleanup and treatment methods have been employed worldwide, with reverse osmosis (RO) being one of the most popular. However, the amount of wastewater released by such methods as RO is high and alarming. Effective water treatment techniques can be developed by researching the adsorption and desorption capacities of single- and

*Corresponding Author: Fatima Boukhlifi
Email: f.boukhlifi@umi.ac.ma
https://doi.org/10.24200/amecj.v7.i04.341

multi-walled carbon nanotubes [7,8], air exposure evaluations, and biological monitoring using dispersive ionic liquid-liquid microextraction [9,10]. Furthermore, speciation of heavy metals in water, human blood, and food samples based on pyrrolic and pyridinic nitrogen-doped porous graphene nanostructures [11]. RO reject water is unsuitable for drinking or agricultural use but can be treated for other applications. However, it is essential to properly manage and dispose of RO-rejected water to prevent environmental contamination and ensure compliance with local regulations. Due to the multiple contaminants present, it is impossible to recover water from the rejected bulk water [12]. 15% of the water in the system recovers input; the remaining portion is released as waste. Recovering water from the rejected bulk is unfeasible due to the numerous contaminants. The kernel of *Strychnos Potatorum* and *Moringa oleifera* seeds can remove impurities from the water and make it suitable for secondary purposes. *Strychnos Potatorum* is effective for low, medium, and high turbidity water. Turbidity may be eliminated using the kernels of Moringa oleifera and *Strychnos Potatorum* seeds. As experimented by *Strychnos Potatorum, it* is effective for low, medium, and high turbidity water while having a lower removal effectiveness than *Moringa oleifera* for medium and high turbidity water [13]. Defluorination also took place in groundwater within a contact duration of two hours, removing the majority of the high-level fluoride] content at a rate of 86% to 81.25%, as concluded. *Strychnos Potatorum* seeds are a natural coagulant to remove turbidity and fluoride. It offers numerous advantages, including no hazardous effects and safety [14]. The Schultz-Hardy rule and particle collision function provide coagulant demand and variations in particle number in the flocculation process [15]. Different models in ANN can be used for modeling, but NARX(non-linear autoregressive models with exogenous inputs) was preferred because of its dynamic neural architecture [16]. Given the system's experimental input and output data, ANN is a sophisticated computational approach that can accurately and appropriately forecast the performance of a system [17]. In contrast to conventional recurrent neural models, NARX has limited feedback structures from output neurons. At the very least, NARX networks are used for traditional recurrent networks equivalent to Turing machines [18]. Various models can be used for water quality analysis and prediction. A recurrent dynamic neural network called the non-linear autoregressive exogenous (NARX) model has a few network layers surrounded by feedback connections. The NARX model simulates various non-linear processes, including time-series modeling [19]. This model has been widely used in environment-related research, including wastewater treatment. The NARX model was chosen to compare the FANN and NARX models because it performed better and had a better R-squared value. Also, by creating a NARX model, the removal of mercury ions from the water was explored and functionalized multi-walled carbon nanotubes were used as an adsorbent [20]. Mainly based on bench-scale testing, plant-based coagulants derived from *Moringa oleifera*, *Strychnos Potatorum* Linn, *Plantago ovate*, *Trigonella foenum graecum*, and *Opuntia ficus indica* are promising alternatives to chemicals [21]. Natural, water-soluble, organic, ionic, and non-ionic polymers of various molecular weights generated from multiple plant components are called plant-based coagulants [22]. Nano adsorbents and nanocomposite materials like metal-organic frameworks and carbon nanotubes can effectively adsorb specific ions. While electro-spun nanofibers and ion-exchange nanoparticles offer high surface areas and selective ion exchange capabilities for efficient water purification, methods like nano-photocatalysis and magnetic nanoparticles break down pollutants and make separation easier [23]. The method described in [BDMIM][PF6] for USA-DIL-SSPME for CysSB/MetSB@MWCNTs effectively separates and determines nickel and cobalt in human blood samples. This procedure guarantees precise concentration measurements by ET-AAS by eliminating chloride interference and adjusting pH to

extract Co/Ni (II) without requiring extra ligands [24].

This study aims to develop and validate an artificial neural network (ANN) model that uses Strychnos Potatorum seeds as a natural adsorbent to predict the efficiency of chloride removal from reverse osmosis (RO) reject water. By optimizing the ANN model, this study aims to provide a reliable predictive tool for enhancing the RO reject water treatment process and to better understand the key parameters influencing chloride adsorption.

2. Material and Methods

2.1. Study area

The work was conducted in five different locations of Visakhapatnam, a coastal city in India's south-eastern part of Andhra Pradesh. Geographically the city lies between 17^{O} - 41′ and 17^{O} - 59′ Northern latitude and 83^{O} - 12′ and 83^{O}- 27′ in Eastern latitude. The RO reject water was collected from houses with different reverse osmosis machines from five Visakhapatnam and Andhra Pradesh locations. The locations are marked on the map given in Figure 1.

2.2. Experimental procedure

2.2.1.Natural Coagulant as Analytical Chemical Procedure

The powder of *Strychnos Potatorum* (SPS) seed, commonly known as "Clearing Nut" or "Nirmali seed," was obtained from Poorna Market, Visakhapatnam, Andhra Pradesh. SEM of Strychnos Potatorum seeds and powder were selected, as shown in Figure 2.

To perform this work, we used analytical methods to analyze Nirmali seeds, including the Jar test, pH, and Electrical conductivity before ANN. An analytical technique called the jar test assesses water treatment's flocculation and coagulation processes. It entails treating water samples in several jars with different concentrations of coagulants, mixing, and letting the samples settle. The supernatant water's clarity is evaluated to find the ideal coagulant dose required to eliminate turbidity and suspended particles. This test is essential for optimizing water treatment procedures to ensure effective contaminant removal. Electrical conductivity (EC) measures a solution's ability to conduct electric current, indicating ions' presence.

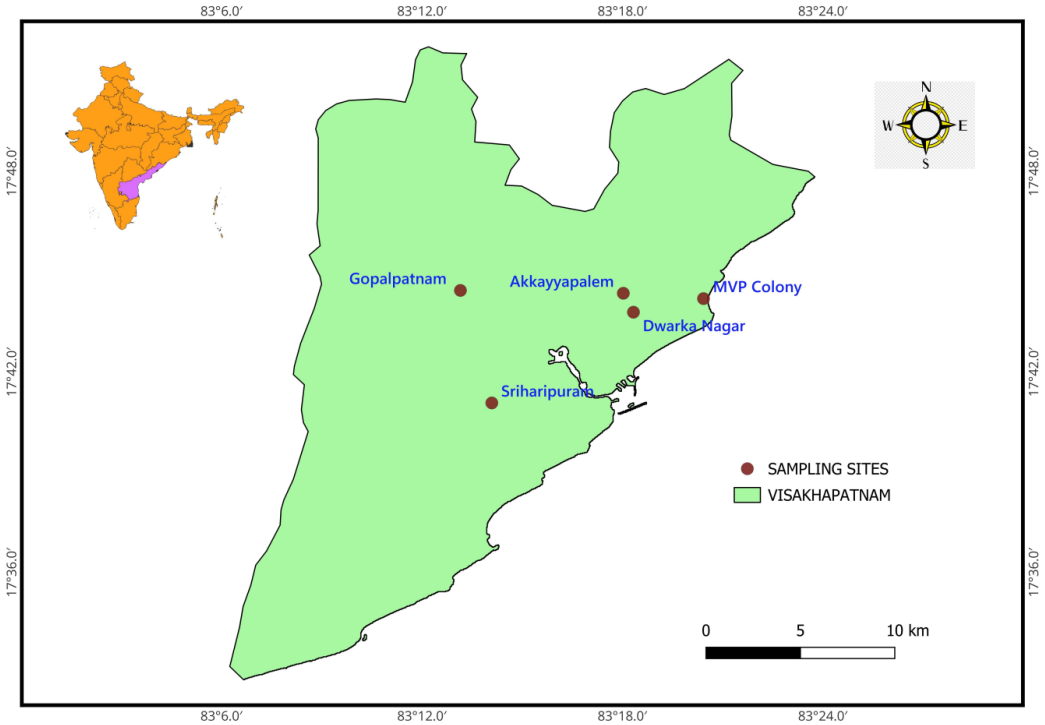

Fig. 1. Sampling sites marked in the map of Visakhapatnam.

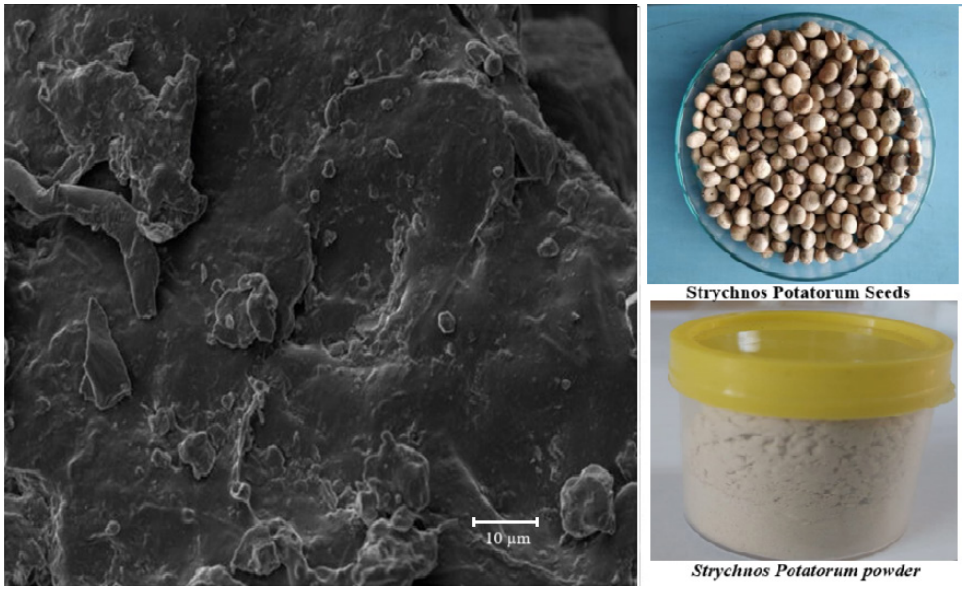

Fig.2. SEM of *Strychnos Potatorum* seeds

High EC values suggest elevated dissolved salts and mineral concentrations in water quality assessment, affecting factors like plant growth and soil health. EC is monitored in water treatment to meet quality standards and adjust processes accordingly. Measurements are made using a conductivity meter, providing quick and accurate water quality evaluations.

2.2.2. The procedure of Algorithm of Artificial Neural Network

Using MATLAB, the authors selected a non-linear autoregressive network with exogenous inputs (NARX). A network was created in which we imported the data from the workspace using the diagram shown in Figure 3. Then, the data was imported into the network, input data as responders and output data as predictors from the workspace. 70 % of the data has been taken as training data in both input and output. The model is then trained using all three algorithms, i.e., the Levenberg-Marquardt algorithm, the Bayesian Regularization, and the Scaled Conjugate Gradient. After training the model, it has been tested with new input data. This model is then exported into the workspace.

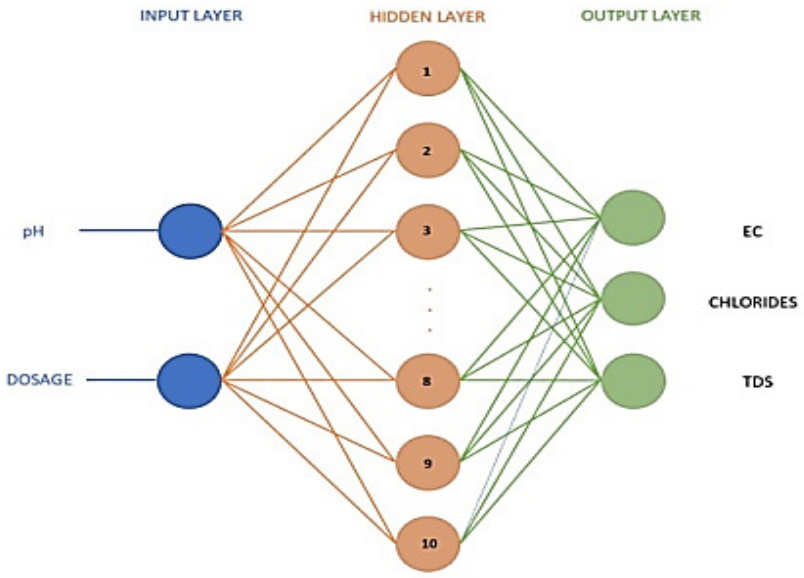

Fig. 3. Diagram of the NARX model

3. Results and Discussion

3.1. Physiochemical characteristics of RO reject water

Various physiochemical parameters were determined to assess the effectiveness of *Strychnos Potatorum* (SPS) seeds on RO-reject water. The parameters like pH, EC, turbidity, TDS, and chloride are determined. The results are tabulated in Table 1.

3.2. Removal percentage of chloride using Strychnos Potatorum seeds

The highest removal percentage of chloride content after adding different dosages of SPS, i.e., 0.2 mg, 0.4 mg, and 0.8 mg per liter, is 21.05%, 29.82%, and 38.59%, respectively; the values of chloride removal percentage are mentioned in Table 2.

3.3. NARX model generated using MATLAB

The model was generated using a Non-linear autoregressive neural network with external input (NARX) in MATLAB. The NARX model using the LM training algorithm achieved an overall R-value of more than 0.93 from 10 hidden neurons. Furthermore, the BR and SCG training models achieved an overall R-value of other than 0.92 and 0.98, respectively. The results are shown in Figure 4. For this, the authors generated the Training State Plot, revealing that 7 and 8 epochs are identified, and the Performance Plot means squared error and epochs are generated. Test plot LB and BR, the R-values of 0.97 and 0.96 were observed. The graphs obtained for LB, BR, and SCG are shown in Figures 4a,4b,4c,4d,4e,4f,4g,4h, and 4i.

Table 1. The pH, EC, TDS, and chloride of RO water samples from different places and after the addition of different dosages of *Strychnos Potatorum* seeds.

Geographical Location	Dosage (mg L^{-1})	pH	EC	TDS (mg L^{-1})	Chloride (mg L^{-1})
MVP Colony	0.0	7.26	0.61	396.5	76.430
	0.2	7.46	0.64	416.0	69.482
	0.4	7.12	0.62	403.0	59.556
	0.8	6.63	0.63	409.5	64.519
Dwarka Nagar	0.0	7.05	0.67	435.5	97.274
	0.2	7.19	0.69	448.5	94.297
	0.4	7.06	0.72	468.0	84.371
	0.8	6.68	0.79	513.5	79.408
Sriharipuram	0.0	6.95	0.84	546.0	150.875
	0.2	6.72	0.86	559.0	134.001
	0.4	7.64	0.88	572.0	114.149
	0.8	6.45	1.00	650.0	129.038
Akkayyapalem	0.0	7.03	0.40	260.0	56.578
	0.2	6.98	0.41	266.5	44.667
	0.4	6.66	0.41	266.5	39.704
	0.8	6.48	0.43	279.5	34.741
Gopalapatnam	0.0	7.13	1.10	715.0	250.135
	0.2	7.11	1.35	877.5	238.224
	0.4	6.63	1.30	845.0	233.261
	0.8	6.53	1.39	903.5	228.298

Table 2. The Removal percentage of chloride from RO Reject water samples at different dosages of Strychnos Potatorum seeds

Geographical Location	Dosage (mg L^{-1})	Chloride content (mg L^{-1})		Removal %
		Initial	Final	
MVP Colony	0.2	76.430	69.482	9.09
	0.4	76.430	59.556	22.07
	0.8	76.430	64.519	15.58
Dwarka Nagar	0.2	97.275	94.297	3.06
	0.4	97.275	84.371	13.26
	0.8	97.275	79.408	18.36
Sriharipuram	0.2	150.875	134.001	11.18
	0.4	150.875	114.149	24.34
	0.8	150.875	129.038	14.47
Akkayapalem	0.2	56.578	44.667	21.05
	0.4	56.578	39.704	29.82
	0.8	56.578	34.741	38.59
Gopalpatnam	0.2	250.135	238.224	4.76
	0.4	250.135	233.261	6.74
	0.8	250.135	228.298	8.73

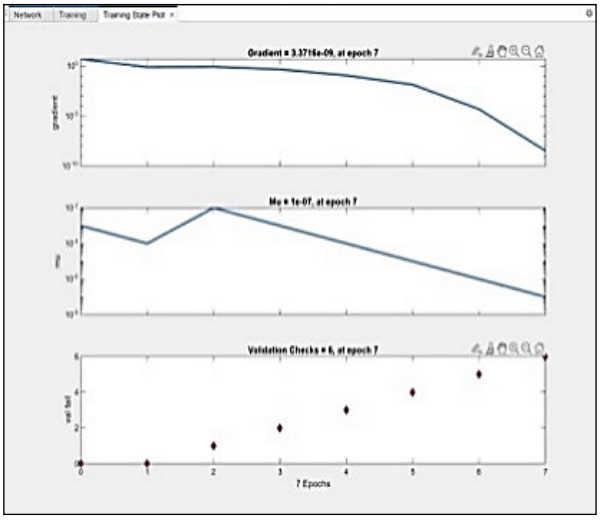

Fig.4a. Training state plot for LB

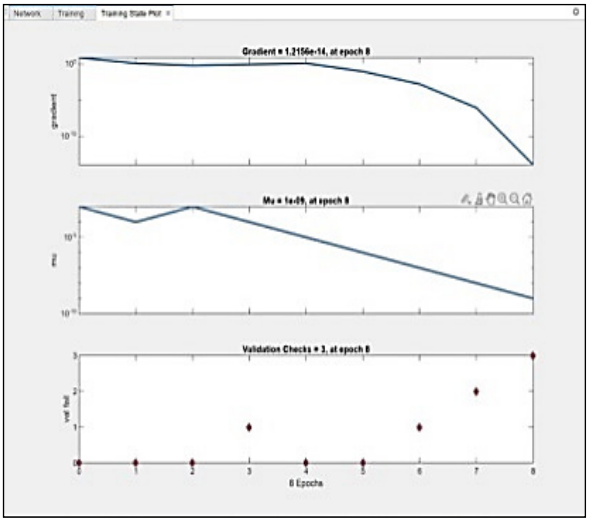

Fig.4b. Training state plot for BR

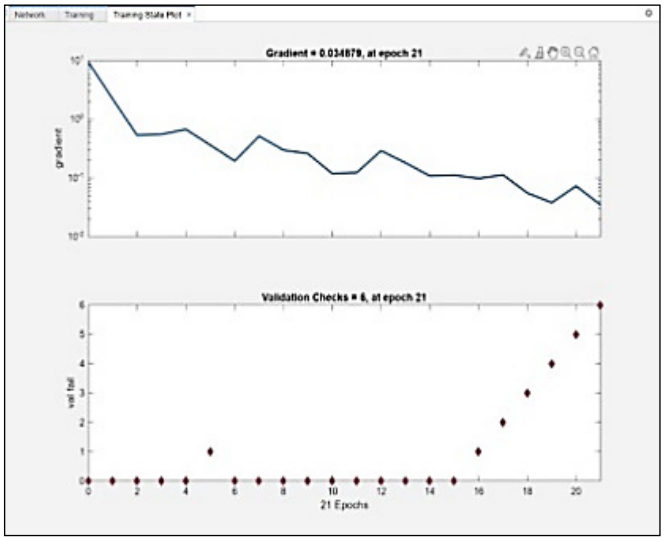

Fig.4c. Training state plot for SCG

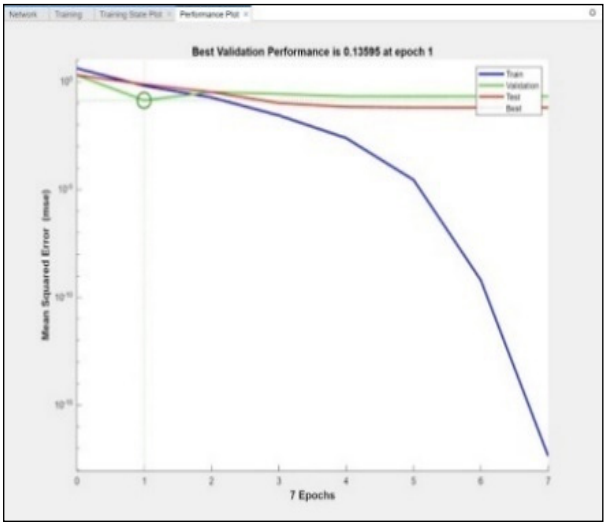

Fig.4d. Performance plot for LB

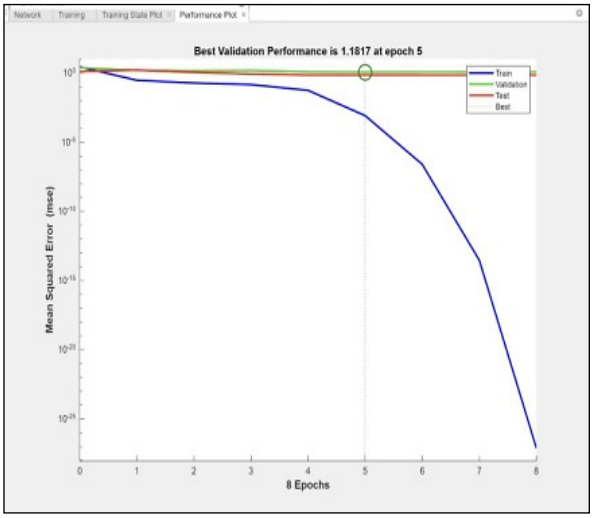

Fig.4e. Performance plot for BR

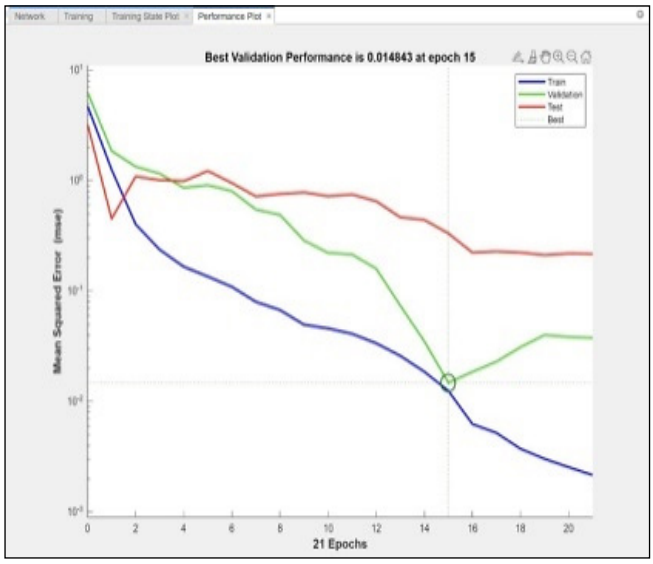

Fig.4f. Performance plot for SCG

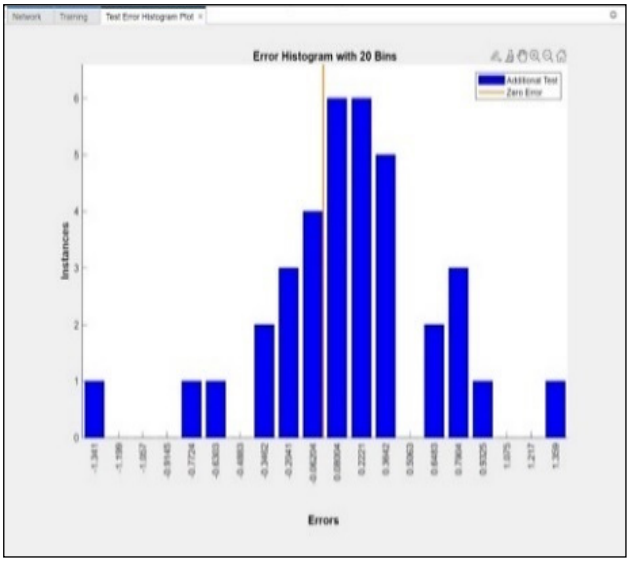

Fig.4g. Test Error histogram for LB

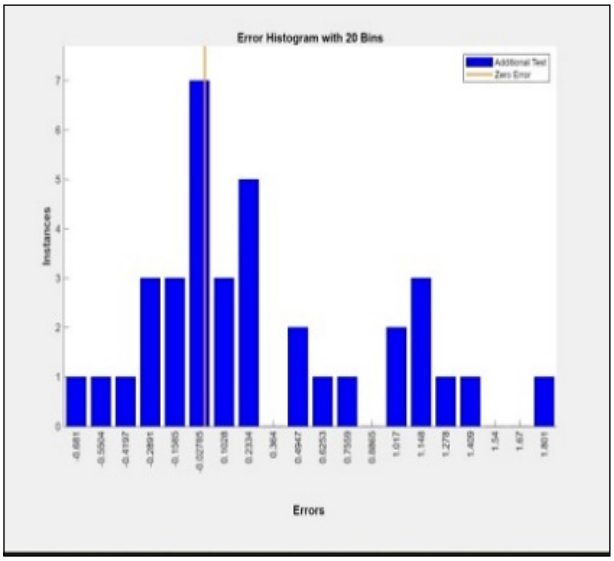

Fig.4h. Test Error histogram for BR

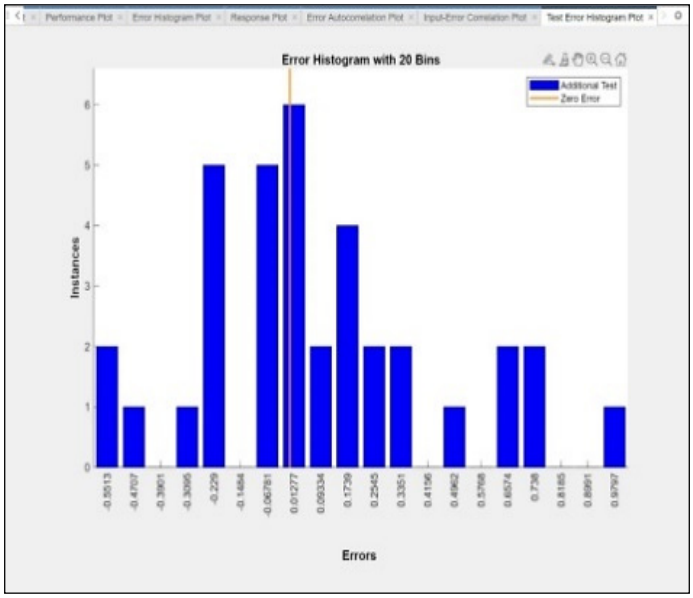

4a-4i Test Error histogram for SCG

3.4. Comparison of all the three algorithms

All three algorithms were compared. The overall R-value of Levenberg-Marquardt (LM), the Bayesian Regularization (BR), and the Scaled Conjugate Gradient (SCG) was observed to be more than 0.95, 0.96, and 0.99, respectively. The results are tabulated in Table 4a-4i**.**

3.5. Statistical Results

Limit of Detection (LOD) and Quantification (LOQ) must be analyzed. For this analysis, the chloride concentration is identified using the titrimetric method. Using the given data, a linear regression to find the slope (S) and intercept of the calibration curve is calculated and shown in Figure 5. The standard deviation (σ) of the blank measurements is 0.0077 mL. The slope (S) of the calibration curve is 0.02. The calculated values are LOD 1.28 mg L^{-1} and LOQ 3.87 mg L^{-1}. These values indicate the sensitivity of your titration method for detecting and quantifying chloride concentrations. The results obtained are represented in the Table 5.

3.6. Discussion

The present study found that the pH of the water sample after adding 0.2 mg L^{-1} and 0.4 mg L^{-1} of SPS seeds remained almost the same. Still, after adding 0.8 mg L^{-1}, the water sample slightly became acidic as the RO water was not acidic. This is likely due to the release of hydrogen ions from the SPS seeds when they come into contact with water. According to the findings, the acidity produced by the SPS seeds is directly proportional to the amount of seed added to the water sample. Adding SPS seeds reduced the chloride content in water samples. The removal percentage of chloride was found to be 9.82%, 19.24%, and

Table 4. MSE and R (Regression Coefficient) value of training, validation, and test of all the three algorithms, i.e., the Levenberg-Marquardt (LB) algorithm, the Bayesian Regularization (BR), and the Scaled Conjugate Gradient (SCG).

Algorithm		**LB**	**BR**	**SCG**
Number of hidden neurons		10	10	10
MSE	Training	0.6461	0.1573	0.0125
	Validation	0.1359	0.3997	0.0148
	Test	0.7566	0.205	0.3335
R	Training	0.9365	0.9999	0.9987
	Validation	0.993	0.9349	0.9991
	Test	0.9244	0.9492	0.981
	Overall	0.9513	0.9613	0.9929

Table 5. Results of Chloride Concentration

Chloride Concentration (mg L^{-1})	Titration Volume (mL)
76.4	1.52
97.2	1.94
150.8	3.01
56.57	1.13
250.135	5.00

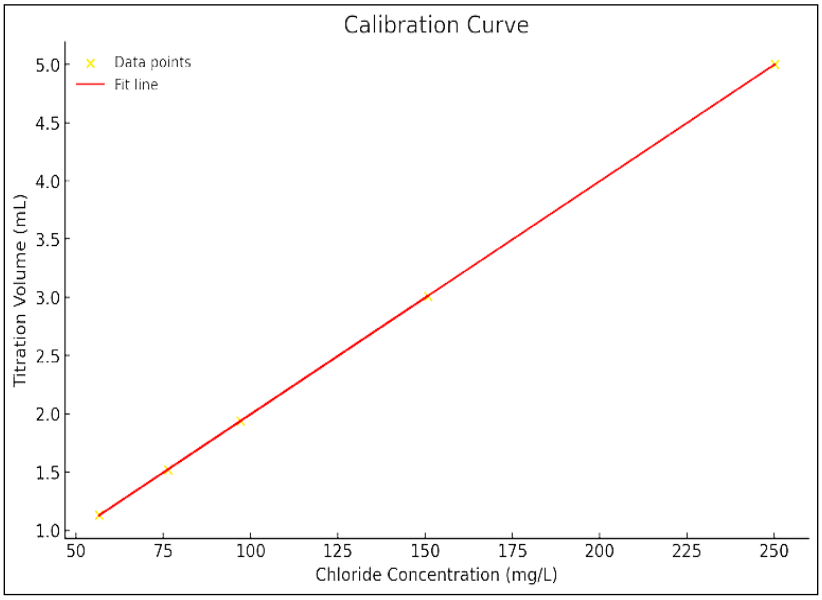

Fig. 5. Calibration curve for Titration

19.14% after adding 0.2 mg L^{-1}, 0.4 mg L^{-1}, and 0.8 mg L^{-1} with a contact time of 1 hour. The addition of SPS seeds acted as the de-chlorination substance and helped reduce the overall chloride content in the water sample. This method effectively lowers chloride content in water samples and can be used in various filtration settings. Many complex systems, especially those with non-linear dynamics, are modeled using the NARX (Non-linear Autoregressive with Exogenous Inputs) model. This model combines the strengths of artificial neural networks with time-series analysis to predict the behaviour of the system based on its historical and current inputs. In this instance, the Levenberg-Marquardt (LB), Bayesian Regularization (BR), and Scaled Conjugate Gradient algorithms were used to train the NARX model, which was created based on experimental findings (SCG). The LB algorithm is a prominent optimization approach in training artificial neural networks. By reducing the difference in error between the expected and actual outputs, this algorithm modifies the network weights at each epoch. The BR algorithm is another optimization method that penalizes the model for having high weights by including a regularisation factor in the loss function. The SCG algorithm is a variation of the conjugate gradient method that scales the search direction to quicken convergence. The overall R (Regression Coefficient) score for the NARX model trained using LB was over 0.95, accounting for 95% of the output's variance. The BR model fared somewhat better with an R-value above 0.96. The most encouraging results, however, came from the SCG algorithm, which had an R-value above 0.99, indicating high output prediction accuracy. Each of the three algorithms utilized in this study had ten hidden layers, although their training data varied regarding the number of epochs. The LB and BR models were trained with 7 and 8 epochs, respectively, while the SCG model attained the best performance with 21 epochs. Comparison studies with other methods are

Table 6. Comparison studies with other methods

Method	Percentage degradation (%)	References
DCl-SPS	38.5	Current work
Chemical Precipitation	About 24.35%	[25]
Bentonite Clay Adsorption	15-20%	[26]
Electrocoagulation	Up to 25%	[27]
LDHs Adsorption	11.2% (specific study)	[28]
Anion Exchange Resins (Weak Anion Type)	Potentially below 30%	[29]
Biosorption using Alginate Beads	22.3	[30]
Microwave-Assisted Electrolysis	18.2% (specific study)	[31]
Moringa Oleifera Seed Extract	10-20%	[32]
Cactus (Opuntia spp.) Cladodes Extract	Up to 15%	[33]

DCl-SPS: Degradation of chloride using Strychnos Potatorum seeds
LDHs: Layered Double Hydroxides

represented in Table 6.

4. Conclusion

The present work focuses on using *Strychnos Potatorum* seeds as a natural coagulant for removing chloride in RO reject water and then building a model using an artificial neural network. The use of natural coagulants for water purification is gaining much popularity nowadays. The results of the combined analytical methods show that *Strychnos Potatorum* seeds considerably lower the concentrations of ions and turbidity in treated water. The study's results support the seeds' usefulness as a natural coagulant, providing a cost-effective and environmentally friendly substitute for conventional chemical coagulants. Additional studies and pilot-scale applications are advised to confirm these results in various water treatment scenarios. Hence, integrating artificial neural networks with experimental results can help fill the gap. The present study has used different dosages of *Strychnos Potatorum* seeds to remove chloride in RO reject water. The removal of chloride after using different dosages was significantly high. The removal percentage of chloride content after adding different dosages of SPS, i.e., 0.2 mg, 0.4 mg, and 0.8 mg per liter, is 21.05%, 29.82%, and 38.59%, respectively. Then, these data were fed to the Non-linear autoregressive neural network with external input (NARX) model that was trained using all three algorithms, i.e., the Levenberg-Marquardt (LM), the Bayesian Regularization (BR), and the Scaled Conjugate Gradient (SCG) in which it was found that model trained using Scaled Conjugate Gradient has the best R-value. So, the study concludes that using the NARX model trained with the SCG algorithm best optimizes chloride removal.

5. Acknowledgments

The authors are thankful to the management of GITAM (Deemed to be University) for providing the necessary facilities to carry out this research. There are no conflicts of interest among the authors in this research work.

6. References

[1] M. Habibnia, A. Rashidi, Simultaneously speciation of mercury in water, human blood and food samples based on pyrrolic and pyridinic nitrogen-doped porous graphene nanostructure, Food Chem., 403 (2023) 134394. https://doi.org/10.1016/j.foodchem.2022.134394

[2] F. Golbabaei, A. Vahid, A. Faghihi Zarandi, A novel nano-palladium embedded on the mesoporous silica nanoparticles for mercury vapor removal from air by the gas field separation consolidation process, Appl. Nanosci. 12 (2022) 1667–1682. https://doi.org/10.1007/s13204-022-02366-0

[3] N. Esmaeili, J. Rakhtshah, E. Kolvari, A. Rashidi, H. Shirkhanloo, Rapid speciation of lead in human blood and urine samples based

on MWCNTs@DMP by dispersive ionic liquid-suspension-micro-solid phase extraction, Biol. Trace Elem Res., 199 (2021) 2496–2507. https://doi.org/10.1007/s12011-020-02382-7

[4] Z. Karamzadeh, J. Rakhtshah, N. M. Kazemi, A novel biostructure sorbent based on CysSB/MetSB@MWCNTs for separation of nickel and cobalt in biological samples by ultrasound assisted-dispersive ionic liquid-suspension solid phase microextraction, J. Pharm. Biomed. Anal., 172 (2019) 285–294. https://doi.org/10.1016/J.JPBA.2019.05.003

[5] Mostafa Dehghani Mobarake, Ultrasound-assisted solid-liquid trap phase extraction based on functionalized multi-wall carbon nanotubes for preconcentration and separation of Nickel in petrochemical waste water, J. Anal. Chem., 74 (2019) 865–876. https://doi.org/10.1134/S1061934819090090

[6] J. Rakhtshah, H. Shirkhanloo, M. Dehghani Mobarake, Simultaneously speciation and determination of manganese (II) and (VII) ions in water, food, and vegetable samples based on immobilization of N-acetylcysteine on multi-walled carbon nanotubes, Food Chem., 389 (2022) 133124. https://doi.org/10.1016/J.FOODCHEM.2022.133124

[7] F. Golbabaei, A. Ebrahimi, Single-walled carbon nanotubes (SWCNTs), as a novel sorbent for determination of mercury in air, Glob. J. Health Sci., 8 (2015) 273. https://doi.org/10.5539/GJHS.V8N7P273

[8] N. Esmaeili, J. Rakhtshah, E. Kolvari, Ultrasound assisted-dispersive-modification solid-phase extraction using task-specific ionic liquid immobilized on multiwall carbon nanotubes for speciation and determination mercury in water samples, Microchem. J., 154 (2020) 104632. https://doi.org/10.1016/J.MICROC.2020.104632

[9] F. Golbabaei, H. Hassani, F. Eftekhar, M. J. Kian, Occupational Exposure to Mercury: Air Exposure Assessment and Biological Monitoring based on dispersive ionic liquid-liquid microextraction, Iran. J. Public Health, 43 (2014) 793–799. https://pmc.ncbi.nlm.nih.gov/articles/PMC4475598/

[10] W. Liu, R. Zhang, Removal of chloride from simulated zinc sulfate electrolyte by ozone oxidation, Hydrometallurgy, 160 (2016) 147-151. https://doi.org/10.1016/j.hydromet.2015.12.006

[11] F. Golbabai, A. Ebrahimi, M. R. Baneshi, A. F. Zarandi, M. J. Kian, Performance comparison survey of multi-walled and single-walled carbon nanotubes for adsorption and desorption of mercury vapors in the air, Iran. Occup. Health, 10, (2013) 20–31. https://ioh.iums.ac.ir/article-1-813-en.html

[12] N. Kumar, V. Bharadwaj, S. Mitra, D. Bose, RO reject water management techniques, World News Nat. Sci., 14 (2017) 1-10. https://www.worldnewsnaturalsciences.com

[13] V. T. Gaikwad, G. R. Munavalli, Turbidity removal by conventional and ballasted coagulation with natural coagulants, Appl. Water Sci., 9 (2019) 130. https://doi.org/10.1007/S13201-019-1009-6

[14] G. Jayanthi, V. Akshaya, Preliminary assessment of defluoridation of groundwater in Tamil Nadu, India, by Strychnos potatorum seeds. Water Air Soil Pollut., 233 (2022)130. https://doi.org/10.1007/s11270-022-05535-7

[15] J. Q. Jiang, The role of coagulation in water treatment, Curr. Opin. Chem. Eng., 8 (2015) 36–44. https://doi.org/10.1016/J.COCHE.2015.01.008

[16] W.W. Wee, M.Y. Siau, S.K. Arumugasamy, Modelling of adsorption of anionic azo dye using Strychnos potatorum Linn seeds (SPS) from aqueous solution with artificial neural network (ANN), Environ. Monit. Assess., 193 (2021) 638. https://doi.org/10.1007/s10661-021-09412-4

[17] J. Zhang, G. SuA, Chapter 22 - Artificial neural network introductions, Nuclear Power Plant Design and Analysis Codes, Book Elsevier publisher, Pages 515-541, 2021. https://doi.org/10.1016/B978-0-12-818190-4.00022-X

[18] H. T. Siegelmann, B. G. Horne, C. Lee Giles, S. Member, Computational capabilities of recurrent NARX neural networks, Cybernetics, 27 (1997) 208-215. https://pubmed.ncbi.nlm.nih.gov/18255858

[19] Z. Boussaada, O. Curea, A. Remaci, H. Camblong, N. M. Bellaaj, A nonlinear autoregressive exogenous (NARX) neural network model for the prediction of the daily direct solar radiation, Energies, 11 (2018) 620. https://doi.org/10.3390/EN11030620

[20] S. S. Fiyadh, Mercury removal from water using deep eutectic solvents-functionalized multi-walled carbon nanotubes: Nonlinear autoregressive network with an exogenous input neural network approach, Environ. Prog. Sustain. Energy, 38 (2019) e13261. https://doi.org/10.1002/EP.13261

[21] M. Saleem, R. T. Bachmann, A contemporary review on plant-based coagulants for applications in water treatment, J. Ind. Eng. Chem., 72 (2019) 281–297. https://doi.org/10.1016/j.jiec.2018.12.029

[22] V. Kumar, N. Othman, S. Asharuddin, Applications of natural coagulants to treat wastewater -A Review, MATEC Web Conf., 103 (2017) 06016. https://doi.org/10.1051/MATECCONF/201710306016

[23] Y. Li, Z. Yang, Removal of chloride from water and wastewater: Removal mechanisms and recent trends, Sci. Total Environ., 821 (2022) 153174. https://doi.org/10.1016/j.scitotenv.2022.153174

[24] M. Osanloo, H. Hassani, Validation of a new and cost-effective method for mercury vapor removal based on silver nanoparticles coating on micro glassy balls, Atmos, Pollut. Res., 8 (2017) 359-365. https://doi.org/10.1016/j.apr.2016.10.004

[25] L. P. Wang, W. H. Lee, S. M. Tseng, T. W. Cheng, Removal of chloride ions from an aqueous solution containing a high chloride concentration through the chemical precipitation of Friedel salt, Mater. Trans., 59 (2018) 297–302. https://doi.org/10.2320/MATERTRANS.M2017273

[26] C. Mota-Heredia, J. Cuevas, R. Fernández, Effect of iron chloride (II) on bentonites under hydrothermal gradients: A comparative study between sodium bentonite and calcium bentonite, Minerals, 14 (2024) 132. https://doi.org/10.3390/MIN14020132/S1

[27] H. El Karamany, I. Salah, Electrocoagulation process for the removal of chromium and cadmium from synthetic industrial Wastewater, J. Mater. Environ. Sci., 11 (2020) 1794-1806. https://www.researchgate.net/publication/370472928

[28] X. Xu, The performance and mechanism of a Mg-Al double-layer oxide in chloride ion removal from an aqueous solution, Nanomaterials, 12 (2022) 846. https://doi.org/10.3390/NANO12050846/S1

[29] S. Takagi Ahmad, A. Saeid, S. Abolfazl, Nitrate removal methods from drinking water, Iran. Water Research J.,16 (2022) 63-78. https://sid.ir/paper/1057725/en

[30] V. C. Deivayanai, S. Karishma, P. Thamarai, P. R. Yaashikaa, A. Saravanan, A comprehensive review on electrodeionization techniques for removal of toxic chloride from wastewater: Recent advances and challenges, Desalination, 570 (2024) 117098. https://doi.org/10.1016/J.DESAL.2023.117098

[31] Y. Gendel, G. Amikam, P. Nativ, Chapter 9-Seawater electrolysis, electrochemical power sources: Fundamentals, systems, and applications, Elsevier Publisher, pp. 305–326, 2022. https://doi.org/10.1016/B978-0-12-819424-9.00003-3

[32] Z. Y. Makarfi, M. Ali, L. Mu'azu, Application of moringa oleifera seeds extracts in the purification of groundwater, South Asian Res. J. Biol. Appl. Biosci., 4 (2022) 68-73. https://doi.org/10.36346/sarjbab.2022.v04i03.005

[33] G. Hussain, S. Haydar, Textile effluent treatment using natural coagulant opuntia stricta in comparison with alum, Clean-Soil Air Water, 49 (2021) 2000342. https://doi.org/10.1002/CLEN.202000342

Anal. Methods Environ. Chem. J. 7 (4) (2024) 63-77

AMECJ

Research Article, Issue 4
Analytical Methods in Environmental Chemistry Journal
Journal home page: www.amecj.com/ir

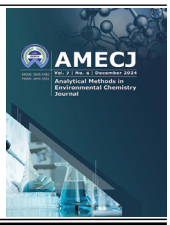

Removing textile dyes from wastewater using a novel natural polymer-based flocculant: Synthesis, characterization, and evaluation of the flocculant performance by UV-visible spectrophotometer method

Asep Nurohmat Majalis[a,*], Yosi Aristiawan[a], Bientang Matacachimi Z Sidiq[b], Fuzi Suciati[c], Vany Nursanti[d], and Andreas[a]

[a] Research Center for Chemistry, National Research and Innovation Agency, South Tangerang, Banten, Indonesia
[b] Department of Chemistry, Jendral Soedirman University (UNSOED), Purwokerto, Indonesia
[c] Research Center for Environment and Clean Technology, National Research and Innovation Agency, South Tangerang, Banten, Indonesia
[d] Research Center for Mining Technology, National Research and Innovation Agency, South Lampung, Lampung, Indonesia

ARTICLE INFO:

Received 30 July 2024
Revised form 8 Oct 2024
Accepted 17 Nov 2024
Available online 29 Dec 2024

Keywords:
Natural polymer-based flocculant,
Starch,
Chitosan,
Flocculation,
Textile dye in wastewater
UV-visible spectrophotometer

ABSTRACT

Natural polymer-based flocculants have become a promising option for wastewater treatment to replace Fe and Al-based coagulants and synthetic polymer-based flocculants. This research introduces a novel flocculant, namely Stc-EGDMA-Cts, that can act as a coagulant and a flocculant. The characteristics of Stc-EGDMA-Cts were obtained, and its effectiveness in eliminating textile dye from wastewater was evaluated using the UV-visible spectrophotometer method. The change of Stc: Cts mass ratio from 0.5 to 8 g g^{-1} increased the zeta potential value and the yield percent of Stc-EGDMA-Cts from 23.1 to 46.4 mV and 15.64 to 59.93%, respectively. Specifically, Stc-EGDMA-Cts with Stc: Cts mass ratio of 0.5, 1, 2, and 4 g g^{-1} removed textile dye from wastewater by 91.01, 92.26, 92.84, and 80.85%, respectively. However, Stc-EDGMA-Cts with a Stc: Cts mass ratio of 8 g g^{-1} could only remove less than 20%. The Stc-EGDMA-Cts performance in removing dye was also affected by the initial pH of wastewater, the Stc-EGDMA-Cts dosage, and the sedimentation time. Characterization and flocculation test results suggest that the possible mechanisms of flocculation by Stc-EGDMA-Cts are charge neutralization, adsorption, and inter-polymer linking.

1. Introduction

Water quality is essential for human life, affecting health and the economy. The contamination of the water itself is an inevitable consequence of human civilization. The analytical methods used to identify and quantify hazardous contaminants in water, such as organic materials and heavy metals, are crucial for monitoring and assessment. Gas chromatography (GC) is one of the analytical methods that can be employed to detect organic pollutants, as evidenced by the use of GC-MS and GC-FID instruments [1-4]. In parallel with establishing traditional and advanced analytical methods to monitor water quality, developing materials to remove or extract hazardous chemicals in water to produce a more beneficial water source is becoming a research concern. Teimoori et al. studied the removal of benzene,

*Corresponding Author: Asep Nurohmat Majalis
Email: asep039@brin.go.id
https://doi.org/10.24200/amecj.v7.i04.344

ethylbenzene, toluene, and xylene contaminants from water samples using a carbon nanostructure, functionalized multi-walled carbon nanotubes, and modified graphene oxide [3,5,6]. There is a growing interest in the flocculation technique as an alternative method for removing contaminants in water and wastewater [7]. Flocculation is commonly employed in wastewater treatment to eliminate heavy metals or dyes due to its convenient handling, high effectiveness, minimal energy usage, and low initial expenses [8,9]. Flocculants are utilized to rapidly divide solids and liquids by inducing colloidal particles to aggregate in a process called flocculation [8,10]. Two categories of flocculants exist: inorganic coagulants like iron and aluminum salts and organic flocculants comprising synthetic organic and natural polymer-based flocculant [11–13]. Unfortunately, secondary pollution can happen when leftover substances from aluminum and iron coagulants and synthetic polymer flocculants such as polyacrylamide are present in treated water or wastewater [14,15]. Aluminum residue has been linked to Alzheimer's disease [16,17], whereas iron residue can lead to the corrosion of metal equipment, decreasing its lifespan and increasing the expenses of wastewater treatment [18]. Polyacrylamide and other synthetic polymers could potentially be harmful to the environment because of their toxic and carcinogenic properties [18]. Furthermore, natural decomposition is difficult to achieve with synthetic polymers [19]. Natural polymers show potential as effective flocculants for treating wastewater [20]. Cellulose, chitosan, tannin, and starch are natural polymers with chemical structures and functional groups that can efficiently disrupt pollutants in wastewater [18,21,22]. Cellulose and chitosan have demonstrated high flocculation efficiency in removing textile dyes and heavy metals from wastewater because of their amino and polysaccharide functional groups, hydrophobicity, polyfunctionality, reactivity, and complexing properties. At the same time, tannin and starch showed good flocculation ability in removing anionic and cationic dye dispersions [11,21,23]. Moreover, polymers made from natural substances are cheaper and more sustainable but less harmful, able to decompose, and compatible with living organisms [18,24]. The mechanisms of flocculation by natural polymers based on flocculants are divided into six categories: neutralization of particle charge, inter-polymer bridging, charge patching, net trapping, sweeping, and adsorption [8,18,21]. Based on these mechanisms, polymer grafting can improve the performance of natural polymers as flocculants [8,25]. The grafting can produce a higher molecular weight due to the new branch in the primary molecular chain [26,27]. The grafting can combine functional groups from different compounds that have superiority in binding pollutants from wastewater. The benefits of grafting natural polymers are synergistically efficient at low doses, low cost, shear resistant, produces less sludge after the sedimentation process, biodegradable, regeneration performance, high molecular weight, no require additional coagulant, longer molecular chain, and fast sedimentation [24,28]. The grafting of starch or chitosan with a monomer or binary polymer has been widely studied and proven to improve flocculation performance [15,21,29,30]. However, the grafting of starch-monomer-chitosan or ternary polymer to produce a flocculant still needs to be improved. It is thought that grafting starch-monomer-chitosan produces a flocculant that brings the advantages of each component; chitosan is excellent in reducing heavy metals, and starch is superior in reducing dyes [21,31–33]. Starch is an abundant material consisting of a mixture of amylopectin and amylase with many hydroxyl groups in its molecular chain structure [34].Chitin deacetylation produces chitosan, a linear copolymer containing D-glucosamine and N-acetyl-D-glucosamine, along with hydroxyl and amino functional groups [27,35,36]. The mass ratio determines the impact of grafted natural polymers on inducing flocculation. The ratio of the crosslinker dose, the crosslinking temperature,

and the reaction duration [10,37]. Additionally, You and colleagues [10] found the best conditions for the effectiveness of the cationic starch/chitosan crosslinking-copolymer, with key factors being mass ratios of 4 to 5 g g^{-1} for cationic starch to chitosan, a crosslinker dosage ratio of 0.75 mg g^{-1} to cationic starch, a crosslinking temperature of 70 ºC, and a reaction time of at least 1.5 hours.

This research studied the synthesis of natural polymer-based flocculant, the starch-ethylene glycol dimethacrylate-chitosan or Stc-EGDMA-Cts, and its performance in removing dyes from wastewater. Stc-EGDMA-Cts was prepared via free radical polymerization under hydrothermal conditions, with varied mass ratios of starch to chitosan or Stc: Cts mass ratio (g g^{-1}). The characteristics of Stc-EGDMA-Cts were evaluated using Fourier transform infrared (FTIR) spectroscopy, X-ray diffraction (XRD), scanning electron microscopy (SEM), and zeta potential analyzer. The effectiveness of Stc-EGDMA-Cts in removing dye was evaluated using the UV-visible spectrophotometer method. Furthermore, the effect of the initial pH of textile dye wastewater, the Stc-EGDMA-Cts dosage, and the sedimentation time on flocculant performance was investigated.

2. Material and Methods

2.1. Materials

Soluble starch (CAS No.: 9005-84-9), EGDMA (CAS No.: 97-90-5), acetic acid (CAS No.: 64-19-7), sulfuric acid (CAS No.: 7664-93-9), sodium hydroxide (CAS No.: 1310-73-2), and azobisisobutyronitrile or AIBN (CAS No.: 78-67-1), all in analytical grade, were purchased from Sigma-Aldrich Canada Co. Low molecular weight chitosan (CAS No.: 9012-76-4) with a degree of deacetylation of 75%, and a maximum limit of impurities of 10% was purchased from Central Drug House (CDH) India. In analytical grade, Acetonitrile (CAS No. 75-05-8) and ethanol (CAS No. 64-17-5) were obtained from Merck. Professional Fabric Dyes Ltd obtained Dypro multi-purpose dye 19 deep blue or Dypro 19 (product code: 0101603119).

2.2. Instruments

The synthesis process of Stc-EGDMA-Cts was supported with an autoclave (Thermo Fisher Scientific, USA), an oven (Thermo Fisher Scientific, USA), and a centrifuge (Eppendorf, Germany). Characterization of both the raw material and Stc-EGDMA-Cts was performed by FTIR spectroscopy (Bruker-Tensor II, USA) for the study of functional groups, X-ray diffraction with a Copper (Cu) X-ray source (Malvern Panalytical AERIS, UK) for the evaluation of physical properties, SEM (PhenomProX Desktop Scanning Electron Microscope, Thermo Fisher Scientific, USA) for the analysis of surface morphology. A zeta potential analyzer (Horiba SZ 100, Japan) was employed to measure the zeta potential (ζ) of the dispersed material of Stc-EGDMA-Cts obtained from synthesis. Jar test experiments were conducted using the FC6S Jar Test instrument (VELP Scientifica, Italy). A digital pH meter (Hanna HI 2002, ITM, Canada) was used in this study. A single-beam UV-visible spectrophotometer (Agilent Cary 60 UV-Vis, USA) equipped with a 1 cm quartz cuvette was used for the dye analysis carried out in this work. A digital microscope VHX-5000 series (Keyence, Japan) was used to image the settled flocs from the jar test experiment.

2.3. The synthesis of Stc-EGDMA-Cts

Stc-EGDMA-Cts was synthesized through dissolution, mixing, homogenization, and free radical polymerization under hydrothermal conditions. A starch solution containing 2% starch by weight was blended with EGDMA (at a ratio of 0.7 mLg^{-1} of starch) at 850 rpm for 15 minutes at ambient temperature. A mixture was prepared with Stc: Cts ratios of 0.5, 1, 2, 4, and 8 g g^{-1} by adding 2% (w/v) chitosan solution in acetic acid 1% and mixing at 850 rpm for 30 minutes at room temperature. The AIBN initiator was subsequently added to the mixture (AIBN: starch mass ratio 0.8% g g^{-1}) and mixed at 850 rpm for 60 minutes at 60 ºC. Finally, the mixture was placed into an autoclave and then polymerized under

hydrothermal conditions at 90 ºC for 5 hours in the oven. The solid of Stc-EGDMA-Cts was obtained by settling a polymerized mixture for 48 hours at room temperature after adding ethanol (ethanol: starch ratio of 2.5 mLg^{-1}), followed by centrifugation at 6500 rpm for 25 minutes, filtration, and finally drying at 50 ºC for 12 hours. The yield (%) of Stc-EGDMA-Cts was calculated by Equation 1:

$$\text{Yield (\%)} = \frac{W_p}{W_c} * 100 \quad \text{(Eq.1)}$$

where W_p is the weight of the product (Stc-EGDMA-Cts) (g), and Wc is the total weight of starch and chitosan as constituents (g).

2.4. Characterization of Stc-EGDMA-Cts

2.4.1. FTIR Spectroscopy

FTIR spectrophotometer was used to characterize the functional groups in Stc-EGDMA-Cts across different Stc: Cts mass ratios. The results were evaluated against the functional groups present in starch, EGDMA, and chitosan. For FTIR analysis, Stc-EGDMA-Cts powder was processed with KBr at 25 ºC, formed into a pellet, and examined using FTIR over the range of 4000 to 500 cm^{-1}, with 45 scans per second and a resolution of 2.0 cm.

2.4.2. X-ray diffraction (XRD) analysis

XRD analysis was performed on starch, chitosan, and Stc-EGDMA-Cts at various Stc: Cts mass ratios. The instrument used a scattering angle (2θ) from 5 to 85º, a scanning speed of 0.2 deg s^{-1}, and a step size of 0.02 deg.

2.4.3. The study of the surface morphology

An SEM analysis examined the surface morphology of starch, chitosan, and Stc-EGDMA-Cts at various Stc: Cts mass ratios. The compounds were analyzed by fixing a few drops of their powder on the iron stub of the SEM coated with gold.

2.4.4. Zeta potential (ζ)

The zeta potential (ζ) of the dispersed material of Stc-EGDMA-Cts obtained from synthesis was measured by laser Doppler electrophoresis using a zeta potential analyzer ranging from -500 to +500 mV. The data were acquired in triplicate. Additionally, the zeta potential of wastewater containing Dypro 19 at pH 5, pH 7, and pH 8 was measured using the same instrument.

2.5. Flocculation experiments

2.5.1. Jar test

Jar test experiments were conducted to determine the effect of initial pH and Stc-EGDMA-Cts dosage in different mass ratios (Stc: Cts 0.5, 1, 2, 4, and 8 g g^{-1}) on the dye reduction from wastewater. The experiments were carried out on artificial wastewater by dissolving 0.25 g of Dypro 19 powder in water and then diluting it until 8 litres. A 500 ml dye solution was poured into a beaker glass and placed at the jar test instrument for flocculation experiments. The best initial pH level was determined by testing the textile dye wastewater at initial pH levels of 5, 6, 7, 8, and 9. In contrast, the amount of wastewater, Stc-EGDMA-Cts dosage, rapid mixing, gentle mixing, settling time, and temperature remained fixed at 500 mL, 2 mL L^{-1}, 200 rpm for 4 minutes, 30 rpm for 15 minutes, 60 minutes, and room temperature, respectively. The dosage optimization of Stc-EGDMA-Cts was conducted by varying dosages from 1.4 to 3.0 mL L^{-1}. On the other hand, the quantity of wastewater, initial pH, rapid mixing, gentle mixing, settling time, and temperature were maintained at 500 mL, the best initial pH, 200 rpm for 4 minutes, 30 rpm for 15 minutes, 60 minutes, and ambient temperature, respectively. Following establishing an optimum condition from the jar test, the sedimentation experiment was carried out with different settling times ranging from 0 to 1440 minutes. Ultimately, the settled flocs were examined using a digital microscope at 50 and 100 times magnification.

2.5.2. Dye analysis using UV-visible spectrophotometer and calculation of dye removal

Dye analysis was performed using a single-beam UV-visible spectrophotometer with a 1 cm quartz cuvette. The baseline and zeroing were corrected using demineralized water. The maximum absorbance of Dypro 19 was measured by scanning it in 400–800 nm wavelength ranges. The wavelength that resulted in maximum absorbance was used to measure the absorbance of the sample. The calibration curve for Dypro 19 was constructed using concentrations of 5, 10, 20, 30, 40, and 50 ppm. The limit of detection (LOD) and quantification (LOQ) were calculated using the linear regression of the calibration curve following Equations 2 and 3.

$$LoD = \frac{\sigma}{s} * 3 \qquad \text{(Eq.2)}$$

$$LoQ = \frac{\sigma}{s} * 10 \qquad \text{(Eq.3)}$$

where σ and s are the intercept standard deviation and the slope of the calibration curve, respectively. Furthermore, the percentage of dye removal can be calculated using Equation 4.

$$\text{Dye removal (\%)} = \frac{A_0 - A_t}{A_0} * 100 \qquad \text{(Eq.4)}$$

where A_0 is the dye absorption before treatment with Stc-EGDMA-Cts, and A_t is the absorption of dye after treatment with Stc-EGDMA-Cts.

3. Results and Discussion

3.1. Synthesis and characterization of Stc-EGDMA-Cts

Stc-EGDMA-Cts was synthesized through a free radical polymerization process under hydrothermal conditions. The synthesis process involves dissolving starch, chitosan, and AIBN initiator, followed by mixing, homogenization, and polymerization under hydrothermal conditions. The desired product was produced even though nitrogen purging was not carried out during the polymerization process. This synthesis method offers a simple and environmentally friendly approach. Although the AIBN initiator is classified as harmful, it is less toxic than the cerium ammonium nitrate used in a previous study [15]. The characteristics of Stc-EGDMA-Cts were determined using FTIR, XRD, SEM, and zeta potential. FTIR was used to determine the functional groups of Stc-EGDMA-Cts at various Stc: Cts mass ratios and compare them with the functional groups of the constituents (starch, chitosan, and EGDMA). Characterization using XRD was carried out to demonstrate the crystallinity of Stc-EGDMA-Cts at various Stc: Cts mass ratios, starch, and chitosan. SEM was used to evaluate the morphology of Stc-EGDMA-Cts at various Stc: Cts mass ratios and compare it with starch and chitosan as constituents. Zeta potential measurements were performed to determine the particle charge of Stc-EGDMA-Cts at various Stc: Cts mass ratios. Based on FTIR spectra in Fig 1a, the evidence found is: First, the functional groups of starch identified are OH, CH, CH_2, CH_3, and CO. A broad peak at 3284 cm-1 denotes the O-H stretching. The C-H stretching peaks at 2926 cm^{-1} (C-H) and 1337 cm^{-1} (C-H_2 and C-H_3). The 1148, 1077, and 995 cm-1 peaks suggested the C-O stretching. The FTIR also identified intramolecular H-bonding with carboxyl groups in the starch. The peak reveals it at 1641 cm^{-1}. The starch FTIR spectrum in Fig. 1a is similar to the FTIR spectra described by previous researchers [10,38,39]. Second, chitosan functional groups are identified as NH, OH, CH, and CO. The vibration mode at 3365, 3279, 2873, 1645, and 1023 cm^{-1} is N-H, O-H, C-H, C=O, and C-O stretching, respectively. The vibration mode at 1569 cm^{-1} and 1373 cm^{-1} is NH_2 and CH_2 bending. The intramolecular H-bonding with carboxyl groups and CH_3 deformation are indicated at 1645 cm^{-1} and 1373 cm^{-1}. The FTIR spectrum of chitosan in Figure 1a is identical to those observed in previous research [30,40–42]. Third, identified EDGMA functional groups are CH, C=O, C=C, and C-O. The vibration modes at 2959, 1716, and 1635 cm^{-1}, 1293 cm^{-1}, and 1143

cm^{-1} are C-H, C=O, C=C, and C-O stretching, respectively, while at 1450 cm^{-1} are CH_2 bending and CH_3 deformation. Finally, Stc-EGDMA-Cts shows peaks corresponding to its constituents' functional groups (starch, chitosan, and EGDMA), including OH, NH, CH, C=O, C=C, NH_2, CH_2, CH_3, and C-O. The vibration mode at 3304, 2930, 1724, 1637, and 1148 cm^{-1}, 1078 cm^{-1} and 1018 cm^{-1} is O-H and N-H, C-H, C=O, C=C, and C-O stretching, respectively, while the vibration mode at 1558 and 1449 cm^{-1} is NH_2 bending and CH_2 and CH_3 deformation.

The FTIR spectra of Stc-EGDMA-Cts at various Stc: Cts mass ratios are presented in Figure 1b. The spectral pattern shows a similar trend, indicating that the functional groups of Stc-EGDMA-Cts at various Stc: Cts mass ratios from 0.5 to 8 g g^{-1} are identical. A slight difference in intensity was observed in the characteristic absorption at 1558 cm-1, which showed the N-H group originating

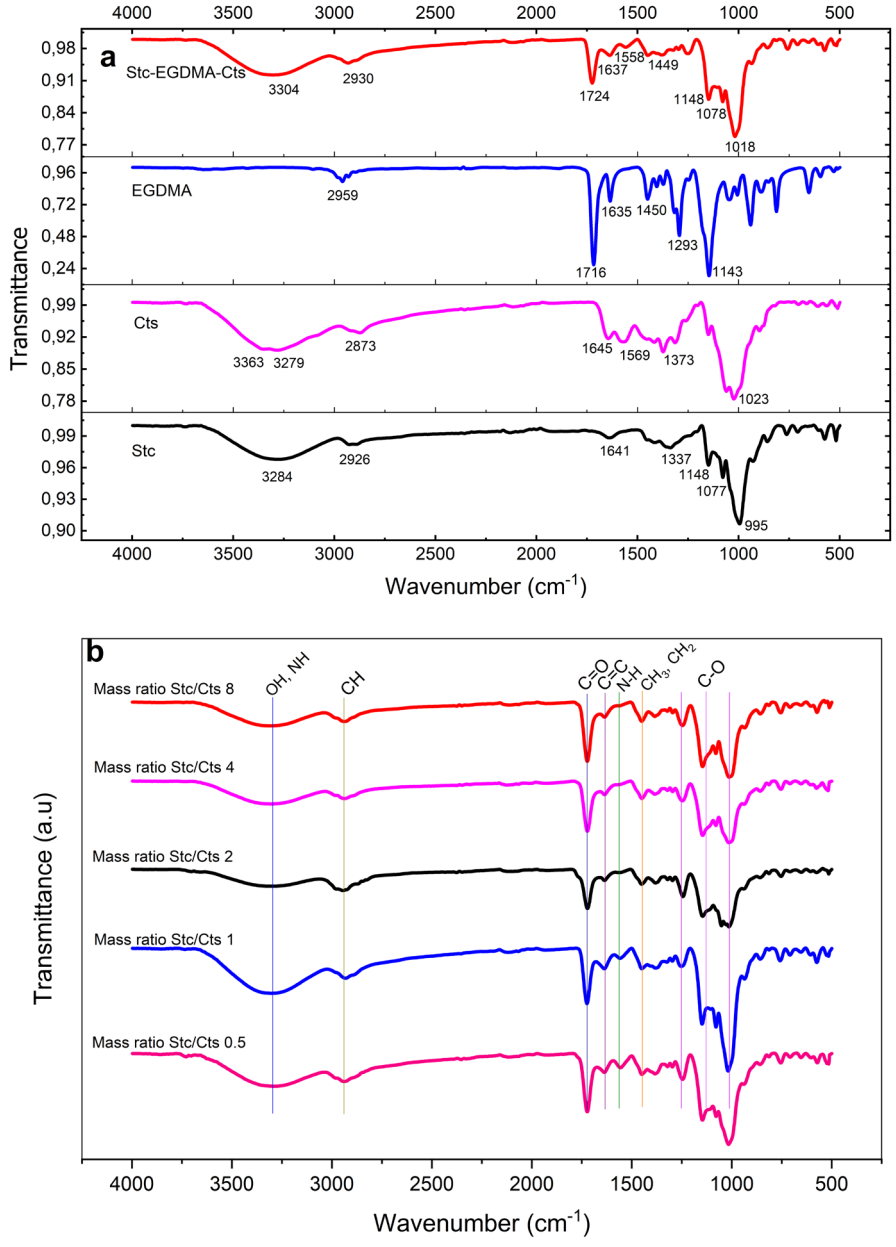

Fig. 1. (**a**) FTIR spectra of starch (Stc), chitosan (Cts), ethylene glycol dimethacrylate (EGDMA), Stc-EGDMA-Cts, and (**b**) Stc-EGDMA-Cts at various Stc:Cts mass ratios

from chitosan. The absorption band decreases as the Stc: Cts mass ratio increases. Starch's presence becomes more dominant than chitosan as the Stc: Cts mass ratios increase.

The XRD patterns in Figure 2a show a noticeable disparity in peak intensities among the component substances (starch, chitosan) and Stc-EGDMA-Cts at a Stc:Cts mass ratio of 0.5. Starch shows peaks at 14.5º, 16.9º, and 21.9º. Chitosan shows peaks at 20.2º, 31.6º, and 45.3º. Stc-EGDMA-Cts shows a peak at 16.7º. In terms of quality, starch has higher crystallinity compared to chitosan. The Origine Lab program processed data with smoothing and baseline correction to determine the crystallinity. The crystallinity of starch and chitosan is 97.25 and 73.68%, respectively. The XRD spectra of Stc-EGDMA-Cts in Figure 2b demonstrate that changing Stc:Cts mass ratio from 0.5 to 8 g g^{-1} does not cause a noticeable change in the peak spectra pattern. Nevertheless, there was a minor variation in the

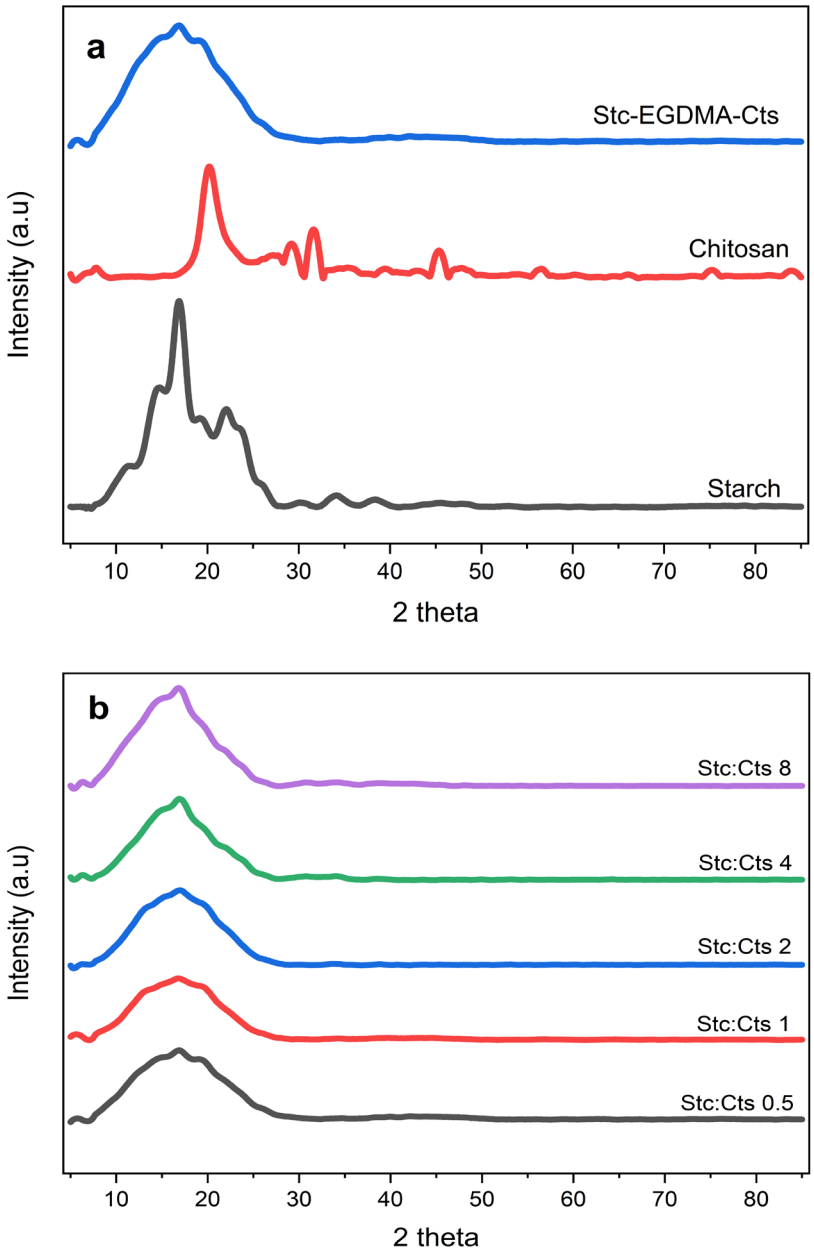

Fig. 2. (**a**) XRD spectra of starch (Stc), chitosan (Cts), Stc-EGDMA-Cts and (**b**) Stc-EGDMA-Cts at various Stc:Cts mass ratios

crystallinity of Stc-EGDMA-Cts at varying Stc:Cts mass ratios. Stc-EGDMA-Cts crystallinity was 95.68, 95.73, 99.99, 96.55, and 95.61% at Stc:Cts mass ratios of 0.5, 1.0, 2.0, 4.0, and 8.0 g g^{-1}, respectively. The XRD analysis results were confirmed by SEM investigation. Figure 3 presents SEM photos of starch, chitosan, and Stc-EGDMA-Cts at various Stc:Cts mass ratios. The SEM photos show that the surface of Stc-EGDMA-Cts at Stc:Cts mass ratios of 0.5, 1, 2, and 4 g g^{-1} is rougher than Stc:Cts mass ratio of 8 g g^{-1}. Stc-EGDMA-Cts has a rougher and larger surface than starch and chitosan, facilitating a better adsorption process. Stc:Cts mass ratio influences the percent yield and the zeta potential value of Stc-EGDMA-Cts. Table 1 shows that as the Stc:Cts mass ratio increases from 0.5 to 8 g g^{-1}, the percent yield rises from 15.64 to 59.93%, and the zeta potential increases from 21.3 to 46.4 mV. These results indicate that increasing the Stc:Cts mass ratios from 0.5 to 8 g g^{-1} produces Stc-EGDMA-Cts with longer and larger molecular structures. A long molecular structure with a high molecular charge promotes its function as a suitable flocculant. The molecule allows the bridging mechanism between particles to produce large flocs, facilitating the sedimentation process of the flocs. However, if the molecule is too long and large, it can reduce flocculation activity because of insolubility. This study demonstrated poor flocculant activity by Stc-EGDMA-Cts at a Stc:Cts mass ratio of 8 g g^{-1}.

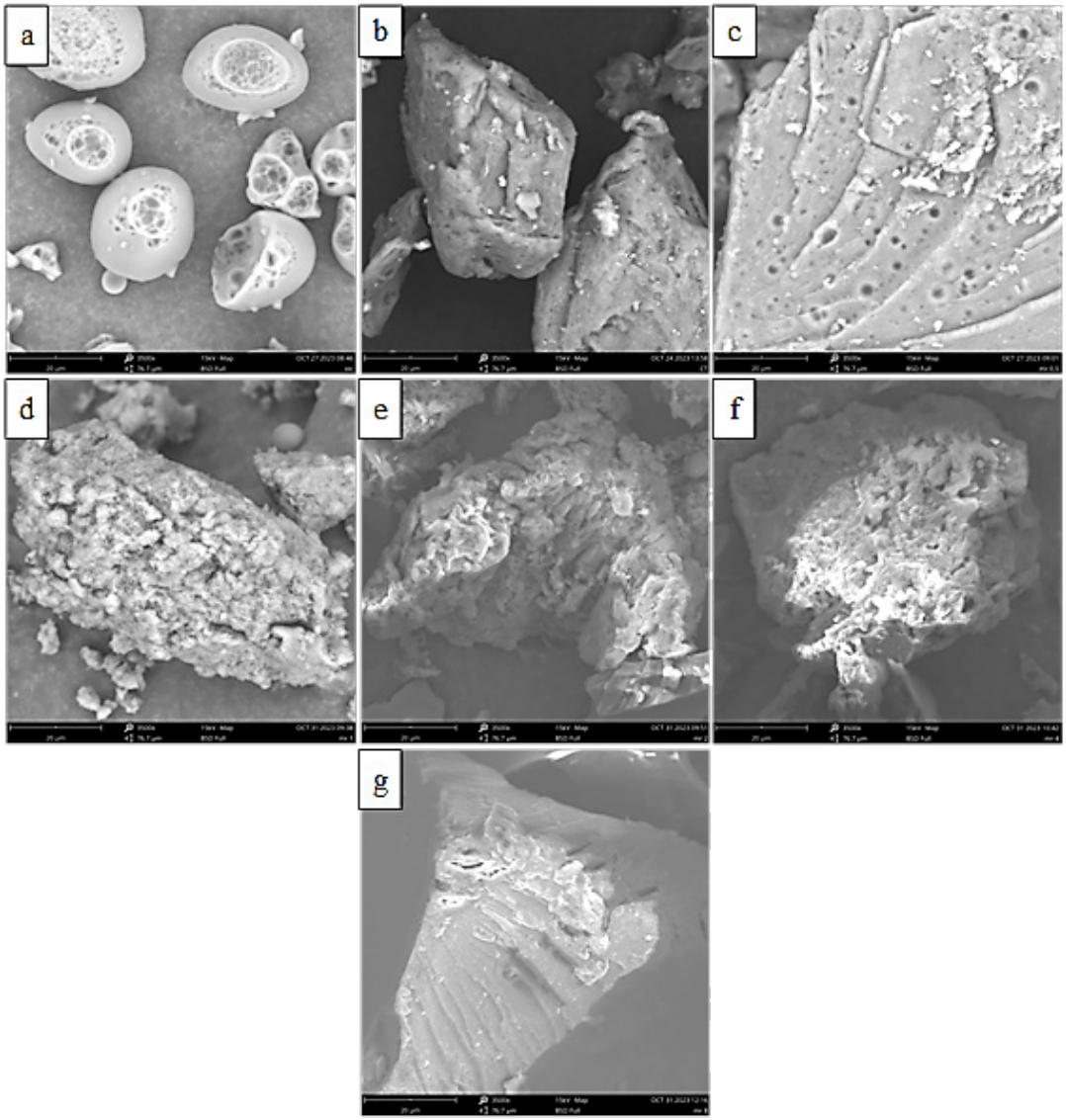

Fig. 3. SEM photos at 3,500 times magnification of starch (**a**), chitosan (**b**), and Stc-EGDMA-Cts at Stc:Cts mass ratio of 0.5 (**c**), 1 (**d**), 2 (**e**), 4 (**f**), and 8 (**g**)

Table 1. The percent grafting and the zeta potential of Stc-EGDMA-Cts at various Stc:Cts mass ratios

Stc:Cts mass ratio (g g^{-1})	Grafting (%)	Zeta potential (mV)
0.5	15.64 ± 13.21	23.1 ± 0.0
1.0	34.73 ± 21.99	30.2 ± 0.0
2.0	49.71 ± 21.74	40.1 ± 0.1
4.0	54.19 ± 12.14	42.3 ± 0.0
8.0	59.93 ± 12.41	46.4 ± 0.2

3.2. The performance of Stc-EGDMA-Cts in removing dye from wastewater

Stc-EGDMA-Cts performance in removing Dypro 19 from wastewater is evaluated using a UV-visible spectrophotometer. The absorbance of Dypro 19 standard solution and the standards calibration curve are presented in Figure 4. The maximum absorbance of Dypro 19 was measured at 588 nm (Fig. 4a). LOD and LOQ were determined from linear regression of standard calibration curve Y=0.0114*X + 0.00472, with the intercept standard deviation (σ) of 0.00425 (Fig. 4b). The LOD and LOQ values were found to be 1.12 and 3.73 mg L^{-1} (ppm), respectively. The highest and the lowest absorbance values observed in the flocculation performance test were 0.3435 and 0.019, respectively, corresponding to concentration values of 29.72 and 1.25 mg L^{-1} (ppm). Consequently, the measured concentrations remain above the LOD.

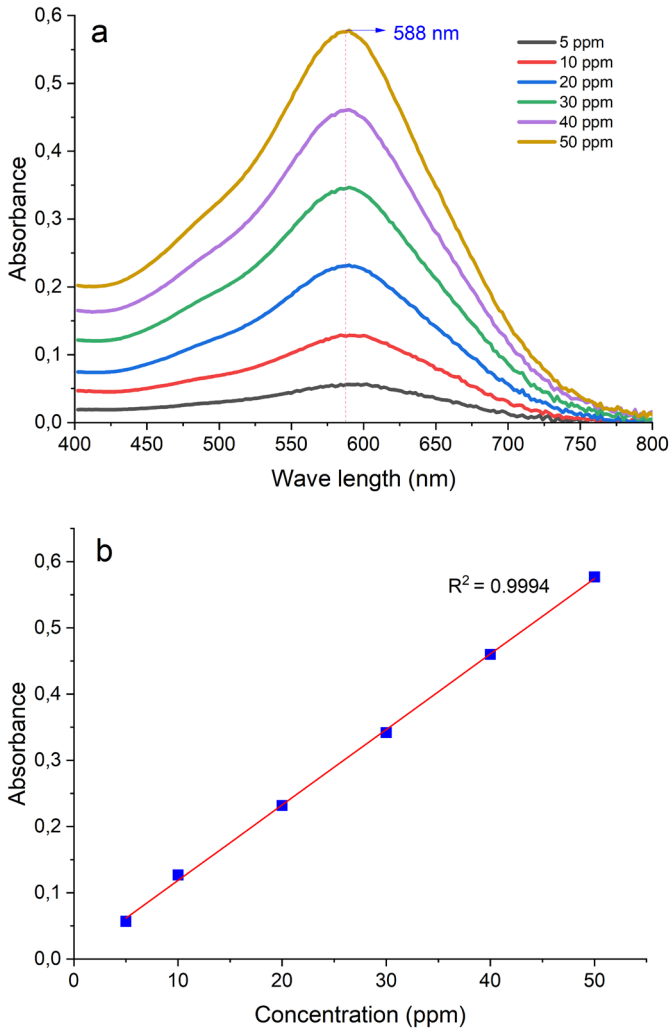

Fig. 4. UV spectra of standards solution (a), standards curve (b)

The performance of Stc-EGDMA-Cts at a certain Stc:Cts mass ratio (g g^{-1}) in removing Dypro 19 depends on the initial pH. Figure 5a shows that the best Stc-EGDMA-Cts performance is at an initial pH of 9, 8, 7, and 5 with Stc: Cts mass ratios of 0.5, 1, 2, and 4 g g^{-1}, respectively. The highest percentage of Dypro 19 removal achieved under these circumstances was 86.82, 76.47, 80.11, and 76.80%, respectively. At a Stc:Cts mass ratio of 8 g g^{-1}, Stc-EGDMA-Cts performance was poor, as it only reduced the Dypro 19 by less than 20%. According to the data presented in Figure 5a, it is possible that the best performance of Stc-EGDMA-Cts at a Stc:Cts mass ratio of 8 g g^{-1} is at a pH below 5. The optimum performance of Stc-EGDMA-Cts at various Stc:Cts mass ratios, which is highly dependent on an initial pH as described, is supported by the fact that the higher the value of the mass ratio of Stc:Cts, the more positive the zeta potential value of Stc-EDGMA-Cts. Conversely, the zeta potential value becomes more negative as the pH value of wastewater containing Dypro 19 decreases. Therefore, Stc-EGDMA-Cts at a larger mass ratio will achieve optimal flocculation performance at a low wastewater pH and vice versa. The dose is one of the critical factors in the coagulation-flocculation process, in addition to pH and mixing. The effect of the Stc-EGDMA-Cts dosage on removing Dypro 19 was investigated at various Stc:Cts mass ratios (0.5, 1, 2, and 4 g g^{-1}) under an optimum initial pH condition, as illustrated in Figure 5b. The optimum dosage was obtained at the highest percent dye removal. The optimum dosage for Stc:Cts mass ratios of 0.5, 1, 2, and 4 g g^{-1} is 2.0, 1.6, 2.4, and 2.0 mL L^{-1}, respectively, resulting in the percent dye removal of 91.01, 92.26, 92.84, and 80.85%, respectively. Figure 5c shows that the floc deposition time of the destabilized Dypro 19 was rapid enough. Deposition times of 15, 30, and 60 minutes resulted in dye removal of 91.06, 93.56, and 96.60%, respectively. From 60 to 1440 minutes, the dye removal rate remained relatively constant. This condition indicates that the generated flocs from the destabilization process of Dypro 19 from wastewater by Stc-EGDMA-Cts are relatively dense, heavy, and large, making them easy to settle quickly. Based on the graph in Figure 5a and Figure 5b, the optimum initial pH and the optimum dosage range obtained by Stc-EGDMA-Cts at mass ratio Stc:Cts 0.5, 1, 2, and 4 g g^{-1} is relatively narrow. Those suggest that the flocculation mechanism is the neutralization of particle charge. Below an optimum initial pH and dosage value, particle charge neutralization has yet to occur, resulting in stable dye particles. Above an optimum initial pH and an optimum dosage value, excess dosage and OH may cause a reversal of the day particle charge, leading to their stability.

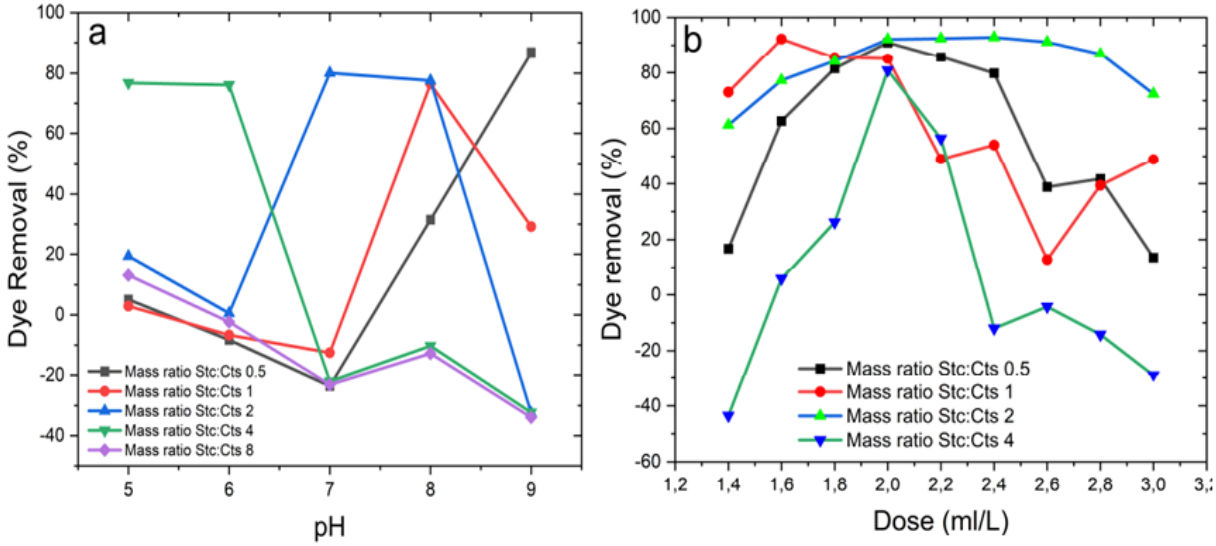

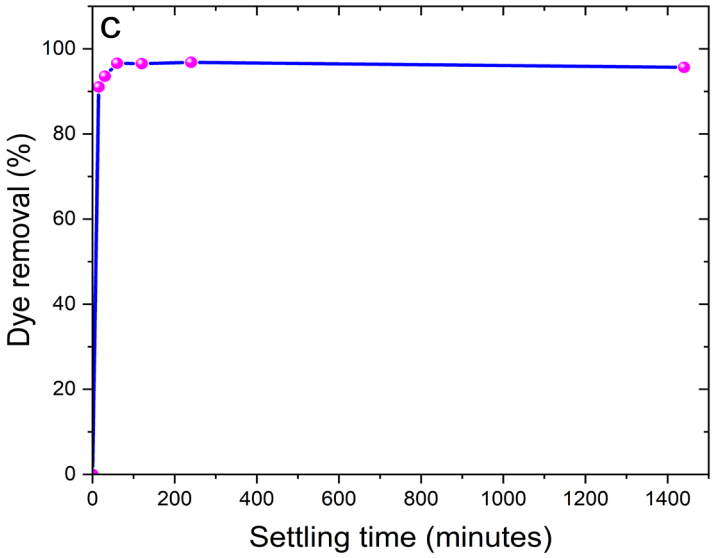

Fig. 5. The performance of Stc-EGDMA-Cts in removing Dypro 19 at various pH (**a**), at various doses (**b**), and settling time of destabilized Dypro 19 by STc-EGDMA-Cts (**c**)

The zeta potential value indicates the particle charge. Figure 6 illustrates the zeta potential value of Stc-EGDMA-Cts at Stc:Cts mass ratios of 1, 2, and 4 g g^{-1}, as well as the Dypro 19 wastewater pH. The zeta potential values indicate that particle charge neutralization is one of the mechanisms of Dypro 19 particle destabilization by Stc-EGDMA-Cts. In addition to adsorption and charge neutralization, the flocculation mechanism by Stc-EGDMA-Cts involves polymer bridging. The flocs image in Figure 7 shows floc sizes larger than 100 µm, indicating that polymer bridging has occurred between destabilized dye particles. This bridging causes the flocs to agglomerate, making them settle quickly.

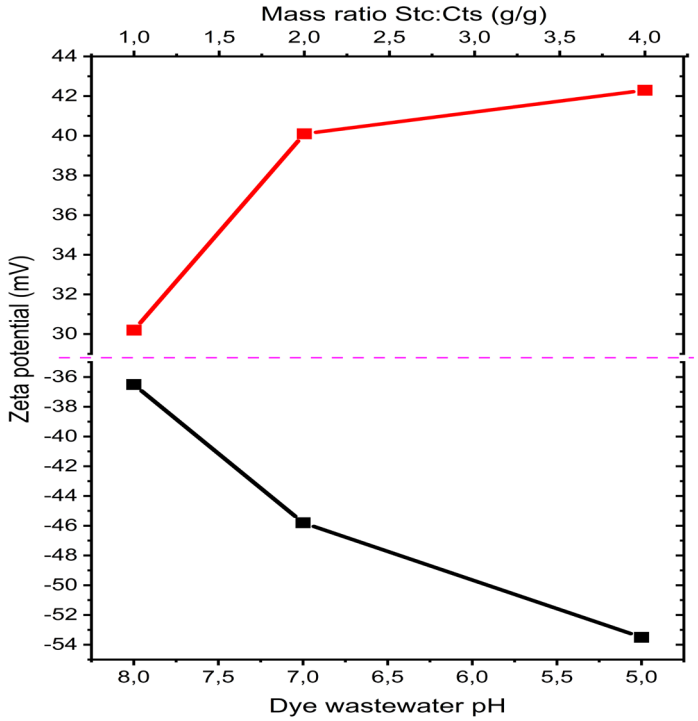

Fig. 6. Zeta potential values of Stc-EGDMA-Cts and the Dypro 19 wastewater before flocculation

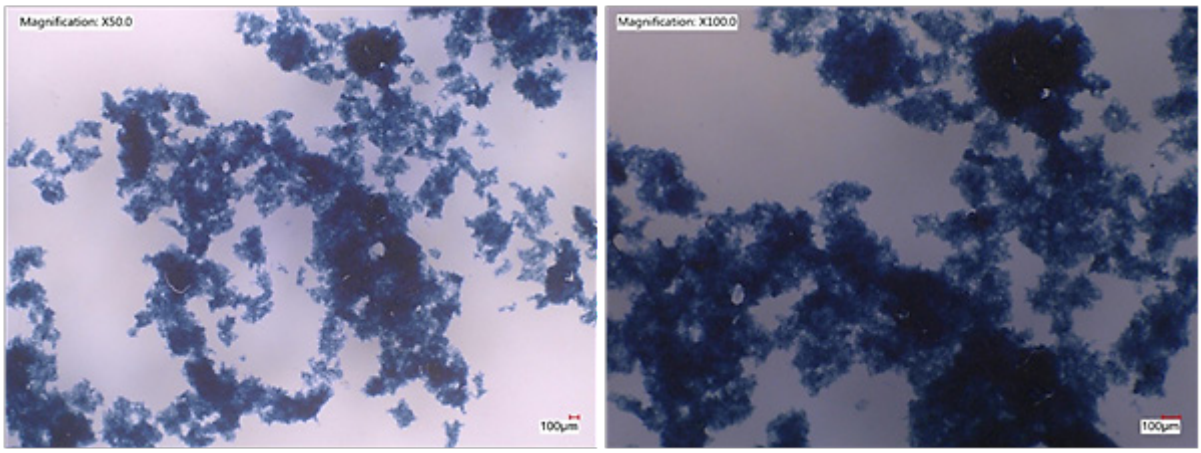

Fig. 7. The flocs image of Dypro 19 destabilized by Stc-EGDMA-Cts flocculant

4. Conclusion

Stc-EGDMA-Cts, a natural polymer-based flocculant, has been successfully synthesized simply and environmentally friendly through free radical polymerization under hydrothermal conditions without purging nitrogen gas. The mass ratio of Stc:Cts (g g^{-1}) influences the characteristics of the synthesized Stc-EGDMA-Cts and its performance in removing dye from wastewater. The mass ratio of Stc:Cts from 0.5 to 8 g g^{-1} increased the percent yield and the zeta potential value of the Stc-EGDMA-Cts. The Stc-EGDMA-Cts at mass ratios of 0.5 to 8.0 g g^{-1} have similar functional groups, high crystallinity, and qualitatively rougher and larger surface area than starch and chitosan. The performance of Stc-EGDMA-Cts at various Stc:Cts mass ratios in removing dyes above 80% evaluated by a UV-visible spectrophotometer method was determined by a specific pH, a specific flocculant dosage, a floc size, and settles quickly. Based on the results of characterization and flocculation performance tests, Stc-EGDMA-Cts was found to employ charge neutralization, adsorption, and polymer bridging as mechanisms for dye flocculation.

5. Acknowledgements

The authors would like to thank The Research Organization of Life Sciences and Environment, The National Research and Innovation Agency (BRIN), Indonesia, for funding this research under the scheme of Rumah (Home) Program 2023 for the Results of the Disclosure and Utilization of Indonesian Biodiversity. There are no conflicts of interest to disclose.

6. References

[1] E. Hogue, The Importance of Water Quality, National Ocean Service, 2021. https://sanctuaries.noaa.gov/news/aug21/water-quality-month.html (accessed June 13, 2024)

[2] M. Arjomandi, A review: Analytical methods for heavy metals determination in environment and human samples, Anal. Methods Environ. Chem. J. (2019) 97–126. https://doi.org/10.24200/amecj.v2.i03.73

[3] S. Teimoori, A.H. Hassani, M. Panahi, New extraction of toluene from water samples based on nano-carbon structure before determination by gas chromatography, Int. J. Environ. Sci. Technol., 20 (2023) 6589–6608. https://doi.org/10.1007/s13762-023-04906-9

[4] R. Ashouri, A.M. Rashidi, S.A.H. Mirzahosseini, N. Mansouri, Dynamic and static removal of benzene from air based on task-specific ionic liquid coated on MWCNTs by sorbent tube-headspace solid-phase extraction procedure, Int. J. Environ. Sci. Technol., 18 (2021) 2377–2390. https://doi.org/10.1007/s13762-020-02995-4

[5] S. Teimoori, A.H. Hassani, M. Panahi, Rapid

extraction of BTEX in water and milk samples based on functionalized multi-walled carbon nanotubes by dispersive homogenized-micro-solid phase extraction, Food Chem., 421 (2023) 136229. https://doi.org/10.1016/j.foodchem.2023.136229

[6] S. Teimoori, M. Panahi, N. Mansouri, An immobilization of aminopropyl trimethoxysilane-phenanthrene carbaldehyde on graphene oxide for toluene extraction and separation in water samples, Chemosphere, 316 (2023) 137800. https://doi.org/10.1016/j.chemosphere.2023.137800

[7] C.S. Lee, J. Robinson, M.F. Chong, A review on application of flocculants in wastewater treatment, Process Saf. Environ. Prot., 92 (2014) 489–508. https://doi.org/10.1016/j.psep.2014.04.010

[8] X. Jiang, Y. Li, X. Tang, J. Jiang, Q. He, Z. Xiong, H. Zheng, Biopolymer-based flocculants: a review of recent technologies, Environ. Sci. Pollut. Res., 28 (2021) 46934–46963. https://doi.org/10.1007/s11356-021-15299-y

[9] Y. Sun, D. Li, X. Lu, J. Sheng, X. Zheng, X. Xiao, Flocculation of combined contaminants of dye and heavy metal by nano-chitosan flocculants, J. Environ. Manage., 299 (2021) 113589. https://doi.org/10.1016/j.jenvman.2021.113589

[10] L. You, F. Lu, D. Li, Z. Qiao, Y. Yin, Preparation and flocculation properties of cationic starch/chitosan crosslinking-copolymer, J. Hazard. Mater., 172 (2009) 38–45. https://doi.org/10.1016/j.jhazmat.2009.06.120

[11] C.S. Lee, J. Robinson, M.F. Chong, A review on application of flocculants in wastewater treatment, Process Saf. Environ. Prot., 92 (2014) 489–508. https://doi.org/10.1016/j.psep.2014.04.010

[12] H. Zhang, G. Guan, T. Lou, X. Wang, High performance, cost-effective and ecofriendly flocculant synthesized by grafting carboxymethyl cellulose and alginate with itaconic acid, Int. J. Biol. Macromol., 231 (2023) 123305. https://doi.org/10.1016/j.ijbiomac.2023.123305

[13] C. Zhao, J. Zhou, Y. Yan, L. Yang, G. Xing, H. Li, P. Wu, M. Wang, H. Zheng, Application of coagulation/flocculation in oily wastewater treatment: A review, Sci. Total Environ., 765 (2021) 142795. https://doi.org/10.1016/j.scitotenv.2020.142795

[14] M.A.A. Razali, A. Ariffin, Polymeric flocculant based on cassava starch grafted polydiallyldimethylammonium chloride: Flocculation behavior and mechanism, Appl. Surf. Sci., 351 (2015) 89–94. https://doi.org/10.1016/j.apsusc.2015.05.080.

[15] J. Xun, T. Lou, J. Xing, W. Zhang, Q. Xu, J. Peng, X. Wang, Synthesis of a starch–acrylic acid–chitosan copolymer as flocculant for dye removal, J. Appl. Polym. Sci., 136 (2019) 47437. https://doi.org/10.1002/app.47437

[16] S.Y. Choy, K.M.N. Prasad, T.Y. Wu, M.E. Raghunandan, R.N. Ramanan, Utilization of plant-based natural coagulants as future alternatives towards sustainable water clarification, J. Environ. Sci., 26 (2014) 2178–2189. https://doi.org/10.1016/j.jes.2014.09.024

[17] S. Mohd Asharuddin, N. Othman, W.A.H. Altowayti, N. Abu Bakar, A. Hassan, Recent advancement in starch modification and its application as water treatment agent, Environ. Technol. Innov., 23 (2021) 101637. https://doi.org/10.1016/j.eti.2021.101637

[18] N. Das, N. Ojha, S.K. Mandal, Wastewater treatment using plant-derived bioflocculants: green chemistry approach for safe environment, Water Sci. Technol., 83 (2021) 1797–1812. https://doi.org/10.2166/wst.2021.100

[19] J. Bendoraitiene, E. Lekniute-Kyzike, R. Rutkaite, Biodegradation of cross-linked and cationic starches, Int. J. Biol. Macromol., 119 (2018) 345–351. https://doi.org/10.1016/j.ijbiomac.2018.07.155

[20] B. Zaman, N. Hardyanti, M. Arief Budiharjo, S. Budi Prasetyo, A. Ramadhandi, A. Tri

Listiyawati, Natural flocculant VS chemical flocculant where is better to used in Wastewater treatment, IOP Conf. Ser. Mater. Sci. Eng., 852 (2020) 12014. https://doi.org/10.1088/1757-899X/852/1/012014

[21] J. El-Gaayda, F.E. Titchou, R. Oukhrib, P.-S. Yap, T. Liu, M. Hamdani, R. Ait Akbour, Natural flocculants for the treatment of wastewaters containing dyes or heavy metals: A state-of-the-art review, J. Environ. Chem. Eng., 9 (2021) 106060. https://doi.org/10.1016/j.jece.2021.106060

[22] M. Nasrollahzadeh, M. Sajjadi, S. Iravani, R.S. Varma, Starch, cellulose, pectin, gum, alginate, chitin and chitosan derived (nano)materials for sustainable water treatment: A review, Carbohydr. Polym., 251 (2021) 116986. https://doi.org/10.1016/j.carbpol.2020.116986

[23] T.G. Ambaye, M. Vaccari, S. Prasad, E.D. Van Hullebusch, S. Rtimi, Preparation and applications of chitosan and cellulose composite materials, J. Environ. Manage., 301 (2022) 113850. https://doi.org/10.1016/j.jenvman.2021.113850

[24] S.A. Ishak, M.F. Murshed, H. Md Akil, N. Ismail, S.Z. Md Rasib, A.A.S. Al-Gheethi, The application of modified natural polymers in toxicant dye compounds wastewater: A review, Water (Basel), 12 (2020) 2032. https://doi.org/10.3390/w12072032

[25] V.H. Dao, N.R. Cameron, K. Saito, Synthesis, properties and performance of organic polymers employed in flocculation applications, Polym. Chem., 7 (2016) 11–25. https://doi.org/10.1039/C5PY01572C

[26] C. Feng, Y. Li, D. Yang, J. Hu, X. Zhang, X. Huang, Well-defined graft copolymers: from controlled synthesis to multipurpose applications, Chem. Soc. Rev., 40 (2011) 1282–1295. https://doi.org/10.1039/B921358A

[27] M.Á. Vega-Hernández, G.S. Cano-Díaz, E. Vivaldo-Lima, A. Rosas-Aburto, M.G. Hernández-Luna, A. Martinez, J. Palacios-Alquisira, Y. Mohammadi, A. Penlidis, A review on the synthesis, characterization, and modeling of polymer grafting, Processes, 9 (2021) 375. https://doi.org/10.3390/pr9020375

[28] S.S. Ngema, A.K. Basson, T.S. Maliehe, Synthesis, characterization and application of polyacrylamide grafted bioflocculant, Phy. Chem. Earth, Parts A/B/C, 115 (2020) 102821. https://doi.org/10.1016/j.pce.2019.102821

[29] H. Wu, Z. Liu, A. Li, H. Yang, Evaluation of starch-based flocculants for the flocculation of dissolved organic matter from textile dyeing secondary wastewater, Chemosphere, 174 (2017) 200–207. https://doi.org/10.1016/j.chemosphere.2017.01.120

[30] D. Wang, T. Zhao, L. Yan, Z. Mi, Q. Gu, Y. Zhang, Synthesis, characterization and evaluation of dewatering properties of chitosan-grafting DMDAAC flocculants, Int. J. Biol. Macromol., 92 (2016) 761–768. https://doi.org/10.1016/j.ijbiomac.2016.07.087

[31] M.T. ALSamman, J. Sánchez, Recent advances on hydrogels based on chitosan and alginate for the adsorption of dyes and metal ions from water, Arab. J. Chem., 14 (2021) 103455. https://doi.org/10.1016/j.arabjc.2021.103455

[32] L. Zhang, Y. Zeng, Z. Cheng, Removal of heavy metal ions using chitosan and modified chitosan: A review, J. Mol. Liq., 214 (2016) 175–191. https://doi.org/10.1016/j.molliq.2015.12.013

[33] Y. Zhang, M. Zhao, Q. Cheng, C. Wang, H. Li, X. Han, Z. Fan, G. Su, D. Pan, Z. Li, Research progress of adsorption and removal of heavy metals by chitosan and its derivatives: A review, Chemosphere, 279 (2021) 130927. https://doi.org/10.1016/j.chemosphere.2021.130927

[34] A. Apriyanto, J. Compart, J. Fettke, A review of starch, a unique biopolymer – Structure, metabolism and in planta modifications, Plant. Sci., 318 (2022) 111223. https://doi.org/10.1016/j.plantsci.2022.111223

[35] N.J. Arsad, N. Ngadi, S.F. Mohamed Razak, Preparation of chitosan-grafted nanocellulose via microwave-initiate method, Appl. Mech. Mater. 818 (2016) 281–284. https://doi.org/10.4028/www.scientific.net/AMM.818.281

[36] L. Qiao, S. Wang, T. Wang, S. Yu, S. Guo, K. Du, High-strength and low-swelling chitosan/cellulose microspheres as a high-efficiency adsorbent for dye removal, Cellulose, 28 (2021) 9323–9333. https://doi.org/10.1007/s10570-021-04111-2

[37] T.Adali,E.Yilmaz,Synthesis,characterization and biocompatibility studies on chitosan-graft-poly(EGDMA), Carbohydr. Polym., 77 (2009) 136–141. https://doi.org/10.1016/j.carbpol.2008.12.017

[38] N. Alvarado, R.L. Abarca, J. Urdaneta, J. Romero, M.J. Galotto, A. Guarda, Cassava starch: structural modification for development of a bio-adsorber for aqueous pollutants. Characterization and adsorption studies on methylene blue, Polymer Bull., 78 (2021) 1087–1107. https://doi.org/10.1007/s00289-020-03149-9

[39] A. Hebeish, A.A. Aly, A. El-Shafei, S. Zaghloul, Synthesis and characterization of cationized starches for application in flocculation, finishing and sizing, Egypt. J. Chem., 52 (2009) 0449-2285. https://ejchem.journals.ekb.eg/

[40] E.S. de Alvarenga, Characterization and properties of chitosan, biotechnology of biopolymers, InTech Publisher book, 2011. https://doi.org/10.5772/17020

[41] A. Drabczyk, S. Kudłacik-Kramarczyk, M. Głąb, M. Kędzierska, A. Jaromin, D. Mierzwiński, B. Tyliszczak, Physicochemical investigations of chitosan-based hydrogels containing Aloe Vera designed for biomedical use, Materials, 13 (2020) 3073. https://doi.org/10.3390/ma13143073

[42] S. Yasmeen, M. Kabiraz, B. Saha, Md. Qadir, Md. Gafur, S. Masum, Chromium (VI) ions removal from tannery effluent using chitosan-microcrystalline cellulose composite as adsorbent, Int. Res. J. Pure Appl. Chem., 10 (2016) 1–14. https://doi.org/10.9734/IRJPAC/2016/23315

Anal. Methods Environ. Chem. J. 7 (4) (2024) 78-95

AMECJ

Research Article, Issue 4
Analytical Methods in Environmental Chemistry Journal
Journal home page: www.amecj.com/ir

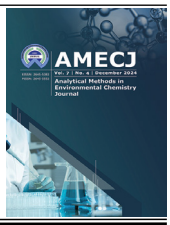

Zinc adsorption from synthetic wastewater using synthesis activated carbons from sugarcane bagasse and Cashew nut shells before determination by atomic absorption spectrometry

Yusufu Luka[a, *], Timothy Musa Chiroma[a], Abdulhalim Musa Abubakar[a], and A'aron Donidamini Kachalla[a]
[a]*Department of Chemical Engineering, Faculty of Engineering, Modibbo Adama University, PMB 2076, Yola, Adamawa State, Nigeria*

ARTICLE INFO:

Received 9 Aug 2024
Revised form 13 Oct 2024
Accepted 11 Nov 2024
Available online 30 Dec 2024

Keywords:
Zinc,
Activated carbon,
Adsorption,
Atomic absorption spectrometry,
Synthetic Wastewater,
Optimization

ABSTRACT

The present study examined its application in removing Zinc (Zn) from synthetic water. The mechanism for the adsorption of Zn by sugarcane bagasse (SCB) and cashew nut shell (CNS) is linked to the role played by the vital stretching functional groups such as hydroxyl (-OH) and other phenol and aromatic groups, as revealed by the Fourier Transform Infrared (FTIR) characterization technique. The existence of porous channels on the activated carbon (AC) revealed by Scanning Electron Microscopy (SEM) and depleted Zn ions in the water after sorption by Atomic Adsorption Spectrometry (AAS) analysis was an added merit. The effect of varying contact time (0-50 min) and initial Zn concentration (30-100 mg L^{-1}) resulted in good fits of the predicted adsorption capacity and removal responses (%), described by 3 quadratic and one linear model. Statistical metrics, 3D surface, and contour plots based on Central Composite Design (CCD) Response Surface Methodology (RSM) carried out put CNS-AC ahead of SCB-AC as the most efficient adsorbent for ion removal under shorter and longer contact times. In optimized conditions, the parameters such as initial concentration, contact time, removal, adsorption capacity, and desirability for CNS and SCB were achieved at (98.74 mg L^{-1}, 50 min, 98.51%, 7.83 mg $g^{-1,}$ and 0.995) and (77.61 mg L^{-1}, 5 min, 95.8529%, 6.01 mg g^{-1} and 0.816), respectively. Where the need to use these adsorbents is found, it is important to consider the abundance of the plant waste in the location or contrive a scheme for their massive production.

1. Introduction

In recent years, the contamination of water bodies by heavy metals has emerged as a pressing environmental concern, prompting intensive research into effective and sustainable remediation strategies. Among these heavy metals, zinc (Zn) stands out due to its widespread industrial use and potential detrimental effects on ecosystems and human health [1–3]. Synthetic wastewater, mimicking industrial effluents, often contains elevated concentrations of Zn, necessitating efficient treatment methods for its removal. In this situation, using activated carbons (AC) derived from renewable biomass sources [4, 5] presents a promising avenue for the remediation of Zn-

*Corresponding Author: Yusufu Luka
Email: sufuluka@mau.edu.ng
https://doi.org/10.24200/amecj.v7.i04.345

contaminated water. Several agricultural waste biomass can be harnessed in that direction [6–9]. Synthesis and characterization of AC derived from two abundant agricultural byproducts, sugarcane bagasse (SCB) [10, 11] and cashew nut shell (CNS) [12], for the removal of Zn from synthetic wastewater will address this issue. Targeted characteristics must make their AC a good adsorbent [13]. Apart from that, the abundance of waste materials must be considered. For example, Nigeria produced 1588.97 tons of sugarcane in 2023 [14], which is very low despite its enormous capability [15]. Worldwide production grew from 177.28 to 187.88 million metric tons in 2023 [16, 17]. Kogi state in Nigeria is the largest producer of cashews in the country, but discrepancies exist in reports regarding the volume/number of cashews produced in the country [18–20]. Thus, tonnage and location/availability are essential in selecting sugarcane and cashew waste as biosorbents. If there is a need for large-scale remediation applications using those materials, Brazil and the Ivory Coast, with large outputs, will have a better comparative advantage. The implications of this study extend beyond mere pollution mitigation, encompassing broader environmental sustainability and resource utilization objectives. Apart from water cleansing of heavy metals [21–24], adsorbents have proven effective in addressing air pollution [24–28]. By repurposing agricultural waste materials such as SCB and CNS to produce ACs, this research contributes to the valorization of biomass resources and the reduction of waste accumulation. Additionally, developing efficient and cost-effective adsorbents for Zn removal offers tangible benefits for industries tasked with wastewater treatment [29–31], potentially leading to improved regulatory compliance and reduced environmental impact. Previous studies have demonstrated the efficacy of AC for heavy metal removal; however, comprehensive investigations into the precursor characteristics and optimization of synthesis parameters are still needed to enhance their performance further. Notable studies failed to incorporate the most influential parameters [32–36]. This study partly addresses this research gap by employing Response Surface Methodology (RSM) Central Composite Design (CCD) to optimize the preparation conditions of SCB and CNS-AC, thereby maximizing their efficacy in Zn removal from synthetic wastewater. However, CNS has not been fully recognized as a favorable adsorbent for Zn removal, apart from isotherm and kinetic studies conducted by Kumar et al. (2012) previously [37]. It was done without optimization by elucidating the relationship between precursor characteristics (determined via various laboratory analyses), synthesis parameters (contact time and initial metal concentration), and adsorption performance. Zinc (Zn) is naturally available in water bodies, where an amount exceeding 5 mg L^{-1} would result in Zn poisoning. Implementing a remediation strategy to curb its menace is not difficult using plant-based adsorbents. Due to the promise showcased by sugarcane bagasse (SCB) and cashew nut shell (CNS) activated carbon (AC) in previous studies to eliminate other harmful substances from wastewater [38, 39]. This research aims to provide a valuable understanding of the design and optimization of sustainable CNS and SCB-ACs for Zn metal remediation, thereby contributing to the advancement of environmental science and engineering practices.

2. Material and Methods

2.1. Production of Activated Carbon

About 100g of SCB and 200g of CNS were collected from wheelbarrow vendors in Jimeta, Adamawa State of Nigeria, and impurities or foreign materials on them were removed by washing with distilled water. These materials were dried by exposing them to the open environment under the sun, as did Kakom et al. (2023), until a considerable amount of moisture is removed. They were then used to prepare carbon by a process called carbonization. Essentially, SCB and CNS samples were carbonized by heating in an Sx-25-12 muffle furnace at 400 and 600°C, respectively, for one hour to obtain their carbons – similar to the temperature range in Suntharam (2022) and

Guillaume et al. (2019). The carbon obtained was mixed with 10g phosphoric acid and water solution activating agents. A ratio of 1:3 of the carbon to the solution was used before feeding it to WHL-254 oven set at 105 for 24 hours to allow its activation. The AC product produced was washed to remove any remaining impurities and dried at 110°C. After burning, it was hit with distilled water several times before oven-drying at 110-120°C for a few hours to obtain the ACs. Only 4000 mL of distilled water was used for washing and cleaning raw materials. Figure 1 shows a synthesis flow diagram specific to the production of grade AC of CNS and SCB in this study. ACs produced from CNS and SCB were then used as adsorbent to remove Zn from a water sample.

2.2. Characterization of AC

Functional group detection was performed using a PerkinElmer spectrum version 10.4.3 FTIR machine domiciled in Modibbo Adama University Central Laboratory, between 500 and 4000 cm^{-1} transmittances with a PE service. Adsorbent morphology was observed through a SEM and EDX (Gold Testing X-ray) spectrophotometer. In this research, SEM analysis was conducted to produce a high-resolution image of the ACs before and after the Zn adsorption process to ascertain the presence of the heavy metal on the activated surface. EDX and AAS (model: AA500) were carried out for metal concentration after adsorption, . For Zn, the limit of detection (LOD) and the linear range are 1-10 µg L^{-1} and 10-5000 µg L^{-1}, respectively.

2.3. Zinc Metal-Contaminated Wastewater Treatment

Raw or contaminated water was initially prepared from the 13 runs data generated from RSM CCD by varying the initial concentration of Zn, Ci, (Factor A: mg L^{-1}) and contact time (Factor B: min) and keeping the volume of the solution (V) and adsorbent dosage (M) constant (i.e., V = 0.4 mL and M = 5g). The Design Expert 7.0.0 software generates the runs. Table 1 was generated by the Expert tool after setting the time range to 0-50 min and Ci range to 30-100 mg L^{-1}. Essentially, the wastewater or raw water was simulated by injecting a specific concentration of Zn in accordance with every run, forming a solution in the process.

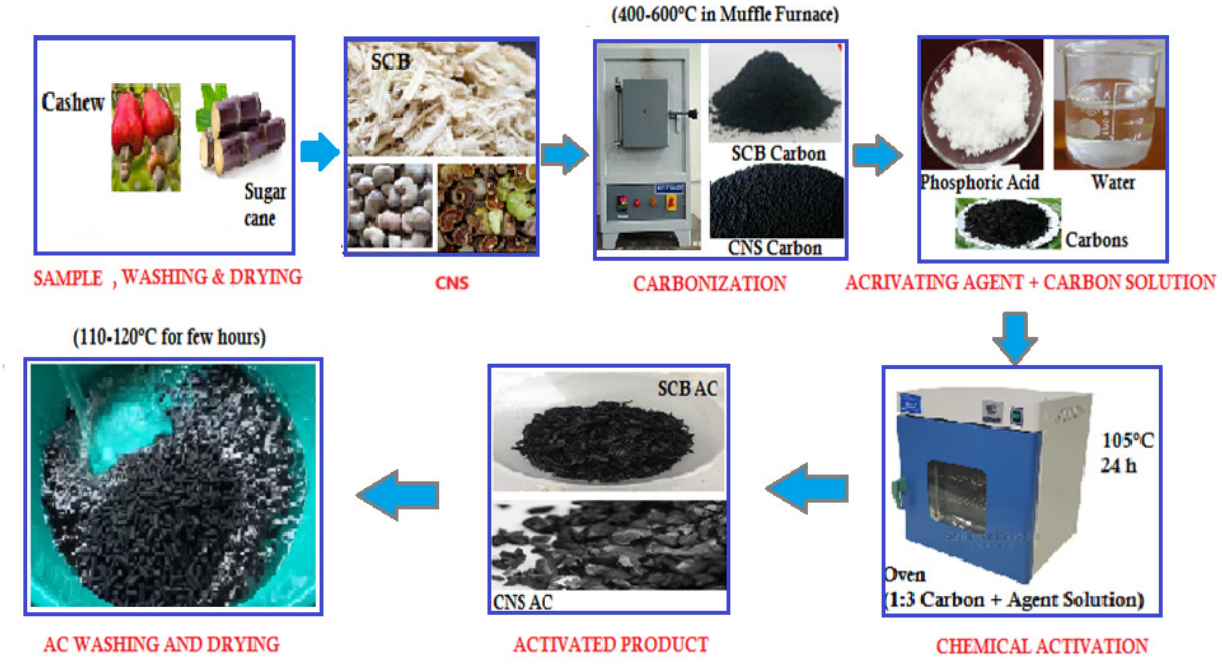

Fig. 1. AC Production Steps from SCB and CNS Waste Biomass

Table 1. Design of Experiment for Zn Adsorption

Run	A: Initial Metal Conc. (mg L^{-1})	B: Contact Time (min)
1.	50	25.0
2.	50	46.2
3.	50	25.0
4.	50	25.0
5.	70	40.0
6.	78.3	25.0
7.	70	10.0
8.	30	40.0
9.	50	25.0
10.	50	25.0
11.	50	3.8
12.	21.7	25.0
13.	30	10.0

2.4. EDX and AAS Analysis

In every run, the AC samples were put in a DFS-KW-1000B water bath shaker according to the run's contact time and filtered using filter paper. This is done to separate the ACs from the water. The experiment was carried out separately using CNS- and SCB-AC. An AAS machine capable of identifying 62 different metals in a solution was used to test for the presence of Zn in the treated water. Other metals were also identified using the EDX machine. Usually, an AAS instrument looks for a particular metal by focusing a beam of UV light at a specific wavelength through a flame and into a detector [40,41]. The sample of interest is aspirated into the flame, and if that metal is present in the sample, it will absorb some of the light, thus reducing its intensity. For the sake of optimization, this final concentration of Zn measured through AAS is used to determine the equilibrium adsorption capacity, qe, (mg g^{-1}), and the removal efficiency, RE (% removal), in line with Equations 1 and 2 [42] respectively.

$$q_e = \frac{(C_i - C_e)V}{M} \qquad \text{(Eq.1)}$$

$$RE(\%) = \frac{C_i - C_e}{C_i} \times 100 \qquad \text{(Eq.2)}$$

2.5. Optimization

Calculated RE and qe were then defined as response 1 (R1) and response 2 (R2) to kick-start the CCD statistical analysis, fit and surface plot generation, and optimum selections of contact time and Zn Ci corresponding to a maximum qe and RE. It is carried out for CNS and SCB adsorbent data. Optimization is carried out for two cases. Case 1 is the optimal conditions at a set/specified low contact time where adsorption is expected to be rapid. Case 2 is the optimal conditions at maximum contact time in which adsorption is expected to be slow.

3. Results and Discussion

3.1. Effect of Specific Functional Groups Present

The FTIR technique was formerly used to identify the characteristics of the functional groups involved in the adsorption of Zn ions on both the SCB and CNS adsorbent produced. Figure 2 depicts the infrared spectroscopy image of the SCB-AC before and after Zn adsorption from the wastewater. As expected, peaks of various functional groups on the samples are illustrated.

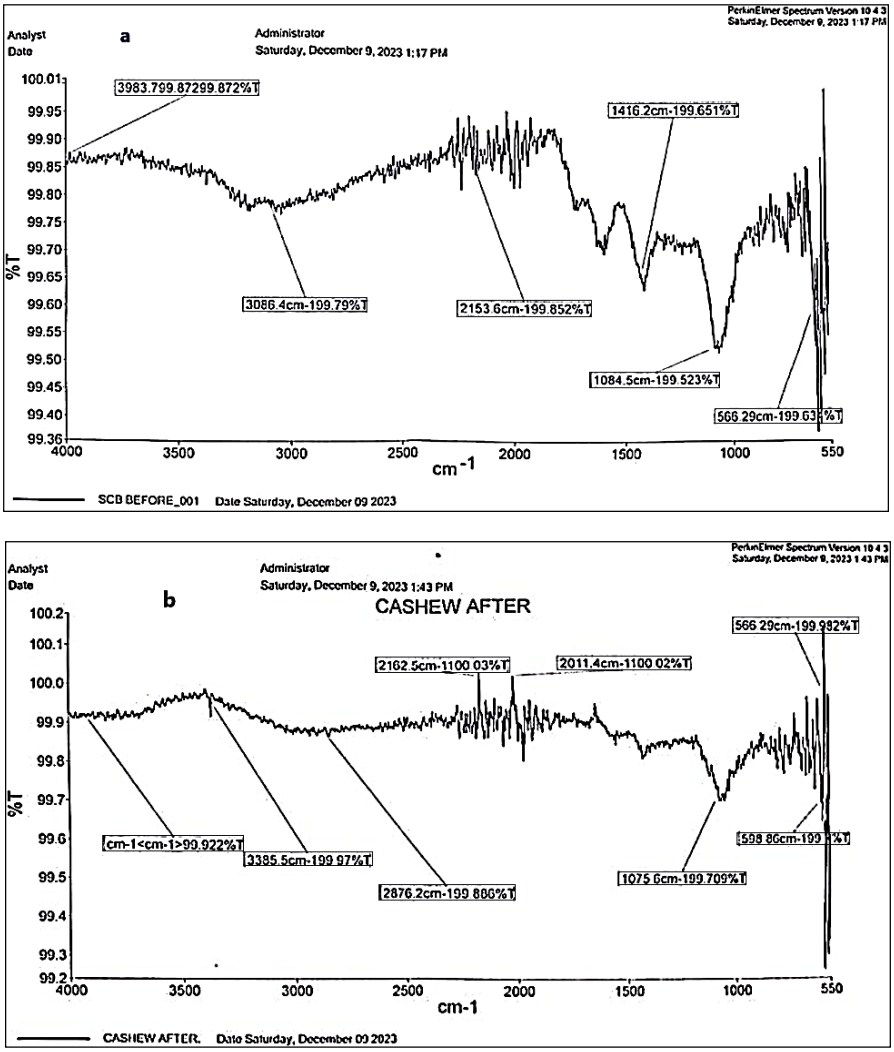

Fig. 2. FTIR Spectra of SCB-AC **(a)** Before and **(b)** After Treatment/Adsorption of Zn

In Figure 2a, a peak equivalent to: 3983.799 cm^{-1} could be indicative of O-H stretching vibrations, typically associated with alcohols or phenols [43]; 3086.4 cm^{-1} portrays C-H stretching vibrations often associated with alkanes or alkyl groups; 2153.6 cm^{-1} is quite high for typical functional groups and might be indicative of an instrument-related artifact or an unusual feature; 1416.2 cm^{-1} signifies a C-H bending vibrations usually observed in alkanes; 1084.5 cm^{-1} represents C-O stretching vibrations suggesting the presence of ether or an ester group and; 566.29 cm^{-1} before adsorption, stands for C-Br stretching vibrations, aligning with the presence of an alkyl bromide. Peaks for SCB-AC after adsorption are described as follows: 3809 cm^{-1} suggests the presence of O-H stretching vibrations often associated with alcohol or phenol functional groups; 3347 cm^{-1} indicates N-H stretching vibrations often found in amines or amides; 2532.6 cm^{-1} is a high wave number implying a possible interference or instrument-related artifact; 1596.8 cm^{-1} could be attributed to C=C stretching vibrations in an aromatic ring; 563.33 cm^{-1} is C-Cl stretching vibrations pointing towards the presence of an alkyl chloride and lastly; 886.12 cm^{-1} might be associated with C-H bending vibrations in an aromatic ring or alkane. Secondly, Figure 3 shows the FTIR peaks and wave numbers of the CNS-AC adsorbent showing the functional group before and after Zn adsorption.

Spectrum in Figure 3 presents the characteristic bands corresponding to cellulose besides lignin before Zn adsorption onto CNS-AC, which can be interpreted

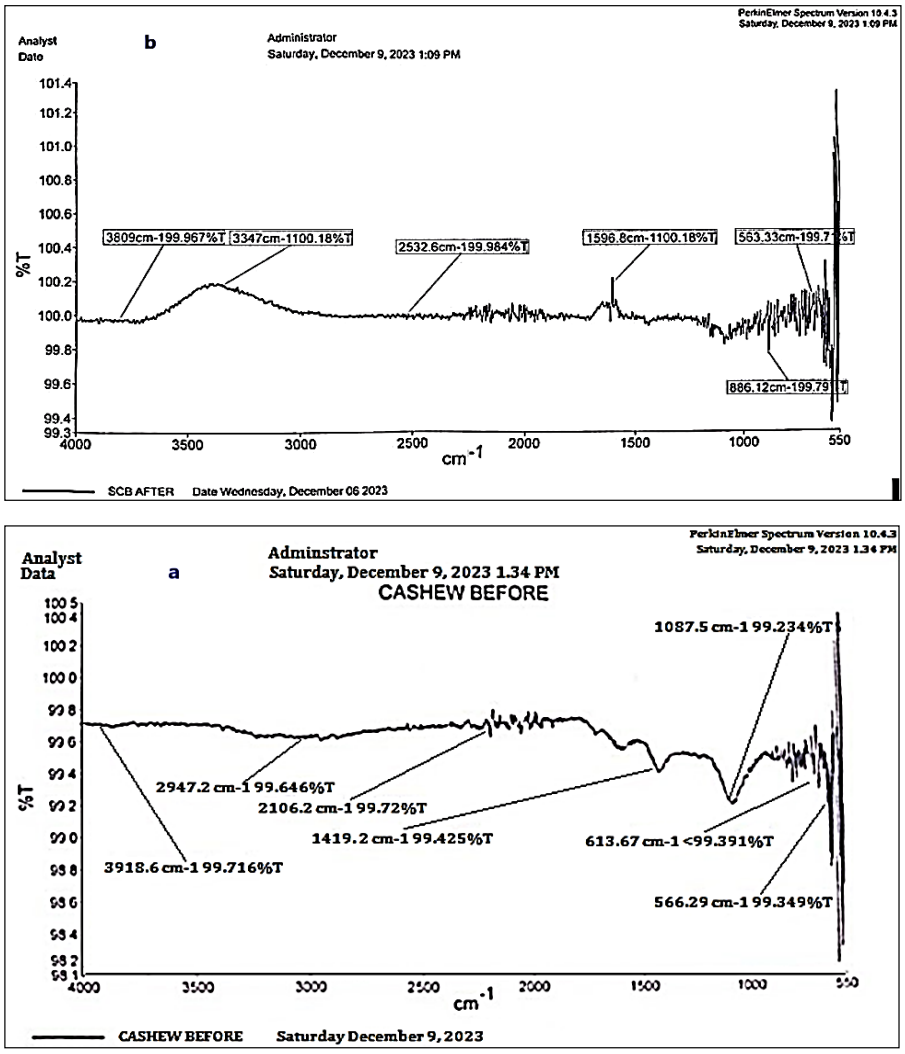

Fig. 3. FTIR Spectra of CNS-AC (a) Before and (b) After Treatment/Adsorption of Zn

as follows: 3918.6 cm^{-1} is a broad peak indicative of O-H stretching [44,45], typically associated with alcohol or phenol functional groups; 2947.2 cm^{-1} implied a C-H stretching vibrations often linked to alkanes or alkyl groups; 2106.2 cm^{-1} is a wavelength value that is unusually high for typical functional groups and might be an instrument-related artifact; 1419.2 cm^{-1} correspond to the C-H bending vibrations usually seen in alkanes; 1087.5 cm^{-1} stands for C-O stretching vibrations representing the presence of an ether or an ester group; 613.67 cm^{-1} points to C-Cl stretching vibrations linked to the presence of an alkyl chloride and; 566.29 cm^{-1} illustrates a C-Br stretching vibrations indicating the presence of an alkyl bromide. After adsorption, the peaks shown can be interpreted differently as follows: a peak at 3385.5 cm^{-1} in an FTIR spectrum typically corresponds to the stretching vibration of the O-H (hydroxyl) functional group; 2876.2 cm^{-1} C-H stretching (alkane or alkyl group); 2162.5 cm^{-1} C≡C triple bond stretching (alkyne), also reported in Amoo et al. (2022) 2011.4 cm^{-1} C≡N triple bond stretching (nitrile); 1075.6 cm^{-1} C-O stretching (alcohol or ether); 598.86 cm^{-1} C-Cl stretching (alkyl chloride) and; 566.29 cm^{-1} C-Br stretching (alkyl bromide).

3.2. SEM Microstructures and EDX Elemental Compositions

SEM-EDX analysis of CNS- and SCB-AC before and after Zn ion adsorption are represented in Figures 4 and 5, respectively.

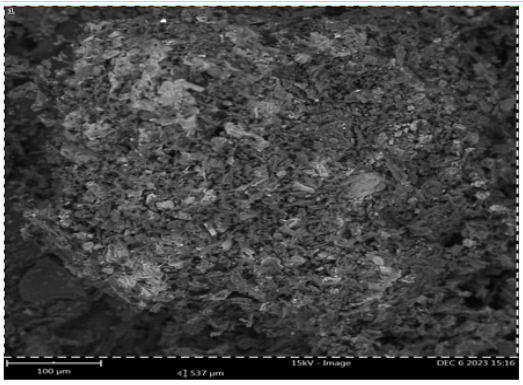

Element Number	Element Symbol	Element Name	Atomic Conc.	Weight Conc.
6	C	Carbon	75.22	69.16
7	N	Nitrogen	21.63	23.19
16	S	Sulfur	2.17	5.33
19	K	Potassium	0.21	0.62
13	Al	Aluminium	0.15	0.31
20	Ca	Calcium	0.09	0.28
12	Mg	Magnesium	0.15	0.27
14	Si	Silicon	0.12	0.26
15	P	Phosphorus	0.10	0.25
11	Na	Sodium	0.11	0.20
17	Cl	Chlorine	0.04	0.12
22	Ti	Titanium	0.00	0.00
26	Fe	Iron	0.00	0.00

a) FOV: 537 μm, Mode: 15kV-Image, Detector: BSD Full Time: DEC 6 2023 15:16

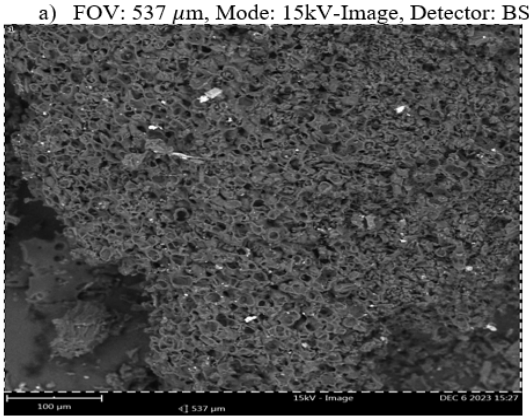

Element Number	Element Symbol	Element Name	Atomic Conc.	Weight Conc.
6	C	Carbon	90.94	88.19
7	N	Nitrogen	7.71	8.72
11	Na	Sodium	0.34	0.63
16	S	Sulfur	0.21	0.55
13	Al	Aluminium	0.18	0.40
14	Si	Silicon	0.17	0.39
12	Mg	Magnesium	0.17	0.34
15	P	Phosphorus	0.11	0.29
19	K	Potassium	0.06	0.19
20	Ca	Calcium	0.05	0.16
17	Cl	Chlorine	0.05	0.14
26	Fe	Iron	0.00	0.00
22	Ti	Titanium	0.00	0.00

b) FOV: 537 μm, Mode: 15kV-Image, Detector: BSD Full Time: DEC 6 2023 15:27

Fig. 4. SEM-EDX of CNS Adsorbent (**a**) Pre and (**b**) Post-adsorption of Metal

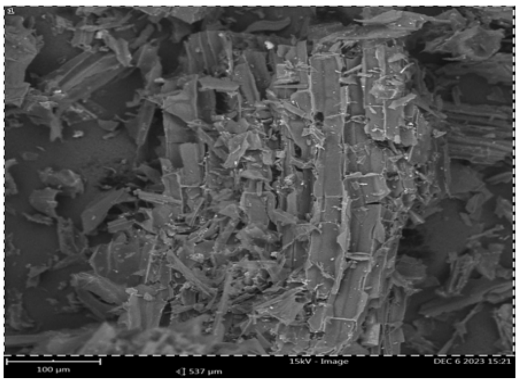

Element Number	Element Symbol	Element Name	Atomic Conc.	Weight Conc.
6	C	Carbon	82.45	77.53
7	N	Nitrogen	15.16	16.63
16	S	Sulfur	0.84	2.11
14	Si	Silicon	0.40	0.87
13	Al	Aluminium	0.32	0.67
26	Fe	Iron	0.11	0.50
17	Cl	Chlorine	0.15	0.43
11	Na	Sodium	0.20	0.35
15	P	Phosphorus	0.13	0.32
12	Mg	Magnesium	0.12	0.22
20	Ca	Calcium	0.06	0.19
19	K	Potassium	0.06	0.17
22	Ti	Titanium	0.00	0.00

a) FOV: 537 μm, Mode: 15kV-Image, Detector: BSD Full Time: DEC 6 2023 15:21

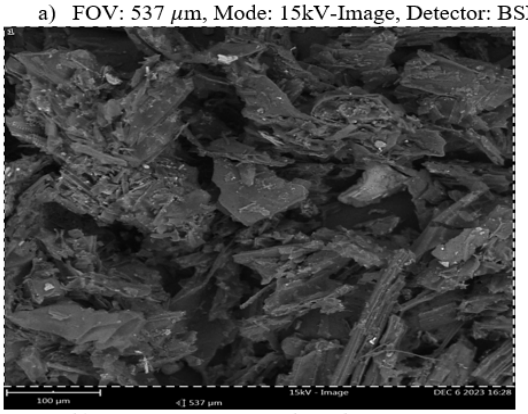

Element Number	Element Symbol	Element Name	Atomic Conc.	Weight Conc.
6	C	Carbon	80.84	75.37
7	N	Nitrogen	16.03	17.43
16	S	Sulfur	1.02	2.54
14	Si	Silicon	0.67	1.47
11	Na	Sodium	0.42	0.76
13	Al	Aluminium	0.36	0.74
17	Cl	Chlorine	0.16	0.44
15	P	Phosphorus	0.18	0.44
19	K	Potassium	0.13	0.38
12	Mg	Magnesium	0.12	0.23
20	Ca	Calcium	0.06	0.20
22	Ti	Titanium	0.00	0.00
26	Fe	Iron	0.00	0.00

b) FOV: 537 μm, Mode: 15kV-Image, Detector: BSD Full Time: DEC 6 2023 16:28

Fig. 5. SEM-EDX of SCB Adsorbent (**a**) Pre and (**b**) Post-adsorption of Metal

Superficial porous channels were observed in Figures 4a and 5a for CNS and SCB SEM images, respectively, with a spongy adsorbent surface. After adsorption, an irregular morphology was evidenced in Figures 4b and 5b. An alkaline activating agent could be the reason behind the fiber swelling and rupture, thereby favoring the appearance of pores. SEM photograph shows that the AC has a wide variety of pores [46,47] along with the fibrous structure. The shiny surface spotted in the SEM figures is due to the reaction of the impregnating agent (phosphoric acid). It is also observed that the particle sizes are irregular, containing a high surface area available for adsorption of the adsorbate. As a result of carbonization and activation, volatiles are removed, producing a fixed carbon mass with wide pore networks observed in AC samples. The presence of micro-pores contributed to the adsorption occurrence [10]. Alongside the images in Figures 4 and 5 is the metallic elemental composition present in the biomass AC samples before and after biosorption. EDX of CNS-AC reveals a reduction in K (0.62-0.19) and Ca (0.28-0.16 ppm) weight concentrations after adsorption with no evidence of the presence of Zn, as shown in Figure 4. However, only Fe was adsorbed by SCB-AC due to a reduction in its weight concentration from 0.5-0.00 mg L-1(ppm), as showcased in Figure 5, with no Zn detected. This is in consonance with Sawasdee & Watcharabundit's study, which collectively affirmed the possibility of removing Fe from wastewater using SCB and SCB-AC. The presence of Zn ion (after sorption, i.e.,Ce) can be ascertained using the AAS machine since the initial values were already specified for several runs by Desing Expert 7.0.0.

3.3. Design-Expert Analysis

3.3.1.Design Response Table

Responses in Tables 2 and 3 are computed using the Ce of Zn using Equations 1 and 2 for each run. The mean and standard deviations (SD) of the Ci used are 50 and 15.688 mg L^{-1}, and the contact time is 25 and 11.766 mins. The mean and standard division of R1 values for SCB-AC treatment computed is 95.16 and 1.898%, and R2 is 3.82 and 1.232 mg g^{-1}, with a ratio of 1.075 and 3.753, respectively. Mean and standard division of R1 values for CNS-AC treatment computed are 94.561 and 3.359%, and R2 is 3.819 and 1.284 mg g^{-1}, with a ratio of 1.132 and 4.079, respectively. In Table 2, the optimal values from the design matrix for the responses are 97.229% and 6.002 mg g^{-1} at 25min contact time for 5.0 g of adsorbent dosage.

Table 2. Experimental Data for Adsorption Capacity and RE of SCB-AC Adsorbent

Run	A: (mgL^{-1})	B: time (min)	(mgL^{-1})	R1:RE (%)	R2:qe(mg g^{-1})
1.	50	25	1.88	96.24	3.8496
2.	50	46.21	3.12	93.76	3.7504
3.	50	25	1.88	96.24	3.8496
4.	50	25	1.88	96.24	3.8496
5.	70	40	3.45	95.07	5.3240
6.	78.28	25	3.26	95.84	6.0016
7.	70	10	1.94	97.23	5.4448
8.	30	40	2.87	90.43	2.1704
9.	50	25	1.88	96.24	3.8496
10.	50	25	1.88	96.24	3.8496
11.	50	3.79	1.76	96.48	3.8592
12.	21.72	25	1.73	92.03	1.5992
13.	30	10	1.66	94.47	2.2672

Table 3. Experimental Data for Adsorption Capacity and RE of CNS-AC Adsorbent

Run	A: (mg L^{-1})	B: Time (min)	(mg L^{-1})	R1:RE (%)	R2: qe(mg g^{-1})
1.	50	25.0	2.15	95.7	3.828
2.	50	46.2	1.45	97.1	3.884
3.	50	25	2.15	95.7	3.828
4.	50	25	2.15	95.7	3.828
5.	70	40	1.89	97.3	5.449
6.	78.3	25	1.15	98.5	6.171
7.	70	10	2.99	95.7	5.361
8.	30	40	3.52	88.3	2.118
9.	50	25	2.15	95.7	3.828
10.	50	25	2.15	95.7	3.828
11.	50	3.8	2.15	95.7	3.828
12.	21.7	25	2.81	87.1	1.513
13.	30	10	2.67	91.1	2.186

3.3.2.ANOVA for Suggested Model

For R1-SCB-AC data, the model F-value of 48.98 implies that the model is significant. There is only a 0.01% chance that a "model F-value" this large could occur due to noise. Values of "Prob > F" less than 0.05 indicate that model terms are significant [48]. In this case, B, A^2 & B^2 are significant model terms. Values > 0.1000 indicate that the model terms are not significant [43]. If there are many insignificant model terms (not counting those required to support hierarchy), model reduction may improve the model. For R2-SCB-AC data, the model F-value of 14778.32 implies that the model is significant. There is only a 0.01% chance that a "Model F-value" this large could occur due to noise. Values of "Prob > F" < 0.0500 also indicate significant model terms [34]. Also, A, B, $A^{2,}$ and B^2 are significant model terms. The foregone explanation of the R1 & R2 SCB analysis of variance (ANOVA) in Table 4 was given by the Design Expert's 7.0.0 description. Ideally, Factors A and B and Response R1 and R2 were entered for the RSM, and different numerical models, including 2FI, linear, quadratic, and cubic models, were analyzed electronically for best fit. Hence, ANOVA for the suggested best model fit (i.e., quadratic in this study) is shown in Table 4.

Model F-value of 29.59 for R1-CNS-AC data implies that the model is significant, where there is only a 0.01% chance that a "model F-value" this large could occur due to noise. [49,50]. In addition, values of "Prob > F" < 0.0500 signify a significant model term. Hence, A^2 is a considerable model term. The Design Expert tool explains that values > 0.1000 correspond with insignificant model terms. If many insignificant model terms exist except those supporting hierarchies, model reduction may improve the R1 model equation generated. The same applies to the R2-CNS-AC data in Table 4, where 'A' is a significant model term. The quadratic models discussed are given by Equations 3-6.

$$RE_{SCB} = \begin{matrix} 87.01978 + 0.34315A - 0.02472B + 0.00156349AB \\ -0.00302385A^2 - 0.00274211B^2 \end{matrix} \quad \text{(Eq.3)}$$

$$q_{eSCB} = \begin{matrix} -0.24067 + 0.085202A + 0.00293825B - 2 \times 10^{-5}AB \\ -6.2135 \times 10^{-5}A^2 - 1.00682 \times 10^{-4}B^2 \end{matrix} \quad \text{(Eq.4)}$$

$$RE_{CNS} = \begin{matrix} 79.31225 + 0.55177A - 0.17201B + 0.00367063AB \\ -0.00456767\ A^2 - 1.10703 \times 10^{-4}B^2 \end{matrix} \quad \text{(Eq.5)}$$

$$q_{eCNS} = -0.29291 + 0.081829A + 8.26658 \times 10^{-4}B \quad \text{(Eq.6)}$$

Table 4. ANOVA for Response Surface Quadratic Model of SCB and CNS Data

SCB

Source	Sum of Squares		df		Mean Square		F value		p-value (Prob > F)	
	R1	R2	R1	R2	R1	R2	R1	R2	R1	R2
Model	45.54	19.73	5	5	9.11	3.95	48.98	14778.3	< 0.0001*	< 0.0001*
A-	0.11	5.24	1	1	0.11	5.24	0.57	19602.0	0.4763	< 0.0001
B-Time	3.07	0.00977	1	1	3.07	0.00977	16.51	36.57	0.0048	0.0005
AB	0.88	0.00014	1	1	0.88	0.00014	4.73	0.54	0.0661	0.4866
A^2	10.17	0.00430	1	1	10.17	0.00430	54.71	16.08	0.0001	0.0051
B^2	2.65	0.00357	1	1	2.65	0.00357	14.23	13.36	0.007	0.0081
Residual	1.3	0.00187	7	7	0.19	0.00026				
Lack of Fit	1.3	0.00187	3	3	0.43	0.00062				
Pure Error	0.0	0.000	4	4	0	0				
Cor Total	46.84	19.74	12	12						

CNS

Source	Sum of Squares		df		Mean Square		F value		p-value (Prob > F)	
	R1	R2	R1	R2	R1	R2	R1	R2	R1	R2
Model	140.05	21.43	5	2	28.0	10.71	29.59	5926.22	0.0001*	< 0.0001*
A-	2.21	21.42	1	1	2.21	21.42	2.33	11851.7	0.1707	< 0.0001
B-Time	3.16	0.00123	1	1	3.16	0.00123	3.33	0.68	0.1106	0.4287
AB	4.85		1		4.85		5.12		0.058	
A^2	23.21		1		23.2		24.52		0.0017	
B^2	0.00431.0		1		0.00431		0.00456		0.9481	
Residual	6.63	0.018	7	10	0.95	0.00181				
Lack of Fit	6.63	0.018	3	6	2.21	0.00301				
Pure Error	0.0	0.00	4	4	0.00	0.00				
Cor Total	146.68	21.44	12	12						

* *implied 'significant'*

Only Model Equation 6 is linear. Ogundeji & Jimoh (2021) obtained a 4-factor quadratic model for RE_{SCB} Comprising of time, pH, temperature, and dosage. Predicted R^2 of 0.8024 for RE_{SCB} (Table 5) is in reasonable agreement with its adjusted R^2 of 0.9524. A ratio > 4 (19.469) is desirable for adequate precision in measuring the signal-to-noise ratio. Because of this adequate signal, Model Equation 3 can be used to navigate the design space.

The same faith is observed for RE_{SCB} with larger sets of R^2 values, demonstrating a better fit by model Equation 4. Not as expected, predicted R^2 of 0.6788 for RE_{SCB} is not as close to the adj. R^2 = 0.9226, portraying a significant block effect or possible model issues and data. Things to consider are model reduction, response transformation, outliers, etc. Adeq. precision that measures the signal-to-noise ratio is > 4 (i.e., 18.168) and desirable, implying an adequate signal [36]. Model Equation 5 can thus be used to navigate the design space. There is, however, a reasonable agreement between the predicted R^2 = 0.9982 and the adj. R^2 = 0.9990 for qe CNS. A desirable signal-to-noise ratio (Adeq Prec = 226.605 > 4) was achieved, showing that Model Equation 6 can navigate the design space due to the adequate signal it portrays.

Table 5. Statistics results of SCB-AC and CNS-AC models

Parameter	SCB-AC		CNS-AC	
	R1	R2	R1	R2
Std. Dev.	0.43	0.016	0.97	0.043
Mean	95.12	3.82	94.56	3.82
C.V. %	0.45	0.43	1.03	1.11
PRESS*	9.26	0.013	47.12	0.04
R^2	0.9722	0.9999	0.9548	0.9992
Adj. R^2	0.9524	0.9998	0.9226	0.999
Pred. R^2	0.8024	0.9993	0.6788	0.9982
Adeq Prec.	19.469	399.846	18.168	226.605

* PRESS: Predicted Residual Sum of Squares

SD mean and coefficient of variation (C.V.%) are measures of the model's precision and accuracy. The PRESS (Predicted Residual Sum of Squares) measures the model's predictive ability. For the R1 and R2 responses of SCB-AC and CNS-AC, the mean values are close to 95% and 3.8 mg g^{-1}, respectively, indicating that the models can predict the response values accurately. Also observed are low SD values, indicating that the data points are close to the mean and the model is precise; low CV(%) values, indicating that the precision of the model is high; low PRESS values for the RSM models, indicating that the models have good predictive ability; high R^2 values for the models, indicating that the models fit the data well and; high adjusted R^2 values [49-52], indicating that the models do not overfit the data. As such, the fit statistics in Table 5 suggest that the RSM models developed for the SCB-AC and CNS-AC data are accurate, precise, and have good predictive ability.

3.3.3.3D Optimal Depictions and Extent of Fit

Figures 6 and 7 provide a comprehensive visual representation of the statistical analysis and optimization of Zn sorption using SCB-AC and CNS-AC adsorbents, respectively. These provide valuable insights for efficient metal removal processes in water treatment applications.

In the 3D surface plot of Figures 6a and 7a, an upward curve indicates an increase in the response variable as the independent variables increase. In this context, the Zn sorption efficiency and capacity (R1 and R2) increase as factors A and B. Respectively, the optimal combination is 39.656 mg L^{-1}, 27.12 min, and 96.4375% RE for SCB and 60.175 mg L^{-1}, 24.9 min, and 99.35% RE for CNS. Figures 6d and 7d show that as the contact time and Ci both increases, the Zn sorption RE and qe also increases, which means there is a positive relationship between these variables. In addition, the highest Zn RE and qe is achieved at the highest values of both factors, A and B. Thus, the optimal combination occurs at constant time, 71.038 mg L^{-1} and 6.1 mg g^{-1} for SCB, and constant time, 72.245 mg L^{-1} and 6.199 mg g^{-1} for CNS. Figure 6b and 7b contour lines are closely spaced, demonstrating a steep gradient and a strong relationship between the independent variables and the response variable. It also shows that the highest Zn sorption performance is achieved at the highest values of both factors A and B using SCB and CNS-AC. In Figures 6e and 7e, the contour plots show that the highest Zn RE and qe is achieved at intermediate values of both factors A and B. The contour lines are more widely spaced, indicating a weaker relationship between the independent and response variables. Predicted vs. observed RE plot (Figures 6c and 7c) for SCB and CNS outcomes did not fit as perfectly as that in qe relationship (Figure 6f and 7f). Similar REs fit with those in Figures 6c and 7c were obtained by Salihi et al. (2016) using SCB ash to adsorb Zn. Predictions by the four modeled equations are satisfactory, only that those of qe are nearly 100% accurate and precise.

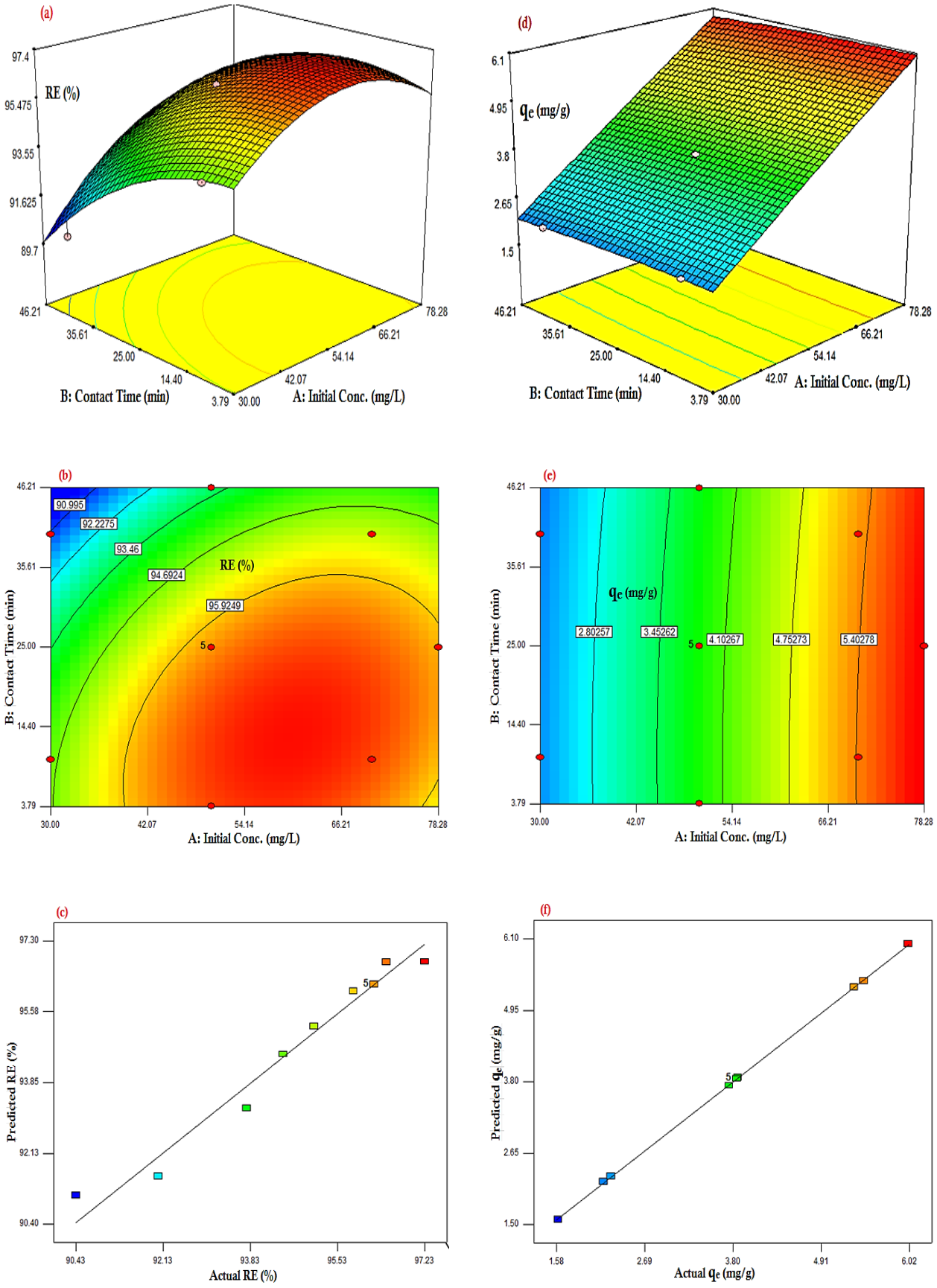

Fig. 6. SCB-AC Zn sorption 3D surface, contour, and correlated responses plots

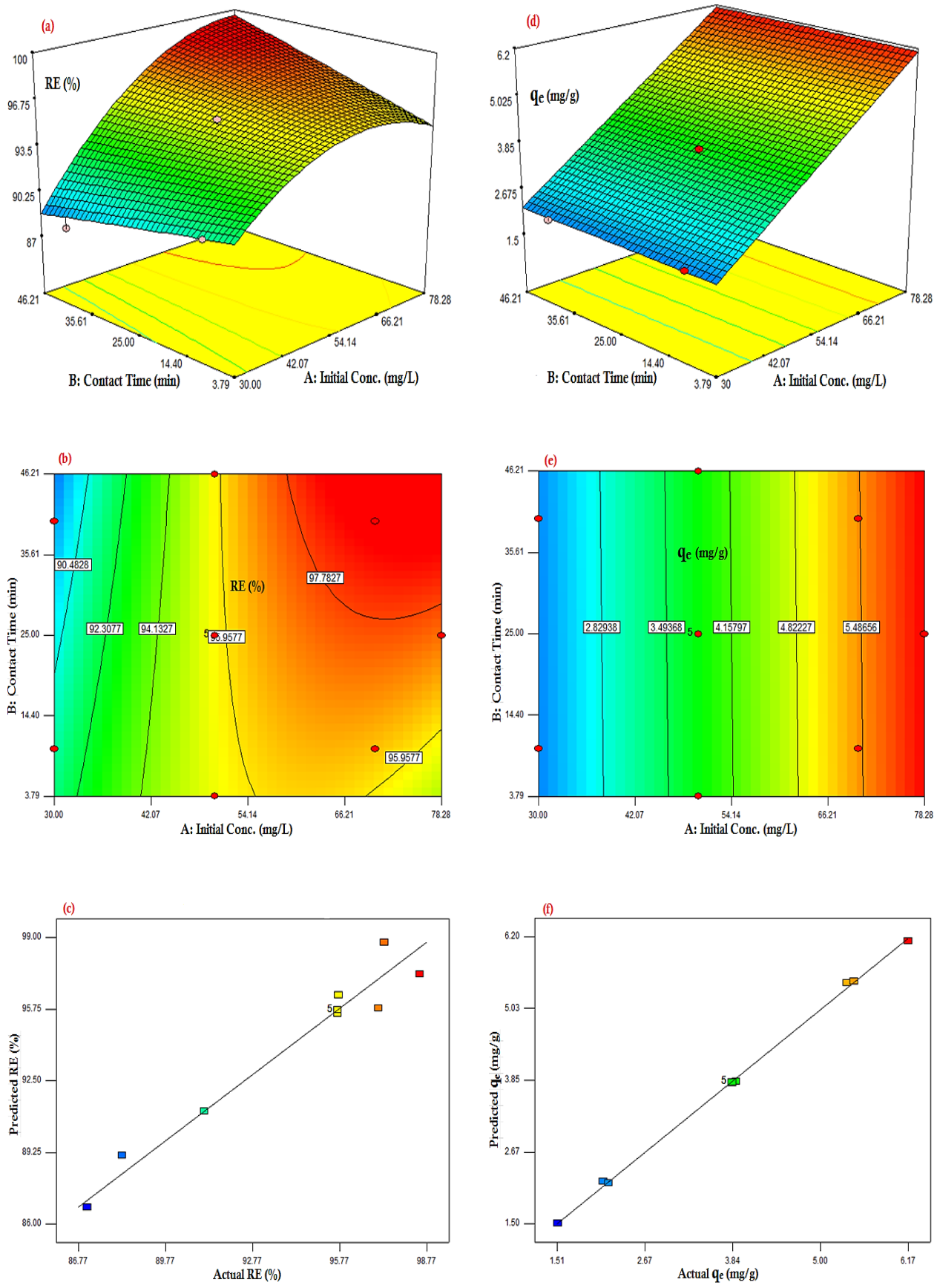

Fig. 7. CNS-AC Zn sorption 3D surface, contour, and correlated responses plots

3.4. Maximum Adsorption Condition

Table 6 provides the optimal conditions for Zn sorption for both SCB-AC and CNS-AC adsorbents under different scenarios: rapid and slow adsorption. Rapid means a shorter contact time, while slow means a longer one. Rapid adsorption may be desirable if efficiency is not compromised and cost-effectiveness and practicality are significant concerns. So, at the recovery of SCB-AC (95.85%) and CNS-AC (94.88%) for Zn sorption, a contact time set at 5 min is desirable given that large amounts of Zn (77.61 and 79.64 mg L^{-1}) are sorbed at optimal qe of 6.002 and 6.228 mg g^{-1}, respectively. During Zn sorption RSM optimization using SCB where time, dosage, and Ci were varied, Salihi et al. (2016) obtained 55.99%, proving a less efficient process than the one obtained herein. Adamu et al. (2021) surpassed the optimal RE in this study by getting a 100% RE at 5.9895 mg g^{-1} during the SCB-AC Pb removal study. Long contact times (slow adsorption) may be preferable if higher REs are needed, and cost-effectiveness and practicality allow for the extended process duration. This is valid at the given REs for both sorbents in Table 6, with higher qe compared to the rapid sorption situation. Considering both the removal and qe along with the desirability values, CNS is the superior adsorbent for removing Zn in both rapid and slow adsorption conditions, as it consistently demonstrates higher qe desirability values. CNS benefits from longer contact times, showing significantly higher performance and desirability than SCB, especially under slow adsorption conditions. Therefore, an adsorbent dosage of 5.0 g can adsorb approximately 99 mg L^{-1} of Zn from water. It is considered highly effective if an adsorbent maintains high adsorption efficiency across a range of initial Zn concentrations, as does SCB and CNS-AC. When Hasar et al. increased Zn concentration to 200 mg L^{-1}, a significant reduction in the RE was witnessed.

4. Conclusions

Following laboratory-designed steps, AC was produced from SCB and CNS and used as an adsorbent to eliminate Zn from synthetic water. Changes in peaks recorded after FTIR for both SCB or CNS-ACS and their morphology confirm that the adsorbents have porous regions and active sites for Zn sorption. Characterizing the ACs by running an AAS analysis presents a further reduction in the concentration of Zn below the specified initial values added to the water sample. The CCD optimization RSM type chosen provided experimental runs to quantify qe and RE at different contact times and Zn Ci . These Ci amounts are way above 5.0 mg L^{-1} permissible Zn concentration in water, and the fact that optimization carried out shows that 77.61-98.74 mg L^{-1} optimal value can be removed (at 94.79-98.51% RE) under slow or rapid adsorption hinted to the efficiency of the two analyzed adsorbents for Zn removal. Juxtaposing the adsorbent performance, it was found that CNS-AC is more efficient at removing the ions from synthetic water than SCB-AC. At higher RE, CNS-AC achieved 7.8279 mg g^{-1} adsorption capacity at 99.5% desirability with fitted quadratic model prediction (R^2 = 0.9992). Still, qe and RE obtained for SCB-AC are best compared to the RSM findings in the literature. Both ACs are favorable biosorbents for Zn metal. It is recommended that the spent adsorbent be regenerated to maintain a continuous bioremediation process. Optimization shouldn't be restricted to two factors only.

Table 6. Optimal Conditions for Zn sorption for both SCB-AC and CNS-AC adsorbents

Cases:	Optimal Conditions				
	A (mgL^{-1})	B (min)	R1 (%)	R2 (mg g^{-1})	Desirability
			SCB		
Rapid Adsorption	77.61	5	95.8529%	6.00163	0.816
Slow Adsorption	80.97	38.94	94.7885	6.1494	0.776
			CNS		
Rapid Adsorption	79.64	5	94.8826	6.2284	0.785
Slow Adsorption	98.74	50	98.5058	7.82794	0.995

5. References

[1] P. S. Kumar, A. Saravanan, K. A. Kumar, R. Yashwanth, S. Visvesh, Removal of toxic zinc from water/wastewater using eucalyptus seeds activated carbon: non-linear regression analysis, IET Nanobiotechnol., 10 (2016) 244–253. https:// doi.org/ 10.1049 / iet-nbt. 2015.0087

[2] R. R. Karri, J. N. Sahu, Modeling and optimization by particle swarm embedded neural network for adsorption of zinc (II) by palm kernel shell based activated carbon from aqueous environment, J. Environ. Manage., 206 (2017) 178–191. https://doi.org/10.1016/j.jenvman.2017.10.026

[3] S. Tuomikoski, Zinc adsorption by activated carbon prepared from lignocellulosic waste biomass, Appl. Sci., 9 (2019) 1–15. https://doi.org/10.3390/app9214583

[4] Y. X. Gan, Activated carbon from biomass sustainable sources, C–J. Carbon Res., 7 (2021) 1–33. https://doi.org/10.3390/c7020039

[5] M. A. Suryawanshi, A. Bandgar, C. Mhaske, S. Shetty, Production of activated carbon from various natural resources and its application, J. Emerg. Technol. Innov. Res., 7 (2020) 560–565.http://www.jetir.org/papers/JETIR2009075.pdf

[6] J. K. Ratan, M. Kaur, B. Adiraju, Synthesis of activated carbon from agricultural waste using a simple method: Characterization, parametric and isotherms study, Mater. Proc., 5 (2018) 3334–3345. https://doi.org/10.1016/j.matpr.2017.11.576

[7] Y. Luka, B. K. Highina, A. Zubairu, The promising precursors for development of activated carbon: Agricultural waste materials-A review, Int. J. Adv. Sci. Res. Eng., 4 (2018) 45–59. https://doi.org/10.7324/IJASRE.2018.32615

[8] A. Bhatnagar, M. Sillanpää, A. Witek-Krowiak, Agricultural waste peels as versatile biomass for water purification–A review, Chem. Eng. J., 270 (2015) 244–271. https://doi.org/10.1016/j.cej.2015.01.135

[9] S. R. Binti Jamaludin, A production of activated carbon using local agricultural waste for groundwater treatment in Universiti Malaysia Pahang, Bachelor of civil engineering degree thesis, Faculty of Civil Engineering and Earth Resources, University Malaysia Pahang, 2010. https://webopac.kmlink.com.my/neuaxis-e/Record/ump-2548

[10] M. A. M. Razi, A. Al-Gheethi, Removal of heavy metals from textile wastewater using sugarcane bagasse activated carbon, Int. J. Eng. Technol., 7 (2018) 112–115. https://doi.org/10.14419/ijet.v7i4.30.22066

[11] S. M. Kakom, N. M. Abdelmonem, I. M. Ismail, A. A. Refaat, Activated carbon from sugarcane bagasse pyrolysis for heavy metals adsorption, Sugar Tech., 25 (2023) 619–629. https://doi.org/10.1007/s12355-022-01214-3

[12] K. B. Cuillaume, N. S. Serpokrylov, A. S. Smolyanichenko, E. G. Cheblakova, V. A. Gorina, Preparation of activated carbon from cashew nut shells for water purification, Russ. J. Non-ferrous Metals, 61 (2020) 112–118. https://doi.org/10.3103/S1067821220010058

[13] G. Kalaba, J. Nyirenda, O. Munyati, Characterisation of activated carbons for removal of organic and heavy metal pollutants from water in resource limited countries, Desalin. Water Treat., 261 (2022) 224–233. https://doi.org/10.5004/dwt.2022.28531

[14] H. Bakker, Sugar cane cultivation and management, Springer Publisher,1999. https://doi.org/10.1007/978-1-4615-4725-9

[15] J.W. Wayagari, G.B. Ayoola, E.D. Imolehin, Economic evaluation of chewing sugarcane production in the central zone of Nigeria. Sugar Tech., 5 (2003)81–84. https://doi.org/10.1007/BF02943771

[16] I. Hamawand, W. P. Da Silva, S. Seneweera, J. Bundschuh, Value proposition of different methods for utilisation of sugarcane wastes, Energies, 14 (2021) 1–30. https://doi.org/10.3390/en14175483

[17] A. C. Wada, A. Abo-Elwafa, M. T. Salaudeen,

L. Y. Bello, E. H. Kwon-Ndung, Sugar cane production problems in Nigeria and some Northern African countries, Direct Res. J. Agric. Food Sci., 5 (2017) 141–160. http://directresearchpublisher.org/aboutjournal/drjafs

[18] G. Odogun, Kogi, largest producer of cashew in Nigeria-Commissioner, Punch, 2023. https://punchng.com/kogi-to-become-cashew-production-hub-government/

[19] The United States Agency for International Development (USAID), subsector assessment of the Nigerian cashew industry, Washington DC, 2002. https://pdf.usaid.gov/pdf_docs/PNACY675.pdf

[20] O. O. Adeigbe, F. O. Olasupo, B. D. Adewale, A. A. Muyiwa, A review on cashew research and production in Nigeria in the last four decades, Sci. Res. Essays, 10 (2015) 196–209. https://doi.org/10.5897/SRE2014.5953

[21] J. Rakhtshah, H. Shirkhanloo, M. D. Mobarake, Simultaneously speciation and determination of manganese (II) and (VII) ions in water, food, and vegetable samples based on immobilization of N-acetylcysteine on multi-walled carbon nanotubes, Food Chem., 389 (2022) 133124. https://doi.org/10.1016/j.foodchem.2022.133124

[22] Z. Karamzadeh, J. Rakhtshah, N. M. Kazemi, A novel biostructure sorbent based on CysSB/MetSB@MWCNTs for separation of nickel and cobalt in biological samples by ultrasound assisted-dispersive ionic liquid-suspension solid phase micro extraction, J. Pharm. Biomed. Anal., 172 (2019) 285–294. https://doi.org/10.1016/j.jpba.2019.05.003

[23] N. Esmaeili, J. Rakhtshah, E. Kolvari, A. Rashidi, Rapid speciation of lead in human blood and urine samples based on MWCNTs@DMP by dispersive ionic liquid-suspension-micro-solid phase extraction, Biol. Trace Elem. Res., 199 (2021) 1–12. https://doi.org/10.1007/s12011-020-02382-7

[24] K. Merchant, M. D. Mobarake, Ultrasound-assisted solid-liquid trap phase extraction based on functionalized multi wall carbon nanotubes for preconcentration and separation of nickel in petrochemical waste water, J. Anal. Chem., 9 (2019) 865–876. https://doi.org/10.1134/s1061934819090090

[25] F. Golbabaei, A. Vahid, A. Faghihi-Zarandi, A novel nano-palladium embedded on the mesoporous silica nanoparticles for mercury vapor removal from air by the gas field separation consolidation process, Appl. Nanosci., 12 (2022) 1667–1682. https://doi.org/10.1007/s13204-022-02366-0

[26] F. Golbabaei, H. Hassani, F. Eftekhar, M. J. Kian, Occupational exposure to mercury: Air exposure assessment and biological monitoring based on dispersive ionic liquid-liquid microextraction, Iran. J. Public Health, 43 (2014) 793–799. https://www.ncbi.nlm.nih.gov/pmc/articles/PMC4475598/

[27] F. Golbabaei, A. Ebrahimi, A. Koohpaei, A. Faghihi-Zarandi, Single-walled carbon nanotubes (SWCNTs), as a novel sorbent for determination of mercury in air, Glob. J. Health Sci., 8 (2015) 273–280. https://doi.org/10.5539/gjhs.v8n7p273

[28] F. Golbabaei, A. Ebrahimi, H. Shirkhanloo, M. R. Baneshi, A. Faghihi-Zarandi, M. J. Kian, Performance comparison survey of multi-walled and single-walled carbon nanotubes for adsorption and desorption of mercury vapors in the air, Iran. Occup. Health J., 10 (2013) 21–31. https://espace.library.uq.edu.au/view/UQ:9d03f02

[29] L. Lupa, L. Cocheci, Heavy metals removal from water and wastewater, heavy metals – recent advances, InTech Open, pp. 1–29, 2023. https://doi.org/10.5772/intechopen.110228

[30] N. A. A. Qasem, R. H. Mohammed, D. U. Lawal, Removal of heavy metal ions from wastewater: A comprehensive and critical review, NPJ Clean Water, 4 (2021) 1–15. https://doi.org/10.1038/s41545-021-00127-0

[31] B. Von Klock, R. S. Patel, Method for removal of heavy metals from water, US006153108A, 2000. https://patents. google.com/ patent/US6153108A/ en

[32] G. Ravindran, M. R. Madhavi, B. S. Abusahmin, Optimization of zinc(II) adsorption using agricultural waste, Int. J. Eng. Technol., 7 (2018) 300–304. https://doi.org/10.14419/ijet.v7i3.34.19212

[33] N. M. Mubarak, Statistical optimization of zinc removal using activated carbon and magnetic biochar, Adv. Environ. Biol., 8 (2014) 686–691. http://www.aensiweb.com/aeb.html

[34] U. K. Garg, H. K. Garg, Optimization of process parameters for metal ion remediation using agricultural waste materials, Int. J. Theor. Appl. Sci., 8 (2016) 17–24. https://www.researchtrend.net/ijtas/pdf/

[35] T. Van Tran, Q. T. P. Bui, T. D. Nguyen, V. T. T. Ho, L. G. Bach, Application of response surface methodology to optimize the fabrication of ZnCl2-activated carbon from sugarcane bagasse for the removal of Cu_2, Water Sci. Technol., 75 (2017) 2047–2055. https://doi.org/10.2166/wst.2017.066

[36] S. M. Beyan, S. V. Prabhu, T. T. Sissay, A. A. Getahun, Sugarcane bagasse based activated carbon preparation and its adsorption efficacy on removal of BOD and COD from textile effluents: RSM based modeling, optimization and kinetic aspects, Bioresour. Technol. Reports, 14 (2021) 1–9. https://doi.org/10.1016/j.biteb.2021.100664

[37] P. S. Kumar, S. Ramalingam, R. V Abhinaya, S. D. Kirupha, T. Vidhyadevi, S. Sivanesan, Adsorption equilibrium, thermodynamics, kinetics, mechanism and process design of zinc (II) ions onto cashew nut shell, Can. J. Chem. Eng., 90 (2012) 973–982. https://doi.org/10.1002/cjce.20588

[38] N. M. Suntharam, Removal of zinc (II) ions from industrial wastewater by activated carbon synthesized from mangrove (Rhizophora mangle), Degree of Bachelor of Chemical Engineering, Universiti Sains Malaysia, 2022. https://eprints.usm.my/55589/

[39] G. Farid, J. Carlos Moreno-Piraján, Cashew nut shell biomass: A source for high-performance CO_2/CH_4 adsorption in activated carbon J. CO_2 Util., 83 (2024) 102799. https://doi.org/10.1016/j.jcou.2024.102799

[40] M. Rezaee. P. Tajer-Mohammad-Ghazvini, Rapid and efficient determination of zinc in water samples by graphite furnace atomic absorption spectrometry after homogeneous liquid-liquid microextraction via flotation assistance, Bull. Chem. Soc. Ethiop., 36 (2022) 1–11. https://doi.org/10.4314/bcse.v36i1.1

[41] M. Khaleghi Abbasabadi, Speciation of cadmium in human blood samples based on Fe_3O_4-supported naphthalene-1-thiol-functionalized graphene oxide nanocomposite by ultrasound-assisted dispersive magnetic micro solid phase extraction, J. Pharm. Biomed. Anal.,189 (2020) 113455. https://doi.org/10.1016/j.jpba.2020.113455

[42] B. A. Ezeonuegbu, Agricultural waste of sugarcane bagasse as efficient adsorbent for lead and nickel removal from untreated wastewater: Biosorption, equilibrium isotherms, kinetics and desorption studies, Biotechnol. Reports, 30 (2021) e00614. https://doi.org/10.1016/j.btre.2021.e00614

[43] O. J. Ogundeji, A. Jimoh, Characterization of sugarcane bagasses as a potential treatment of heavy metal effulents by the response surface methodology, Int. J. Pure Appl. Sci., 20 (2021) 1–24. https://www.cambridgenigeriapub.com/wp-content/uploads/2021/06/CJPAS_Vol20_No9_March_2021-1.pdf.

[44] M. B. Genet, A. L. Jembere, G. A. Tafete, Economical adsorbent developed from sugarcane bagasse for zinc (II) removal from wastewater, Water Air Soil Pollut., 233 (2022) 295. https://doi.org/ 10.1007/ s11270-022-05770-y

[45] T. E. Amoo, K. O. Amoo, O. A. Adeeyo, C. O. Ogidi, Kinetics and equilibrium studies of the adsorption of copper(II) ions from industrial wastewater using activated carbons derived from sugarcane bagasse, Int. J. Chem. Eng., 2022 (2022) 6928568. https://doi.org/10.1155/2022/6928568

[46] W. Somyanonthanakun, A. Greszta, A. J.

Roberts, S. Thongmee, Sugarcane bagasse-derived activated carbon as a potential material for lead ions removal from aqueous solution and supercapacitor energy storage application, Sustainability, 15 (2023) 5566. https://doi.org/10.3390/su15065566

[47] S. Sawasdee, P. Watcharabundit, Adsorption of Fe(II) solution by sugarcane bagasse and activated carbon prepared from sugarcane bagasse, Chian. Mai Uni. J. Nat. Sci, Food Appl. Biosci. Innov. Technol., 18 (2019) 190–213. https://doi.org/10.12982/CMUJNS.2019.0015

[48] M. Mutah, K. Akira, A. M. Zaiton, J. Jafariah, S. M. Razman, I. N. Eman, Production of sugarcane bagasse based activated carbon for Cd_{2+} removal using factorial design, Int. J. Innov. Technol. Explor. Eng., 2 (2013) 121–125. https://www.ijitee.org/wp-content/uploads/papers/v2i4/D0541032413.pdf

[49] H. Z. Mousavi, Chromium speciation in human blood samples based on acetyl cysteine by dispersive liquid–liquid biomicroextraction and in-vitro evaluation of acetyl cysteine/cysteine for decreasing of hexavalent chromium concentration, J. Pharm. Biomed. Anal., 118 (2016) 1-8. https://doi.org/10.1016/j.jpba.2015.10.018

[50] I. U. Salihi, S. R. M. Kutty, M. H. Isa, N. Aminu, Process optimization of zinc removal using microwave incinerated sugarcane bagasse ash (MISCBA) through response surface methodology, Res. J. Appl. Sci. Eng. Technol., 12 (2016) 395–401. https://doi.org/10.19026/rjaset.12.2378

[51] A. D. Adamu, U. A. Abubakar, B. S. Sani, A. Umar, Modelling and optimization of lead adsorption onto sugarcane bagasse activated carbon, Niger. Res. J. Eng. Environ. Sci., 6 (2021) 520–529. http://doi.org/10.5281/zenodo.5805110

[52] H. Hasar, Y. Cuci, E. Obek, M. F. Dilekoglu, Removal of zinc(II) by activated carbon prepared from almond husks under different conditions, Adsorpt. Sci. Technol., 21 (2003) 799–808. https://doi.org/10.1260/026361703607440

Anal. Methods Environ. Chem. J. 7 (4) (2024) 96-111

AMECJ

Research Article, Issue 4
Analytical Methods in Environmental Chemistry Journal
Journal home page: www.amecj.com/ir

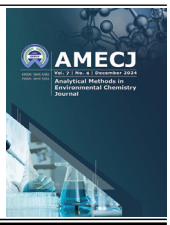

Simultaneous hybrid liquid-liquid extraction of PAHs, OCPs, and PCBs from seawater before determination by gas chromatography-mass spectrometry

Davoud Jahedi Vaighan[a], Ali Mehdinia [a,*], Abolfazl Saleh[a], Somaye Abedi[a] , and Neda Sheijooni Fumani[a]
[a] *Iranian National Institute for Oceanography and Atmospheric Science, P.O. Box: 1411554781, Tehran, Iran*

ARTICLE INFO:
Received 4 Aug 2024
Revised form 16 Oct 2024
Accepted 14 Nov 2024
Available online 30 Dec 2024

Keywords:
Hybrid liquid-liquid extraction,
Gas chromatography-mass spectrometry,
Organochlorine pesticides,
Polycyclic aromatic hydrocarbons,
polychlorinated biphenyls,
Seawater

ABSTRACT
A simple hybrid liquid-liquid extraction (HLLE) has been developed to preconcentrate some persistent organic pollutants (POPs) such as organochlorine pesticides (OCPs), polycyclic aromatic hydrocarbons (PAHs), and polychlorinated biphenyls (PCBs) from water samples before analysis by gas chromatography-mass spectrometry (GC–MS). The studied variables were extraction solvent type and volume and replication of extraction steps. The optimum experimental conditions of the HLLE method were 15 mL dichloromethane with two replicates as the first extraction solvent and 10 mL n-hexane with two replicates as the second extraction solvent. Under optimum conditions, the calculated calibration curves gave high-level linearity for all target analytes with average correlation coefficients higher than 0.996 for ΣOCPs, 0.998 for ΣPAHs, and 0.999 for ΣPCBs. The average amount of relative standard deviations (RSDs) was 4.3% for ΣOCPs, 5.01% for ΣPCBs and 5.9 % for ΣPAHs, and the detection limits were in the range of 0.09–58.67 ng L^{-1} for PAHs, 0.1–45.6 ng L^{-1} for OCPs and 0.03–14.51 ng L^{-1} for PCBs. Also, the accuracy of the method explained with relative recovery, was higher than 95.6%, 87.8%, and 105.7% for ΣOCPs, ΣPAHs, and ΣPCBs, respectively. The result of recoveries indicated the method's accuracy is suitable and indicated low uncertainty in the theoretical preconcentration factor (PF=1000).

1. Introduction

Persistent organic pollutants (POPs) are chemicals of global concern because of their long-range transport potential, pronounced persistence against chemical and biological degradation, and bioaccumulation in ecosystems due to high lipophilicities. POPs have harmful biological effects, including toxicity, mutagenicity, and carcinogenicity [1,2]. Also, human agricultural and industrial actions cause the dissemination of POPs in the marine ecosystem [3]. The most important classes of POPs are polychlorinated biphenyls (PCBs), organochlorine pesticides (OCPs), and polycyclic aromatic hydrocarbons (PAHs) [1]. They split heavily into solids in aquatic systems and soils, particularly organic matter, thus escaping the aqueous phase [4, 5]. The oceans comprise the largest biome on the planet [6]. International conventions, such as the United Nations Environment Programmer Stockholm Convention on POPs, aims to control primary POPs sources and to eliminate POPs emissions globally by 2020 [7]. Therefore, monitoring and controlling POPs in the marine ecosystem is very

*Corresponding Author: Ali Mehdinia
Email: mehdi_3848@yahoo.com
https://doi.org/10.24200/amecj.v7.i04.354

important, and a robust, accurate, and repeatable analytical method is needed to compare data gained over many years. Unfortunately, identifying and determining trace and ultra-trace POPs in complex matrices remains a challenge to analytical chemists [8, 9]. For extraction of POPs from water, the United States Environmental Protection Agency (EPA) recommends the liquid-liquid extraction (LLE) method (EPA method 610) and solid-phase extraction (SPE) method (EPA method 508.1) for PAHs and OCPs pretreatment, respectively. However, these methods need time-consuming procedures and clean water samples, which are not applicable for the extraction of PCBs, PAHs, and OCPs by simultaneous extraction of the sample. Many novel analytical methods, such as micro-extraction methods for the concentration and determination of PAHs and OCPs in environmental aqueous samples, have been proposed [10, 11, 12]. They have the advantages of high enrichment, simplicity of operation, small amount of solvent used, rapidity, high sensitivity, and low cost [13,14]. However, micro-extraction methods are equilibrium-based methods [15]. The equilibrium of extraction reduces the reproducibility of extraction. A slight change in one of the parameters affects the extraction, and the amount of extraction changes affects the measurement accuracy [16, 17]. Given that in oceanography, the trend of POPs changes over the years is constantly studied and researched; we need a precise, accurate, and powerful method to observe the small changes that occur in the amount of ocean water pollution over the years.

In this study, we introduce a hybrid liquid-liquid extraction (HLLE) method for POPs extraction, which has high extraction recovery and uses less solvent than the traditional liquid-liquid extraction method before determination by GC-MS. This method can extract a wide range of organic compounds with different degrees of polarity. In this method, two solvents with varying degrees of polarity are used, in which the primary extracting solvent has a higher polarity than the second extracting solvent. Its solubility in water is higher than that of the second extracting solvent, and it interacts well with polar organic compounds. The first extraction solvent is easily separated from the water using the second extraction solvent, and the analyte is separated from the water.

2. Experimental

2.1. Chemicals

Seventeen organochlorine pesticides were used in the present studies, namely alpha-hexachlorocyclohexane (HCH, CAS Number: 319-84-6), beta-HCH, gamma-HCH, delta-HCH, Heptachlor, Aldrin, Heptachlor epoxide, alpha-Endosulfan, 4,4'-DDE, Dieldrin, Endrin, beta-Endosulfan,4,4'-DDD,Endrinaldehyde,Endosulfan sulfate, 4,4'-DDT and Methoxychlor, all obtained from Dr. Ehrenstorfer (Augsburg, Germany). Polycyclic aromatic hydrocarbons included Naphthalene, Acenaphthylene, Acenaphthene, Fluorene, Phenantrene, Anthracene, Fluranthene, Pyrene, Benz(a)Antheracen, Chrysene, Benz(b) Fluoranthene, Benzo(k)Fluorantene, Benzo(a) Pyrene, Indeno(1,2,3-cd) Pyrene, Dibenzo (a,h) Antheracene and Benzo(g,h,i)Perylene was purchased from Sigma-Aldrich (USA). A standard mixture of six PCB congeners (PCB-28, 52, 101, 138, 153, and 180) was purchased from Sigma-Aldrich (USA), and a standard mixture of twelve PCB congeners (PCB-77, 81, 105, 114, 118, 123, 126, 156, 157, 167, 169 and 189) was purchased from NEOCHEMA (Germany). Standard p-Terphenyl-d14 (CAS Number: 1718-51-0) was purchased from Merck (Germany) and used as an internal standard for PAHs and OCPs. An internal standard, Decachlorobiphenyl (PCB-209) (CAS Number: 2051-24-3) was purchased from Santa Cruz Biotechnology (USA) and used as an internal standard for PCBs. Acenaphthene-d10 (CAS Number: 15067-26-2), Chrysene-d12 (CAS Number: 1719-03-5), and Perylene-d12 (CAS Number: 1520-96-3) were prepared by Sigma-Aldrich (USA) and used as injection standards in PAHs analysis (Table 1). For organic trace analysis, N-Hexane (CAS Number: 110-54-3) was obtained from Merck (Germany). Dichloromethane (DCM)

(CAS Number: 75-09-2) and Isooctane (CAS Number: 540-84-1) for gas chromatography analysis were purchased from Merck (Germany). The stock standard solution of target compounds was prepared in isooctane. Working solutions were prepared by dilution of standard stock solution in n-hexane. All solutions were stored in the dark at 4°C.

2.2. Instrumental analysis

Analyses of the extracts were performed with a gas chromatography (GC, Agilent 6890N, Agilent Technologies, USA) equipped with a mass selective detector (MS, Agilent 5973, Agilent Technologies, USA). Instrument control, data acquisition, and data treatment were performed using Agilent ChemStation software. The chromatographic separation was performed with OPTIMA®-5-MS capillary column (30 m length × 0.25 mm diameter and 0.25 µm film thickness). Helium (purity 99.9995%) was used as carrier gas at a constant flow of 1 mL min^{-1}. 1 µL of extracts were injected in a splitless mode. The mass spectrometer was operated in the electron impact mode (EI) at 70 eV. Quadrupole and ion source temperature were set at 150°C and 230°C, respectively. The injector and interface were maintained at 270°C and 310 °C, respectively. A separate injection with a separate oven temperature program is used to analyze each of the subsets of POPs. The oven temperature program for separation of PCBs was initially held at 130°C for 2 min, then ramped to 160°C at 15 °C min^{-1}, and finally ramped to 300 °C at 5 °C min^{-1}, and was held for 6 min. The oven temperature program for separation PAHs was initially held at 60 °C for 2 min, then ramped to 120 °C at 30 °C min^{-1}, and finally ramped to 300 °C at 5°C min^{-1}, and was held for 5 min. The oven temperature program for separation OCPs was initially held at 100 °C for 2 min, then ramped to 160 °C at 15 °C min^{-1}, held at 160 °C for 5 min, and finally ramped to 280 °C at 5 °C min^{-1}, and was held for 5 min. Full scan mode was used for the qualification of compounds, and selected ion monitoring (SIM) mode was used for the quantitative analysis of compounds (Tables 2-4).

Table 1: Native PAHs and deuterated PAHs used as injection standards

Compound name	Deuterated injection standards
Naphthalene Acenaphthylene Acenaphthene Fluorene Phenanthrene Anthracene	Acenaphthene-d10
Fluranthene Pyrene p-Terphenyl-d14	(Acenaphthene-d10 & Chrysene-d12)*
Benz(a)Antheracene Chrysene	Chrysene-d12
Benz(b)Fluoranthene Benzo(k)Fluorantene Benzo(a)Pyrene Indeno(1,2,3-cd)Pyrene Dibenzo(a,h)Antheracene Benzo(g,h,i)Perylene	Perylene-d12

* Average area of Acenaphthene-d10 and Chrysene-d12 used as injection standard area for Fluranthene, Pyrene and p-Terphenyl-d14.

Table 2. Ions monitored in GC-MS SIM mode for PCBs

Compound name	CAS Number	Retention Time (min)	m/z of target ions
2,4,4′-Trichlorobiphenyl (PCB-28)	7012-37-5	12.50	186, 188
2,2′,5,5′-Tetrachlorobiphenyl (PCB-52)	35693-99-3	13.69	290, 294
2,2′,4,5,5′-Pentachlorobiphenyl (PCB-101)	37680-73-2	16.78	254, 324
3,4,4’,5-Tetrachlorobiphenyl (PCB-81)	70362-50-4	17.76	290
3,3′,4,4′-Tetrachlorobiphenyl (PCB-77)	32598-13-3	18.12	290
2’,3,4,4’,5-Pentachlorobiphenyl (PCB-123)	65510-44-3	18.93	324, 326
2,3′,4,4′,5-Pentachlorobiphenyl (PCB-118)	31508-00-6	19.02	324, 326
2,3,4,4’,5-Pentachlorobiphenyl (PCB-114)	74472-37-0	19.42	324, 326
2,2′,4,4′,5,5′-Hexachlorobiphenyl (PCB-153)	35065-27-1	19.80	358, 360, 362
2,3,3′,4,4′-Pentachlorobiphenyl (PCB-105)	32598-14-4	19.96	326, 328
2,2′,3,4,4′,5′-Hexachlorobiphenyl (PCB-138)	35065-28-2	20.77	326, 358, 360
3,3’,4,4’,5-Pentachlorobiphenyl (PCB-126)	57465-28-8	21.12	328, 330
2,3’,4,4’,5,5’-Hexachlorobiphenyl (PCB-167)	52663-72-6	21.77	360, 362
2,3,3′,4,4′,5-Hexachlorobiphenyl (PCB-156)	38380-08-4	22.57	360, 362
2,3,3’,4,4’,5’-Hexachlorobiphenyl (PCB-157)	69782-90-7	22.76	360, 362
2,2′,3,4,4′,5,5′-Heptachlorobiphenyl (PCB-180)	35065-29-3	23.13	394, 396, 398
3,3’,4,4’,5,5’-Hexachlorobiphenyl (PCB-169)	32774-16-6	23.89	360, 362
2,3,3’,4,4’,5,5’-Heptachlorobiphenyl (PCB-189)	39635-31-9	25.14	396, 398
Decachlorobiphenyl (PCB-209)*	2051-24-3	28.56	496,498, 500

*used as surrogate.

Table 3. Ions monitored in GC-MS SIM mode for PAHs

Compound name	**CAS Number**	**Retention Time (min)**	**m/z of target ions**
Naphthalene	91-20-3	7.14	128
Acenaphthylene	208-96-8	11.53	152
Acenaphthene-d10**	15067-26-2	12.10	164
Acenaphthene	83-32-9	12.21	154
Fluorene	86-73-7	14.16	166
Phenantrene	85-01-8	18.15	178
Anthracene	120-12-7	18.34	178
Fluranthene	206-44-0	23.54	202
Pyrene	129-00-0	24.50	202
p-Terphenyl-d14*	1718-51-0	25.69	244
Benz(a)Antheracen	56-55-3	30.18	228
Chrysene-d12**	1719-03-5	30.25	240
Chrysene	218-01-9	30.35	228
Benz(b)Fluoranthene	205-99-2	34.93	252
Benzo(k)Fluorantene	207-08-9	34.98	252
Benzo(a)Pyrene	50-32-8	36.19	252
Perylene-d12**	1520-96-3	36.43	264
Indeno(1,2,3-cd)Pyrene	193-39-5	40.34	276
Dibenzo(a,h)Antheracene	53-70-3	40.50	278
Benzo(g,h,i)Perylene	191-24-2	41.23	276

*used as surrogate. ** used as injection standard

Table 4. Ions monitored in GC-MS SIM mode for OCPs

Compound name	CAS Number	Retention Time (min)	m/z of target ions
Alpha-HCH	319-84-6	14.03	181, 183, 219
Gamma-HCH	58-89-9	15.36	181, 183, 219
Beta-HCH	319-85-7	15.57	181, 183, 219
Delta-HCH	319-86-8	16.73	181, 183, 219
Heptachlor	76-44-8	18.76	100 , 272
Aldrin	309-00-2	20.21	66 , 263
Alpha-Heptachlorepoxide	1024-57-3	22.06	81, 183, 185, 217, 252.9
Alpha-Endosulfan	959-98-8	23.32	195, 240.9
P-Terphenyl-d14*	1718-51-0	24.43	244
Dieldrin	60-57-1	24.43	79
4,4'-DDE	72-55-9	24.43	318
Endrin	72-20-8	25.19	81, 263
Beta-Endosulfan	33213-65-9	25.55	159, 195, 236.8
4,4'-DDD	72-54-8	25.99	165, 235, 237
Endrin-aldehyde	7421-93-4	26.27	67, 249.9, 344.9
Endosulfan-sulfate	1031-07-8	27.17	228.9, 271.9, 273.8
4,4'-DDT	50-29-3	27.36	165.1, 235, 237
Methoxychlor	72-43-5	29.50	152.1, 227.1, 228.1

*used as surrogate

2.3. Extraction procedures

Water samples were sampled with Niskin bottles by a Rosette sampler at different depths of the Persian Gulf. After sampling, the water samples were stored in the dark at 4°C and analyzed without filtration. For extracting POPs, 500 mL of water sample was poured into a separating funnel after spiking of PCB-209 and p-Terphenyl-d14 as internal standards, then 15 mL of dichloromethane was poured into the funnel and stirred for 3 min. After 5 min, the phases were separated, and the organic phase was placed in an Erlenmeyer flask, and the dichloromethane repeated the extraction step. Then, 10 mL of n-Hexane was added to the separating funnel and stirred for 3 min, and after 5 min, the organic phase was collected into the Erlenmeyer flask and repeated the extraction stage by n-Hexane (Figure 1). Then, about 1g of sodium sulfate was added to the Erlenmeyer flask containing the extract solution to remove the water. The extract solution is then concentrated to 0.5 mL using a rotary evaporator and nitrogen blowing. For analysis, 1µL of the extract was injected into the GC-MS device. Also, for PAHs analysis, injection standards of Acenaphthene-d10, Chrysene-d12, and Perylene-d12 were added in extract before injection into the GC-MS device.

3. Results and discussion.

3.1. Optimization of method

To avoid contamination and analytes losses during the development of the extraction methods, all glass materials were previously cleaned following the protocol established by the United States Environmental Protection Agency (US-EPA) Method 1668B for PCBs in water, soil, sediments, biosolids, and tissue [18]. To optimize the different variables, deionized water samples were spiked with each OCP, PCBs, and PAHs. Different kinds of extraction solvents, the volume of extraction solvents, and a repeat of the extraction step were evaluated in the extraction process.

3.1.1.Selection of extraction solvents

To achieve satisfactory HLLE recovery, several principles for selecting the organic solvent phase

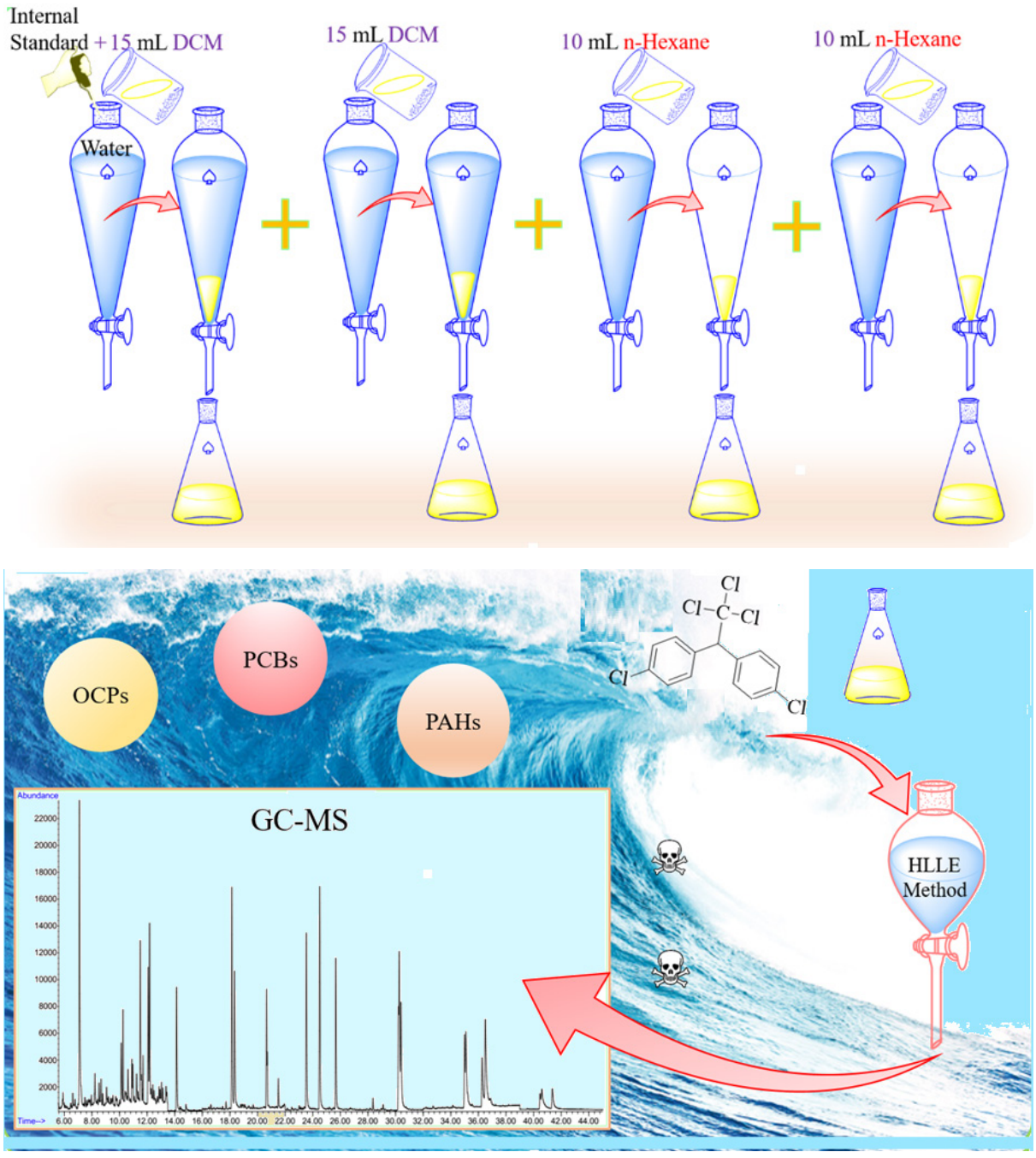

Fig. 1. Scheme of extraction procedures and determination

or extractant should be considered. First, extraction solvents must be immiscible with aqueous solution. Second, the solvent should have a low vapor pressure to prevent loss during agitation. The target analytes should also have good solubility in the selected solvent to ensure high extraction enrichment [19]. Accordingly, in the book Manual of Oceanographic Observations and Pollutant Analyses Methods (MOOPAM), n-hexane is recommended for the extraction of organic pollutants such as PAHs from water samples. The United States Environmental Protection Agency (EPA) methods 8081 and 3510 used dichloromethane to extract OCPs from water samples. Therefore, n-hexane and dichloromethane were selected for evaluation of the simultaneous extraction of PAHs, OCPs, and PCBs from seawater

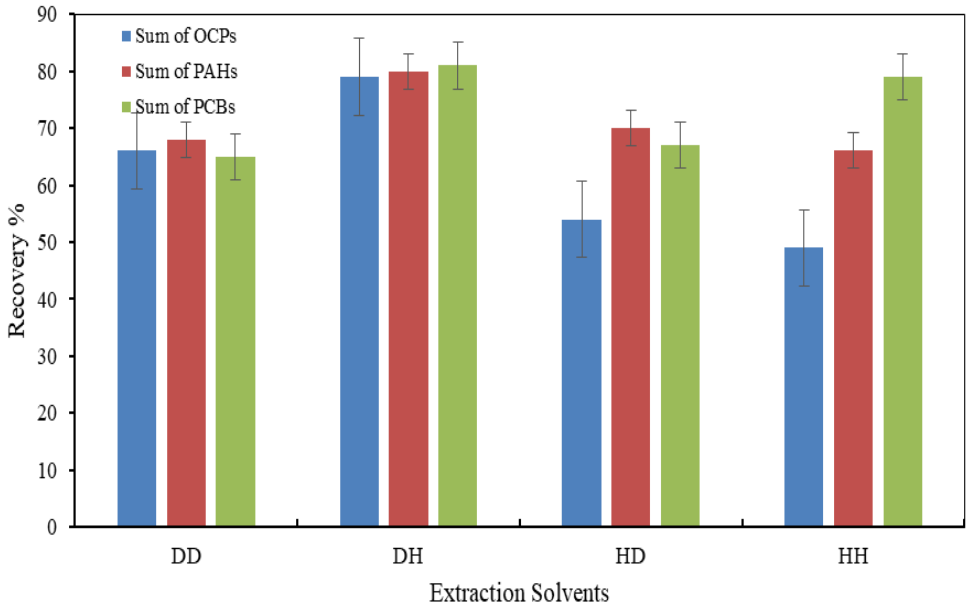

Fig. 2. Evaluation of the effect of extraction solvents on extraction recovery.

samples. For this proposal, a spiked pure water sample (500 mL) with PAHs, OCPs, and PCBs as standard solutions was extracted when other extraction conditions were constant. Recovery of, and was evaluated. The effect of four solvent arrays used in extraction was also investigated. After repeating the extraction step twice, the extraction recovery is recorded in Figure 2. Applied solvent arrays for this investigation were as follows:

In type 1, dichloromethane is used in the first and second extraction steps (DD). At type 2, dichloromethane is used in the first extraction step, and n-hexane is used in the second extraction step (DH). In Type 3, n-hexane is used in the first extraction step; dichloromethane is used in the second extraction step (HD), and in Type 4. n-hexane is used in the first and second extraction steps (HH).

According to the results illustrated in Figure 2, a good result was obtained for the model DH array of extraction solvent. A comparison of models DD and HH indicated that due to the high polarity of OCPs rather than PAHs, the recovery of extraction of OCPs in the DD model was better than that in the HH model. OCPs have the best interaction with dichloromethane, and PAHs have the best interaction with n-hexane. However, the solubility of dichloromethane in water was 17.5 g L^{-1} (25 °C), which is higher than the solubility of n-hexane. Due to the high dichloromethane solubility, the extraction solution's separation from the aqueous phase was less recoverable in the DD model. This causes a loss of recovery of OCPs in the DD model. In the DH model, one part of dichloromethane was solved in water in the first extraction step. This part of the solved dichloromethane interacted with n-hexane in the second extraction step, and this extraction step is named the Hybridization step in the LLE process. Hybridization of solvents in LLE causes enhanced separation of dichloromethane from the aqueous phase and enhances recovery of OCPs extraction. Also, the hybridization of solvents causes the simultaneous extraction of a wide variety of organic compounds, from polar to nonpolar compounds. Therefore, due to the synergetic effect of hybridizing solvents in the DH model, the recovery of simultaneous extraction of PAHs, OCPs, and PCBs was enhanced. Thus, the DH model was selected as the optimum condition for the extraction solvent.

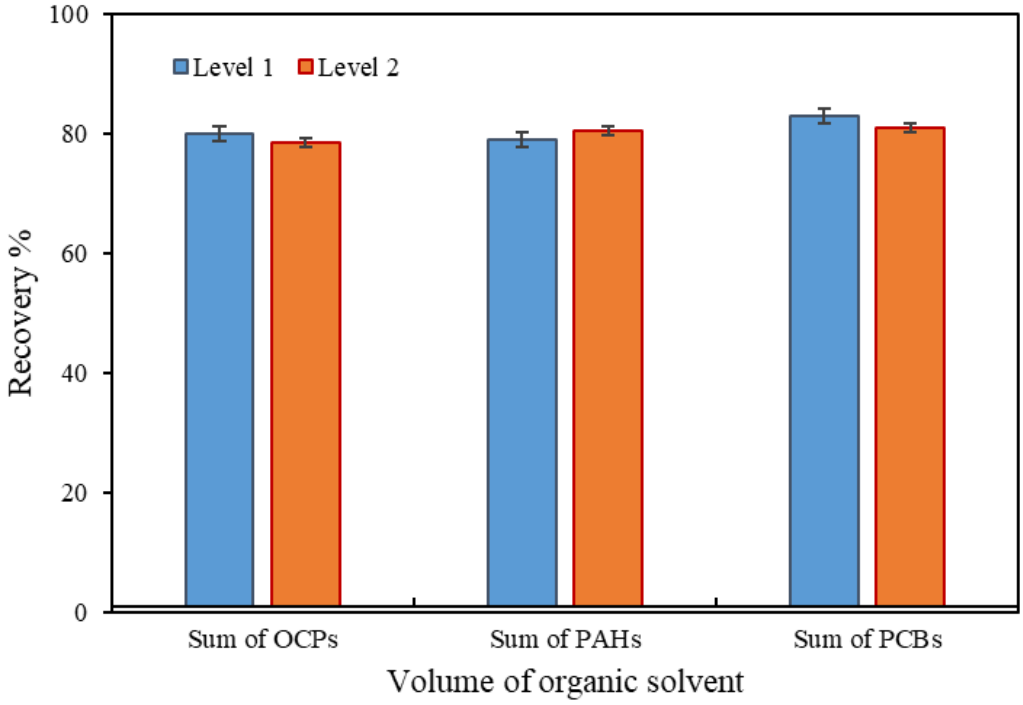

Fig. 3. Recoveries of different volumes of extraction solvent

3.1.2. Volume of solvents extraction and repetition times

In LLE, using many small volumes of extraction solvents is more effective than using a few large volumes of extraction solvents. In traditional LLE, high volumes of organic solvents are usually used, but HLLE focuses on the effect of combination extraction steps by different extraction solvents while using a low volume of extraction solvents. Also, two levels of solvent volume were considered. Level 1 of volume was 30 mL dichloromethane and 30 mL n-hexane. Level 2 of volume was 15 mL dichloromethane and 10 mL n-hexane. By evolution recovery of extraction, there was no significant effect on the recovery results of these two levels of extraction solvent (Figure 3). Thus, 15 mL and 10 mL were selected for dichloromethane and n-hexane, respectively, as the optimum volume of extraction solvent in each extraction step.

A few extraction experiments were performed to evaluate the optimum number of repeats of the HLLE extraction steps. Thus, recoveries of different replications of extraction steps with other constant conditions were evaluated (Figure 3). The order of replication of extraction steps and applied solvents in each experiment was listed as follows (Table 5).

In experiment 1, dichloromethane with one replicate as the first extraction solvent and n-hexane with one replicate as the second extraction solvent (DH), and in experiment 2, dichloromethane with two replicates as the first extraction solvent and n-hexane with one replicate as the second extraction solvent (DDH). Also, due to experiment 3, dichloromethane with one replicate as the first extraction solvent and n-hexane with two replicates as the second extraction solvent (DHH), and based on experiment 4, dichloromethane has two replicates as the first extraction solvent and n-hexane has two replicates as the second extraction solvent (DDHH). Experiment 5 showed that dichloromethane has three replicates as the first extraction solvent, and n-hexane has three replicates as the second extraction solvent (DDDHHH).

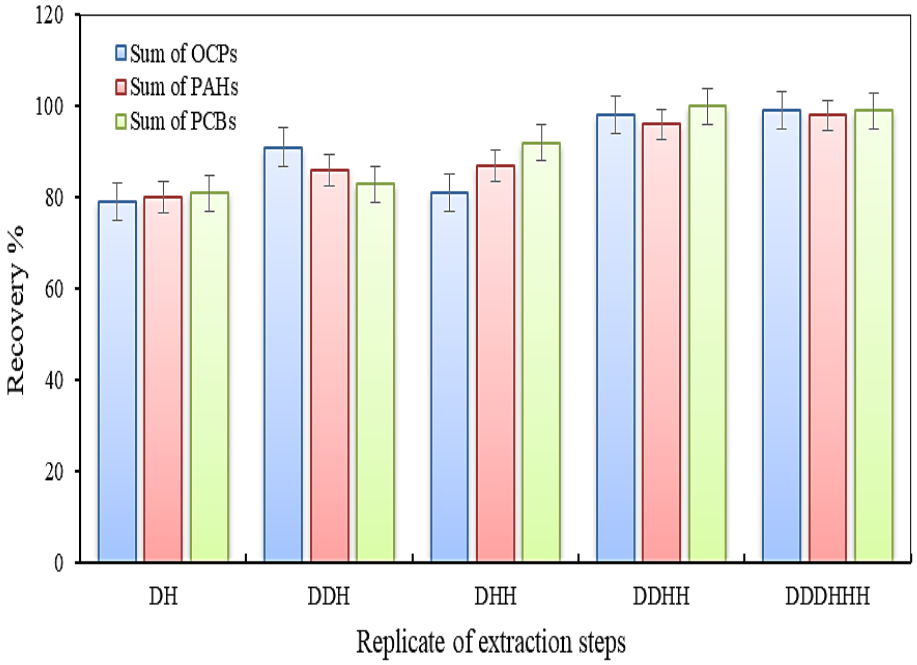

Fig. 4. Recovery of different replicas of extraction steps

Also, a mixture of solvents was tested as an extraction solvent. Considering that the density of the solvent mixture (dichloromethane: n-hexane = 1:1, 1:2, 2:1) is not much different from water. Therefore, the possibility of two phasing and separation of extraction solvents decreases. Thus, the extraction recovery is significantly reduced (recovery% < 60%). From the results obtained from Figure 4, the DDHH model showed maximum recovery for all three groups of POPs pollutants. Therefore, the DDHH model was selected as the optimum order to replicate.

3.2. Analytical characteristics and application to real samples

The optimum HLLE experimental conditions were used to assess the applicability of the proposed method for the quantitative determination of target analytes by GC–MS. A calibration study was performed by spiking analytes in deionized water over the 4.0 – 60 ngL^{-1} concentration range for OCPs, 0.4 – 6 ngL^{-1} for PCBs, and 10 – 160 ngL^{-1} for PAHs. The calibration curves were calculated in terms of the ratio of the area of each one of the analytes to the area of the spiked surrogate, gave a high level of linearity for all the target analytes with the best correlation coefficients (R2) (Tables 6, 7, and 8). The repeatability of the proposed method, expressed as relative standard deviation (RSD), was evaluated by extracting consecutive aqueous samples (spiked at 50 ngL^{-1} with each target OCPs, spiked at 4.0 ngL^{-1} with each target PCBs and spiked at 80 ngL^{-1} with each target PAHs) (Tables 6, 7 and 8). The limits of detection (LOD) are defined as the equation LOD=3SD/m (where SD is the standard deviation signal of the blank sample and m is the slope of the extraction calibration course, respectively).

Table 5. Order of replication of extraction steps and applied solvents

Experiment	Step 1	Step 2	Step 3	Step 4	Step 5	Step 6
1	Dichloromethane	n-hexane				
2	Dichloromethane	Dichloromethane	n-hexane			
3	Dichloromethane	n-hexane	n-hexane	n-hexane		
4	Dichloromethane	Dichloromethane	n-hexane	n-hexane		
5	Dichloromethane	Dichloromethane	Dichloromethane	n-hexane	n-hexane	n-hexane

Table 6. The parameters for extracting OCPs from water samples using the optimized HLLE method (RSD% 50 ngL^{-1})

Analyte	Slope	Intercept	R^2	RSD% (n=5)	LOD HLLE (ngL^{-1})	LOD EPA 525.2 (ngL^{-1})
Alpha-HCH	0.0058	0.0014	0.9992	5.1	0.5	110
Gamma-HCH	0.0031	0.0242	0.9946	4.9	3.0	84
Beta-HCH	0.0044	0.1490	0.9997	2.5	45.6	85
Delta-HCH	0.0025	0.0074	0.9779	4.5	0.4	49
Heptachlor	0.0016	0.0014	0.9996	7.6	4.5	61
Aldrin	0.0030	-0.0001	1.0000	7.6	1.8	45
Heptachlor epoxide	0.0027	0.0195	0.9999	9.5	34.2	130
Alpha-Endosulfan	0.0009	0.0069	0.9974	3.1	1.6	110
Dieldrin	0.0016	0.0052	0.9999	0.6	4.8	150
4,4'-DDE	0.0031	-0.0003	0.9994	1.7	2.4	70
Endrin	0.0005	0.0008	0.999	2.2	0.1	340
Beta-Endosulfan	0.0008	0.0089	0.9982	7.0	9.1	74
4,4'-DDD	0.0047	0.0025	0.9978	1.4	0.4	55
Endrin-aldehyde	0.0007	0.0782	0.9871	4.1	6.1	150
Endosulfan-sulfate	0.0010	0.0001	0.9987	0.5	0.1	93
4,4'-DDT	0.0014	0.0101	0.9821	8.9	16.2	39
Methoxychlor	0.0011	0.0015	0.9993	1.9	0.1	130
Average			**0.9959**	**4.3**		

Table 7. Method parameters for extracting PCBs from water samples using the optimized HLLE method (RSD% 4 ngL^{-1})

Analyte	Slope	Intercept	R^2	RSD% (n=5)	LOD HLLE (ngL^{-1})
PCB-28	0.2018	-0.0003	0.9991	11.94	0.04
PCB-52	0.1319	0.0059	0.9989	14.51	0.29
PCB-101	0.5212	-0.0237	0.9995	4.46	0.43
PCB-81	0.2682	-0.0118	0.9968	12.84	0.15
PCB-77	0.2653	-0.0076	0.9986	3.35	0.06
PCB-123	0.4801	0.0082	0.9991	3.61	0.04
PCB-118	0.5687	-0.0197	0.9998	5.64	0.06
PCB-114	0.4913	-0.0075	0.9993	5.40	0.17
PCB-153	0.557	-0.0001	0.9994	3.05	0.06
PCB-105	0.4918	-0.0146	0.9982	8.35	0.01
PCB-138	0.3452	-0.0114	0.9998	1.43	0.06
PCB-126	0.2282	-0.0066	0.9996	7.56	0.08
PCB-167	0.4884	-0.0021	0.9988	2.75	0.13
PCB-156	0.4742	0.0107	0.9997	0.03	0.01
PCB-157	0.4639	0.0024	0.9992	1.48	0.03
PCB-180	0.4524	0.0101	0.9993	0.94	0.10
PCB-169	0.4504	-0.0195	0.9999	1.14	0.03
PCB-189	0.3124	-0.0028	0.9991	1.72	0.05
Average			**0.9991**	**5.01**	

Table 8. Method parameters for extracting PAHs from water samples using the optimized HLLE method (RSD% 80 ngL^{-1})

Analyte	Slope	Intercept	R^2	RSD% (n=5)	LOD HLLE (ngL^{-1})
Naphtalene	0.0165	0.0936	0.9993	9.3	36.80
Acenaphthylene	0.0171	-0.0208	0.9999	10.4	0.50
Acenaphthene	0.0176	0.0206	0.9999	12.7	7.22
Fluorene	0.0131	-0.0203	0.9999	11.6	10.53
Phenantrene	0.0185	-0.0673	0.9989	6.2	58.67
Anthracene	0.0162	-0.103	0.9965	8.1	6.42
Fluranthene	0.0167	-0.0257	0.9995	2.6	11.23
Pyrene	0.0173	0.0024	0.9994	5.7	30.33
Benz(a)Antheracen	0.0092	-0.0311	0.9971	3.2	1.23
Chrysene	0.0117	0.0006	0.9998	4.5	2.10
Benz(b)Fluoranthene	0.0138	-0.0799	0.9968	3.9	0.18
Benzo(k)Fluorantene	0.0243	-0.1376	0.9972	1.6	0.61
Benzo(a)Pyrene	0.0121	-0.0819	0.9968	5.8	0.09
Indeno(1.2.3-cd)Pyrene	0.0054	-0.011	0.9987	5.8	0.14
Dibenzo(a,h)Antheracene	0.0101	-0.0531	0.9995	3.6	0.09
Benzo (g.h. I)Perylene	0.0096	0.0075	0.9959	4.7	1.04
Average			**0.9984**	**5.9**	

During the present investigations, matrix effects upon extraction were also evaluated by investigating the applicability of the proposed method to determine OCPs, PCBs, and PAHs in seawater samples. Spiked samples (50 ngL^{-1} for OCPs, 4 ngL^{-1} for PCBs, and 80 ngL^{-1} for PAHs) were extracted using the developed HLLE method, and the extracts were analyzed by GC–MS. Chromatograms of analysis of these samples were presented in Figures 5, 6, and 7. The method's accuracy was confirmed by analyzing a sample with a certain amount of analytes added (relative recoveries); the following formula is used to calculate relative recovery as Equation 1.

$$Relative\ Recoveries(\%) = \frac{(C_{found} - C_{initial}) \times 100}{C_{added}} \quad \text{(Eq. 1)}$$

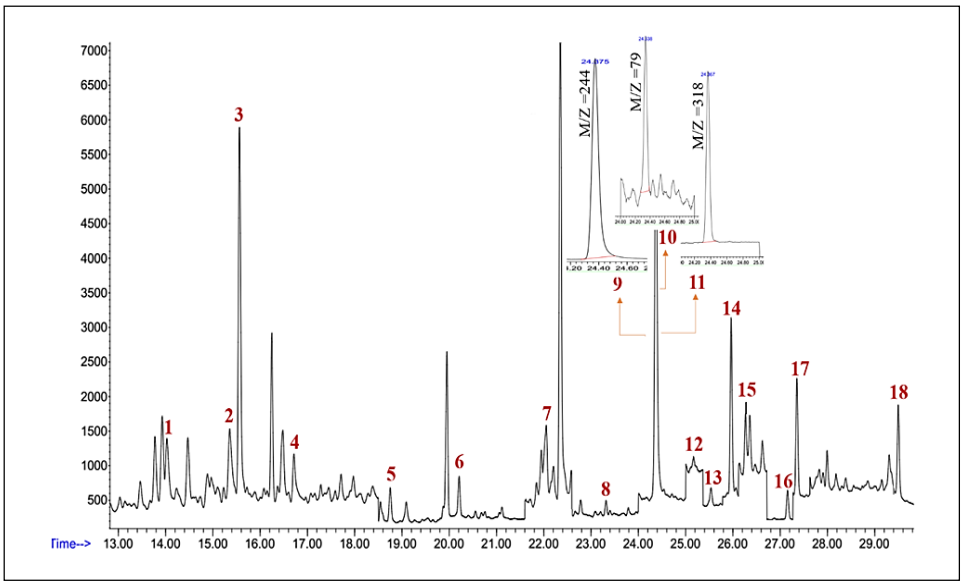

Fig. 5. Chromatogram of spiked sea water sample analysis with 50 ngL^{-1} of OCPs. Alpha-HCH[1], Gamma-HCH[2], Beta-HCH[3], Delta-HCH[4], Heptachlor[5], Aldrin[6], Alpha-Heptachlorepoxide[7], Alpha-Endosulfan[8], d14-P-Terphenyl[9], Dieldrin[10], 4,4'-DDE[11], Endrin[12], Beta-Endosulfan[13], 4,4'-DDD[14], Endrin-aldehyde[15], Endosulfan-sulfate[16], 4,4'-DDT[17], Methoxychlor[18]

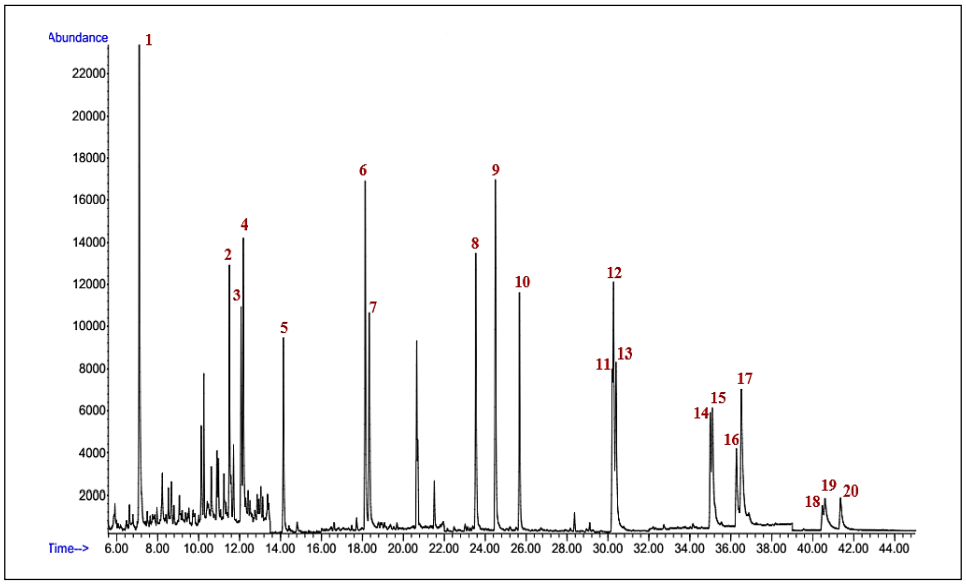

Fig. 6. Chromatogram of spiked sea water sample analysis with 80 ngL^{-1} PAHs. Naphthalene[1], Acenaphthylene[2], d10-Acenaphthene[3], Acenaphthene[4], Fluorene[5], Phenantrene[6], Anthracene[7], Fluranthene[8], Pyrene[9], d14-p-Terphenyl[10], Benz(a)Antheracen[11], d12-Chrysene[12], Chrysene[13], Benz(b)Fluoranthene[14], Benzo(k)Fluorantene[15], Benzo(a)Pyrene[16], d12-Perylene[17], Indeno(1,2,3-cd)Pyrene[18], Dibenzo(a,h)Antheracene[19], Benzo(g,h,i)Perylene[20]

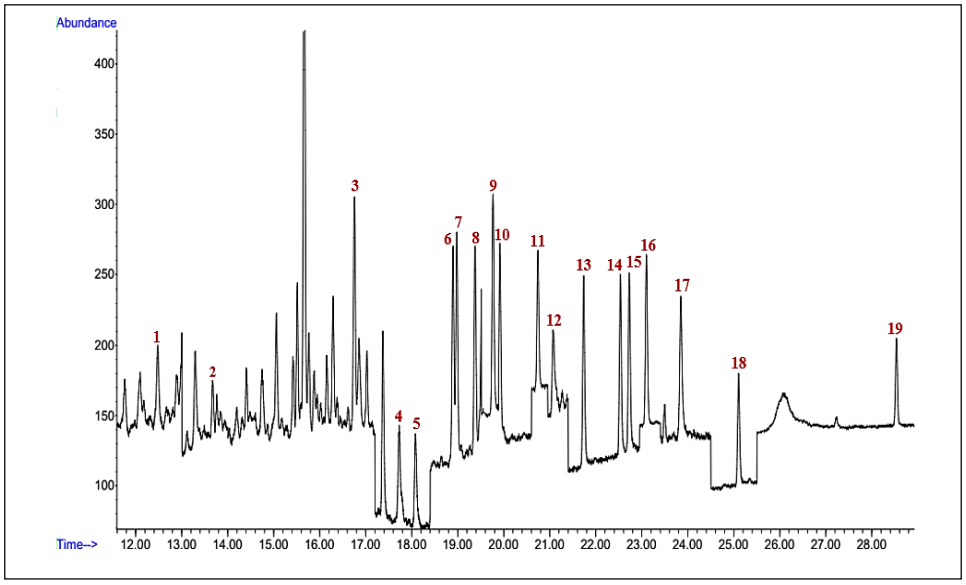

Fig. 7. Chromatogram of spiked sea water sample analysis with 4 ngL^{-1} PCBs. (PCB-28)[1], (PCB-52)[2], (PCB-101)[3], (PCB-81)[4], (PCB-77)[5], (PCB-123)[6], (PCB-118)[7], (PCB-114)[8], (PCB-153)[9], (PCB-105)[10], (PCB-138)[11], (PCB-126)[12], (PCB-167)[13], (PCB-156)[14], (PCB-157)[15], (PCB-180)[16], (PCB-169)[17], (PCB-189)[18], (PCB-209)[19].

That $C_{initial}$ (ngL^{-1}) is the initial concentration of compounds in the real sample. C_{added} (ngL^{-1}) is an amount of analytes added to the water sample. C_{found} (ngL^{-1}) is the concentration obtained from extracting and analyzing the real sample after adding analytes. The results for each set of experiments are summarized in Tables 9, 10, and 11. A good agreement was reached between the amounts of added analytes and the amount of obtained analytes. Obtained Relative recoveries indicate the accuracy and validity of the method for extracting and determining POPs in similar samples.

Table 9. Relative recoveries of the OCPs in water samples

Samples	$C_{initial}$ (ngL^{-1})	C_{added} (ngL^{-1})	C_{found} (ngL^{-1})	Recovery (%)
Alpha-HCH	0.6	50	50.7	100.2
Gamma-HCH	30.3	50	73.2	85.9
Beta-HCH	213.7	50	252.5	77.7
Delta-HCH	-2.8	50	38.2	82.0
Heptachlor	6.5	50	57.1	101.3
Aldrin	2.2	50	40.3	76.2
Heptachlorepoxide	22.2	50	82.1	119.8
Alpha-Endosulfan	9.0	50	46.9	75.7
Dieldrin	9.7	50	54.4	89.4
4,4'-DDE	4.7	50	49.6	89.7
Endrin	1.4	50	44.1	85.3
Beta-Endosulfan	10.7	50	55.7	90.0
4,4'-DDD	1.4	50	52.6	102.3
Endrin-aldehyde	72.0	50	130.6	117.1
Endosulfan-sulfate	-0.3	50	50.5	101.7
4,4'-DDT	27.1	50	85.2	116.2
Methoxychlor	3.7	50	61.1	114.8
Sum of OCPs	**412.2**	**850**	**1224.9**	**95.6**

Table 10. Relative recoveries of the PCBs in water samples

Samples	$C_{initial}$ (ngL^{-1})	C_{added} (ngL^{-1})	C_{found} (ngL^{-1})	Recovery (%)
PCB-28	0.51	4	5.05	113.4
PCB-52	0.46	4	3.98	88.0
PCB-101	0.39	4	4.49	102.5
PCB-81	0.38	4	4.56	104.5
PCB-77	0.27	4	4.42	103.8
PCB-123	0.03	4	4.47	111.1
PCB-118	0.02	4	4.08	101.4
PCB-114	0.08	4	4.32	105.9
PCB-153	0.08	4	4.36	106.9
PCB-105	0.03	4	4.24	105.4
PCB-138	0.10	4	4.24	103.4
PCB-126	0.60	4	5.26	116.7
PCB-167	0.07	4	4.29	105.7
PCB-156	0.03	4	4.30	106.8
PCB-157	0.01	4	4.40	109.7
PCB-180	0.03	4	4.25	105.6
PCB-169	0.04	4	4.29	106.4
PCB-189	0.00	4	4.21	105.3
Sum of PCBs	**3.10**	**72.00**	**79.21**	**105.7**

Table 11. Relative recoveries of the PAHs in water samples.

Samples	$C_{initial}$ (ngL^{-1})	C_{added} (ngL^{-1})	C_{found} (ngL^{-1})	Relative Recovery (%)
Naphtalene	89.54	80	163.57	92.5
Acenaphthylene	2.04	80	71.35	86.6
Acenaphthene	12.19	80	82.18	87.5
Fluorene	14.88	80	88.24	91.7
Phenantrene	62.22	80	131.17	86.2
Anthracene	11.98	80	85.13	91.4
Fluranthene	14.20	80	86.13	89.9
Pyrene	32.95	80	105.44	90.6
Benz(a)Antheracen	4.94	80	83.63	98.4
Chrysene	2.65	80	67.30	80.8
Benz(b)Fluoranthene	9.94	80	78.19	85.3
Benzo(k)Fluorantene	9.73	80	71.29	77.0
Benzo(a)Pyrene	9.52	80	64.58	68.8
Indeno(1.2.3-cd)Pyrene	5.05	80	79.86	93.5
Dibenzo(a,h)Antheracene	10.51	80	86.96	95.6
Benzo(g.h.i)Perylene	-0.95	80	69.92	88.6
Sum of PAHs	**291.4**	**1280**	**1414.9**	**87.8**

4. Conclusion

A sensitive analytical method comprising HLLE coupled with GC–MS has been developed to simultaneously determine trace levels of OCPs, PAHs, and PCBs from environmental water samples. The optimized HLLE method uses perfect extraction to reduce the disadvantages of non-enhanced equilibrium extraction in terms of the method's repeatability. Hybridization of extraction solvents leads to enhanced recovery and accuracy in the simultaneous extraction of different categories of compounds with different polarities. The linear range (LR) of calibration curves was 4 – 60 ngL^{-1} for OCPs, 0.4 – 6 ngL^{-1} for PCBs, and 10 – 160 ngL^{-1} for PAHs. The average amount of relative standard deviations (RSDs) was 4.3% for ΣOCPs, 5.01% for ΣPCBs and 5.9 % for ΣPAHs. The detection limits were in the range of 0.09–58.67 ng L^{-1} for PAHs, 0.1–45.6 ng L^{-1} for OCPs and 0.03–14.51 ng L^{-1} for PCBs. This easy-to-handle and repeatable method represents an attractive alternative to the sample preparation method, as it affords better extraction conditions for a broader range of analytes in environmental water samples.

5. Acknowledgements

The authors thank the Iranian National Institute for Oceanography and Atmospheric Science. There are no conflicts of interest.

6. References

[1] J. Lee, S.Y. Lee, K.W. Park, H.H. Lim, H.S. Shin, Simultaneous determination of PCBs, OCPs and PAHs in mussel by ultrasound-assisted cloudy extraction and gas chromatography–tandem mass spectrometry, Food Addit. Contam. Part A, 37 (2020) 1730–1743. https://doi.org/10.1080/19440049.2020.1798029

[2] J. Rakhtshah, Air pollution control: The evaluation of TerphApm@ MWCNTs as a novel heterogeneous sorbent for benzene removal from air by solid phase gas extraction, Arab. J. Chem., 13 (2020) 1741-1751. https://doi.org/10.1016/j.arabjc.2018.01.011

[3] N. Berrojalbiz, J. Dachs, S. Del Vento, M.J. Ojeda, M.C. Valle, J. Castro-Jiménez, G. Mariani, J. Wollgast, G. Hanke, Persistent organic pollutants in mediterranean seawater

and processes affecting their accumulation in plankton, Environ. Sci. Technol., 45 (2011) 4315–4322. https://doi.org/10.1021/es103742w

[4] H. Alshemmari, An overview of persistent organic pollutants along the coastal environment of Kuwait, Open Chem., 19 (2021) 149–156. https://doi.org/10.1515/chem-2021-0198

[5] J. Rakhtshah, BB. Yarahmadi, A rapid removal of xylene vapor from environmental air based on bismuth oxide coupled to heterogeneous graphene/graphene oxide by UV photo-catalectic degradation-adsorption procedure, J. Environ. Chem. Eng., 8 (2020) 104193. https://doi.org/10.1016/j.jece.2020.104193

[6] C. Cortada, L. Vidal, R. Pastor, N. Santiago, A. Canals, Determination of organochlorine pesticides in water samples by dispersive liquid-liquid microextraction coupled to gas chromatography-mass spectrometry, Anal. Chim. Acta, 649 (2009) 218–221. https://doi.org/10.1016/j.aca.2009.07.041

[7] G. Everaert, F. De Laender, P.L.M. Goethals, C.R. Janssen, Relative contribution of persistent organic pollutants to marine phytoplankton biomass dynamics in the North Sea and the Kattegat, Chemosphere, 134 (2015) 76–83. https://doi.org/10.1016/j.chemosphere.2015.03.084

[8] J. Rakhtshah, A rapid extraction of toxic styrene from water and wastewater samples based on hydroxyethyl methylimidazolium tetrafluoroborate immobilized on MWCNTs by ultra-assisted dispersive cyclic conjugation-micro-solid phase extraction, Microchem. J., 170 (2021) 106759. https://doi.org/10.1016/j.microc.2021.106759

[9] S. Xie, M.C. Paau, C.F. Li, D. Xiao, M.M.F. Choi, Separation and preconcentration of persistent organic pollutants by cloud point extraction, J. Chromatogr. A, 1217 (2010) 2306–2317. https:// doi.org/ 10.1016/ j.chroma. 2009.11.075

[10] S. Teimoori, N. Mansouri, New extraction of toluene from water samples based on nano-carbon structure before determination by gas chromatography, Int. J. Environ. Sci. Technol., 20 (2023) 6589–6608. https://doi.org/10.1007/s13762-023-04906-9

[11] M.M. Asl, Functionalized graphene oxide with bismuth and titanium oxide nanoparticles for efficiently removing formaldehyde from the air by photocatalytic degradation–adsorption process, J. Anal. Test., 7 (2023) 444-458. https://doi.org/10.1007/s41664-023-00272-0

[12] A. Faghihi-Zarandi, New method for removal of hazardous toluene vapor from air based on the ionic liquid-phase adsorbent, Int. J. Environ. Sci. Technol., 16 (2019) 2797–2808. https://doi.org/10.1007/s13762-018-1975-5

[13] S. Huang, S. He, H. Xu, P. Wu, R. Jiang, F. Zhu, T. Luan, G. Ouyang, Monitoring of persistent organic pollutants in the Pearl River Estuary seawater with rapid on-site active SPME sampling technique, Environ. Pollut., 200 (2015) 149–158. https://doi.org/10.1016/j.envpol.2015.02.016

[14] S. Teimoori, M. Panahi, N. Mansouri, Rapid extraction of BTEX in water and milk samples based on functionalized multi-walled carbon nanotubes by dispersive homogenized-micro-solid phase extraction, Food Chem., 421 (2023) 136229. https://doi.org/10.1016/j.foodchem.2023.136229

[15] A. Mehdinia, D. Jahedi Vaighan, A. Jabbari, Cation exchange superparamagnetic Al-based metal-organic framework (Fe_3O_4/MIL-96 (Al)) for high efficient removal of Pb (II) from aqueous solutions, ACS Sustain. Chem. Eng., 6 (2018) 3176-3186. https://doi.org/10.1021/acssuschemeng.7b03301

[16] S. Teimoori, A.H. Hassani, M. Panahi, N. Mansouri, An immobilization of aminopropyl trimethoxysilane-phenanthrene carbaldehyde on graphene oxide for toluene extraction and separation in water samples, Chemosphere, 316 (2023) 137800. https://doi.org/10.1016/j.chemosphere.2023.137800

[17] M. Arjomandi, A review: Analytical methods

for heavy metals determination in environment and human samples, Anal. Methods Environ. Chem. J., 2 (2019) 97–126. https://doi.org/10.24200/amecj.v2.i03.73

[18] N. Barco-Bonilla, A.J. Nieto-García, R. Romero-González, J.L. Martínez Vidal, A.G. Frenich, Simultaneous and highly sensitive determination of PCBs and PBDEs in environmental water and sediments by gas chromatography coupled to high-resolution magnetic sector mass spectrometry, Anal. Methods, 7 (2015) 3036–3047. https://doi.org/10.1039/C5AY00017C

[19] Z.-G. Shi, H.K. Lee, Dispersive liquid-liquid microextraction coupled with dispersive μ-solid-phase extraction for the fast determination of polycyclic aromatic hydrocarbons in environmental water samples, Anal. Chem., 82 (2010) 1540–1545. https://doi.org/10.1021/ac9023632

Anal. Methods Environ. Chem. J. 7 (4) (2024) 112-124

Research Article, Issue 4
Analytical Methods in Environmental Chemistry Journal
Journal home page: www.amecj.com/ir

Analysis and evaluation of Soy milk, Kunu, and Zobo Beverages in Nigeria by atomic absorption spectrophotometry and UV-Vis spectrometry

Tyover David Ortil [a,*], Peter Agorye Adie[a], Aondoungwa Silas Aondoaver[a], and Ahemba Segun Akaahimbe[b]
[a] *Department of Chemistry, Benue State University, Makurdi, Benue State, Nigeria*
[b] *Department of Materials Science, South Ural State University, Chelyabinsk, Russia*

ARTICLE INFO:
Received 1 Aug 2024
Revised form 10 Oct 2024
Accepted 7 Nov 2024
Available online 30 Dec 2024

Keywords:
Food samples,
Analytical methods,
Characterization,
Mineral composition,
Atomic absorption spectrophotometry,
UV-Vis spectrometry

ABSTRACT
Soy milk, Kunu, and Zobo are popular soft drinks in Nigeria. Thus, Information about their nutritional composition is crucial for assessing their energy and nutritional relevance. This study utilized standard methods to analyze the proximate composition, physicochemical properties, and mineral content of beverages in Nigeria. The results showed that the percentages (%) of moisture content, ash content, crude fiber, crude protein, crude fat, and carbohydrate content were highest in Zobo (82.89±1.33), Soy milk (1.02±0.05), Kunu (5.40±1.50), Soymilk (12.17±1.25), Soymilk (2.10±0.22) and Zobo (4.54±1.55) respectively. Additionally, the physicochemical properties, such as titratable acidity, pH, apparent colloidal stability, viscosity, total solids, and the mineral composition of the drinks, were determined using the AOAC (2001) standard method. The minerals zinc (Zn), calcium (Ca), magnesium (Mg), potassium(K), and phosphorus(P) were determined by atomic absorption spectrophotometry (F-AAS) and UV-Vis spectrometry. These findings indicate that these locally produced beverages are rich sources of a balanced diet.

1. Introduction

The quest for affordable yet nutritious alternatives to industrially processed protein-rich beverages has sparked interest in locally sourced plant-based options. Soy milk, Zobo (Sorrel Zoborodo), and Kunu (Kunun-zaki) stand out for their considerable protein content. Soy milk is derived from whole soybeans (Glycine max). At the same time, Zobo and Kunu are extracts made from Zobo leaves (Hibiscus sabdariffa) and either corn (Zea mays) or millet (Panicum miliaceum), respectively [1]. These beverages are not only popular globally but are particularly favored in developing and underdeveloped regions where access to commercial drinks like Coca-Cola and Malt drinks may be limited due to economic, social, cultural, or religious reasons. Local alternatives have gained traction as health beverages due to their rich nutritional profiles. They are abundant in fatty acids, oils, proteins, B-vitamin complexes, calcium, amino acids, and essential minerals such as magnesium, zinc, iron, phosphorus, and potassium. Furthermore, they boast natural antioxidants like isoflavones and phytoestrogens [2]. Sold commonly in public spaces like markets, motor

*Corresponding Author: Tyover David Ortil
Email: ortildavid12@gmail.com
https://doi.org/10.24200/amecj.v7.i04.348

parks, and educational institutions [3], these drinks serve as dairy milk substitutes, being non-caloric, cholesterol-free, and suitable for individuals with lactose intolerance. While extensive literature exists on the proximate and physicochemical analyses of various food items, little attention has been given to locally produced soy milk, Zobo, and Kunu drinks. Despite their high consumption in developing countries like Nigeria, the nutritional composition of these beverages remains underexplored. Therefore, this investigation aims to elucidate the nutritional profile of these drinks, enhancing consumer awareness of the quality parameters inherent in these products. Moreover, recent nanotechnology advancements have provided new mineral analysis methodologies that could significantly enhance the accuracy and sensitivity of nutritional profiling. For instance, nano-palladium embedded on mesoporous silica nanoparticles has been effectively used for mercury vapor removal from air, showcasing the potential of nanotechnology in environmental and health sciences [4]. Similarly, dispersive ionic liquid-liquid microextraction has been employed for air exposure assessment and biological monitoring of mercury, demonstrating the utility of nanotechnology in precise chemical analysis [5]. Single-walled carbon nanotubes (SWCNTs) have also been explored as novel sorbents for determining mercury in air, indicating the versatility of nanomaterials in analytical applications [6]. Additionally, comparative studies on multi-walled and single-walled carbon nanotubes for mercury vapor adsorption and desorption further emphasize the advanced capabilities of nanotechnology in analytical processes [7]. Various advanced analytical techniques have also been employed to evaluate and analyze traditional beverages such as soy milk, Kunu, and Zobo. For instance, speciation and determination of manganese ions in these beverages have been effectively carried out using N-acetylcysteine immobilized on multi-walled carbon nanotubes (MWCNTs), demonstrating the capability of these nanotubes in enhancing detection sensitivity and selectivity in complex matrices [8]. Similarly, the separation of essential trace elements in soy milk and Zobo using a novel biostructure sorbent based on cysteine and methionine functionalized MWCNTs has been achieved with high efficiency [9]. Moreover, ultrasound-assisted dispersive-modification solid-phase extraction with ionic liquids immobilized on MWCNTs has shown promising results in the speciation and determination of heavy metals in Kunu samples [10]. Additionally, the preconcentration and separation of nickel in traditional beverage samples using functionalized MWCNTs via ultrasound-assisted solid-liquid trap phase extraction highlight the versatility of these nanotubes in food sample analysis [11]. Furthermore, the rapid speciation of contaminants in these beverages using MWCNTs combined with dispersive ionic liquid-suspension-micro-solid phase extraction underscores the potential of this method for food safety and quality assessments [12]. These advanced nanotechnological and analytical methods based on F-AAS and UV-vis spectrometry applied to the analysis of soy milk, Zobo, and Kunu provide more detailed and accurate insights into their mineral content, ultimately enhancing the understanding of their nutritional benefits and supporting their promotion as valuable dietary components.

2. Materials and methods

2.1. Materials and Apparatus

Soy Milk, Kunu, and Zobo Samples prepared from Nigeria (Soy Milk: Locally sourced from a local soy milk producer in Nigeria, Kunu is obtained from traditional Kunu brewers in Nigeria, and Zobo is purchased in Nigeria, made from dried Hibiscus sabdariffa calyces). Other materials and apparatus such as Weighing Balance (Model: Sartorius Practum 213-1S, Germany); Filter paper (Whatman Filter Paper Grade 1, United Kingdom); Beakers (Pyrex Beaker, Corning Inc., USA); Kjeldahl flask (Model: Kjeldahl Digestion Flask, 500 mL, DWK Life Sciences, Kimble, Germany); Distillation Chamber (Model: Kjeltec™ 8400, Foss, Denmark); Digester (Model: Gerhardt Kjeldahl Digestion Unit, C. Gerhardt GmbH & Co. KG, Germany); Oven (Model: Air Clean Oven

YPO-720, China); Furnace (Model: Carbolite ELF 11/6B Furnace, Carbolite Gero, UK); Stirrer (Model: IKA RCT Basic Magnetic Stirrer, IKA Works, Inc., Germany); Test Tubes (Model: Borosilicate Glass Test Tubes, DWK Life Sciences, Kimble, Germany); Crucibles (Model: Porcelain Crucibles with Lid, CoorsTek, USA); Funnels (Model: Polypropylene Funnels, Dynalon Labware, USA); Desiccator (Model: Standard Vacuum Desiccator, Thermo Fisher Scientific, USA); Soxhlet Apparatus (Model: Soxhlet Extraction Unit, BUCHI Labortechnik AG, Switzerland); Measuring Cylinder (Model: Graduated Measuring Cylinder, 1000 ml, VITLAB, Germany); Retort Stand (Model: Standard Laboratory Retort Stand with Clamps, Philip Harris, UK); pH Meter (Model: Hanna Instruments HI 2211 pH/ORP Meter, Romania); Standard Brookfield Viscometer (Model: Brookfield DV-E Viscometer, AMETEK Brookfield, USA); Volumetric Flask (Product Number: BR36182, Sigma-Aldrich, USA; Hand Gloves (Model: Nitrile Examination Gloves, Kimberly-Clark Professional, USA); Water Bath (Model: Grant SUB Aqua Pro, Grant Instruments, UK); UV-Visible Spectrophotometer (UV-Vis) (Model: UV-2600, Shimadzu Corporation, Japan), and Flame Atomic Absorption Spectrometer (AAS) (Model: Analyst 400, PerkinElmer, USA) were prepared.

2.2. Reagents

Hydrochloric acid (HCl, CAS Number: 7647-01-0, Sigma-Aldrich, Germany), sodium hydroxide (NaOH, CAS Number: 1310-73-2, Sigma-Aldrich, Germany), sodium thiosulphate ($Na_2S_2O_3$, CAS Number: 7772-98-7, Sigma-Aldrich, Germany), sulphuric acid (H_2SO_4, CAS Number: 7664-93-9, Sigma-Aldrich, Germany), potassium hydroxide (KOH, CAS Number: 1310-58-3, Sigma-Aldrich, Germany), sodium chloride (NaCl, CAS Number: 7647-14-5, Sigma-Aldrich, Germany), boric acid (H_3BO_3, CAS Number: 10043-35-3, Sigma-Aldrich, Germany), catalyst (CAS Number: 7778-80-5, Potassium (K, Sigma-Aldrich, Germany), distilled water (from the Benue State University laboratory) were prepared.

2.3. Sample collection and preparation

Samples of these beverages were prepared in three different locations within the Benue State University environment and taken to the laboratory (Department of Chemistry) for analysis. The samples were stored in a refrigerator at 4 ºC and used periodically until the analysis was completed.

2.4. Proximate analyses

2.4.1.Determination of moisture content

Moisture was determined using the previous methods [13]. 2.0 g of the sample was mixed and placed into the weighed crucible, and the weight of the crucible plus the weight of the un-dried sample was recorded as W_2. The crucible and contents were kept in a moisture oven at 105 °C for 1 hour. The samples were removed from the oven, cooled in a desiccator for 30 minutes, and weighed. This process continued until a constant weight was observed, and the observed weight was recorded as W_3 [14]. The moisture content was calculated by Equations 1 and 2.

$$\% \text{ Moisture} = \frac{\text{weight loss}}{\text{Sample weight}} \times 100 \quad \text{(Eq.1)}$$

$$\% \text{ Moisture } \frac{W2-W3}{W2-W1} \times 100 \quad \text{(Eq.2)}$$

Where W_1 = weight of the empty crucible

W_2 = weight of crucible + food sample before drying.

W_3 = weight of crucible + food sample after drying.

2.4.2.Determination of ash content

The ash was determined using the method described by Akobundu et al. [15]. A crucible was placed in an oven regulated at 105°C for 30 minutes to dry. It was removed, cooled in a desiccator, weighed, and recorded as W_1. 2.0 g of the sample was placed in the crucible, and the weight of the crucible plus sample was recorded as W_2. The crucible containing the sample was heated or incinerated

in a muffle furnace at 200ºC for 4 h. The ash was cooled in a desiccator and weighed; the weight was recorded as W_3. The ash content was calculated using Equations 3 and 4.

$$\% \text{ Ash} = \frac{\text{weight of ash}}{\text{Weight of sample}} \times 100 \quad \text{(Eq.3)}$$

$$= \frac{W3-W1}{W2-W1} \times 100 \quad \text{(Eq.4)}$$

Where: W_1= weight of the empty crucible
W_2= weight of crucible + food before drying and/or ashing
W_3= weight of crucible + ash

2.4.3.Determination of crude fibre

The fiber was determined using the method described by Amusa et al. [16]. 2.0 g of the sample was weighed in a beaker, 100 mL of a solution containing 1.25 g of NaOH was added, and the volume was made up to 200 mL with distilled water. The final mixture was boiled for 30 minutes and then filtered through a thin, closed pad of washed and ignited asbestos in a Gooch crucible. The final residue was put in a crucible, dried in an oven at 100°C for 30 minutes, and then cooled in a desiccator. The weight of the oven-dried residue was recorded as W1. It was afterward incinerated in a muffle furnace at 200°C for 1 hour until a constant weight was observed. The weight of the crucible and ash were equally noted. The loss in weight after incineration multiplied by 100 is the percentage of the crude fiber (Eq.5).

$$\% \text{ Crude fibre} = \frac{W1-W2}{W0} \times 100 \quad \text{(Eq.5)}$$

Where: W_1 = Weight of crucible + residue before ashing
W_2 = Weight of crucible + ash
W_0 = Weight of sample

2.4.4.Determination of fat content

Fat in the samples was determined using the standard method described by Thiex et al. [17]. 250 mL clean boiling flask was dried in an oven at 105 – 110°C for 30 minutes and placed in a desiccator to cool. 2.0 g of the sample was weighed accurately to a labeled extraction thimble. 300ml of petroleum ether (boiling point 40-60°C) was filled into previously weighed, cooled boiling flasks (250 mL). The extraction thimble was plugged lightly with cotton wool. The Soxhlet apparatus was assembled with its contents and allowed to reflux for about 6 hours. The petroleum ether in the flask was distilled and drained into a container for reuse. Almost free of petroleum ether, the flask was dried in an oven at 105-110°C for 1 hour. The flask and the contents were placed into a desiccator, allowed to cool, and then weighed. The amount of fat extracted was obtained from the difference between the weight of the flask before and after the extract was dried, as Equations 6 [18]. The obtained weight was expressed as a percentage of the 2.0 g sample used.

$$\% \text{ Total fat} = \frac{W3-W2}{W1} \times 100 \quad \text{(Eq.6)}$$

Where: W_1 = Weight of sample (g)
W_2 = Weight of flask (g)
W_3 = Weight of flask + fat (g)

2.4.5.Determination of crude protein content

Protein in the samples was determined using the standard method described by Wilson et al. [19]. 2.0 g of sample was weighed and poured into the Kjeldahl flask. 2.0 g of catalyst was similarly weighed and transferred into the flasks. 20 mL concentrated H_2SO_4, and a glass bead (glass beads prevent bumping during heating) were added, and the heat was done gently in the heating mantles. There was occasional shaking till the solution assumed a green color (the temperature of the digester was above 300 °C for 2 hours). The resultant solution was cooled and washed down with distilled water and rinsed gently until the green colour disappeared, and then it was allowed to cool. The digest was transferred with several washings into a 250 mL volumetric flask and made up to the mark with distilled water. The resultant solution was distilled using a Markham distillation apparatus.

2.4.6.Determination of Protein distillation,

Titration and Carbohydrate

The Markham distillation apparatus was steamed through for about 15 minutes before use. A 100 mL conical flask containing 30 mL of 4 % boric acid was placed under the condenser such that the condenser tip was under the liquid. 10 mL of the digest was pipetted into the body of the apparatus via the small funnel aperture, washed down with 50 mL distilled water, and added 50 mL of 40 % NaOH. The distillation was run at 200 °C until about 100 mL of distillate was collected. The receiving flask was removed, the tip of the condenser was washed down into the flask, and the condensed water was removed. The solution in the receiving flask was titrated using HCl (0.1 N) and a few drops of methyl red indicator. The colour changed from transparent yellow to orange, and the final burette reading was recorded. The nitrogen content was finally calculated, hence the protein content of the drinks [20]. The nitrogen (%) and crude protein (%) were calculated by Equations 7 and 8. The crude carbohydrate content was obtained using the difference (AOAC method). The major components of any foodstuff are expressed in terms of 100 %. Therefore, the sum of all the other components determined subtracted from 100 gives the crude carbohydrate content. The percentage of crude carbohydrate content was determined by a differential method as follows by Equation 9.

$$\% \text{ Nitrogen} = \frac{\text{Titre value} \times \text{NA} \times \text{AF} \times \text{MW } N_2}{\text{Weight of sample} \times \text{DF}} \quad \text{(Eq.7)}$$

$$\% \text{ Crude Protein} = \% \text{ N} \times \text{F} \times \text{DF} \quad \text{(Eq.8)}$$

$$\% \text{ Carbohydrate} = 100 - (\% \text{ Moisture} + \% \text{ Ash} + \% \text{ fiber} + \% \text{ fat} + \% \text{ protein}) \quad \text{(Eq.9)}$$

Where F is the conversion factor = 6.25
DF=Dilution Factor, NA: Normality of Acid, AF: acid Factor, MW: Molecular Weight

2.5. Physico-chemical characterization

Titratable acidity was determined using the method described by Adeiye et al. [21]. Approximately 20 g of the sample was weighed into a 250 mL conical flask and diluted with twice its volume of distilled water. 2 mL of phenolphthalein indicator was added to the mixture, and the mixture was titrated with 0.1 N NaOH to a persistent pink color. The titratable acidity was reported as % lactic acid by weight using 1 mL of NaOH (0.1M) = 0.0090 g [22]. The pH of the sample was measured by an electrometric method using a laboratory pH Meter Hanna model H1991300, and the value was recorded. Approximately 40 mL of the sample was filled into a 50 mL beaker for the viscosity test. The viscosity test was measured using a standard Brookfield viscometer, and the value was recorded. Osanloo et al. reported validating a new and cost-effective method based on AgNPs coating on micro glassy balls for mercury vapor removal [23]. Also, apparent colloidal stability was measured using the method of Omueti et al. [24]. The sample was placed in a graduated tube and held in racks in the refrigerator undisturbed at 4°C. Changes in apparent colloidal stability were indicated by separation into two layers. The level of the visible line of demarcation between the settled and remaining portion of the sample solution was measured (height in cm) and recorded over 72 h [25].

2.6. Analysis Procedures

Flame atomic absorption spectrophotometry (F-AAS) and UV-Vis spectrometry (Schema 1) determined zinc, calcium, magnesium, potassium, and phosphorus minerals. One gram of each was dry-ash in a muffle furnace at 550 ºC for 5 hours until a white residue of constant weight was obtained. The minerals were extracted from ash by adding 20.0 mL of 2.5 % HCl and heating in a steam bath to reduce the volume to about 7.0 mL, and this was transferred quantitatively to a 50 mL volumetric flask. It was diluted to volume (50 mL) with deionized water and stored in clean polyethylene bottles. The mineral contents were determined using F-AAS (model 2380 spectrophotometer, PerkinElmer, Waltham, MA, USA).

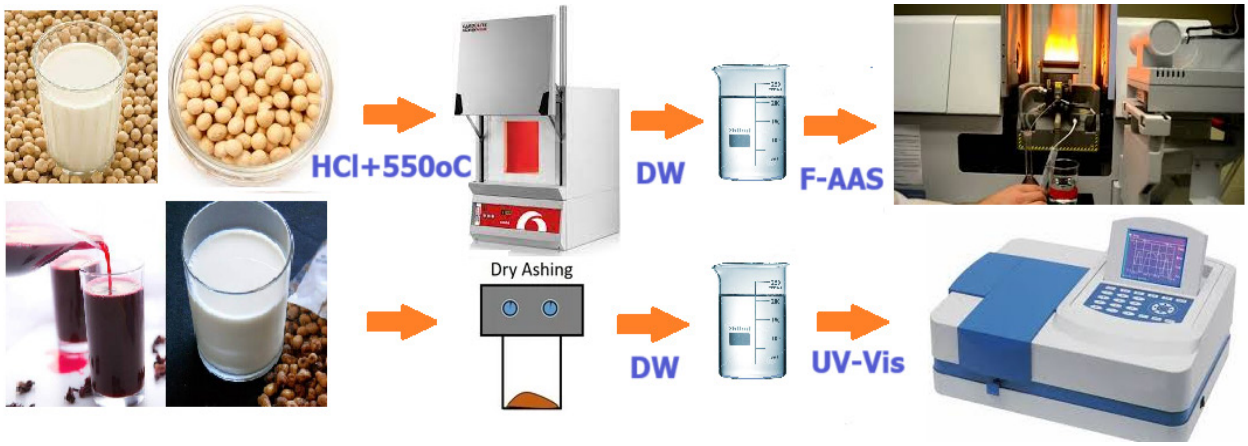

Schema 1. The procedure for determination of Zn, Ca, Mg, K, and P by F-AAS and UV-Vis spectrometry

3. Results and Discussion

In this research, the proximate analyses, physicochemical characterization, and mineral composition of soy milk, Kunu, and Zobo sold within the Benue State University environment were analyzed, and the results are presented in Tables 1-3 and Figures 1-3. Also. The Comparative Analysis of the proximate, physicochemical, and mineral composition of soy milk, Kunu, and Zobo compared to other works in Table 4.

Table 1. The proximate analyses of soy milk, *Kunu,* and *Zobo* (%)

S/N	Parameters	Soy milk	Kunu	Zobo
1	Moisture content	77.18 ± 2.10	80.20 ± 1.21	82.89 ± 1.33
2	Ash content	1.02 ± 0.05	0.25 ± 0.01	0.31 ± 0.02
3	Crude fibre	4.16 ± 1.12	5.40 ± 1.50	4.12 ± 1.10
4	Crude protein	12.17 ± 1.25	8.75 ± 1.11	6.54 ± 1.05
5	Crude fat	2.10 ± 0.22	1.80 ± 1.01	1.60 ± 0.01
6	Carbohydrate content	3.37 ± 1.15	3.60 ± 1.51	4.54 ± 1.55

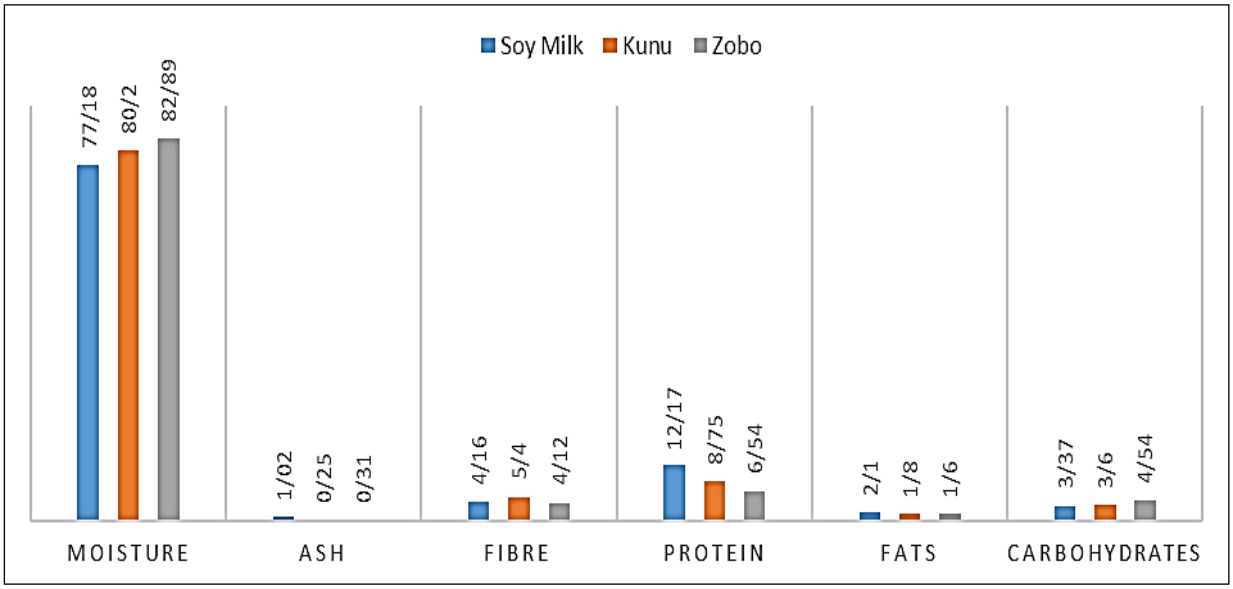

Fig. 1. Shows the graphical representation of the proximate analyses of soy milk, *Kunu* and *Zobo* (%)

Table 2. The physicochemical characterization of soy milk, *Kunu* and *Zobo*

S/N	Parameters	Soy milk	Kunu	Zobo
1	Titratable acidity (%)	0.28 ± 0.03	0.24 ± 0.02	0.18 ± 0.01
2	pH (%)	6.50 ± 1.25	4.00 ± 1.52	2.90 ± 0.22
3	Apparent colloidal stability (%)	60.40 ± 3.25	68.90 ± 3.55	88.40 ± 3.95
4	Viscosity (Centipoise (cP)	0.45 ± 0.02	0.23 ± 0.01	0.22 ± 0.01
5	Total solids (%)	39.82 ± 2.23	33.80 ± 2.32	29.99 ± 1.11

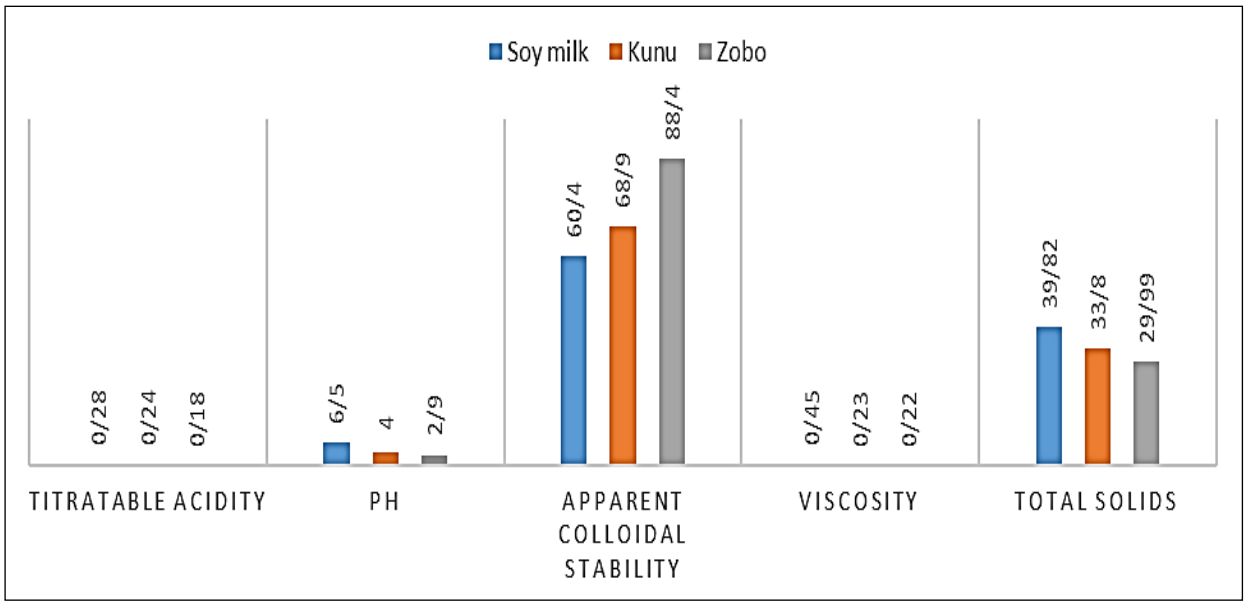

Fig. 2. Shows the graphical representation of the Physico-chemical Characterization of soy milk, *Kunu* and *Zobo* in %, viscosity in Centipoise (cP)

Table. 3. The results of the mineral composition of Soy milk, *Kunu* and *Zobo* in mg 100 g^{-1}

S/N	Parameters	Soy milk	Kunu	Zobo	WHO limit (2021)
1	Zinc	1.35 ± 0.03	3.61 ± 0.23	2.57 ± 0.11	3.00
2	Calcium	38.13 ± 2.55	27.48 ± 2.22	99.20 ± 3.55	75.00
3	Magnesium	12.61 ± 1.25	33.24 ± 2.01	51.84 ± 3.52	50.00
4	Potassium	64.02 ± 3.43	102.58 ± 4.25	91.19 ± 3.22	65.00
5	Phosphorus	0.320.03	0.570.02	0.540.01	0.36

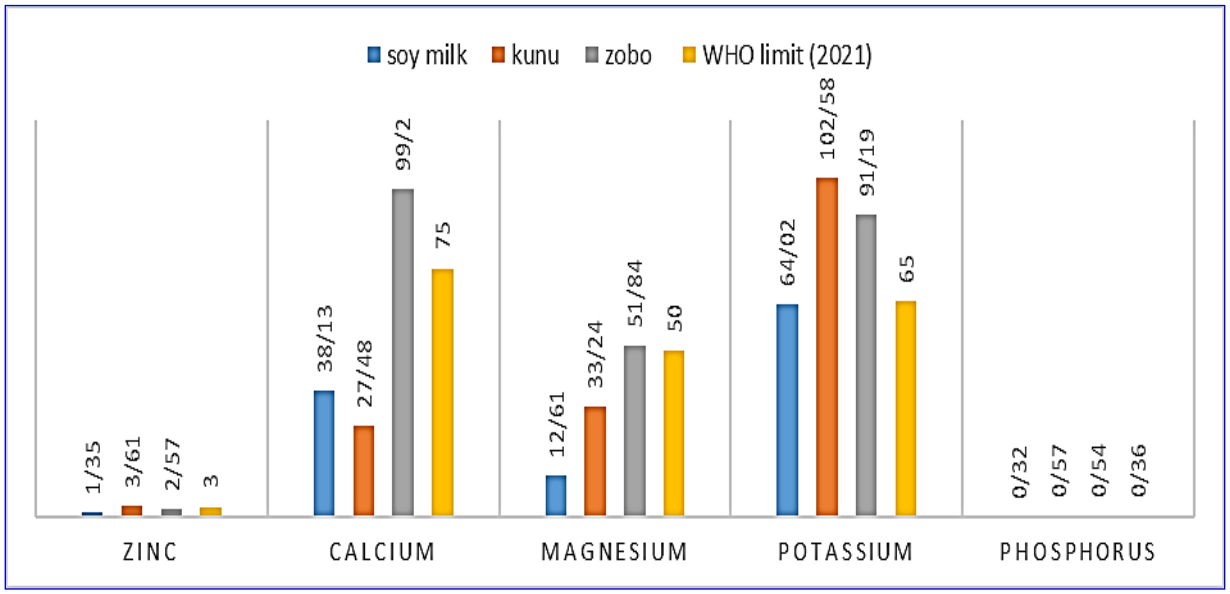

Fig. 3. Mineral composition of soy milk, *Kunu,* and *Zobo* in mg 100 g^{-1}

Table 4. Comparative Analysis of the proximate, physicochemical, and mineral composition of soy milk, Kunu, and Zobo

Parameter	Soy Milk (Found)	Kunu (Found)	Zobo (Found)	Other Studies	Ref.
Moisture Content (%)	77.18±2.10	80.20±1.21	82.89±1.33	75-85% (varies)	[13]
Ash Content (%)	1.02±0.05	0.25±0.01	0.31±0.02	0.5-1.5% (soy milk)	[15]
Crude Fibre (%)	4.16±1.12	5.40±1.50	4.12±1.10	3-6% (varies)	[16]
Crude Protein (%)	12.17±1.25	8.75±1.11	6.54±1.05	10-12% (soy milk)	[19]
Crude Fat (%)	2.10±0.22	1.80±1.01	1.60±0.01	1.5-3% (varies)	[17]
Carbohydrate Content (%)	3.37±1.15	3.60±1.51	4.54±1.55	3-5% (varies)	[20]
pH	6.50±1.25	4.00±1.52	2.90±0.22	6.0-7.0 (soy milk	[22]
Viscosity (Centipoise (cP)	0.45±0.02	0.23±0.01	0.22±0.01	0.4-0.5 (soy milk	[23]
Total Solids (%)	39.82±2.23	33.80±2.32	29.99±1.11	30-40% (soy milk	[24]
Zinc (mg 100 g^{-1})	1.35±0.03	3.61±0.23	2.57±0.11	1-3 mg 100 g^{-1} (varies)	[26]
Calcium (mg 100 g^{-1})	38.13±2.55	27.48±2.22	99.20±3.55	25-100 mg 100 g^{-1} (varies)	[27]
Magnesium (mg 100 g^{-1})	12.61±1.25	33.24±2.01	51.84±3.52	10-50 mg 100 g^{-1} (varies)	[28]
Potassium (mg 100 g^{-1})	64.02±3.43	102.58±4.25	91.19±3.22	50-100 mg 100 g^{-1} (varies)	[29]
Phosphorus (mg 100 g^{-1})	0.32±0.03	0.57±0.02	0.54±0.01	mg 100 g^{-1} (varies)	[30]

3.1. Discussion

The parameters obtained for the proximate analyses, physicochemical characterization, and mineral composition of Soy milk, Kunu, and *Zobo* sold within Benue State University environment are presented in Tables1-3. Table 1 presents the proximate analyses of soy milk, Kunu, and Zobo, indicating their respective percentages of various nutritional components. The moisture content is highest in Zobo (82.891.33%) and lowest in soy milk (77.182.10%). Soy milk has the highest ash content (1.020.05%), while Kunu has the lowest (0.250.01%). In terms of crude fiber, Kunu leads with 5.401.50%, followed by soy milk (4.161.12%) and Zobo (4.121.10%). Soy milk also has the highest crude protein content at 12.171.25%, with Kunu and Zobo trailing at 8.751.11% and 6.541.05%, respectively. The crude fat content is

slightly higher in soy milk (2.100.22%) compared to Kunu (1.801.01%) and Zobo (1.600.01%). Lastly, carbohydrate content is highest in Zobo (4.541.55%), with Kunu (3.601.51%) and soy milk (4.541.55%) having slightly lower values. Table 2 presents the physico-chemical characterization of three beverages: soy milk, Kunu, and Zobo. The titratable acidity values indicate that soy milk has the highest acidity (0.28±0.03%), followed by Kunu (0.24±0.02%) and Zobo (0.18±0.01%). The pH levels show that soy milk is the least acidic (pH 6.50±1.25), Kunu is more acidic (pH 4.00±1.52), and Zobo is the most acidic (pH 2.90±0.22). Apparent colloidal stability is highest in Zobo (88.40±3.95%), indicating better suspension of particles, while soy milk has the lowest stability (60.40±3.25%). Viscosity measurements reveal that soy milk is the most viscous (0.45±0.02), whereas Kunu and Zobo have similar, lower viscosities (0.23±0.01 cP and 0.22±0.01 cP, respectively). Total solids content is highest in soy milk (39.82±2.23%), followed by Kunu (33.80±2.32%) and Zobo (29.99±1.11%). These parameters highlight significant differences in the physical and chemical properties of the three beverages. Table 3 presents the mineral composition of soy milk, Kunu, and Zobo, compared to the WHO limit [26]. Zinc content is highest in Kunu (3.61±0.23 mg 100 g^{-1}), exceeding the WHO limit of 3.00 mg 100 g^{-1}, while soy milk has the lowest zinc content (1.35±0.03 mg 100 g^{-1}). Calcium levels are highest in Zobo (99.20±3.55 mg 100 g^{-1}), surpassing the WHO limit of 75.00 mg 100 g^{-1}, with soy milk having a moderate amount (38.13±2.55 mg 100 g^{-1}). Magnesium content is highest in Zobo (51.84±3.52 mg 100 g^{-1}), also above the WHO limit of 50.00 mg 100 g^{-1}, whereas soy milk has the lowest (12.61±1.25 mg 100 g^{-1}). Potassium is most abundant in Kunu (102.58±4.25 mg 100 g^{-1}), exceeding the WHO limit of 65 mg 100 g^{-1}, with soy milk containing the least (64.02±3.43 mg 100 g^{-1}). Phosphorus levels are low across all beverages but highest in Kunu (0.57±0.02 mg 100 g^{-1}) and slightly above the WHO limit of 0.36 mg 100 g^{-1} [27]. This table highlights the varying mineral profiles of these beverages and their compliance with WHO standards. Moisture content determines a sample's water content and, indirectly, its dry matter content. It is also an indicator of the flour sample's storage stability [28]. Moisture levels above 14% make substances susceptible to microbial growth, reducing their storability [29]. Unfortunately, the moisture levels of soy milk, Kunu, and Zobo drinks in this investigation exceed the 14% spoilage threshold. This means these beverages are prone to microbial growth and have a shorter shelf life. These results are consistent with previous findings by Tunde et al. [30], who reported that the moisture content in these drinks is greater than 80%. Ash content measures the total minerals present in a product. The ash values of soy milk, Kunu, and Zobo drinks are 1.02 ± 0.01, 0.31 ± 0.05, and 0.23 ± 0.03, respectively, indicating that soy milk contains the highest mineral content among the evaluated products. Fiber has been shown to improve digestion and reduce the risk of constipation in consumers [31]. Kunu drink has the highest crude fiber content at 5.40 ± 1.50, likely due to ingredients such as potatoes or ginger. Soy milk was found to have the highest protein content among the analyzed products. This is because its main ingredient, soybeans, is a high-protein food, unlike Kunu and Zobo, which primarily contain minerals. The crude fat content also varies among the products, with soy milk having the highest fat content due to its oilseed base. The carbohydrate content of soy milk, Kunu, and Zobo drinks was found to be 3.37 ± 1.15, 3.60 ± 1.51, and 4.54 ± 1.55, respectively [32]. These results are significantly higher than those reported by Hopkins et al. [33]. As shown in Table 2, the titratable acidity values for soy milk, Kunu, and Zobo were found to be 0.28 ± 0.03, 0.24 ± 0.02, and 0.18 ± 0.01, respectively. The higher acidity of soy milk could provide better storage stability against acid-intolerant microorganisms. The pH of Kunu, recorded at 4.00 ± 1.52, was higher than that of Zobo at 2.90 ± 0.22 but lower than that of soy milk at 6.50 ± 1.25. The pH of soy milk was also higher than the 5.37-5.84 range

reported by Crowley et al. [34]. High levels of acetic amino acids in soybean-based beverages might contribute to the higher pH of soy milk. The more acidic pH of these drinks could be advantageous as it may inhibit the growth of pathogens that cause gastrointestinal problems [35]. Sugars and other macromolecules typically affect viscosity in food systems through their interaction with the solution or solvent [36]. The viscosities of soy milk, Kunu, and Zobo were found to be 0.45 ± 0.02, 0.23 ± 0.01, and 0.22 ± 0.01, respectively. The high sugar content in soybeans might contribute to the increased viscosity of soy milk. The total solids content values of 39.82 ± 2.23 for soy milk, 33.80 ± 2.32 for Kunu, and 29.99 ± 1.11 for Zobo observed in this study may be attributed to the processing methods. Soaking and blanching improve total solids extraction [37]. The higher level of total solids in soy milk may be due to the higher levels of suspended particles contributed by the soybeans [38,39], suggesting that the total solids of soy milk could be improved by adding soybean flour. Increasing the total solids enhances the nutritive value of the product and improves quality sustainability [40]. The mineral composition of soy milk, Kunu, and Zobo reveals varying compliance with WHO permissible limits. The amounts of zinc, calcium, magnesium, potassium, and phosphorus in soy milk fall within the WHO-recommended limits. For Kunu, zinc, potassium, and phosphorus levels slightly exceed the WHO limits. In Zobo, calcium, magnesium, potassium, and phosphorus levels are slightly above the WHO limits. This indicates that while soy milk meets all WHO standards for these minerals, Kunu and Zobo exceed some of these recommended levels. Table 4 displays a comparative analysis of the findings from this study with those obtained through various methods in prior research for soy milk, Kunu, and Zobo. The results indicate that the values obtained generally align with those reported in other studies, albeit with slight deviations attributed to distinct preparation techniques and ingredient origins. Soy milk typically contains a higher moisture content than Kunu and Zobo, falling within 75-85% [41], whereas Kunu and Zobo exhibit slightly lower moisture levels. The ash content of soy milk is generally higher (0.5-1.5%) than Kunu and Zobo (0.2-0.5%). However, all three beverages share similar ranges in crude fiber content, typically falling between 3-6%. In terms of protein content, soy milk stands out with a higher proportion (10-12%) compared to Kunu and Zobo (5-8%) [42,43]. Similarly, soy milk contains more crude fat content (1.5-3%) than Kunu and Zobo. Carbohydrate content, however, remains comparable across all beverages, ranging from 3-5%. Regarding pH levels, soy milk tends to be more neutral (pH 6.0-7.0) compared to the acidic nature of Kunu and Zobo (pH 3.0-4.5) [42,43]. Viscosity measurements show soy milk has a higher viscosity (0.4-0.5 cP) than Kunu and Zobo (0.2-0.3 cP). Total solids content varies, with soy milk generally having a higher range (30-40%) compared to Kunu and Zobo (25-35%) [44]. The mineral composition also differs among the beverages. For instance, soy milk contains higher levels of calcium (25-100 mg 100 g^{-1}) compared to Kunu and Zobo. Conversely, Kunu and Zobo exhibit higher levels of zinc (1-3 mg 100 g^{-1}) and potassium (50-100 mg 100 g^{-1}) than soy milk.

4. Conclusion

From this study, locally made (processed) soy milk, *Kunu*, and Zobo beverage drinks sold at Benue State University, Makurdi, contain appreciable amounts of fats, moisture, fiber, ash, carbohydrates, and high amounts of protein and can supply the protein requirements for the proper functioning of the body. The results show that the pH values of soy milk, *Kunu* drink, and Zobo beverage drinks are low (acidic); this is an advantage because the drinks inhibit the growth of disease-causing microorganisms that can facilitate spoilage. In conclusion, locally made soy milk, *Kunu*, and Zobo drinks sold at Benue State University, Makurdi, Nigeria, contain essential ingredients in a good range of proportions and are safe for consumption.

5. Acknowledgements

The authors would like to thank the Department of Chemistry, Benue State University, Makurdi, Benue State, Nigeria.

6. References

[1] B. Abbasi, M. Mirlohi, M. Daniali, R. Ghiasvand, Effect of probiotic soymilk on lipid panel in type 2 diabetic patients with nephropathy: A double-blind randomized clinical trial, Prog. Nutr., 20 (2018) 70–78. https://doi.org/10.23751/pn.v20i2-S.5342

[2] F. Afroz, W. Anjum, Md. Nurulislam, A. Kabir, K. Hossain, Abu. Sayed, Preparation of soymilk using different methods, Food Nutr. Sci., 4 (2016) 11– 17. https://doi.org/10.11648/j.jfns.20160401.13

[3] A. Bukar, A. Uba, T.I. Oyeyi, Occurrence of some entropathogenic bacteria in some minimally and fully processed ready–to-eat foods in Kano metropolis, Nigeria, African J. Food Sci., 4 (2010) 032 – 036. https://academicjournals.org/article/article1380705484_Bukar%20et%20al.pdf

[4] F. Golbabaei, A. Vahid, A. Faghihi Zarandi, A novel nano-palladium embedded on the mesoporous silica nanoparticles for mercury vapor removal from air by the gas field separation consolidation process, Appl. Nanosci., 12 (2022) 1667-1682. https://doi.org/10.1007/s13204-022-02366-0

[5] F. Golbabaei, H. Hassani, F. Eftekhar, M.J. Kian, Occupational exposure to mercury: air exposure assessment and biological monitoring based on dispersive ionic liquid-liquid microextraction, Iran. J. Public Health, 43(2014) 793-799. http://ijph.tums.ac.ir

[6] F Golbabaei, A Ebrahimi, A Koohpaei, A Faghihi-Zarandi, Single-walled carbon nanotubes (SWCNTs), as a novel sorbent for determination of mercury in air, Global J. Health Sci., 8 (2016) 273-280. https://doi.org/10.5539/gjhs.v8n7p273

[7] F. Golbabai, A. Ebrahimi, Performance comparison survey of multi-walled and single-walled carbon nanotubes for adsorption and desorption of mercury vapors in the air, Iran. Occup. Health, 10 (2013) 21-31. https://espace.library.uq.edu.au/view/UQ:9d03f02

[8] J. Rakhtshah, M. Dehghani Mobarake, Simultaneously speciation and determination of manganese (II) and (VII) ions in water, food, and vegetable samples based on immobilization of N-acetylcysteine on multi-walled carbon nanotubes, Food Chem., 389 (2022) 133124. https://doi.org/10.1016/j.foodchem.2022.133124

[9] J. Rakhtshah, E. Kolvari, Ultrasound assisted-dispersive-modification solid-phase extraction using task-specific ionic liquid immobilized on multiwall carbon nanotubes for speciation and determination mercury in water samples, Microchem. J., 154 (2020) 104632. https://doi.org/10.1016/j.microc.2020.104632

[10] J. Rakhtshah, N.M. Kazemi, A novel biostructure sorbent based on CysSB/MetSB@ MWCNTs for separation of nickel and cobalt in biological samples by ultrasound assisted-dispersive ionic liquid-suspension solid phase micro extraction, J. Pharm. Biomed. Anal., 172 (2019) 285-294. https://doi.org/10.1016/j.jpba.2019.05.003

[11] M.D. Mobarake, Ultrasound-assisted solid-liquid trap phase extraction based on functionalized multi wall carbon nanotubes for preconcentration and separation of nickel in petrochemical wastewater, J. Anal. Chem., 74 (2019) 865-876. https://doi.org/10.1134/s1061934819090090

[12] L.D. Johnson, Influence of soybean variety and processing method on tofu manufacturing, quality and consumer acceptability, Retrospective Theses and Dissertations, 12 (1984) 1-128. https://doi.org/10.31274/rtd-180813-10934

[13] S.C. Achinewhu, L.I. Barber, I.O. Ijeoma, Physicochemical properties and garification (gari yield) of selected cassava cultivars in Rivers State, Nigeria, Plant Foods Hum.

Nutr., 52 (1998) 133-140. https://doi.org/10.1023/a:1008029101710

[14] I.G. Adanlawo, V.A. Ajibade, Nutritive value of the two varieties of roselle (Hibiscus sabdariffa) calyces soaked with wood ash, Pakistan J. Nutr., 5 (2006) 555-557. https://doi.org/10.3923/pjn.2006.555.557

[15] E. N. T. Akobundu, J.P. Cherry, Simmonds, chemical, functional and nutritional properties of Egusi (Coloeynthis citrullus L.) seed protein products, J. Food Sci. 47 (1982) 829-835. https://doi.org/10.1111/j.1365-2621.1982.tb12725.x

[16] N.A. Amusa, O.A. Ashaye, Effect of processing on nutritional, microbiological and sensory properties of Kunun-Zaki (A sorghum based non-alcoholic beverage) widely consumed in Nigeria, Pakistan J. Nutr., 8 (2009) 288-292. https://doi.org/10.3923/pjn.2009.288.292

[17] N. Thiex, L. Novotny, A. Crawford, Determination of ash in animal feed: AOAC official method 942.05 revisited, J. AOAC Int., 95 (2012) 1392-1397. https://doi.org/10.5740/jaoacint.12-129

[18] S. Kumaresan, V. Veerichetty, S. Nachimuthu, B. Sadhasivam, R. Ponnusamy, Antidiabetic potential of the combination of fermented soy milk and flaxseed milk in alloxan-induced diabetic rats, Int. J. Green Pharm., 12 (2018) S763– S768. https://doi.org/10.22377/ijgp.v12i03.2115

[19] D.L. Erickson, Practical Handbook of Soybean Processing and Utilization. Publisher AOCS Press, Pages 1-130, 2015. https://www.amazon.com/Practical-Handbook-Soybean-Processing-Utilization/dp/0935315632

[20] S.C. Achinewhu, L.I. Barber, O. Ijeoma, Physicochemical properties and garification (gari yield) of selected cassava cultivars in Rivers State, Nigeria, Plant Foods Hum. Nutr., 52 (1998) 133-140. https://doi.org/10.1023/a:1008029101710

[21] O.A. Adeiye, S.O. Gbadamosi, A.K. Taiwo, Effects of some processing factors on the characteristics of stored groundnut milk extract, African J. Food Sci., 7 (2013) 134-142. https://doi.org/10.5897/AJFS12.149

[22] K. Liu, Soybean trypsin inhibitor assay: Further improvement of the standard method approved and reapproved by American oil chemists' Society and American Association of Cereal Chemists, Int. J. Am. Oil Chem. Soc., 96 (2019) 635–645. https://doi.org/10.1002/aocs.12205

[23] M. Osanloo, Validation of a new and cost-effective method for mercury vapor removal based on silver nanoparticles coating on micro glassy balls, Atmos. Pollut. Res., 8 (2017) 359-365. https://doi.org/10.1016/j.apr.2016.10.004

[24] O. Omueti, Chemical and sensory attributes of soy-corn milk types, African J. Biotechnol., 4 (2005) 847-851. https://academicjournals.org/article/article1380097477_Omueti%20and%20Ajomale.pdf

[25] M.O. Aremu, H. Ibrahim, S.O. Aremu, Lipid composition of black variety of raw and boiled tigernut (Cyperus esculentus L) grown in North-East Nigeria, Pakistan J. Nutr., 15 (2016) 427-438. https://doi.org/10.3923/pjn.2016.427.438

[26] J.A. Ayo, H. Umianze, T. Gaffa, Microbiological evaluation of "Kunun zaki" and "Zoborodo" drink (beverage) locally produced and sold in a polytechnic community in Nigeria, Niger Food J., 22 (2005) 119-126. https://doi.org/10.4314/nifoj.v22i1.33576

[27] A. J. Adekunle, I.B. Oluwalana, Production and evaluation of millet- egg-soybean hull composite flour: A weaning food, J. Food Nutri., 1 (2011) 7-13. https://doi.org/10.5251/ajfn.2011.1.1.7.13

[28] O.A. Fabiyi, R.O. Alabi, Nanoparticles' synthesis and their application in the management of phytonematodes: an overview, Management of phytonematodes: recent advances and future challenges, Singapore Springer Publisher, pp 125–140, 2020. https://doi.org/10.1007/978-981-15-4087-5_6

[29] O. A. Effiom, Choriostoma of the gingivae following trauma: An unusual case in a Nigerian with review of relevant literature, Niger. J. Den. Res., 3 (2018) 45-49. https://www.njdres.com/index.php/njdres/article/view/292/178

[30] A. Tunde, O. Sowonola, F. Adedeji, Nutritional and sensory qualities of soymilk - kunnu blends, African J. Food, Agri., 5 (2005) 1-12. https://doi.org/10.18697/ajfand.9.1500

[31] A.R. Gbadegesin, S.O. Gbadamosi, Pineapple flavoured roselle drink concentrates: nutritional, physicochemical and sensory properties, Annals: Food Sci. Technol., 18 (2017) 164-172. https://afst.valahia.ro/wp-content/uploads/2022/09/I.7_Ronke.pdf

[32] M.A. Belewu, O.A. Abodunrin, Preparation of Kunu from unexploited rich food source: tigernut (Cyperus esculentus), Pakistan J. Nutri., 7 (2008) 109-111. https://doi.org/10.3923/pjn.2008.109.111

[33] A.L. Hopkins, M.G. Lamm, J. Funk, C. Ritenbaugh, Hibiscus sabdariffa L. in the treatment of hypertension and hyperlipidemia: a comprehensive review of animal and human studies, Fitoterapia, 85 (2013) 84 -94. https://doi.org/10.1016/j.fitote.2013.01.003

[34] A. Bezie, The effect of different heat treatment on the nutritional value of milk and milk products and Shelf-Life of milk products, a review, Dairy Vet. Sci. J., 11 (2019) 001-008. https://doi.org/10.19080/JDVS.2019.11.555822

[35] R. Kuriyan, D.R. Kumar, R. Rajendran, A.V. Kurpad, An evaluation of the hypolipidemic effect of Hibiscussabdariffa leaves in hyperlipidemic Indians, BMC Complement. Altern. Med., 10 (2010) 27. http://www.biomedcentral.com/1472-6882/10/27

[36] L.O. Omoigui, A.Y. Kamara, Guide to soybean production in northern Nigeria, published by International Institute of Tropical Agriculture (IITA), Ibadan, Nigeria, 2020. https://www.iita.org/

[37] S. Y. Kiptiyah, E. Harmayani, The effect of blanching and extraction method on total phenolic content, total flavonoid content and antioxidant activity of Kencur (Kaempferia galanga. L) extract, IOP Conf. Ser.: Earth Environ. Sci., 709 (2021) 012025. https://doi.org/10.1088/1755-1315/709/1/012025

[38] G. Igor Vidigal, M. P. Melo, P. C. M. Da Rós, Rheological and physical properties effected by the thermal processing of fruit: A bibliometric analysis, Processes, 11 (2023) 2874. https://doi.org/10.3390/pr11102874

[39] O. Jennifer Nnenna, S. Nwiyege, Microbial quality of sliced and packaged fruits in polyethylene sold in port Harcourt rivers state, south-south Nigeria, J. Life Bio Sci. Res., 4 (2023) 25-30. https://doi.org/10.38094/jlbsr40197

[40] O.R. Ezeigbo, M.U. Ekaiko, N.G. Agomo, Antimicrobial effect of lime juice treatment on the shelf-life of Zobo drink, British Microbiol. Res. J., 6 (2015) 147-153. https://doi.org/10.9734/BMRJ/2015/15534

[41] Ar. Saini, A Review based study on Soymilk: Focuses on production technology, prospects and progress Scenario in last Decade, Pharm. Innov., 10 (2021) 486-494. https://doi.org/10.22271/tpi.2021.v10.i5g.6254

[42] E. Chiamaka Frances, Proximate, mineral and microbial analysis of locally produced juice (Kunu, Soymilk and Tigernut), Asian J. Food Res. Nutri., 2 (2023) 36-47. https://www.journalajfrn.com/index.php/AJFRN/article/view/36

[43] Y. Li, Y. Wan, Aggregation and gelation of soymilk protein after alkaline heat treatment: Effect of coagulants and their addition sequences, Food Hydrocoll., 135 (2023) 108178. https://doi.org/10.1016/j.foodhyd.2022.108178

[44] I. U. Nwiyi, Evaluation of food safety and nutritional quality of indigenous beverages vended in informal market of Nasarawa state, north central, Nigeria, Eurasian J. Food Sci. Technol., 6 (2022) 100-112. https://dergipark.org.tr/en/download/article-file/2466740